UNIVERSITY OF BIRMINGHAM

Supramolecular Surfaces for Protein Immobilisation

PhD in Chemical Engineering

Giuseppe Di Palma

A thesis submitted to the University of Birmingham

School of Chemical Engineering

College of Engineering and Physical Science

Supervisor: Professor Paula Mendes

September 2019

Abstract

Protein immobilisation represents nowadays one of the most challenging fields in science, and many technologies have been developed based on this idea. Biosensors, using the interaction of the protein with glucose, DNA, or antibody are only a few examples of the massive amount of applications related to the concept of protein immobilisation. Despite many signs of progress that have been made in this field, the best method to immobilise protein on the surface is still not well defined. The immobilisation of proteins on the surface is nowadays obtained mostly through chemical or physical adsorption. Both methods, even considering the considerable amount of applications that are possible to find nowadays, still present some disadvantages. The supramolecular chemistry has the potential to overcome all these problems in a very elegant, fast and straightforward way, implying the host-guest interaction between a scaffold molecule and a protein. According to this, the development of a protein immobilising technique on the surface represents one of the most challenging tasks nowadays. This work is focused on the study of supramolecular complex proteins-scaffold and on the conditions to reach a well-packed self-assembled monolayer of these scaffolds on a surface. This method, with better control of its physiological conditions, can be used for a deeper study on protein activity for the development of highly accurate biochips.

<<Science is but a perversion of itself unless it has as its ultimate goal the betterment of humanity>>

<<The progressive development of man is vitally dependent on invention.
It is the most important product of his creative brain.
Its ultimate purpose is the complete mastery of mind over the material world,
the harnessing of the forces of nature to human needs. >>

<<I am credited with being one of the hardest workers and perhaps I am, if thought is the equivalent of labor, for I have devoted to it almost all of my waking hours.
But if work is interpreted to be a definite performance in a specified time according to a rigid rule, then I may be the worst of idlers.
Every effort under compulsion demands a sacrifice of life-energy.
I never paid such a price.
On the contrary, I have thrived on my thoughts.>>

<<Originality thrives in seclusion,
free of outside influences beating upon us to cripple the creative mind.
Be alone, that is the secret of invention; be alone, that is when ideas are born.>>

Nikola Tesla

Acknowledgements

Voglio ringraziare la mia famiglia per ricordarmi sempre,
che per essere bravo in un gioco bisogna allenarsi molto,
e che per eccellere in un lavoro bisogna giocare tanto.

I want to thank my supervisor Professor Paula Mendes and Dr Stefano Tommasone, for their guidance and leadings.

Dr Lewis Hart, from University of Reading Department of Chemistry, for his inputs during the beginning of my PhD and for being such an amazing organic chemist (even better than me!).

Dr David J. Scurr and Anna M. Kotowska, from University of Nottingham School of Pharmacy for the TOF-SIMS surface characterisation experiments.

Dr Chi Tsang, from University of Birmingham School of Chemistry, for his inputs for the mass spectrometry experiments.

Dr Cecile Le Duff, from University of Birmingham School of Chemistry, for her advices during the NMR experiments.

Dr Daniel Escalera López, from University of Birmingham School of Chemical Engineering for his inputs in the Cyclic Voltammetry technique.

Dr Dominik Daisenberger, from the Diamond Light Source Crystallography Science Group, for his skills in the Diamond Anvil Cell technique and for exploring with me this new synthetic method at the borders and unmapped fields of organic chemistry.

I want to thank the version of myself back in 2015-2016.

Thank you for not giving up,
Thank you for believing every day in what you are doing.
Thank you for never letting your judgement be influenced by your angriness and sadness.
Thank you for always seeing a drop of solution where others just saw a sea of problems.

Your opinion about science is about to have a huge hit,
plus you will experience some health issues.
You will recover at 100%, but this experience will let you completely drained from a mental point of view.

Thank you for not let it knock you down.
Thank you for always being focused on your objectives and never look far away from your purposes.

Times are always hard for dreamers,
but at least you always have been honest to the people whom you have promised the prize.

It is during and after the recovery that you will be forced to look at the world from a different point of view.

Your priorities will be turned upside down,
the same things will start having different value to you,
the smallest details in the picture, will become the most important peculiarities.

From that moment and for an inexplicable reason,
your mind will become much clearer and your criticism much accurate.

With more accurate criticism,
you will not need anymore to look for anything.
The ideas for your research instead, will start coming at you automatically.

You will first understand that the biggest mistake that a scientist can do
is watching a phenomenon from one single aspect and assuming that the truth only has one single face.

You will learn that when nature starts having no sense,
it is time to change the interpretation that we have of it.

You will soon realise that it is time to change your inspirators.
You will soon start to appreciate more, understand better and consider further those scientists that, with their discoveries, changed the fate of the entire mankind.

Your ideas are good, your willing even better and stronger.
Keep always on this way and let the intuition and creativity being always part of your everyday work.

For your job,
follow your instincts and you will never regret anything.
Follow your passions and you will never work a single day of your life.

These sensors are good, you are on a good path.
They represent the prevention and the prevention will be the key to overcome easily in any battle:

<<Victorious warriors win first and then go to war, while defeated warriors go to war first and then seek to win>> Sun Tzu, The Art of War.

Do not forget that you are NOT pointing to the unique achievement that everybody is looking after, but anything that surrounds it.

Remember that you will be capable to reach it not by excelling in just one field,
but by being good enough to mix biology, applied chemistry and quantum physics.

The more topics you will own, the smoother will be the path.
The more theories you will be managing, the more problems will be resolved.

Choose your collaborators and the people around you carefully,
Choose always the quality over the quantity
Choose always the most passionate people over the skilled ones.

Because the skills can always be learned from anyone,
the passions only found inside someone.

Skills without passion represent a dangerous weakness.
While instead skills and passion together represent an incredible strength.

If you decide to keep working in academia, leave this research line only if you will be sure to reach the cure.

The cure will represent more difficulties to challenge and more mistakes to manage but the victory will be the most honourable one,

for the simple reason that no one deserves to be left behind.

<<Do not repeat those tactics which have gained you one victory, but let your methods be regulated by the infinite variety of circumstances.>> Sun Tzu, The Art of War

Table of Contents

List of illustrations

Figure 3.3 Example of a SAM molecule with a terminal group (green), backbone(black) and a head group (red).

Figure 3.3.1 Formation of a SAM. The head group (thiol) first interact with the surface (A and B). Then, the molecules start interacting with each other among them to assemble as an ordered structure(C).

Fig 3.3.2 Chemical structures of cystine and the thioctic acid molecules.

Fig. 3.3.3 The pinhole defects (A) derived from a missing molecule during the assembly. Domain defects (B) derived when large aggregates of assembled molecules approach each other. Disorder defects (C) given by a non-well assembled molecule.

Fig. 3.3.4 Example of a typical protein (green) interaction with a SAM. A surface crowded with the substrate (blue left) could determine an incomplete or a partial interaction between the SAM and the protein due to sterical problems. While instead, the addition of a spacer (red right) determines the lower probability of these problems to occur.

Fig. 4.1.1 General illustration of some of the immobilisation techniques explored in this literature review. It is possible to distinguish the physical adsorption (left) where the moieties represented in the picture are in this case antibodies adsorbed with no specific orientation. The obtained layer does not present order, and perhaps its properties (specificity and physical properties) are not well defined. Chemical immobilisation or crosslinking (centre) via covalent bonds where the molecules may present an orientation. The crosslinking could be further used to obtain a bioaffinity immobilisation (right). This picture was taken from reference 88.

Fig.4.1.2 The overall structure of fibrinogen and its side-off and side-on conformations. The shape in the plasma does not trigger an immune response as the Leukocyte

recognition sites are masked inside the structure. The physical adsorption of the same protein on a graphene sheet determines the exposure and the recognition sites triggering the immune response. The picture was taken from reference 105.

Figure 4.1.3. Molecular Dynamic of protein adsorption on single-walled carbon nanotubes. Depending on the diameter of the nanotube, the protein could be possibly adsorbed in the interior or exterior part, providing two new different protein shapes. The picture was taken from reference 113.

Figure 4.1.4 Protein adsorption on different sizes of nanoparticles. It is possible to notice that for a particle with a smaller diameter (in this case 4 nm and 20 nm) the protein conformation was well preserved. While instead for less curved surface, thus bigger diameter (100 nm) the protein structure tends to change once adsorbed. This image was taken from reference 116.

Figure 4.1.5 Corrosion process of the magnesium alloy Mg_2Ca in a saline solution (A) and a glucose solution (B). In the first case, a layer of insoluble salts forms on the surface of the alloy. This is due to the Magnesium and the Calcium forming insoluble salts: $Mg(OH)_2$, $Mg_5(CO_3)_4(OH)_2$, CaO, $CaCO_3$. In the second case, glucose is oxidised in gluconic acid, reacting with the magnesium and forming magnesium gluconate that dissolves later into the solution. This image was taken from reference 118.

Fig 4.2.1 Chemical adsorption where the protein is cross-linked to a surface via a functional molecule. The main strategies include the amine (1), thiol (2), and carboxyl crosslinking (3). The picture was taken from reference 33.

Figure 4.2.2 Chemical crosslinking used for the biorecognition of the substrate. In this case, the crosslinking is immunomediated due to the use of an antibody for the immobilisation of the substrate. The picture was taken from reference 130.

Fig 4.2.3 Crosslinking of two different types of glycosyltransferases. Both methods use the sortase enzyme that catalyses the crosslinking. The picture was taken from reference 130.

Fig 4.2.4 Chemical immobilisation mediated with the breaking of a disulphide bridge present in the protein structure.

Figure 4.2.5 TAMRA labelling of the peptide LRRASLG. If the peptide is not phosphorylated does not interact with the quantum dot, and no FRET is visible. In the opposite case, when the peptide is phosphorylated by a protein kinase, it starts to be excited by the quantum dot and the FRET is observable . The picture was taken from reference 146.

Fig 4.2.6 Chemical immobilisation of an enzyme for pesticides detection. The enzyme AChE is tagged with the peptide histidine (His), necessary for its chemical immobilisation on Ni/NiO nanoparticles surface. This picture was taken from reference 154.

Fig 4.2.7 Working principle of the TNT sensor. (Up) The electrode surface is functionalized with a bipyridine derivative (PBB). Then the Maltose Binding Protein (MBP) serves as a bridge among the PPB and the enzyme nitroreductase in charge of the real TNT detection. (Down). The electrons exchanged among the electrode and the nitrate (NO_2), typical of the TNT molecule, is mediated by the PPB and the nitroreductase. The intensity of the electric signal is proportional to the amount of NO_2 present in the sample. The picture was taken from reference 156.

Figure 4.3.1 (A) Chemical structure of the poly[bis(methacrylate)phosphazene] (PBMAP) hydrogels. (B) The swelling property is determined by the protein entrapment. This picture was taken from reference 167.

Figure 4.3.2 (Up) Chemical Structure of PEG hydrogels and its derivatives. The derivatives are fabricated to change the polarity of the hydrogels. (A)Ethanoic Acid, (B)hydroxy, (C) carboxyl and (D) methoxy-terminated PEG. Two examples of polymer brushes based on (E) poly(MeOEGMA) and (F) poly(HOEGMA). (Bottom) The overall architecture of PEG hydrogels. The SAM of initiator is essential for the anchor point to the surface. The picture was taken from reference 179.

Figure 4.3.3 Synthetic pathway for the fabrication of the polymerised high internal phase emulsion (polyHIPE), where the gel is first functionalised with the tert-butyl acrylate. In the second step, the acrylic group is deprotected to allow the protein binding in the third step. The picture was taken from reference 201.

Figure 4.3.4 Two examples of enzyme redox hydrogel. (Left) The glucose in the sample is transformed in gluconolactone by the Glucose Oxidase (GOx), giving an electron to the DNA hydrogel. Later the electron is transported to the anode and measured (Right). The same principle is applied in the case the enzyme immobilised is the Glucose Dehydrogenase (GDH) where this time the electron is generated by the conversion of the NAD+ in NADH. The picture was taken from reference 221.

Fig 4.4 Protein immobilisation mediated by a phospholipidic bilayer. The proteins (blue) are captured into the phospholipid bilayer macrostructure.

Figure 4.4.1 A schematic representation of the formation of dithiothreitol (DTT) SAMs on gold (Au) support (a) with subsequent fusion of dimyristoyl phosphatidylcholine

(DMPC) vesicles forming lipid bilayers; (b) horseradish peroxidase (HRP) immobilization on lipid bilayers supported on DTT/Au (c) and immunolabeling HRP immobilized on lipid bilayers (d). The picture was taken from reference 249.

Figure 4.4.2 The scheme of the choline immobilised on bilayer for the detection of hydrogen peroxidase (up) and the chemiluminescence reaction occurring at the working area (down). The picture was taken from reference 241.

Fig. 4.5.1 Surface immobilisation of a yellow fluorescent protein (YFP) mediated by a supramolecular cucurbituril-ferrocene system. The picture was taken from reference 269.

Fig. 4.5.2 Supramolecular bioactive surfaces mediated by a self-assembled monolayer (red), a polymer brush (green) and a multilayered film (blue). The picture was taken from reference 270.

Figure 4.5.3 Fabrication of the reversible multilayer via cyclodextrin (CD) host-guest interaction. The PDMS surface functionalised with cyclodextrin is then assembled with a biotinylated monoadamantyl molecule (compound 11), which fits into the CD cavity (i) and works as a linker for the subsequent immobilisation of the streptavidin (SAv) (ii). In order to restore the surface to its original state, fluorescent biotin (compound 10) assembles on the SAv (iii), determining the release of the entire supramolecular architecture (iv). The surface is restored using a cyclodextrin triazide (β-CD-N_3*). The picture was taken from reference 271.*

Figure 4.5.4 Glucose biosensor fabrication mediated by glucose oxidase (GOx) immobilisation. The Calixarene-thiol (Calix-SH) is self-assembled on the surface. The Calix-SH surface is activated with carboinimidazole (CDI), and then the GOx is

immobilised on it. To increase the stability of the complex Glutaraldehyde and Bovine Serum Albumin (BSA) were added afterwards. The picture was taken from reference 272.

Fig. 4.5.5 Histidine (blue line) tagging of a Red fluorescent protein (red). The amount of histidine tagging the protein affects the final orientation on the surface. The picture was taken from reference 266.

Figure 4.5.6 Immobilisation of yellow fluorescent protein on silica. The silica is functionalised with a viologen-based molecule (blue line, MV^{2+}). The protein is bonded to a naphtol molecule (red line). The cucurbituril (green) is the linker that keeps the naphtol and the viologen together for the fluorescence patterning. The picture was taken from reference 273.

Figure 4.5.7 Fabrication diagram of the protein biochip. The first step is the assembly of a supramolecular SAM on the surface. The second step is the immobilisation of a first protein and formation of the surface-protein system. The third step is the formation of a second protein layer interacting with the first one, forming a surface-protein-protein macrostructure. The picture was taken from reference 274.

Figure 4.5.8 (Left) Illustration of the preparation of the layer-by-layer (LBL) cyclodextrin surfaces. The first step includes an LBL formation of several polymers followed by the self-assembly on the cyclodextrin derivative (blue). (Right) The schematic illustration of the re-use property of the surface. Once the concanavalin A (ConA) is immobilised, the surface can be restored using sodium dodecyl-sulphate (SDS). The picture was taken from reference 275.

Fig.5.1 Schematic representation of the work developed in this thesis. The cleaned gold surface (left) is functionalised with a scaffold molecule (centre), where the on-surface

analysis will be performed in order to test the correct self-assembly. Then the protein is immobilised on a surface (right), and the interaction protein-scaffold analysed through SPR experiments.

Figure 5.2 Set-up of the surface plasmon resonance used in this thesis. The flow channel allows the protein to interact with the scaffold (i.e. cyclodextrin) functionalised surface. A set of the prism and reflected light allow measuring the interaction occurring between the surface and the protein.

Fig 6.1 Contact angle measurement on a gold chip (yellow), in which the surface exhibits hydrophilic properties, i.e. CA <90 º.

Fig. 6.2 General illustration of an XPS apparatus. Once the beam is created and focused on the sample surface, the electrons emitted are captured by the detector and then analysed to provide the data peaks.

Fig. 6.3 Diagram of ellipsometry. The beam is generated in the light source and is then polarised. Once it touches the sample, the beam is reflected, and an analyser is rotated until the beam is not capable of passing through and hit the detector.

Figure 6.4 A general illustration of an SPR experiment. A laser emits a beam which is then totally refracted at a critical angle and then hitting a sensor. Depending on the matters present on the surface, the photons of the original beam and the reflected one will present different energy.

Fig 6.4.1 One-to-one representation of an SPR interaction. The analyte represented by the red triangle interact with the SAM at the surface of the gold chip.

Fig.6.4.2 Mass transfer effect (K_d) is an essential factor that can influence the results for those experiments with a high flow rate involving analytes with significant molecular weight.

Fig 6.4.3 SPR experiment involving a divalent analyte which presents a double interaction with the SAM.

Figure 6.6 Schematic illustration of a TOF-SIMS instrument. The ions beam is generated into the primary ions gun and then focused onto a specific point on the sample by the primary ions lens. The beam charges the molecules present at the surface sample and the sample molecule, once ionised, are collected and sent to the detectors through a system of ions lenses and mirrors that separates them in terms of mass and charge.

Fig 6.7 Set up of a diamond anvil cell. The two diamond (blue) are close together within between the sample mixture, the ruby and the gasket. The pressure is applied with screws (yellow).

Fig. 7.1.1 The concept of multivalency used in this thesis, where the β-CD SAM can have multivalent interactions with the hydrophobic moieties (shown as blue hexagons) of the protein.

Fig 7.1.2 The amino acids were chosen as a possible attaching point due to their high hydrophobicity of the side chain. From left to right: Phenylalanine, Tyrosine, Leucine and Tryptophan.

Fig 7.1.3 Cytochrome C and its possible attaching points with CD (blue) 0°-180° (up) 180°-360° (bottom).

Fig 7.1.4 Insulin and its possible attaching point with CD (blue) 0°-180° (up) 180°-360° (bottom).

Fig 7.1.5 RNAase and its possible attaching point CD (blue) 0°-180° (up) 180°-360° (bottom).

Fig 7.1.6 Chymotrypsin and its possible attaching point with CD (blue) 0°-180° (up) 180°-360° (bottom).

Figure 7.2 First attempting of bottom-up fabrication of the supramolecular surface. In the first step, the aminothiol is assembled on the surface, forming the SAM. The next step represents the activation of the surface with DSC, followed by the covalent immobilisation of the cyclodextrin on the surface. A) Surface functionalized with Aminoundecanethiol (AUT). B) AUT+Activator (DSC). C) AUT+Cyclodextrin. The picture was taken from reference 351.

Fig 7.3.1 Dimerisation of the thiol molecules comprising either carboxyl terminated moieties (A) or amino terminated moieties(B). The picture was taken from reference 352.

Fig 7.3.2 Comparison of the ellipsometry results between the two methods with and without the use of TEA. The method not using TEA presents a thickness of 3.5 nm and the 10% TEA method a thickness of 1.5 nm.

Fig 7.3.3 Contact angle of AUT surface comparing the two methods without TEA (left) and with TEA (right).

Figure 7.3.4 Ellipsometry and contact angle data of the AUT+CD surface.

Figure 7.3.5 Scheme of degradation steps of the synthesis of Thiol-CD. Both reagents reaction, Cysteamine (1) and DHS(2), and intermediary compound (3) may be degraded by exposition to the air or water, leading to a low yield product (4).

Figure 7.3.6. Mass spectra of unreacted CD. Two signals can be noticed of the unreacted CD: 1135 m/z which is the signal for the pure CD, and 1152 m/z the signal of the cyclodextrin carries a sodium atom in its cavity.

Figure 7.3.7 The secondary reaction is affecting the SAM nanofabrication. Once the SAM is activated with DSC (Fig 7.3.1-B), it may react with the water of the environment determining two scenarios unable to bind the Cyclodextrin (D and E).

Figure 7.3.8 The β-CD–(SH)7 used in the following series of experiments. It can be noticed that the thiol group (SH) is now substituting the previous hydroxyl group. This is in order to allow the self-assembly of the cyclodextrin to the gold surface.

Figure 7.4.1 Contact angle data of β-CD–(SH)7. The hydrophobicity increases by increasing concentration and incubation time, probably meaning that the β-CD–(SH)7 is assembly with the cavity (the main contributor to the hydrophobic character) facing up.

Figure 7.4.2 The eptamer β-CD–(SH)7 and the monomer TGP and their related 3D projection.

Figure 7.4.3 Contact angle data of the TGP at a concentration of 0.1 and 1 mM with an incubation time of 12, 24 and 48 hours.

Figure 7.4.4 Ellipsometry data of the β-CD–(SH)7 (left) and TGP (right) at a concentration of 0.1 and 1 mM, with an incubation time of 12, 24 and 48 hours. The 1 mM concentration for 48h incubation is the results similar to the expected measurement (0.78 nm) with the smallest standard deviation either for the β-CD–(SH)7(left) and TGP (right).

Figure 7.4.5 The amount of sulphur/gold ratio (left) and the percentage coverage of sulphur for each SAM preparation condition as analysed on the surface during XPS experiments.

Figure 7.4.6 XPS sulphur signal β-CD–(SH)7 at incubation concentration of 0.1 mM (up) and 1 mM (down) and an incubation time of 12 hours. The peak of the unbounded sulphur (SH) has increased with the increasing of the concentration.

Figure 7.4.7 XPS Sulphur signal β-CD–(SH)7 at incubation concentration of 0.1 mM (up) and 1 mM (down) and an incubation time of 24 hours. Again as in figure 7.5.6, the peak of the unbounded sulphur (SH, 164 eV) has increased with the increasing of the concentration.

Figure 7.4.8 XPS Sulphur signal β-CD–(SH)7 at incubation concentration of 0.1 M and 1 M and an incubation time of 48 hours.

Figure 7.4.9 XPS spectra of TGP at 0.1 mM (above) and 1 mM (down) for 24 hours. The peak at 162 is the sulfur bonded to gold, at 164 the sulfur unbonded (SH).

Figure 7.5.1 Scheme of the cyclic voltammetry experiment. In the first step, the surface is functionalized with CD, following by chip incubation into a solution of ferrocene to measure the electrical conductivity of the SAM.

Figure 7.5.2 Cyclic voltagramm of SAMs fabricated with DMF solution of β-CD–$(SH)_7$ at the concentration of 0.1 mM, 1 mM, and bare gold (left). Coverage of the ferrocene over the surface at bare gold, 0.1 mM and 1 mM.

Figure 7.5.3 Plot of the peak current vs the scan rate at different CD SAMs concentration. The linear trend of all the measurements indicates that the redox reactions are occurring only at the surface of the gold chips (electrode).

Figure 8.1.9 RNase A comparation response between TGP SAM (left) and with β-CD–(SH)7 SAM (right). Experiment concentrations 20 μM (orange), 10 μM (green), 5 μM (blue), 2.5 μM (yellow), 1.25 μM (grey), 0.6 μM (red).

Figure 8.1.10 Insulin comparation response between TGP SAM(left) and with β-CD–(SH)7 SAM (right). Experiment concentrations 5 μM (orange), 2.5 μM (green), 1.25 μM (blue), 0.6 μM (yellow), 0.3 μM (grey), 0.15 μM (red).

Figure 8.1.12. SPR responses from 9 SPR cycles that were performed using 2.5 μM Chymotrypsin PBS solution on 1 mM 24 h β-CD–(SH)7 SAMs.

Figure 8.1.13 Injection of 2.5 μM of α-chymotrypsin on bare gold (up) and β-CD–(SH)7 SAM (bottom). Both experiments lasted 1400 seconds in which there was a single injection of α-chymotrypsin followed by three regeneration steps with SDS 10 mM. The black line indicates the baseline. The SPR experiments include three major steps: protein injection (orange line), rinsing (green line), regeneration (dotted line).

Figure 8.1.14 Injection of 2.5 μM of Cytochrome C on bare gold (up) and β-CD–(SH)7 SAM (bottom) The black line indicates the baseline. The SPR experiments include three major steps: protein injection (orange line), rinsing (green line), regeneration (dotted line).

Figure 8.1.15 SPR sensorgram of 2.5 μM of Insulin on bare gold (up) and β-CD–(SH)7 SAM (bottom). For the Insulin on bare gold again, the SPR response was increased and the regeneration impossible. The black line indicates the baseline. Three steps can be noticed: protein injection (orange line), rinsing (green line), regeneration (dotted line).

Figure 8.1.16 Injection of 2.5 μM of RNase on bare gold(up) and β-CD–(SH)7 SAM (bottom). The black line indicates the baseline. Three steps can be noticed: protein injection (orange line), rinsing (green line), regeneration (dotted line).

Figure 8.2.1. Overlay of spectra showing glucose-terminated SAMs and β-CD–(SH)7 SAMs with and without protein and bare gold samples. Regions of spectra focused on a) $C_5H_9N_2O_3^+$ and b)$C_{34}H_{33}N_4O_4Fe^+$ peaks and show no advantageous contaminations from SAM layer.

Figure 8.2.2. TOF-SIMS spectra of the Cyt C on a β-CD–(SH)7 SAM(red) and on glucose terminated SAM (blue). The different patterns between the two SAMs indicate a difference in orientation of the protein on the surface.

Figure 8.2.3. (a) Pattern peak intensities for cytochrome C iron-porphyrin fragment, wherein the protein has been immobilised on either a glucose-terminated SAM or a β-CD–(SH)7 SAM. (b) Peak areas are normalised to total ion count. Each bar shows the peak area average of 12 measurements and standard deviation within the sample set.

Figure 8.2.4 signals from Glucose-terminated SAM and β-CD–(SH)7 SAM.

Figure 8.2.5 The amino acid sequence of Horse heart Cytochrome C. The dimer analysed (145.10 m/z) is underlined (orange).

Figure 8.2.6 The possible orientation of the Cytochrome C. The section of the protein facing up (A), facing down (B) and a lateral section (C). The dimer Gly1-Asp2 is represented in orange. The porphyrin is represented in red. The blue circles indicate the β-CD–(SH)7 cavities.

Figure 9.1 The Arginine (left) and Lysine (right) amino acids that interact strongly with the Cucurbituril. The bond is mostly given by the polarity of the amino group at the end of the side chain.

Figure 9.1.1 Cytochrome C and its possible attaching point with CB (green) 0°-180° (left) 180°-360° (right).

Figure 9.1.2 Insulin and its possible attaching point with CB (green) 0°-180° (left)180°-360° (right).

Figure 9.1.3 RNAase and its possible attaching point with CB (green) 0°-180° (left) 180°-360° (right).

Figure 9.1.4 Chymotrypsin and its possible attaching point with CB (green) 0°-180° (left) 180°-360° (right).

Figure 9.2 Ideal orientation of cucurbituril for this study. The cavity facing up will allow the protein to interact with it.

Figure 9.2.1 Common synthesis of cucurbiturils. Two ureas(1) are added to the Glyoxal (2) to form the glycouril (3). With a condensation reaction with formaldehyde (4) in the acidic condition, the ring is formed.

Figure 9.2.2 Proposed synthesis of thiocucurbiturils. Only the thiourea (1) has changed from the original synthesis of cucurbiturils.

Figure 9.2.3 The first (1) and the second (2) addition in the first step of the synthesis of the thiocucurbituril (fig 9.2.2). The first addition brings to the formation of a racemic solution (R, S) and (R, R). The second addition brings to the thioglycouril (2).

Figure 9.2.4 The NMR of the first step. Each peak is marketed with a coloured mark related to the hydrogen of the functional group.

Figure 9.2.5 NMR spectra after the purification and precipitation. All the peaks describing our molecule have essentially not changed from the previous NMR analysis (fig. 9.2.4).

Figure 9.2.6 Alternative synthesis for the thioglycouril. The thiourea (1) and the glyoxal (2) form the DTI (3) and the hydroxyl groups. After that, before the second addition of the thiourea, the DTI is mixed with the thionyl chloride(4) or the tosyl chloride (5). Both reagents are used to improve the reactivity of the imidazole ring for the addition of the second thiourea.

Figure 9.2.7 NMR spectra of the reaction with thionyl chloride (up) and tosyl chloride (down).

Figure 9.3.1 Proposed mechanism synthesis of the thiocucurbituril. Over the entire molecular structure, it was theorised only to exchange the carbonyl group (C=O) for a thiocarbonyl (C=S).

Figure 9.3.2 Raman Spectra of the cucurbitu[6]uril. The peaks at 444.92 cm^{-1} indicate the N-C-N vibration, at 829.03 cm^{-1} indicates the C-N-C vibration and at 1743.57 indicates the C=O vibration[380].

Figure 9.3.3 Raman Spectra of Sodium Hydrogen Sulfide(NaSH). The peak at 2557.60 represents the thiol group 381.

Figure 9.3.4 Raman Spectra (up) of the mixture into the DAC right after the mixing at 0.6 GPa: the entire spectra (A) and the magnification of the area (B) where the vibration

carbon-sulphur should be visible (500-710 cm^{-1})[384]*. Actual photos (down) taken at the microscope of the DAC chamber with the compound mixture.*

Figure 9.3.5 Raman Spectra at 5.0 GPa after one hour from the mixture.

Figure 9.3.6 Raman Spectra at 9.3 GPa for 24 hours. The peak carbon-sulphur [384] is evident at 595.36 cm^{-1}.

Figure 9.3.7 Raman Spectra 7.7 GPa for 26 hours (above) and 5.0 GPa for 30 hours(below). The carbon sulphur peak area is decreasing, showing that the two atoms are again splitting apart.

Figure 9.3.8 Raman Spectra at 1.8 GPa (above) and 0.7 GPa (below). The peak now has completely disappeared, proving that there is no more interaction among the carbon and the sulphur atom.

Figure 9.4.1 Raman spectra 0-1000 cm^{-1} area of the NaSH salt in a diamond anvil cell at the ambient pressure. The characteristic peak in this area is the peak of the stretch of the Na-S bond.

Figure 9.4.2 Raman spectra 0-1000 cm^{-1} area of the NaSH salt in a diamond anvil cell at the pressure of 0.6 GPa.

Figure 9.4.3 Raman spectra 0-1000 cm^{-1} area of the NaSH salt in a diamond anvil cell at the pressure of 1.92 GPa.

Figure 9.4.4 Raman spectra 0-1000 cm^{-1} area of the NaSH salt in a diamond anvil cell at the pressure of 2.94 GPa.

Figure 9.4.5 Raman spectra 0-1000 cm^{-1} area of the NaSH salt in a diamond anvil cell at the pressure of 4.42 GPa.

Figure 9.4.6 Raman spectra 0-1000 cm^{-1} area of the NaSH salt in a diamond anvil cell at the pressure of 7.78 GPa.

Figure 9.4.7 Raman spectra 0-1000 cm^{-1} area of the NaSH salt in a diamond anvil cell at the pressure of 9.44 GPa.

Figure 9.4.8 Raman spectra 0-1000 cm^{-1} area of the NaSH salt in a diamond anvil cell at the pressure of 7.78 GPa.

Figure 9.4.9 Raman spectra 0-1000 cm^{-1} area of the NaSH salt in a diamond anvil cell at the pressure of 5.59 GPa.

Figure 9.4.10 Raman spectra 0-1000 cm^{-1} area of the NaSH salt in a diamond anvil cell at the pressure of 3.53 GPa.

Figure 9.4.11 Raman spectra 0-1000 cm^{-1} area of the NaSH salt in a diamond anvil cell at the pressure of 2.78 GPa.

Figure 9.4.12 Raman spectra 0-1000 cm^{-1} area of the NaSH salt in a diamond anvil cell at the pressure of 1.37 GPa.

Figure 9.4.13 Raman spectra 0-1000 cm^{-1} area of the NaSH salt in a diamond anvil cell at the pressure of 0.78 GPa.

Figure 9.5.1 Raman spectra 0-1000 cm^{-1} area of the cucurbituril in a diamond anvil cell at the pressure of 0.85 GPa. The peaks at 444.92 cm^{-1} indicate the N-C-N vibration, at 829.03 cm^{-1} indicates the C-N-C vibration[380]

Figure 9.5.2 Raman spectra 0-1000 cm^{-1} area of the cucurbituril in a diamond anvil cell at the pressure of 2.02 GPa.

Figure 9.5.3 Raman spectra 0-1000 cm^{-1} area of the cucurbituril in a diamond anvil cell at the pressure of 4.97 GPa.

Figure 9.5.4 Raman spectra 0-1000 cm^{-1} area of the cucurbituril in a diamond anvil cell at the pressure of 6.62 GPa.

Figure 9.5.5 Raman spectra 0-1000 cm^{-1} area of the cucurbituril in a diamond anvil cell at the pressure of 8.31 GPa.

Figure 9.5.6 Raman spectra 0-1000 cm^{-1} area of the cucurbituril in a diamond anvil cell at the pressure of 9.53 GPa.

Figure 9.5.7 Raman spectra 0-1000 cm^{-1} area of the cucurbituril in a diamond anvil cell at the pressure of 7.07 GPa.

Figure 9.5.8 Raman spectra 0-1000 cm^{-1} area of the cucurbituril in a diamond anvil cell at the pressure of 4.72 GPa.

Figure 9.5.9 Raman spectra 0-1000 cm^{-1} area of the cucurbituril in a diamond anvil cell at the pressure of 2.72 GPa.

Figure 9.5.10 Raman spectra 0-1000 cm^{-1} area of the cucurbituril in a diamond anvil cell at the pressure of 1.51 GPa.

Figure 9.5.11 Raman spectra 0-1000 cm^{-1} area of the cucurbituril in a diamond anvil cell at the pressure of 0.46 GPa.

List of tables

List of abbreviations

Cyclodextrin (CD)

Cyclodextrin glycosyltransferase (CGTase)

Methyl-β-cyclodextrin (MβCD)

cucurbit[n]uril (CB)

Self-assembled monolayers (SAMs)

Oligoethylene glycol thiol (OEGT)

Bovine serum albumin (BSA)

Time-of-flight secondary ion mass spectrometry (TOF-SIMS)

Atomic force microscopy (AFM)

Eagles minimum essential medium (E-MEM)

Dithiothreitol (DTT)

2-mercaptoethylamine (2-MEA)

Tris(2-carboxyethyl)phosphine (TCEP)

Prostate-specific antigen (PSA)

Tetramethylrhodamine (TAMRA)

Fluorescence Resonance Energy Transfer (FRET).

Histidine (His)

Green fluorescent protein (GFP)

Maltose-binding protein (MBP)

2,4,6-trinitrotoluene (TNT)

Polydimethylsiloxane (PDMS)

Gold-binding protein (GBP)

Surface Plasmon Resonance (SPR)

Polyvinyl alcohol (PVA)

Polyethene glycol (PEG)

Dithiothreitol (DTT)

Calixarene-thiol (Calix-SH)

Glucose oxidase (GOx)

Carboinimidazole (CDI)

Aminoundecanethiol (AUT)

Dihydroxy succinimide (DSC)

Trimethylamine (TEA)

Dihydroxysuccinimide (DHS)

Maximum theoretical ferrocene coverage (MTFC)

Cucurbituril (CB)

Tetrahydrofuran (THF)

4,5-dihydroxy-2-thioketo-imidazole (DTI)

Diamond Anvil Cell (DAC)

1. Introduction

Supramolecular chemistry is a field in chemistry focused on the study of the reversible interactions between molecules. While the traditional organic chemistry focuses on the research of covalent bonds, the supramolecular chemistry investigates those weak interactions capable of assembling a discrete number of compounds and their 3D organisation. The forces in question represent weak interactions such as hydrogen bonding, intermolecular forces, π-π interactions, van der Waals forces, and electrostatic interactions. The investigation of non-covalent interactions is essential for a better understanding of many biological processes.

Important phenomena in nature have been better explained through supramolecular chemistry such as host-guest chemistry, hydrophobic folding, mechanically-interlocked molecular architectures, molecular recognition, dynamic covalent chemistry, and molecular self-assembly[1]. The organic chemistry differs significantly from supramolecular chemistry also in terms of thermodynamics, and the laws of the general physics do not entirely describe the phenomena behind a supramolecular system. The supramolecular chemistry deals with artful interactions, and furthermore, high precision is required for the control over the processes involved.

More specific, non-covalent interactions have low or no activation energy for the formation and occur spontaneously, as in the case of the self-assembly. As shown by thermodynamics laws and unlike the covalent bond, the creation of non-covalent interaction does not require an elevated temperature. Instead, due to their shallow bond energy, higher temperatures can determine the breaking of the non-covalent interactions

and, in other words, of the supramolecular complex. On the other hand, supramolecular chemistry allows the molecule to be distorted into a thermodynamically disfavoured conformation, and low temperatures could determine an undesired structure of the supramolecular complex. Supramolecular chemistry also finds a vast application in the field of surface chemistry. A surface can direct new supramolecular architectures changing the thermodynamics of the system altogether.

This work is mostly based using the concept of self-assembly, molecular complexation, and mechanically interlocked architectures and several strategies where both surface chemistry and host-guest interaction are mixed to retain a protein on a surface. The immobilisation of the protein will be possible due to interactions between the protein and the surface. These interactions will maintain the protein on the surface in a stronger and more stable way than physical absorption. On the other hand, in a weaker approach than the chemical absorption, avoiding the formation of new covalent bonds without any perturbation in the protein structure.

The supramolecular immobilization is an important milestone in the development of next generation of biosensor. In medicine, biosensors represent the first step for the diagnosis of a pathological condition. More accurated and precise biosensors are always needed to detect the smallest amount of target molecule, detecting illnesses in an earlier stage and increasing the outcomes for survival rates or management of the syntomps.

In the next section, we will introduce the fundamentals of supramolecular chemistry, discussing the non-covalent interactions, hydrogen bonding, and molecular self-assembly, that constitute the core of this branch of chemistry.

2. Thesis Layout

The chapter 3 will be focusing on the recent advancement of the technology proposed in this thesis. First, concept in supramolecular chemistry will be listed for a better understanding of the technology. Then, an enlisting of the different and actual development of the different protein immobilization approaches, followed by a focus on the lastest advancement of the supramolecular approach.

The chapter 4 will be focusing on the project aims of the research.

Chapter 5 on the tools and on the techniques used for the characterization of the surfaces.

Chapter 6 for the methods and the procedures in order to carry the experiments.

Chapter 7 on the computational study of the Cyclodextrin-protein complex, on the fabrication and the characterization of the cyclodextrin-functionalized surface.

Chapter 8 on the study of the affinity between the supramolecular surface and the proteins

Chapter 9 on the new synthesis of a new organic compound necessary for this research.

Chapter 10 for resuming the conclusion and proposing new idea for the future.

Chapter 11 for the bibliography.

3. Literature review

3.1 Concepts in supramolecular chemistry

Non-covalent interactions

The interactions that involve variations into the magnetic field between two or more molecules that do not include the sharing of two or more electrons are called non-covalent interactions[2]. The chemical energy used for the formation of non-covalent interaction is ranging between 1-20 kcal/mol[3]. Their primary role in nature is the maintenance of biostructure such as DNAs, the secondary, tertiary and quaternary structure of a protein. The non-covalent interaction is also deeply involved in the self-assembly, drug design, and synthesis of biometabolites[2,4–6]. In the next sessions will be showed that non-covalent interactions include a wide range of several weak interactions such as hydrophobic effects, electrostatic effects, π-effects, van der Waals forces[2,3].

Electrostatic interaction

In chemistry, there are three types of electrostatic interactions: Ionic Interaction, hydrogen bonding, and halogen bonding. The ionic interactions imply the full permanent charges of ions or molecules of opposite signs. These bonds typically determine the formation of the salts and are more stable than covalent bonds due to two ions with different charge and the strong ionic interaction between them. However, as ions are highly soluble in polar solvents, this interaction falls apart in aqueous solutions or any other solvents with low polarity.

In the case of the hydrogen bonding is a type of dipole-dipole attraction between a highly electronegative partially negative atom (fluorine atom, sulphur, nitrogen, and oxygen) and a partially positive hydrogen atom. The hydrogen bonding is one of the

strongest non-covalent interactions. The strength of the hydrogen bond is in a range of 0–20 kcal/mol[2].

In the case of the halogen bonding, a halogen atom acts as a nucleophile, donating its electron to an electrophile generating a halogen bond. For this kind of interaction, the nucleophilic agent is either a very electronegative (sulphur, nitrogen, oxygen) or ionic with a complete negative charge.

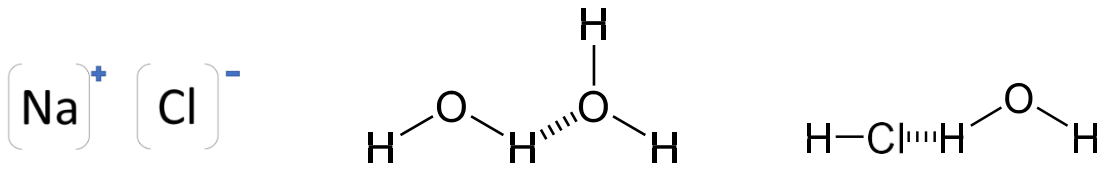

Figure 2.2 Examples of electrostatic interaction: Ionic Bond (left), hydrogen Bond (centre), halogen bond (right).

Van der Walls interactions

Van der Waals Forces represent those electrostatic interactions generated by an induced or permanent dipole. It is possible to distinguish three kinds of dipoles: induced-induced dipoles, induced-permanent dipoles, permanent-permanent dipoles. The induced-induced dipole is the weakest type of non-covalent interaction (London forces)[7]. They are caused by oscillations of the electromagnetic field of a molecule, which are induced by a temporary electron repulsion by a neighbouring molecule and leading to a partial negative charge on one molecule and a partially positive charge on the other molecule[5]. The induced-permanent dipoles (commonly known as Debye forces) is generated by the approach of a permanent dipole to another apolar molecule. This approach causes an oscillation of the electromagnetic field of the apolar molecule, producing the induced dipole[8]. The permanent-permanent dipoles (Keemson Interactions)

are produced by permanent dipoles in molecules and are customarily associated with electronegative atoms, such as oxygen, nitrogen, sulphur, and fluorine[9]. Compared among them, the Keemson interactions are the strongest one, followed by Debye Forces and then the London Forces.

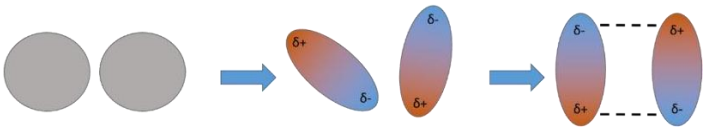

Figure 2.3.1 Interaction between induced-induced dipole (London Force). First, two non-polar molecules approach each other. The momentary and repulsions between atoms determine a change in the electron density, leading to induce dipole interacting between them.

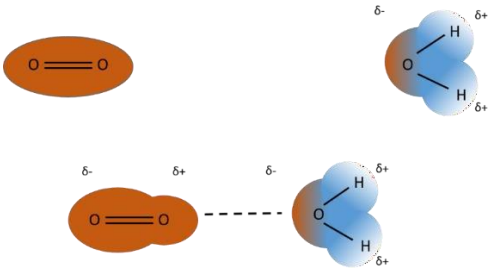

Figure 2.3.2 Induced-permanent dipole (Debye Force). The permanent dipole represented by the molecule of water (red-blue) induces a momentary dipole in the molecule of oxygen(red).

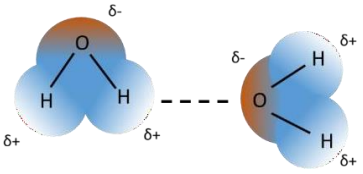

Figure 2.3.3 Permanent-permanent dipole (Keemson Interaction). The net negative charge of one permanent dipole interacts with the positive pole of the near molecule.

π-effect

The π-effects are another type of interactions that can be divided into several categories. The π-π interactions, associated with a specific interaction between the π-systems of conjugated molecules such as benzene. The cation-π interactions, where a cation is sitting atop of a rich π-conjugated system (as in the case of the ferrocene)[10]. The anion-π interactions, which are very similar to the previous ones but reversed, where the anion sits atop of a poor π-conjugated system. Polar-π interactions involve molecules with permanent dipoles (such as water) interacting with the quadrupole moment of a π-system (such as that in benzene)[11].

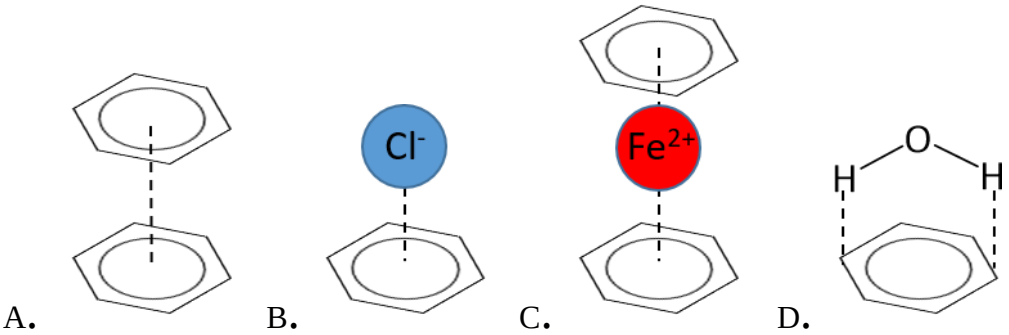

Figure 2.4 Examples of π interactions: π-π interaction (A), anion-π interaction (B), cation-π interaction (C), polar-π interaction (D).

Hydrophobic effect

The hydrophobic effect is the tendency for non-polar molecules to aggregate in aqueous solution. This phenomenon leads to the hydrophobic particles to expose always the minimum surface area to the polar water molecules (typically spherical

droplets)[12.] Hydrophobic particles are allowed to keep apart and never be able to be mixed with water[13]. In the case of protein folding, structures of water-soluble proteins have a hydrophobic core in which side chains are buried from water, which stabilises the folded state. The hydrophobic effect represents one of the essential processes for life on earth[14].

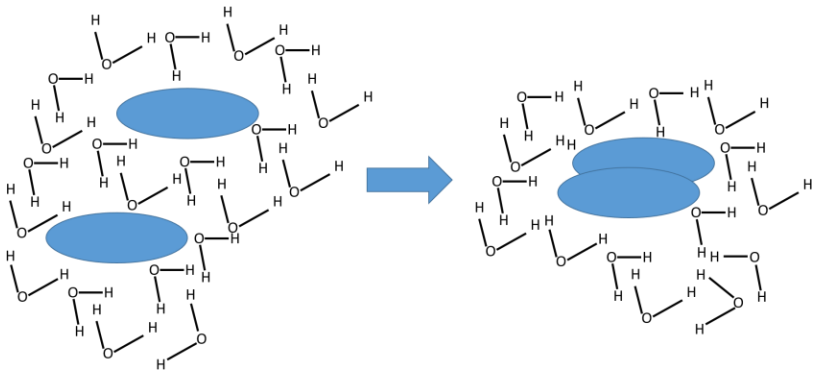

Figure 2.5 Hydrophobic effect. Two apolar aggregates in an aqueous environment tend to aggregate to decrease their surface tension.

Molecular self-assembly

The molecular self-assembly is the building of molecular systems spontaneously without any imposition from an external source. Molecular self-assembly determines the construction of larger biochemical structures such as vesicles, membranes, and micelles[15–17]. The final self-assembled product may be derived from intramolecular self-assembly (interaction between two or more different groups of the same molecule) and intramolecular self-assembly (interaction between two or more different group of the different molecule). In the self-assembly process, the particles are guided to be brought together through non-covalent bonds.

3.2 The general concept of supramolecular biosensing and recognition

In nature, proteins cover a vast array of functions within living organisms, including DNA replication and cell-cycle control,[18,19] response to behavioural stimuli,[20] cellular information exchange[21], and catalysing metabolic reactions.[22,23] In biochemistry and medicine, proteins have attracted attention due to their capacity to act as a biomarker and, consecutively, its presence indicates a particular disease state. More specifically, a biomarker expresses a change in protein state, which corresponds to the risk or progression of a disease and allows early detection for more effective treatments.[24,25] In recent years, protein biochips[26] have represented a promising technology in the field of biomedical science, to provide further information regarding protein functions and interactions and to provide advances, for example, of many applications in clinical diagnostics, proteomics, and drug delivery[27–32]

However, despite the advantages that this technique can provide in the field of biosensing, a facile undertaking of the immobilisation of proteins on the surface is lacking[33–36], due to the complexity of the system and to the chemical properties of the protein. Using the self-assembly capacity of a scaffold thin film on the surface, there is the possibility to catch these proteins with high specificity. The self-assembly is a natural process in which a disordered system of one or several components tends to form an organised structure. This process occurs spontaneously as a consequence of the specific interactions between the single components in the system, and it is one of the main strategies in nature to create life from building blocks[37]. Recently, many signs of progress have been made for a further understanding of self-assembly techniques and, among

them, the formation of a Self-Assembled Monolayer (SAM) is one of the simple ways for the fabrication of an organic film[38–41].

In this thesis, supramolecular biosensing will be explored using two types of ring-shaped molecules: the Cyclodextrin and the Cucurbituril.

The cyclodextrin family

The cyclodextrin (CD) is a group of molecules with glucose as subunits linked between them through the α-1,4 glycosidic bonds[42]. CD is formed naturally by the enzymatic conversation of the starch. They found applications in pharmaceutical and in specific in drug delivery, agriculture, chemical industries and food. CD can be found in nature in different sizes, and molecular weights and the most common are the α-alpha(CD), β-beta(CD) and γ-gamma(CD) respectively made with 6,7, and 8 glucose monomers.

Their production from starch[43] occurs when the α-amylase, the enzyme that catalyses the conversion of starch cuts the sugar chains of starch into small monomers and then another protein, the cyclodextrin glycosyltransferase (CGTase), links the different glucose molecule between each other in a shaped-ring macrocyclic. The scientific interest of cyclodextrin is related to its host-guest chemistry of their cavity, conferring to the entire molecules mixed properties as it presents a hydrophobic cavity and hydrophilic walls.

The cyclodextrin presents very low toxicity with a median lethal dose (LD50) in the range of grams of kilograms. Many studies have been proving evidence that cyclodextrin, in a mixture, can improve the overall hydrophilicity of the other molecules apart from

intensifying the colour and improve light stability by shielding the molecule with their cavity[44]. A very outstanding derivative, the methyl-β-cyclodextrin (MβCD) is widely used to remove cholesterol in biological culture, and it is the main compound in the preparation of the cholesterol-free products.

The cyclodextrin found application also in cosmetics by bind fragrances, acting as a trap and reducing the odour. A recent use is related to the formation of powdered alcohol where a single cyclodextrin molecule acts as nano-encapsulator for the single-molecule of alcohol[45].

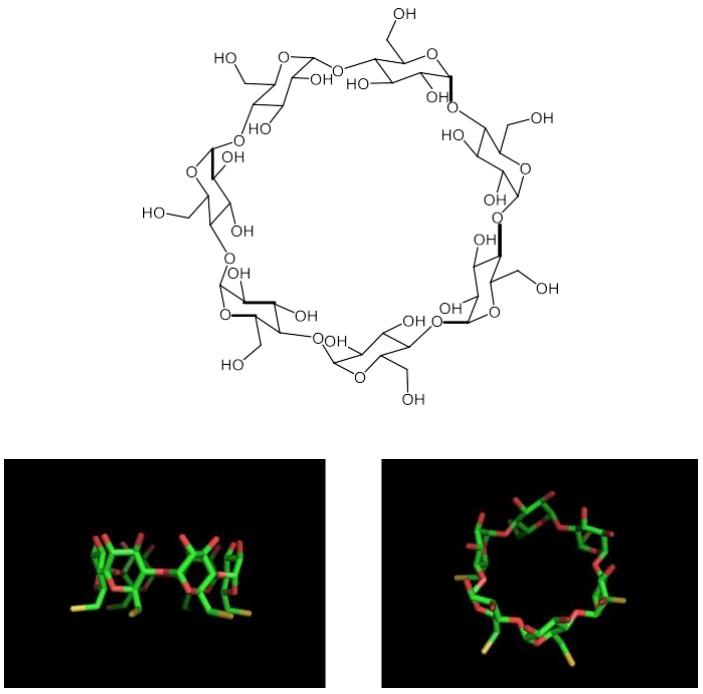

Figure 3.1 The chemical structure of β-cyclodextrin (top) and its 3D projection (bottom). The structures are made with Pymol software.

So far, one of the methods employed in this thesis for the biosensing is the cyclodextrin targeting to specific amino acids inside the protein. It has been demonstrated that a high affinity of the cyclodextrin towards hydrophobic aminoacids[46]. This characteristic is provided by the fact that cyclodextrins possess a hydrophobic cavity[47] rendering them a

potential tool to trap any molecule that presents a marked apolar character. By using this peculiarity, we will be investigating amino acids that present a non-polar characteristic on the outside part of the protein to identify potential attaching points to our cyclodextrin moieties.

The cucurbituril family

The other molecule chosen for our research was the cucurbit[n]uril (CB), where the n indicates the number of monomers involved in the macrocyclic formation. It presents the same shape-ring as the cyclodextrin with the only difference that the CB has the glycouril monomer as a constituent. Its cavity introduces a more hydrophilic character compared to the cyclodextrin. The scientific interest for this molecule is, like the CD, for its cavity and host-guest chemistry properties. Over time, it has been established that cucurbiturils may represent a right candidate for molecular recognition and hence, biosensing[48]. The differences with the CD, in this case, are that the CB also presents a high affinity for positively charged moieties[49]. This high affinity of the cationic compounds is mostly related to the carbonyl group introduced twice in any monomer of the molecule. The synthesis is performed by reacting two moles of urea (1, fig 3.2) with one mole of glyoxal (2, fig 3.2). The reaction product is the glycouril moiety (3, fig 3.2), which then reacts with formaldehyde (4, fig 2.4) in strong acid conditions and with a reaction temperature above 110 °C, determining the formation of the hexamer: cucurbit[6]uril or CB[6]. For a reaction temperature between 75 and 90 °C, other CBs are formed with 5, 7, 8, and 10 monomers[50]. The main application of these compounds is in the pharmaceutical industries as drug delivery vehicles[51] and the catalysts field as it has been proved that the CB can determine a specific orientation of the reagents that can improve the collision among the molecules and the reaction yield[52]. In recent years, the

CB is also investigated for their capabilities of modulating the acidity constant, tuning fluorescent dyes and increasing the photostability of many compounds[53–55].

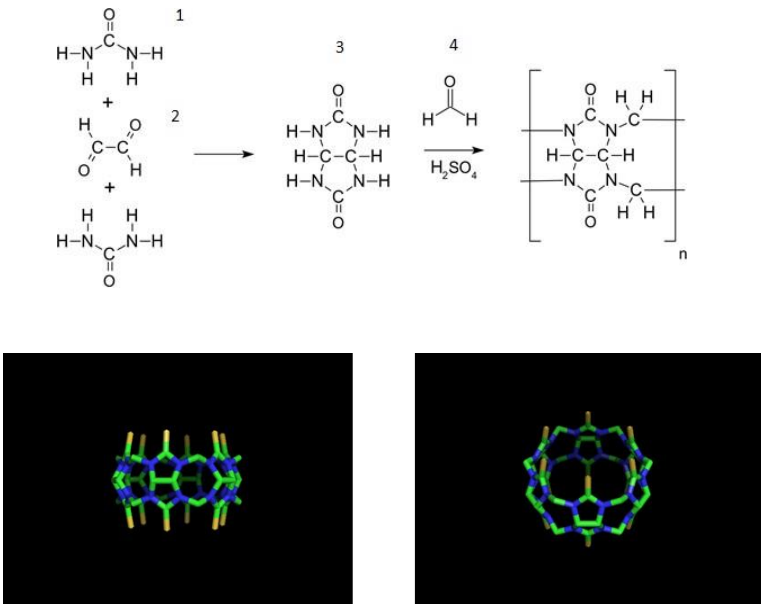

Figure 3.2 General synthesis of cucurbiturils (top) and its 3D-projection (bottom). The first synthetic step is the double addition of urea (1) to a molecule of glyoxal (2). The second step is the cyclisation through a condensation reaction mediated by formaldehyde (4) in strong acidic conditions. The structures are made with Pymol software.

Self-assembled monolayers

Self-assembled monolayers (SAMs) are entities that form spontaneously due to the adsorption of a surfactant either from liquid or vapours phase on a solid support[56]. The driving force of such phenomena is the hydrostatic interaction between the surfactant molecule and the surface. Depending on the nature of the surface, related functional groups will be chosen to lead the correct packing on the surface.

In other words, the SAM physical properties such as thickness, stability and surface energy, can be modulated by the molecule structure[57]. For example, thetriethoxy

silanes on silicon dioxide and the thiol SAMs on gold, are two widely SAMs examples employed to modify the surface properties of inorganic and metallic substrates, respectively[58]. In general, the molecules implied for the fabrication of the SAM presents three specific parts: the head group, backbone, and terminal group. One of the molecules most used for SAMs is the octadecanethiol.

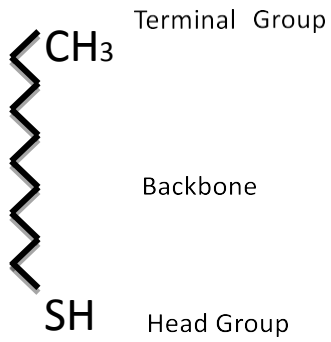

Figure 3.3 Example of a SAM molecule with a terminal group (green), backbone(black) and a head group (red).

The head group determines the adsorption of the molecule on the surface. The backbones determine the packing on the surface, and the terminal group defines the new physiochemical properties of the SAM. The terminal group can be chemically active, determining the anchor point for the substrate or a further step nanofabrication[59–61], or can be passive, changing only the physical properties (i.e. hydrophobicity/hydrophilicity) of the surface.

Thiols on gold

One of the main system surfactant-surface used is the thiols on gold[57]. The surfactant, in this case, presents a sulphur functional group which interacts directly with the gold atom at the surface[57]. This system represents one of the most studied and widely spread methods to obtain a SAM on a gold surface. The thiol molecules can present an

extensive range of terminal groups which make them very versatile in terms of surface functionalization. Apart from fundamental studies, SAMs are also employed in the application of sensor design, self-healing surfaces and microfluidics[61].

From the fundamental study of this architecture, it is now understood that the formation of SAMs goes under two different phases[40]. Kinetics studies of SAM formation illustrate that adsorption occurs mainly within minutes after the immersion of cleaned gold into a thiol solution [62]. For relatively small alkanes, it was proved that after several minutes of immersion, the contact angle is already similar to about 80-90% of the final one[62]. The second step is represented by the surface packing, where it can occur after several hours depending on the structure of the molecule and concentration[63].

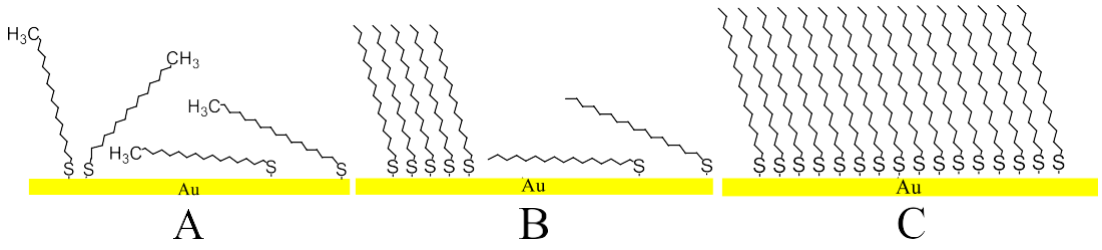

Figure 3.3.1 Formation of a SAM. The head group (thiol) first interact with the surface (A and B). Then, the molecules start interacting with each other among them to assemble as an ordered structure(C).

The thiol head group leads the self-assembly process on the gold surface. The thiol-gold formation is energetically favourable with a stable sulphur-gold bond and an enthalpy of 210 kJ mol^{-1} [64]. The efficient packing is ensured by the backbone of the thiol molecule (using van der Waals and hydrostatic forces). These interactions represent a crucial factor in the formation of the SAMs by determining the configuration of a higher order structure on surface[65].

However, even if this process is well investigated, further study needs to be done to ascertain if the sulphur-gold bond involves the formation of any radicals, ions or other species[63]. The thiol adsorption phenomena seem to be similar for other sulphur species such as disulphides. X-ray photo spectroscopy has been performed but, so far, it has not been possible to understand the differences between the disulfides and thiols adsorption[66]. However, recent studies[66] have been demonstrating that the disulfides and thiols adsorption can occur at a different rate as the thiols are adsorbed more readily, determining that chemical entities are comparable.

On the other way, disulphides can be better involved in the adsorption as they tend to oxidise less than the thiol group, providing more stability to the degradation[67]. This chemical stability can also simplify the nanofabrication step, as generally the protecting group is not needed. Another study also provides evidence that disulphides bring to less surfactant exchange over the surface compared to thiols to avoid possible disulphide molecule to be substituted by another molecule[68]. Several disulphide molecules are used nowadays, among them the cystine and the thioctic acid[69–71].

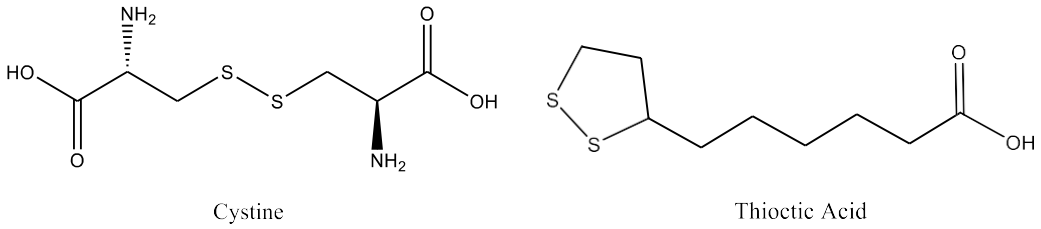

Cystine Thioctic Acid

Figure 3.3.2 Chemical structures of cystine and the thioctic acid molecules.

After the sulfur-gold interaction takes place, it is well known that the surface orientation of the SAMs depends on some factors, such as the structure of the surfactant itself, solvent parameters and morphology of the gold surface. These factors are strongly linked with the final organisation of the SAM[58]. The packing and the morphology of the

SAM are strictly determined by the Au-S interaction and backbones interaction[72]. Surfactants, containing a backbone chain of 12 or more carbon units, present a very well order scenario. This is because the backbone, excluding the terminal and the head group, is symmetric and offers the same grade of static force in all its atoms. However, the tilted configuration of the surfactant will be energetically the most favourable one, due to the sulphur sp^3 hybridisation with a bond angle at around 109.5 degrees.

In the case that other groups are present in the backbone of the molecules, this can strongly affect the final structure of the SAM as the backbone will not possess any more symmetry. Further studies have also been proving that functional groups, such as carboxyl and amine can also change the final structure even if they are contained in the terminal group[73–76]. Other studies have been showing that the shorter is the backbone chain, the more critical will become the terminal and head group polar activity in the formation of the final SAM. Other factors that can influence the final structure are the pH and the surfactant solvatation[70,77]

In the studies of the SAMs to simplify any practical idea, it is ideally assumed that the SAMs are correctly ordered systems free from defects. In a real situation, the SAMs are systems that present defects all over the surface. Among these defects can be highlighted the disorder defects, domain defects and pinhole defects[58]. The pinhole defects are SAM imperfections due to a missed molecule in between the SAMs molecules (fig 3.3.3A).

Domain defects occur at the border of the crystalline lattices where SAMs portions, so-called “island”, meet with a different molecule orientation (fig 3.3.3b)[58,78]. Disorder defects (fig 3.3.3C) are an area of the SAM where the alkane chain is not entirely

extended keeping a gauche configuration, mostly caused by the breaking of the monolayer[79].

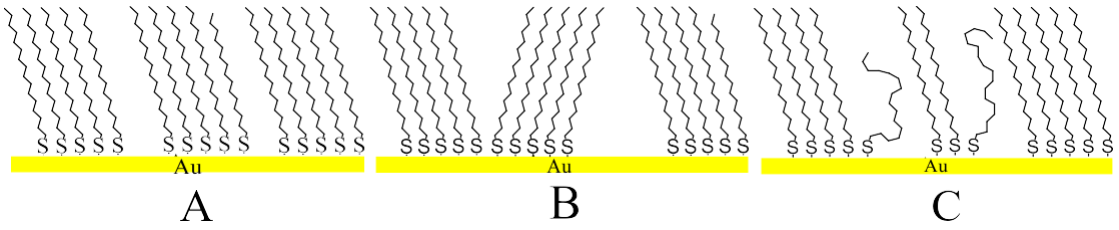

Figure 3.3.3 The pinhole defects (A) derived from a missing molecule during the assembly. Domain defects (B) derived when large aggregates of assembled molecules approach each other. Disorder defects (C) given by a non-well assembled molecule.

The vast number of applications establish the SAMs as one of the most critical architectures in chemistry. The SAMs described so far were only SAMs carrying one type of molecule. Mixed SAMs can be obtained including into the SAMs solution different types of surfactants. The methodology of having monolayers with different molecules can produce hybrid properties[80]. One of the examples that need to be mentioned is the nanofabrication of the oligoethylene glycol thiol (OEGT), and biotinylated peptides to create surfaces for a selective desired binding and simultaneously avoid the non-specific adsorption of unwanted proteins[81]. Another application is the use as a spacer as the passive molecule in a SAM of active surfactants[82] to decrease the risk of crowded substrate adsorption, determining only partial interaction between the protein and the SAM, due to sterical problems (fig.3.3.4).

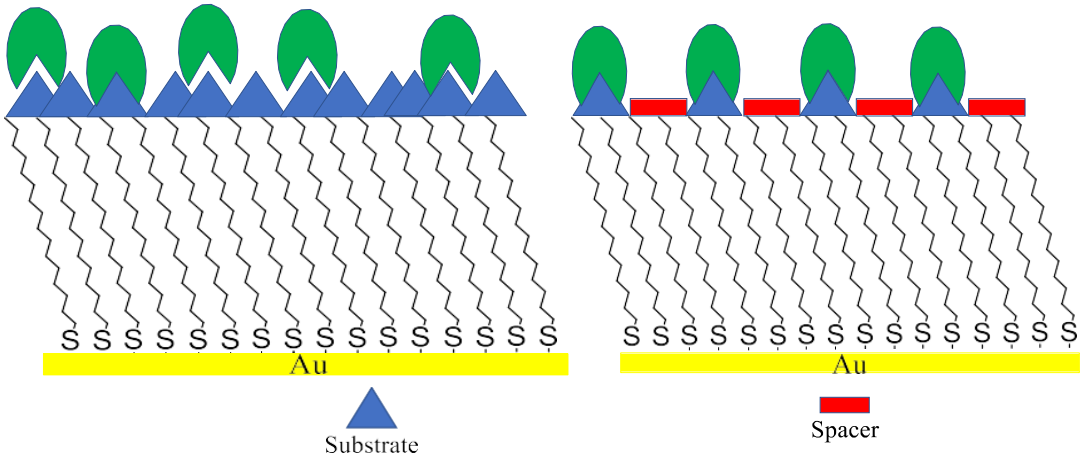

Figure 3.3.4 Example of a typical protein (green) interaction with a SAM. A surface crowded with the substrate (blue left) could determine an incomplete or a partial interaction between the SAM and the protein due to sterical problems. While instead, the addition of a spacer (red right) determines the lower probability of these problems to occur.

The same principle can also be used in the specific case of a switchable surface, where the switch movement can only be ensured if there is a spacer between one SAM domain and the other[81–83]. For mixed SAMs, the factor of the molecule ratio become another factor to take into consideration during the fabrication process because among two or more surfactants there will always be one that has more tendency to assemble on a surface than the other molecule[81,84].

3.3 *Main protein immobilisation techniques on surfaces*

In terms of weak interactions, proteins tend to make non-covalent bonds with surfaces in a spontaneous way. To protect their functionality, the immobilisation in a specific orientation is usually preferred to fabricate surfaces with a specific affinity antibody, enzymes and peptides[85,86]. However, protein immobilisation of flexible protein portion might induce denaturation due to an elevated interaction with the surface[87]. Site-specific immobilisation can be obtained using protein structural studies to introduce residues in specific protein locations[88]. In this section, we will be exploring the several strategies for protein immobilisation: physical adsorption, chemical adsorption, and adsorption mediated by complexed architectures such as hydrogels and lipidic membranes (Figure 4.1).

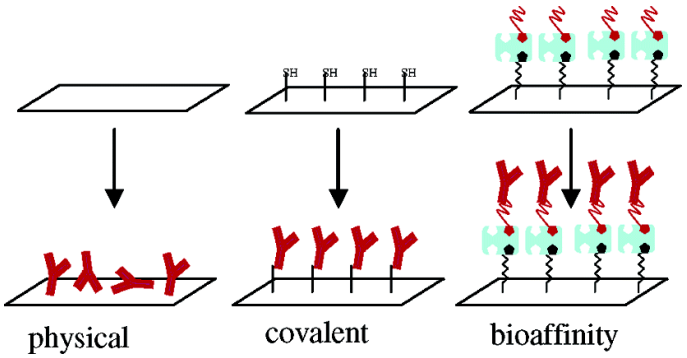

Figure 4.1.1 General illustration of some of the immobilisation techniques explored in this literature review. It is possible to distinguish the physical adsorption (left) where the moieties represented in the picture are in this case antibodies adsorbed with no specific orientation. The obtained layer does not present order, and perhaps its properties (specificity and physical properties) are not well defined. Chemical immobilisation or crosslinking (centre) via covalent bonds where the molecules may present an orientation.

The crosslinking could be further used to obtain a bioaffinity immobilisation (right). This picture was taken from reference[88].

Physical adsorption

The physical adsorption (or physisorption) of proteins at the interface depends on the nature of the protein, solution composition, and surface topography, chemistry and wettability[89,90] . The physisorption is regulated by van der Waals forces[91] thus are influenced by the net charge, the chemical structure, and the size of the protein[33]. For a pure solution that contains only the protein in question, the size of the protein will play an important role, and the bigger is the protein, the larger will be the number of binding sites capable of interacting with the surface[92].

Another important parameter to take in consideration is the net charge of the protein. In the past, it has been demonstrated that for higher adsorption, it is necessary to have the protein in a solution with a pH close to their isoelectric point due to the minimisation of the repulsive charges[93]. However, the proteins may unfold to various degrees leading to increased system disorder, due to the elevated hydrophobicity of a non-functionalized surface. This effect needs to be avoided as the protein is present not anymore with its natural structure, and perhaps its activity is compromised. Any degree of denaturation gives a major possibility of interaction point between the surface and the protein[94].

Several methods are used to study the protein structure changes on the surface after adsorption such as time-of-flight secondary ion mass spectrometry (TOF-SIMS)[95] Quartz crystal microbalance[96] and atomic force microscopy (AFM)[97]. Extensive studies

have been carried on fabricating surfaces coated uniformly with several functional groups not only to prevent non-specific adsorption but also to fabricate biologically inert surfaces. Several strategies can use monolayers (e.g. SAMs) and multilayers (layer-by-layer) coatings with polymers carrying the functional group necessary for the bonding[98]. Previously studies reveal that the protein-surface coverage is higher in those surfaces with high hydrophobicity[99–101]. This is because a hydrophilic surface forms strong interactions with the water in the environment and directly influencing the desorption of the protein previously adsorbed. On the other hand, a too strong hydrophobic surface can determine a possible denaturation.

In elliptically shaped proteins, the protein can find itself in the "side-on" or "side-off" position, depending on which axis lays down on the surface. In this study performing molecular simulations[102], Dragneva et al. suggest that a specific orientation of fibrinogen (fig 4.1.2), so-called "side-on," could trigger an immune response by exposing recognition sites, which are concealed in the native structure[103].

Also, recent studies[104,105] showed that the protein structure, after adsorption, can be influenced by specific topographic patterns on the surface, such as curvature, the spatial arrangement between the surface nanoparticles, roughness. The recent nano- and microfabrication methods have been opening an entire field regarding the topography modification on the surface for studies *in vitro*[106,107]. Taking into account that a protein occupies an area of 10-100 nm^2, it is not unexpected that nano featured surfaces can manipulate the protein adsorption and structure.

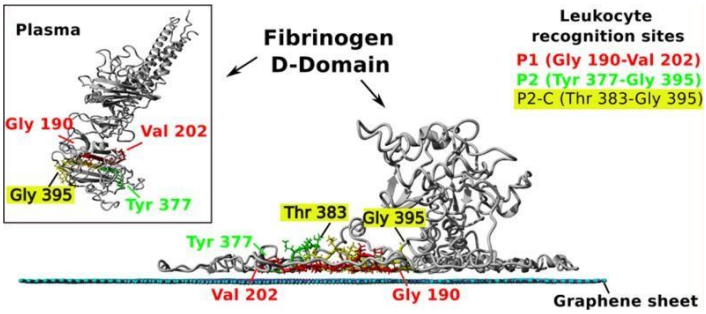

Figure 4.1.2 The overall structure of fibrinogen and its side-off and side-on conformations. The shape in the plasma does not trigger an immune response as the Leukocyte recognition sites are masked inside the structure. The physical adsorption of the same protein on a graphene sheet determines the exposure and the recognition sites triggering the immune response. The picture was taken from reference[105].

As proposed by other studies, the surface curvature is another parameter that needs to be taken in account[108–110]. Gu et al[111,112], with the use of molecular dynamics, expanded, even more, this research field by showing nanostructures that could be used for protein immobilisation (fig 4.1.3).

Vertegel et al.[113] showed not only improved adsorption in the case of 4 nm diameter nanoparticles but also that these nanoparticles were capable of immobilising the protein in its native-like structure in comparison with the same nanoparticles of 100 nm in diameter.

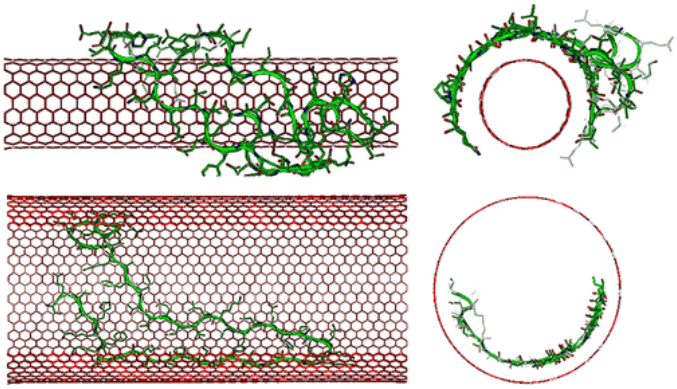

Figure 4.1.3. Molecular Dynamic of protein adsorption on single-walled carbon nanotubes. Depending on the diameter of the nanotube, the protein could be possibly adsorbed in the interior or exterior part, providing two new different protein shapes. The picture was taken from reference[113].

Giamblanco et al[114] emphasise even more the crucial importance of surface curvature on the protein orientation and structure, by showing that the laminin orientation can be predicted from "side–on" to "side-off" with a parameter curvature dependent, γ, and connecting it to the average height and the macromolecular gyration radius R_g. The study of rounded surfaces not only focused on the particles and wires size but also their chemical composition.

Nanoparticles and wires can be used for in-vivo applications, hence need to be toxicologically inert and immunologically inactive. One of the materials used for this approach is magnesium alloys[115]. The magnesium surfaces seem to have very low toxicity and also very good biomolecule adsorption. Once the protein has been adsorbed, it also masks the nanoparticle from too fast degradation, as the body recognises it as their particles. This scenario was first illustrated by Harandi et al[116], where the magnesium

after immersion in a solution of bovine serum albumin (BSA) the degradation was slowed down.

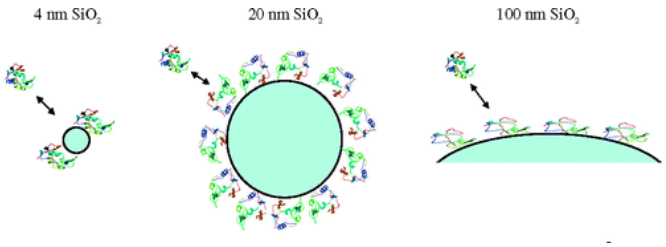

Figure 4.1.4 Protein adsorption on different sizes of nanoparticles. It is possible to notice that for a particle with a smaller diameter (in this case 4 nm and 20 nm) the protein conformation was well preserved. While instead for less curved surface, thus bigger diameter (100 nm) the protein structure tends to change once adsorbed. This image was taken from reference[116].

Yamamoto et al.[117] begun to study the degradation effect of organic and inorganic molecules in the body over the magnesium. They propose that the chelation effect and the related degradation were strongly influenced by specific amino acids called Eagles minimum essential medium (E-MEM). In contrast, thanks to the protein adsorption, the magnesium degradation was inhibited due to the formation of an insoluble salt layer magnesium surface. This salt layer acts as an effective barrier against corrosion, and it is strongly determined by the solution where the magnesium is immersed.

Another scenario is presented in the case of glycoproteins[118] as the corrosion rate increases linearly with the amount of glucose that rapidly transforms into a gluconic acid, which decreases the pH into the environment and determines deterioration of the protein layer on the surface[119,120].

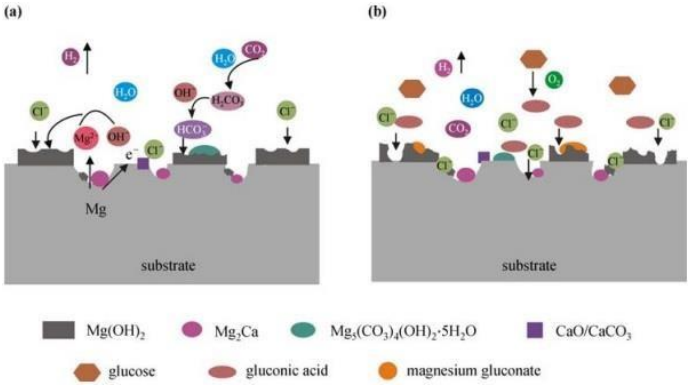

Figure 4.1.5 Corrosion process of the magnesium alloy Mg_2Ca in a saline solution (A) and a glucose solution (B). In the first case, a layer of insoluble salts forms on the surface of the alloy. This is due to the Magnesium and the Calcium forming insoluble salts: $Mg(OH)_2$, $Mg_5(CO_3)_4(OH)_2$, CaO, $CaCO_3$. In the second case, glucose is oxidised in gluconic acid, reacting with the magnesium and forming magnesium gluconate that dissolves later into the solution. This image was taken from reference[118].

Later on, the deterioration of protein immobilised on the surface was studied by Liu et al.[121] in a solution that mimics the condition of the body fluids, in order to study these surfaces in a bio-friendly environment. The inclusion of BSA in the body fluid significantly decreased the corrosion, leaving nanoparticles with a BSA layer properly immobilised.

Physical adsorption on surfaces of proteins is a process occurring spontaneously, which strictly depends on the fundamental properties of the protein and surface. Physical adsorption represents a one-step strategy for surface functionalization and can result in a highly dense monolayer. However, it can also lead to an activity loss due to the multilayer assembly and change in protein physiological structure[122]. Hydrophobicity, hydrophilicity and roughness of the surface are parameters to take into account for

proteins adsorption[101,123–125]. If surface regeneration is needed, protein removal can be achieved by prolonged rinsing with highly ionic solutions, extreme pH, high temperatures, and detergents[126–128].

Chemisorption

The chemisorption provides a better immobilisation method than physical adsorption in terms of improved biorecognition for the substrate in the nanomolar range[129]. As protein widely offer a functional group that can be used for interactions, chemical coupling represents a valid applicable approach for this type of surface functionalization. Examples of chemical coupling include thiol groups, amine groups, and carboxyl groups[33].

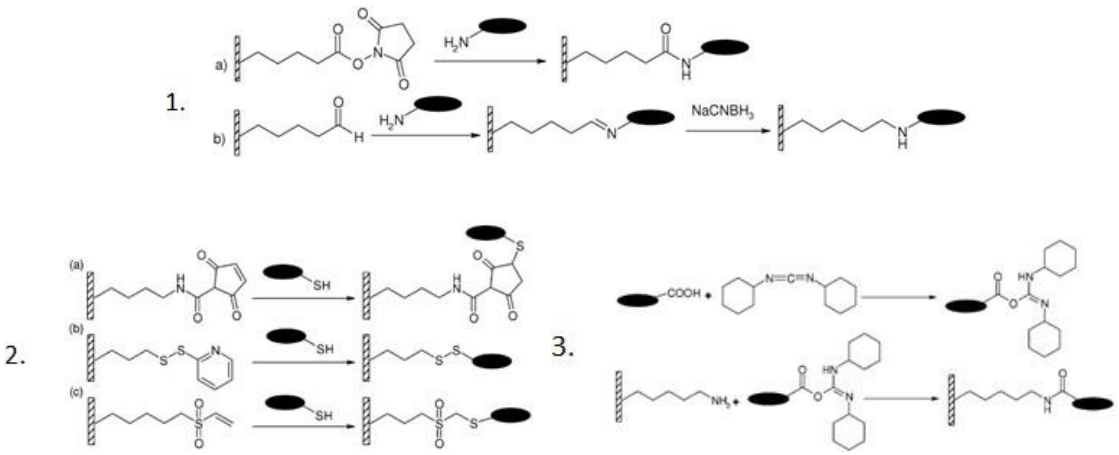

Figure 4.2.1 Chemisorption where the protein is cross-linked to a surface via a functional molecule. The main strategies include the amine (1), thiol (2), and carboxyl crosslinking (3). The picture was taken from reference[33].

However, reagent concentration can bring to a protein denaturation due to an overcrowded surface, and is a parameter needed for keeping protein activity to the maximum level. As adsorption, chemical coupling does not ensure precision regarding the orientation of the protein at the surface and surface regeneration cannot be possible due to the high stability of the chemical bond. Site-specific immobilisation approaches of protein can be pursued by enzymatic biorecognition as an alternative approach in terms of concepts and design[130].

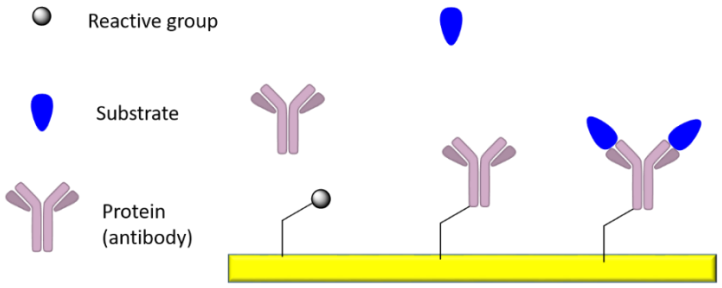

Figure 4.2.2 Chemical coupling used for the biorecognition of the substrate. In this case, the crosslinking is immunomediated due to the use of an antibody for the immobilisation of the substrate. The picture was taken from reference[130].

In this case, the coupling is between a molecule on the surface and an antibody, which will be used for subsequent targeting and immobilising proteins. These immobilisation strategies provide the surface with high specificity and simple interaction with the target proteins[130]. Ito *et al.*[131] proposed a way to immobilise glycosyltransferases on a sepharose resin, where the sepharose is used as support for the coupling of the Glycosyltransferases. These findings were used as biosensors to detect a domain of the epidermal growth factor biomarker receptor[132].

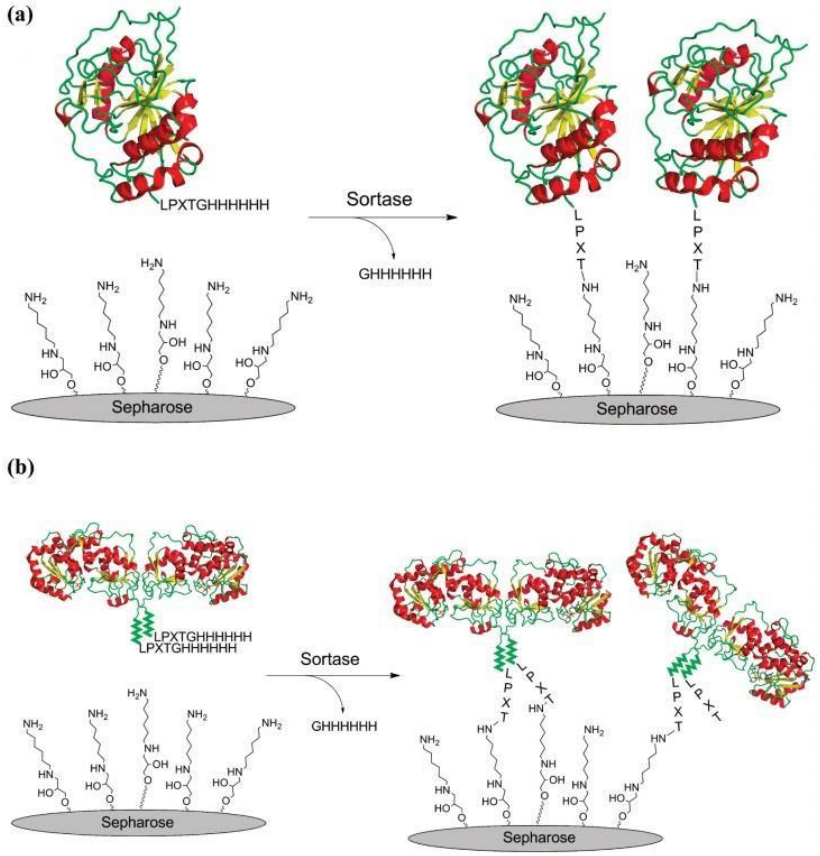

Figure 4.2.3 Coupling of two different types of glycosyltransferases. Both methods use the sortase enzyme that catalyses the crosslinking. The picture was taken from reference[130].

An alternative approach uses different enzymes such as transglutaminase and tyrosinase, to recognise other residues and bond lysines and tyrosines-terminated surfaces[137]. Furthermore, tyrosinase has been covalently bound to a fluorescent protein and tyrosine-terminated surface for antibody recognition[133–135]. Coupling proteins can achieve in-situ protein entrapment. The residues to be recognised should be well exposed in high flexible regions of the protein structure. Residues for enzymatic entrapment may be recognised from the surface, and protein engineering represents a versatile tool to add the desired tags to the desired protein such as sortase and the tyrosine tags[131,134,136].

If the correct chemical groups are used, enzyme chemisorption provides a stable way to retain proteins with a specific orientation. This method is also useful to avoid surface crowding[137].

Several unnatural amino acids having azide, keto or thiol groups have been introduced into the protein structure reaching site-specific immobilisation on surface[138–142]. Another method for immobilisation is to reduce the disulphide bridge of the proteins with reducing agent and later make them bond with the gold surface. In this scenario the disulphide bridge is chemically reduced to two thiols group (Fig 4.2.4); the reducing agents used for this kind of reactions are the dithiothreitol (DTT), 2-mercaptoethylamine (2-MEA) or tris(2-carboxyethyl)phosphine (TCEP)[143–145].

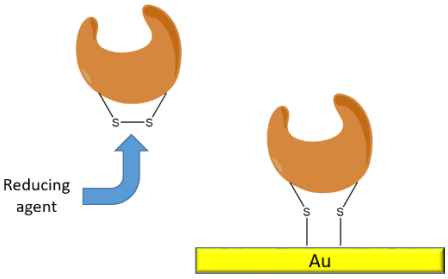

Figure 4.2.4 Chemical immobilisation mediated with the breaking of a disulphide bridge present in the protein structure.

The disadvantages of this technique are that the disulphide bond, depending on the proteins, is one of the main contributors to the structure of the protein and their possible reduction could lead to protein denaturation. An alternative technique based on UV-light and the presence of an aromatic group close to the disulphide bonds have been studied to prevent the denaturation and preserve the biofunctional structure. The UV radicals should generate a rupture in the aromatic of the proximal molecule. The rupture of aromaticity generates a radical group which make them reacting with the gold moieties

on the surface and generating a chemical bond highly stable. This technique has been used for several proteins such as alkaline phosphatase, trypsin, prostate-specific antigen (PSA) and proteases[144].

Another method is to use peptides to intercross proteins on surfaces chemically. Peptides are molecules constituted by less than 50 amino acids, and thus their structure is simpler than proteins due to their smaller size. Furthermore, peptides can be synthesised in the laboratory, which offers the possibility of the insert into specific sites the desired chemical group and makes them valuable for biosensors fabrication. Lim et al[146], a peptide was labelled with a fluorescent tetramethylrhodamine (TAMRA) group to fabricate a kinase biosensor that produces a fluorescent signal only when a kinase phosphorylates it. The surface in question is a quantum dot surface. The results were measured with Fluorescence Resonance Energy Transfer (FRET).

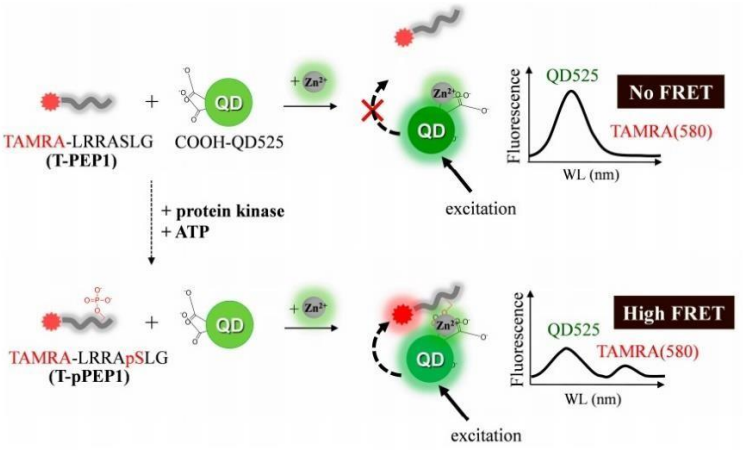

Figure 4.2.5 TAMRA labelling of the peptide LRRASLG. If the peptide is not phosphorylated does not interact with the quantum dot, and no FRET is visible. In the opposite case, when the peptide is phosphorylated by a protein kinase, it starts to be excited by the quantum dot and the FRET is observable. The picture was taken from reference[146].

Another method widely investigated is the fusion of peptides to proteins at the genomic level to provide a new type of affinity and a site-specific orientation, especially a His-tag using sulfotransferases[147]. This kind of peptides of different size can be used for several substrates from graphite[148] to carbon nanotubes[149], from crystalline nanocellulose[150] to polystyrene[151] and from sapphire[152] to gold[153].

The peptide presents universal adaptability and stability to different chemical and reaction condition that can also be tagged with histidine. Ganesana et al[154] immobilised the insecticide paraoxon on nickel through the His-tagged peptide. The results are an enzyme immobilisation onto Nickel nanoparticle surfaces for the detection of pesticides.

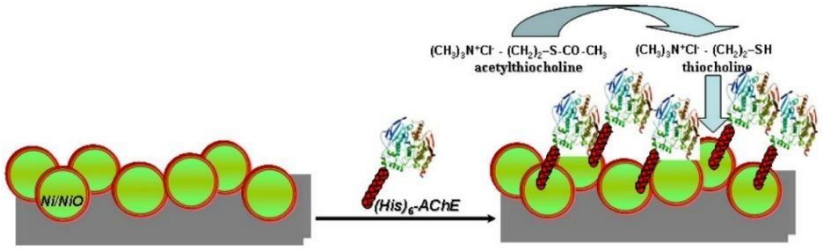

Figure 4.2.6 Chemical immobilisation of an enzyme for pesticides detection. The enzyme AChE is tagged with the peptide histidine (His), necessary for its chemical immobilisation on Ni/NiO nanoparticles surface. This picture was taken from reference[154]

Zhang K. *et at* [155] proposed a polypeptide surface to immobilise glutathione-S-transferase tagged to Green fluorescent protein (GFP). This method not only allows protein immobilisation but also provide further information due to the fluorescent signal. Strategies similar to immobilised peptides have been offered with affinity protein (fig 4.1.1). A simple example has been performed in a study where a maltose-binding protein (MBP) was fused to a nitroreductase. In this way, it was possible to functionalize an electrode previously treated with a bipyridine derivatives[156], and a sensor for 2,4,6-

trinitrotoluene (TNT) was fabricated with a detection limit of 2 microM and with a similar affinity to the wild-type nitroreductase. The complex showed a dissociation equilibrium constant (KD) value of 95 microM, while instead, the wild-type version of the enzyme was around 78 microM in solution with TNT[156].

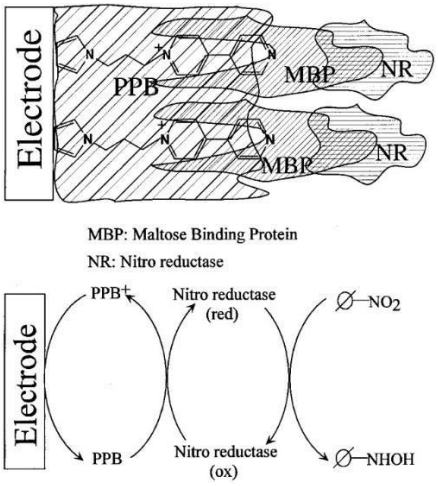

Figure 4.2.7 Working principle of the TNT sensor. (Up) The electrode surface is functionalized with a bipyridine derivative (PBB). Then the Maltose Binding Protein (MBP) serves as a bridge among the PPB and the enzyme nitroreductase in charge of the real TNT detection. (Down). The electrons exchanged among the electrode and the nitrate (NO_2), typical of the TNT molecule, is mediated by the PPB and the nitroreductase. The intensity of the electric signal is proportional to the amount of NO_2 present in the sample. The picture was taken from reference[156].

Other widely used proteins are the hydrophobins, that can be applied to immobilise other proteins onto polystyrene-patterned surface[157]. In this way, hydrophobins found their utility for the fabrication of a biosensor[158]. Hydrophobins have also been investigated to change the properties of both hydrophobic and hydrophilic

surfaces, e.g. the hydrophobicity of polydimethylsiloxane (PDMS) [159] and the hydrophilicity of the mercapto undecyl-ammonium chloride[160]. The hydrophobicity of gold surfaces can also be changed using gold-binding protein (GBP), a protein with a particular affinity for the gold atoms and surfaces. A GBP was used to bond a single-chain antibody for the fabrication of Surface Plasmon Resonance (SPR) sensors in an easy nanofabrication step with a concentration limit of 0.14 ng/ml of the hepatitis virus antigene[153].

In summary, the affinity peptides and proteins provide a controlled site-specific attachment. The advantage of the affinity peptides is mostly provided by the small size that makes them very stable to any condition and reagent used. Surfaces pre-treated with peptides or proteins that offer specific orientation are widely used in the field of immune sensing. Protein A and Staphylococcus aureus are intensively used for immunoglobulins immobilization, due to the fact that they strongly bong the Fc portion of the immunoglobulins. Protein A naturally interacts to the bacterial membrane and its specific interaction is used for sensing of bacteria concentration.

As the immunoglobulin, it is a unique interaction and occurs with a dissociation constant into the nanoMolar range this kind of biosensing happens even in a mixture with another biomolecule of the same nature[161]. Protein A is widely used due to its stability at extreme pH values (1-11) and relatively high temperatures (80 Celsius)[162]. However a prolonged interaction with the surface can determine denaturation, loss of functionality and arrangement in multilayers onto silicon and cellulose surfaces[163].

Immobilisation with hydrogels

In parallel to the chemical methods to immobilise protein on the surface, an alternative and viable way is to take in consideration in the field of biosensing: the protein immobilisation mediated by hydrogels[164]. Hydrogels are an extensive web of a covalent bond and non-covalent interactions between hydrophilic polymer chains in a colloidal solution. The hydrogels are considered biocompatible and over time have become increasingly used in different ways: biointeraction with components at the nanoscale, reaction to an external stimulus, incorporation of varying receptors inside their structure, regulation of viscosity of the material.

Hydrogel biosensors can have their biosensing property in two different ways, with and without receptors. Hydrogels without receptors have been quite used to develop ionic hydrogels for environmental analysis such as temperature, pH and electrical intensity[165]. Biosensors based on hydrogels for pH measurements are capable either to release or retain protons in response to an ionic potential. The value deducted for this kind of sensors is the swelling ratio, which represents the weight variance of the hydrogel before and after water absorption. In strong ionic conditions, the more protons are adsorbed, the more repulsion will be between the polymeric chains of the hydrogels, leading to either positive or negative swelling ratio[166]. The swelling is a property widely studied especially for protein entrapment[167], while instead the deswelling is mainly used for a controlled protein delivery[168]

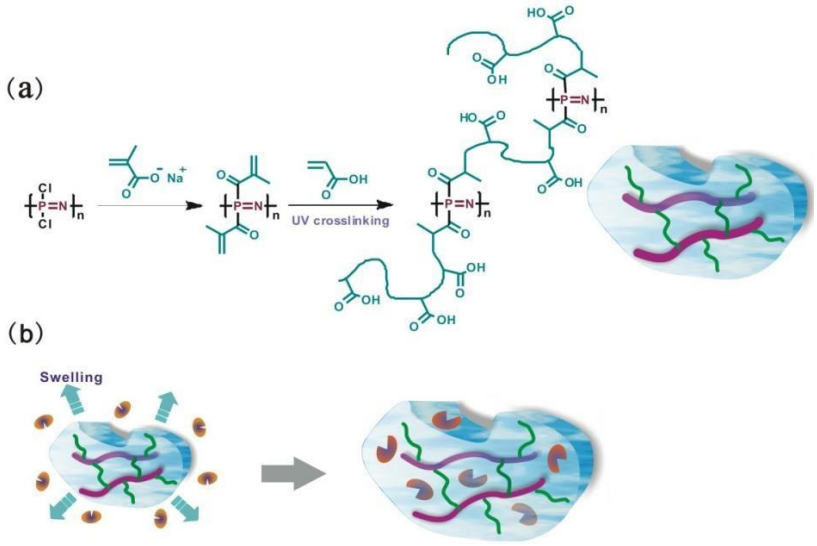

Figure 4.3.1 (A) Chemical structure of the poly[bis(methacrylate)phosphazene] (PBMAP) hydrogels. (B) The swelling property is determined by the protein entrapment. This picture was taken from reference[167].

The hydrogels, including receptors represent a biosensor with a property of detecting molecules at the nanoscale. With this method, the detection of particular bioentities is possible, and a hydrogels biosensors can be obtained through bio-receptors immobilisation. Among all the hydrogels used, polyvinyl alcohol (PVA) represent one of the widespread hydrogels in biomedical applications. Their full usage it is mostly related to their biomechanical properties, polar characteristics, biocompatibility and readily applicable to detect hydrogen peroxide[169,170] ,urea[171–174], triglyceride[175,176],ethanol[177] and genetic derivatives[178].

Thanks to their flexibility and their stability in different environmental conditions, the hydrogels sensors can be easily compatible with soft tissues and minimise inflammation and fibrosis responses. Another hydrogel widely applied is the polyethene

glycol (PEG) and its derivatives, due to their hydrophilic properties, low interfacial energy, cell adhesion and ability to retain protein[179–181]. Nowadays, PEG and its related hybrids have been used for the manufacturing of optical[182–189], electrochemical[190–197] and mass-based biosensors[198–201] thanks to their antifouling characteristics.

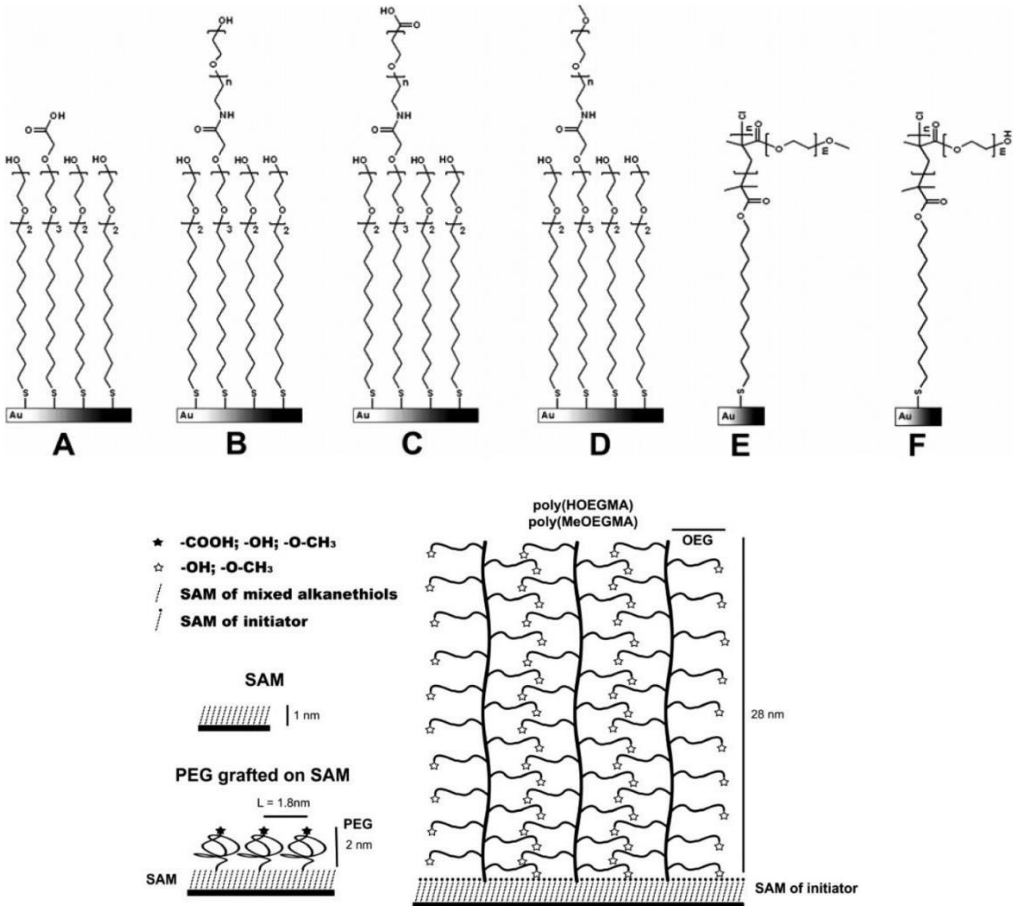

Figure 4.3.2 (Up) Chemical Structure of PEG hydrogels and its derivatives. The derivatives are fabricated to change the polarity of the hydrogels. (A)Ethanoic Acid, (B)hydroxy, (C) carboxyl and (D) methoxy-terminated PEG. Two examples of polymer brushes based on (E) poly(MeOEGMA) and (F) poly(HOEGMA). (Bottom) The overall architecture of PEG hydrogels. The SAM of initiator is essential for the anchor point to the surface. The picture was taken from reference[179].

By choosing different polar properties and behaviour, acrylates and acrylamides derivatives represent a vast category of stimulus-responsive hydrogels. As their physical properties change over an experiment, hydrogels can swell and deswell depending on their charge density of the ionic group. The patterning of these hydrogels represents one of the main steps into their fabrication process. Microcontact-printing, wet-etching, evaporation induced self-assembly and microlithography[202] are only a few examples of methods to pattern hydrogels.

Hydrogels of the acrylate family have been shown to promote protein binding[203,204], allow quantitative or qualitative measurement of glucose[205–207], ammonia [208,209], and environmental measurement of pH [210–213] and humidity[214,215]. Their properties of protein affinity, metal chelation, low cost of preparation, facile fabrication render them as the most versatile tools for the next-generation biotechnology[214].

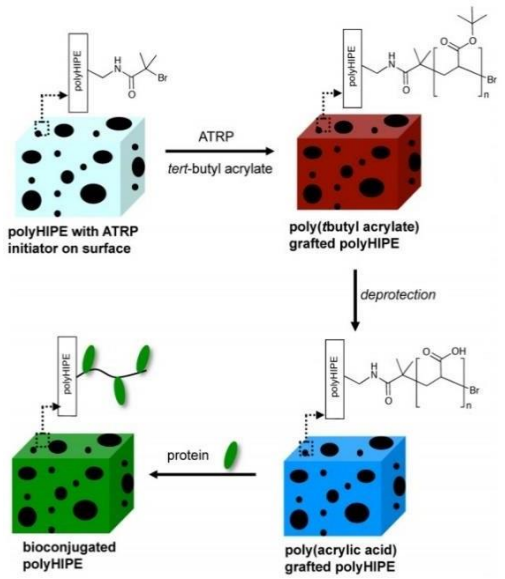

Figure 4.3.3 Synthetic pathway for the fabrication of the polymerised high internal phase emulsion (polyHIPE), where the gel is first functionalised with the tert-butyl acrylate. In

the second step, the acrylic group is deprotected to allow the protein binding in the third step. The picture was taken from reference[201].

Another application for these hydrogels is their responsiveness to the current passing through them [216–218]. Electroconductive hydrogels have been an attractive tool for protein immobilisation and fabrication of biosensors, due to their unique properties of transporting electrons to the sensor for the generation of an electric signal. One of their most appreciated features is to be quite flexible even during the process of electron transport.

The application of redox potential can activate the enzyme-immobilised structure and be modulated on demand by the users. Hence, their activity is modulated by letting pass an electric force through the hydrogels that alters the potential to generate a voltage. In addition, a doping method to change the conductivity of the hydrogels can also lead to variations in surface resistances, voltages, or current. Several redox hydrogels with an immobilised protein have been developed for the measurement of acid lactic[216], DNA[217], dopamine[218], tumors[219], hydrogens peroxide[220], glucose[221] and vitamins[222].

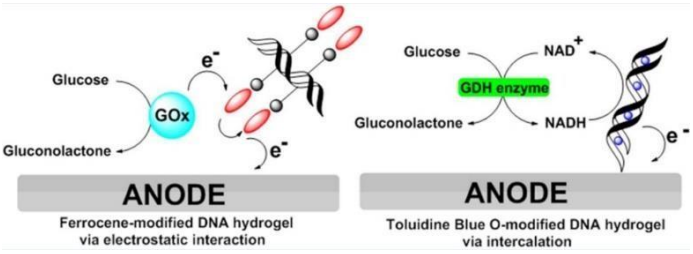

Figure 4.3.4 Two examples of enzyme redox hydrogel. (Left) The glucose in the sample is transformed in gluconolactone by the Glucose Oxidase (GOx), giving an electron to the DNA hydrogel. Later the electron is transported to the anode and measured (Right). The same principle is applied in the case the enzyme immobilised is the Glucose

Dehydrogenase (GDH) where this time the electron is generated by the conversion of the NAD+ in NADH. The picture was taken from reference[221].

Protein-hydrogels systems are mostly preferred in a considerable variety of tissue engineering applications such as 3D scaffolds for cell growth and immobilisation of growth factors. The growth factors, in particular, are widely used in tissue engineering thanks to their property of cellular proliferation, differentiation and regeneration and can be delivered via injections or immobilisation into scaffolds[223]. The immobilisation into hydrogels scaffold is generally quite preferred as a system in ensuring the cell outcome by keeping the stability, minimises the cost of growth factors therapies and growth factor signalling. Chiu et al[224] demonstrate a superior growth factor performance upon immobilisation on hydrogels. Also, Park et al[225] established that the immobilisation of the bone morphogenic protein-2 (BMP2) on hydrogels enhanced the osteogenic activity of the mesenchymal cells[226], while Odedra et al. [227] revealed that the vasoendothelial growth factor (VEGF) on collagen-based hydrogels increase the endothelial cell migration activity. Furthermore, Moore et al. demonstrated that neurotrophin gradients[228] on synthetic hydrogels increased the neurite outgrowth from chick ganglia neurons.

Growth factor immobilisation offers the advantage instead to investigate and to localise the effect of the growth factor within the scaffold instead of allowing it to diffuse into the tissue freely. The growth factor immobilisation also offers a good method for cell migration as it is believed that the cell migrates to the source, towards an increased gradient of concentration. Miyagi et al[229] successfully immobilised VEGF into a collagen-based hydrogel to mediate increase neovascularization in vivo for myocardial repair, by

showing that the hydrogels scaffold with the VEGF presents a greater vascular density that the controls with no VEGF. Choi and coworkers[230] successfully proved that epithelial growth factor immobilised on polyethene glycol (PEG) promoted a greater wound healing *in vivo*. Alberti et al[231] immobilised leukaemia inhibitory factor on PEG-based hydrogels that resulted in a greater pluripotency embryonic stem cell.

The majority of the tissue engineering hydrogels are used to immobilise the protein-based growth factor and used for cellular scaffold and microenvironment. One of the main hydrogels used to represent a PEG-fibrinogen hybrid material as the fibrinogen offers the advantages of cell microenvironment and migration, while the PEG gives to the entire system a major elasticity[232]. Gonen-Wadmany et al[233] reported the comparison of three different PEG-proteins copolymers where the cell migration was guaranteed on PEG-collagen and PEG-fibrinogen and not PEG-albumin due to the missing cell adhesion property of the albumin protein. The three hydrogels also offer different swelling, degradability and elasticity underlining the key parameter between the protein and the polymer.

Hybrid materials composed by collagen and polyanhydrides such as polycaprolactone, polyglycolic acid and polylactic acid have been fabricated as fibrous matrices[234–236], composites gels[237,238], and grafted copolymers[239]. They are extensively used in the tissue engineering of cartilage and bones thanks to their biocompatible composition made of chitosan, fibrin, fibrinogen, agarose and hyaluronic acid[240]. While there is an already established field for physical, chemical and affinity immobilisation of a protein on a surface, the hydrogel approach still represents a method that needs to be improved.

The hydrogels represent a very advantageous way to overcome the other approaches, as the physical adsorption does not offer control over the protein orientation, the chemical immobilisation still represents a "too-hard" approach, determining a possible protein denaturation, and the affinity immobilisation remains an expensive method. However, further studies need to be done to show the real potential of the hydrogels approaches. In the overall, the protein-hydrogels interactions will allow designing engineered tissues for biomimetic approaches for in vivo environment.

3.4 Immobilisation by a lipid bilayer

The lipid membranes approach for application in biosensors represents so far the most intriguing way to obtain protein immobilisation. Among the several reasons for that, there is the fact that a lipid-based biosensor represents a biomimetic environment since it is made out of phospholipids, the main compound of the cell membrane. This concept is even more suitable since a cell membrane is the most natural host for all sorts of protein-derivatives. The immobilisation of molecules such as antibodies, enzymes and receptors can be driven by electrostatic forces, determining a change in the physical properties of the membrane, above all, the electrochemical properties. The immobilisation of several proteins on lipid bilayers leads to the fabrication of a huge variety of biosensors as theoretically any proteins can be possibly immobilised on a lipid membrane.

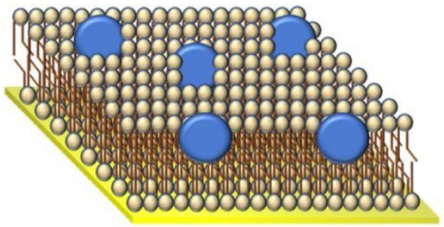

Figure 4.4 Protein immobilisation mediated by a phospholipidic bilayer. The proteins (blue) are captured into the phospholipid bilayer macrostructure.

Several biosensors have been developed for environmental monitoring and clinical diagnosis[241–245] using this approach. The acetylcholinesterase immobilisation on a lipid membrane has been extensively studied for pesticide detection[246–251], while instead peroxidase have been used for the detection of dopamine[249] (Fig. 4.4.1) and redox cascade in glucose oxidase[248]. Bioentities with the lipidic surface have been employed for the monitoring of the amyloid-beta protein fibrilization[252].

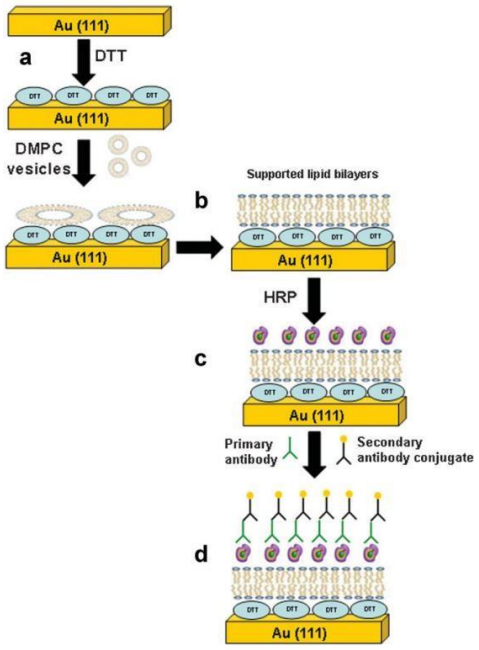

Figure 4.4.1 A schematic representation of the formation of dithiothreitol (DTT) SAMs on gold (Au) support (a) with subsequent fusion of dimyristoyl phosphatidylcholine

(DMPC) vesicles forming lipid bilayers; (b) horseradish peroxidase (HRP) immobilization on lipid bilayers supported on DTT/Au (c) and immunolabeling HRP immobilized on lipid bilayers (d). The picture was taken from reference[249].

Lipids and more in specific phospholipids can be used for sensing enzyme activity through chemiluminescence. In this study[241], the authors employed a choline oxidase, immobilised on a luminol-based bilayer (Fig 4.4.2). The catalytic reaction between the oxidase and the peroxide lead to a luminescent reaction that can be optically detected. General immuno-platforms showed a high affinity at very low substrate concentration for picoMolar detection of chemical pollutants[253]. However, compared to the previous methods of protein immobilisation cited above, the lipid-based immobilisation is the method capable of developing the lowest background noise even at the picoMolar concentration[254,255].

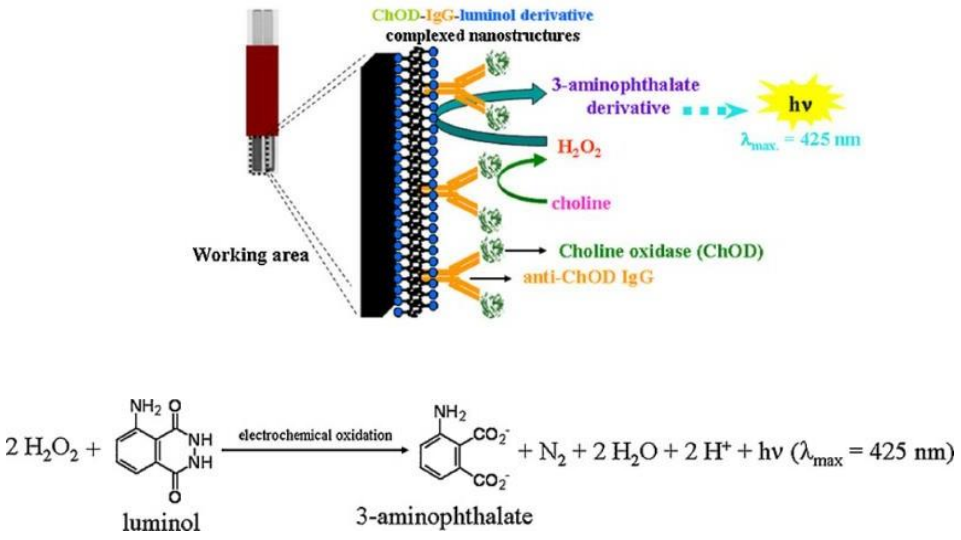

Figure 4.4.2 The scheme of the choline immobilised on bilayer for the detection of hydrogen peroxidase (up) and the chemiluminescence reaction occurring at the working area (down). The picture was taken from reference[241].

Apart from picomolar detection, the lipidic bilayer seems also a good way to protect the protein conformation from denaturation and to ensure even a signal amplification[256,257]. In general, biosensors are tools capable of transducing a biochemical interaction into an electric signal[258].

The interaction at the lipid interface determines a change into the lipid orientation inside the layer, forcing possibly changes into several characteristics of the membrane such as transmembrane potential, membrane fluidity, surface charge density, and dipolar potential. Thus, leading to significant physical and electrical properties changes between the two sides of the bilayer[253]. Briefly, an induced membrane change determines a bilayer ability to transduce a biochemical interaction into an electrochemical signal and amplifying it. In this study,[259] a triazine herbicide that possesses lipophilicity

characteristics determines their adsorption onto lipid membranes forming aggregates among the molecules. This adsorption determines the alteration of the lipids packing into the membrane that induces a change into the membrane current. Similarly, atenolol[260] and vanillin[261] can be detected at micromolar concentration[244].

If incorporated with lipid platform, protein immobilisation mediated by lipid bilayer could arise for sensing of either organic and inorganic molecules[262]. Apart from large proteins also small peptides can determine changes into the lipid membrane for the formation of ion channels. Gramicidin A[263] was used to form a channel into a metal-based lipid membrane for the detection of ammoniums ions. In another study,[264] lysenin, aerolysin, and hemolysin were used for the sensing of a single molecule detector based on a lipidic membrane.

This current raising interest in nanopore and ion channel should support and encourage the next generation of single-molecule sensors and, nowadays, represents an exciting field with many possibilities in terms of discoveries. However, the lipidic biosensor is still lacking suitable mathematical models and phenomena simulations at the nanoscale[253]. The field remains hard to explore, but it is also true that the system modelling, the ion transport phenomena, and the continuous characteristics changing of the membrane represent a huge challenge[258]. Shortly, the use of simulation software may become necessary for the development of biosensors by optimising their design and response time[265].

Supramolecular Immobilisation

All the systems mentioned above represented an elegant way to immobilise protein on the surface. However, any system presented their limitations and use restrictions

related to active site orientation, protein structure preservation, the stability of the protein-SAM system newly formed. An immobilisation method that seems to outstand from all the others in the last years, is to be through the use of supramolecular architectures. This relatively unexplored strategy, although with vast potential involve the use of scaffold molecule, such as cyclodextrins, calixarenes and cucurbiturils or histidine tags[266–268]. Young[269] et al. uses the stable supramolecular bond between the cucurbituril and the ferrocene to immobilise a yellow fluorescent protein on the surface (fig. 4.5.1). In this case, the immobilisation occurred without the protein directly interacting with the surface, avoiding any physical adsorption, and providing a stable and strong way to have these proteins on the surface.

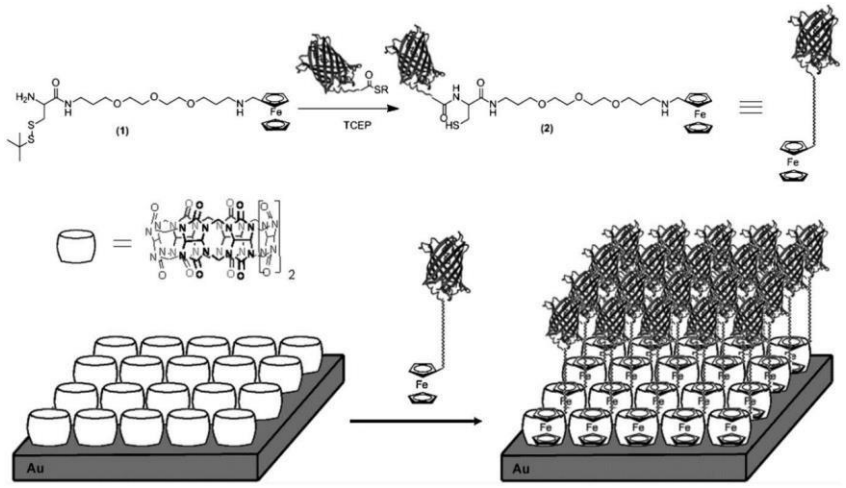

Figure 4.5.1 Surface immobilisation of a yellow fluorescent protein (YFP) mediated by a supramolecular cucurbituril-ferrocene system. The picture was taken from reference[269].

Zhan et al.[270] in this study explains how, in the case of the cyclodextrins, these surfaces can be functionalised in three different ways: with a SAM, a polymer brush, and a multi-layered film (fig.4.5.2). All the three methods provide a stable way to retain a

guest molecule, and in our case a protein, on the surface with no problem regarding the protein structure being modified.

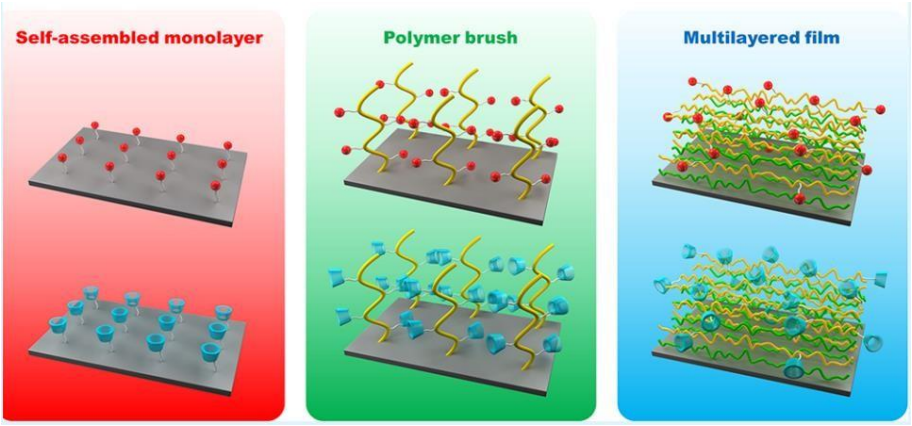

Figure 4.5.2 Supramolecular bioactive surfaces mediated by a self-assembled monolayer (red), a polymer brush (green) and a multilayered film (blue). The picture was taken from reference[270].

Another study enforcing the idea of the use of the supramolecular approach for protein immobilisation is provided by Zhang et al.[271] were a cyclodextrin-based supramolecular system was self-assembled on the surface for the successful immobilisation of biotin protein. Further studies also demonstrate the reversibility of the system and the ability to control the release on-demand only by using an adamantyl derivative (fig. 4.5.3).

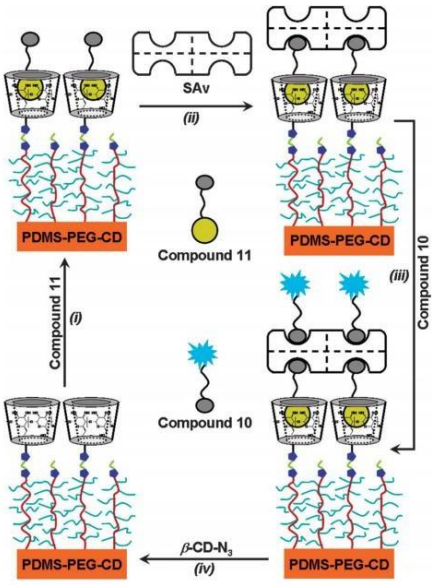

Figure 4.5.3 Fabrication of the reversible multilayer via cyclodextrin (CD) host-guest interaction. The PDMS surface functionalised with cyclodextrin is then assembled with a biotinylated monoadamantyl molecule (compound 11), which fits into the CD cavity (i) and works as a linker for the subsequent immobilisation of the streptavidin (SAv) (ii). In order to restore the surface to its original state, fluorescent biotin (compound 10) assembles on the SAv (iii), determining the release of the entire supramolecular architecture (iv). The surface is restored using a cyclodextrin triazide (β-CD-N_3). The picture was taken from reference[271].

Demirkol et al[272] uses calixarenes on the surface for immobilising glucose oxidase. The thiol-calixarenes were self-assembled on a gold surface, and then the glucose oxidase immobilised (figure 4.5.4). This immobilisation on the surface is mainly used for biosensing application for monitoring glucose.

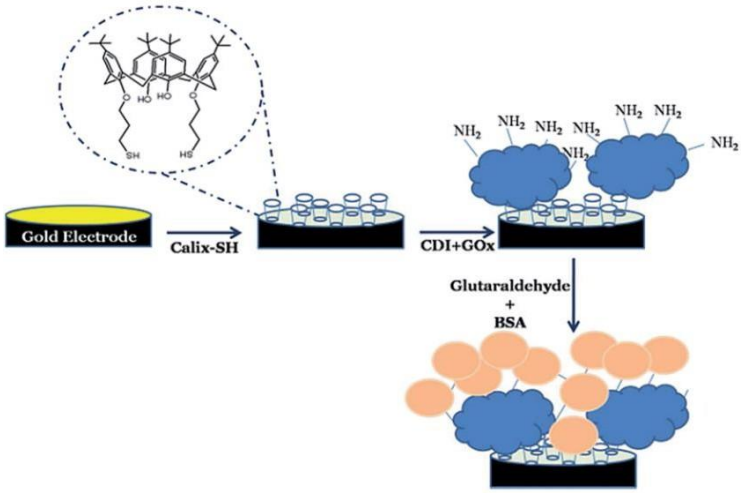

Figure 4.5.4 Glucose biosensor fabrication mediated by glucose oxidase (GOx) immobilisation. The Calixarene-thiol (Calix-SH) is self-assembled on the surface. The Calix-SH surface is activated with carboinimidazole (CDI), and then the GOx is immobilised on it. To increase the stability of the complex Glutaraldehyde and Bovine Serum Albumin (BSA) were added afterwards. The picture was taken from reference[272].

In a recent study[266], proteins have been tagged with several numbers of hexahistidine (His6) in order to be able to control the orientation of the protein over the surface (fig 4.5.5). The ability to modulate the protein orientation over the surface will allow further insight into the protein dynamics and chemistry and to improve the performance of the diagnostic assay by determining the exposure of the active site[266]. This strategy gave access to a high degree of control not only over the orientation of the proteins on the surfaces but also to the binding strength of the proteins with the surface.

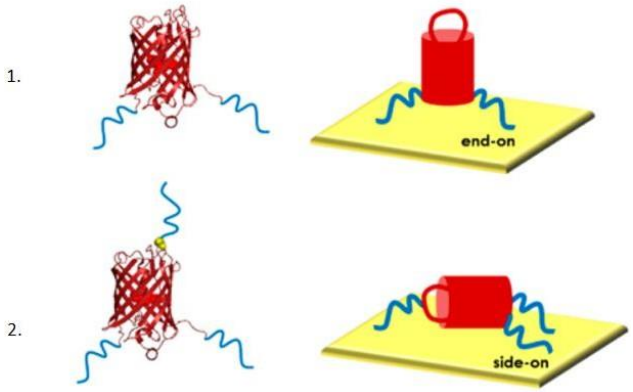

Figure 4.5.5 Histidine (blue line) tagging of a Red fluorescent protein (red). The amount of histidine tagging the protein affects the final orientation on the surface. The picture was taken from reference[266].

Another supramolecular way to orient the protein on the surface was explored by Gonzalez et al.[273]. In this study, a viologen-based guest molecule is self-assembled on a silicate surface, and the naphtol guest moiety is selectively bonded to a yellow fluorescent protein (fig. 4.5.6). In this paper, the cucurbituril is used as a linker between the protein and the surface. Stable and uniform fluorescent patterns are formed with a high ratio of signal-to-noise.

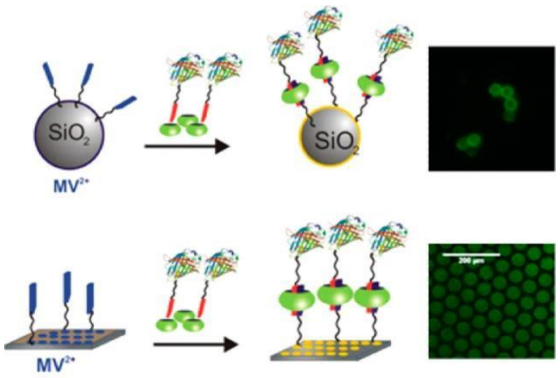

Figure 4.5.6 Immobilisation of yellow fluorescent protein on silica. The silica is functionalised with a viologen-based molecule (blue line, MV^{2+}). The protein is bonded

to a naphtol molecule (red line). The cucurbituril (green) is the linker that keeps the naphtol and the viologen together for the fluorescence patterning. The picture was taken from reference[273].

Lee et al[274] fabricated a protein chip by self-assembling on surface calixarenes molecules that provide efficient capture proteins. The sensitivity of this surface was highly specific, and the substrate detection was reduced to few femtograms. In the study, it is showed how the supramolecular interaction protein-surface appears to be more stable than those protein immobilised by chemical adsorption[274]. After initial immobilisation and formation of a surface-protein system, it was possible to immobilise subsequently another protein determining the formation of a surface-protein-protein macrostructure (fig. 4.5.7)

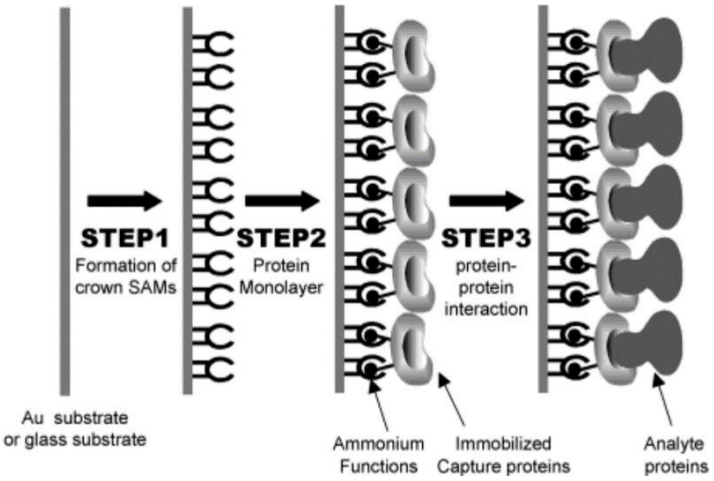

Figure 4.5.7 Fabrication diagram of the protein biochip. The first step is the assembly of a supramolecular SAM on the surface. The second step is the immobilisation of a first protein and formation of the surface-protein system. The third step is the formation of a second protein layer interacting with the first one, forming a surface-protein-protein macrostructure. The picture was taken from reference[274].

Qu et al[275] designs a reusable platform for selectively capture and release of bacteria and proteins, through a layer-by-layer fabrication method. Three types of non-covalent interaction can be distinguished in the fabrication of this supramolecular surface: the electrostatic forces between the different layers, the host-guest interactions of the cyclodextrin-adamantane system, and the carbohydrate-protein interaction (fig. 4.5.8). This platform can be regenerated and reused multiple time without loss of activity.

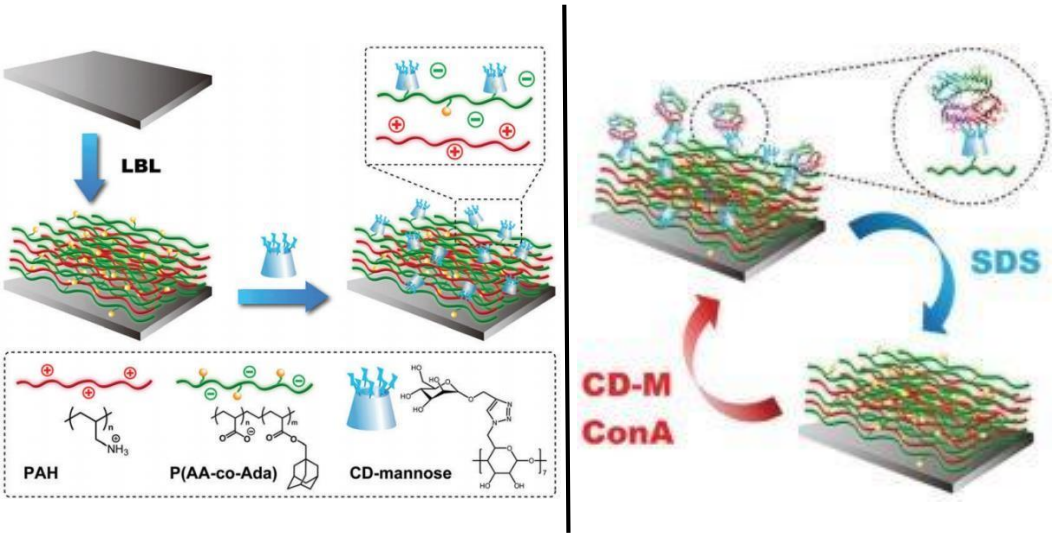

Figure 4.5.8 (Left) Illustration of the preparation of the layer-by-layer (LBL) cyclodextrin surfaces. The first step includes an LBL formation of several polymers followed by the self-assembly on the cyclodextrin derivative (blue). (Right) The schematic illustration of the re-use property of the surface. Once the concanavalin A (ConA) is immobilised, the surface can be restored using sodium dodecyl-sulphate (SDS). The picture was taken from reference[275].

Several other examples have been exploring supramolecular approaches[276–280]. All of them prove a valid scenario for the development of protein immobilisation tools. The ability to retain proteins in a strong way, without inducing any structure change, represents a considerable advantage to measure and study protein still unexplored in their

physiological state[276], also establishing a new and revolutionary strategy to fabricate the next generation of biosensing technologies.

Concluding remarks

From the above review, the protein immobilisation on the surface has been mediated by different strategies. The physical adsorption presented a way to immobilise protein in a simple and inexpensive way. However, this method does not ensure the stability of the protein structure, the stability of the protein on the surface and do not ensure any control over the orientation. The chemical adsorption instead, provide stable immobilisation over the surface and, in some cases, a controlled orientation on surface.

However, the chemical adsorption determines the generation of a covalent bond. This bond requires a relatively high amount of energy to be formed, that could lead to a change in conformation and subsequently of protein activity. Another way to immobilise protein on the surface was then provided by hydrogels. The hydrogels offer a stable interaction protein-surface preserving the original structure of the protein, mainly thanks to the fact that the major component of hydrogels is the water. Despite this advantage, the hydrogels face the problem of relatively high background signal, and its storage seems to be another problem in their way to commercial applications.

On a parallel research line, the phosphate lipid bilayer can also represent an immobilisation tool for biomolecules. It represents relatively stable protein immobilisation and easy preparation. Also confers a native-like environment in the case

of analysis for a membrane protein, as the phospholipidic bilayer offers a very similar behaviour to the cell membrane.

The lipidic bilayer also allows some control over the protein orientation as present either polar and apolar characteristic. The major problem related to the lipidic bilayer is mainly given to its storage and its stability over time, as the integrity of the macrostructure could be quickly deteriorated if not constantly in contact with water.

Above all these methods, the supramolecular immobilisation represents a relatively unexplored strategy, although with vast potential, that involves the use of non-covalent supramolecular interactions between proteins and supramolecular entities (e.g. cucurbituril, calixarenes and cyclodextrins)[266–268,270,281–283]. For example, taking advantage of the highly stable chemistry of cucurbituril-ferrocene inclusion complexes, proteins have been site-specifically modified with ferrocene to be reversibly and stably immobilised onto a cucurbit[7]uril (CB[7]) monolayer[269]. In another recent example[266], proteins have been tagged with a different number of hexahistidine (His6) at specific positions on the protein to understand its effect on protein orientation and binding strength upon interaction with nickel-nitrilotriacetic acid (Ni-NTA) self-assembled monolayers. These and other examples in the literature[273–275] illustrate how supramolecular interactions and their predictability can be used to design protein immobilisation systems with enhanced features and improved ability to tune their properties as required. Much though remains to be uncovered regarding the potential of supramolecular assembly for devising protein immobilisation systems with emergent properties amenable to current needs.

4. Project aims

The overall aim of this thesis is to design an easy fabrication method for protein immobilisation on the surface. The method will be exploring the supramolecular approach for immobilising protein on the surface. The surface will be functionalised with Cyclodextrin, a scaffold molecule capable to capture the amino acids protein portion into its cavity. Four different proteins have been chosen in our research to perform surface plasmon resonance (SPR), which allows monitoring binding events between molecules in solution and molecules immobilised on a surface.The proteins have been chosen differently in charge and size among them, in order to demonstrate the universality of our immobilisation method. Two major scaffold molecules will be investigated to reach our purpose: the cyclodextrin and the cucurbituril. In order to facilitate the self-assembly of these scaffolds onto the surface, sulphur groups will be needed as parts of the molecule.

The Chapter 7 includes a computational study to highlight these protein portions that may be possibly fit into the cavity. To have satisfactory results, a stable and well-packed surface needs to be achieved. The nanolayer is prepared following the conventional method of self-assembly, one of the most popular bottom-up fabrication method to functionalize surfaces. It is a very versatile and easy technique that allows changing the functionality of the new surface. The supramolecular immobilization was choosen as proteins can be detached on surface in a strong way without any structural damage. This approach is very important for the development of new biosensor as it will be possible to study those protein or even reuse them for biocatalysis purposes in their wild structure form.

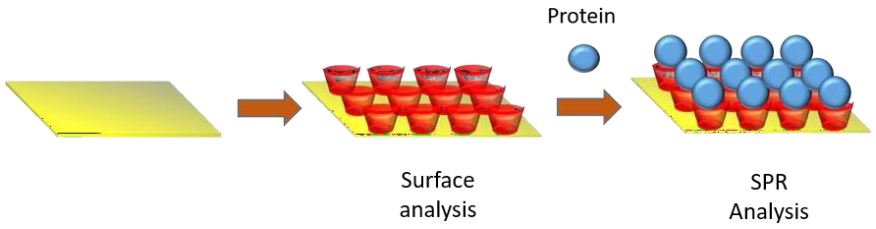

Figure 5.1 Schematic representation of the work developed in this thesis. The cleaned gold surface (left) is functionalised with a scaffold molecule (centre), where the on-surface analysis will be performed in order to test the correct self-assembly. Then the protein is immobilised on a surface (right), and the interaction protein-scaffold analysed through SPR experiments.

In the second step and after the preparation of the cyclodextrin surface, once the chip is entirely functionalised, the SPR is the tool that will be used to measure this interaction. Using this tool, we will be capable to understand the strength of interaction that occurs between the proteins and our surface.

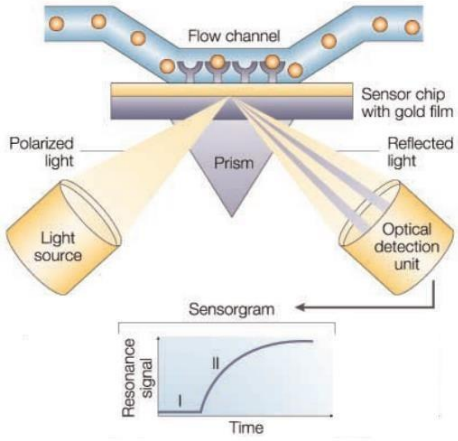

Figure 5.2 Set-up of the surface plasmon resonance used in this thesis. The flow channel allows the protein to interact with the scaffold (i.e. cyclodextrin) functionalised surface. A set of the prism and reflected light allow measuring the interaction occurring between the surface and the protein.

In the third step, we will then start exploring the possibility of using another scaffold molecule: the cucurbituril. As the cucurbiturils that we require is the thio-cucurbituril is commercially unavailable, several synthetic routes will be explored in order to obtain the cucurbiturils desired. Considering that traditionally synthetic pathways may encounter failed attempts, a new pathway synthesis will be explored using the Diamond Anvil Cell. The pressure inside the anvil cell will represent the driving force that will allow us to synthesise the molecule that is needed.

The protein immobilisation on the surface represents a mandatory achievement to develop and to have a deeper biosensing understanding. The possibility to investigate additional protein and the ability to be able to modulate them by interaction with scaffold molecules, represent the most promising achievement nowadays for the development of the next generation of biosensors.

In this project, supramolecular interactions between a nano-characterised surface and a protein were investigated to give fundamental insight into the types of interactions that occur between supramolecular motifs on surface and proteins.

5. Surface characterisation techniques

5.1 Contact angle measurements with the sessile drop technique

In a vapour-liquid-solid system, the contact angle (CA) is the angle measured where a liquid-vapour interface meets a solid surface. From the measurements of this angle, it is possible to quantify the wettability of a solid surface[284]. During an experiment, it is possible to measure two different types of contact angle: CA in static and dynamic condition. The static CA is the angle measured when the liquid drop is laying on the surface at rest. Instead, the CA in the dynamic condition is measured during the injection (advancing CA) or recollection (receding CA) of the liquid from the surface[284,285]. The static CA reflects the relative strength of the molecular interactions at the liquid, solid, and vapour interfaces.

In dynamic CA, a difference between advancing and receding CA is observed, and the difference is called hysteresis, which represents a useful data for the understanding of surface homogeneity[286]. A dynamic CA with a big hysteresis means that the surface has heterogeneous polarity over the surface, often meaning an improper package during the self-assembly on the surface. Instead, a small hysteresis means a homogeneous polarity all over the surface and often a well-packed molecule on the surface. The hysteresis can be influenced by several factor such as the cleaness, the ionization and the roughness of the surface[287]. If the CA of the water on a surface is smaller than 60°, the surface is considered highly hydrophilic, if bigger than 60° the surface is considered less hydrophilic. Metallic or ceramic surfaces generally present hydrophilic characteristics, while instead many polymers and many halogenated materials exhibit hydrophobic surfaces[285].

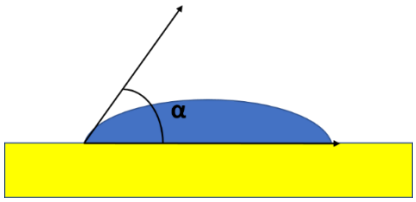

Figure 6.1 Contact angle measurement on a gold chip (yellow), in which the surface exhibits hydrophilic properties, i.e. CA <90 º.

5.2 X-ray photoelectron spectroscopy (XPS)

The XPS is a spectroscopic technique that uses an X-ray source to detect the kinetic energy and numbers of electrons that escape from the surface analysed[288]. It is a spectroscopic technique that provides data regarding the chemical, the empirical formula and electrical state of the elements involved by measuring the elemental composition of a surface. XPS can be a method to characterised surfaces in its as-received state or after a functionalization or a surface treatment such as cutting, ion beam etching, fracturing and scraping[289]. It requires high-vacuum conditions (usually in the range of 10^{-8} – 10^{-9} millibar), and it is generally used to analyse a vast range of materials: metal alloys, semiconductors, catalysts, polymers, ceramics and glasses.

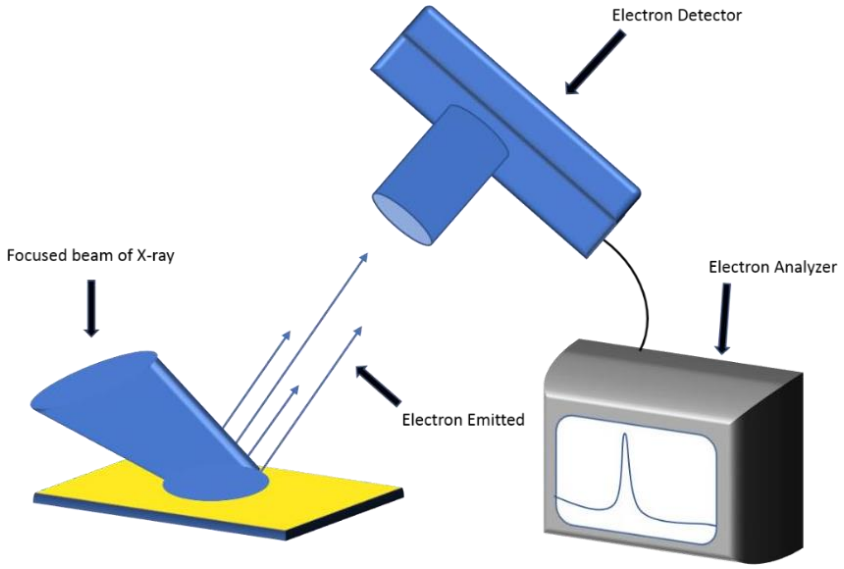

Figure 6.2 General illustration of an XPS apparatus. Once the beam is created and focused on the sample surface, the electrons emitted are captured by the detector and then analysed to provide the data peaks.

Each element will generate a unique peak set, which will give information regarding the type of elements on the surface and its oxidation state[290]. To get a peak set with the minimum error, the electrons must be detected while operating at ultra-high-vacuum conditions (Pressure<10^{-9} millibar) as the electrons find less matter during the long path between the irradiated surface and the electron detector[291]. The XPS is a tool capable of detecting only those electrons escaping from the surface[292]. For an electron to escape from the surface, the surface must be irradiated with an X-ray beam, and it is generally used to determine the type and the quantity of elements on the sample surface in the range of 1-12 nm from the top of the surface and the grade of contamination of the latter[290,291]. Furthermore, it is also used to identify the chemical state of one or more elements and the density and the related binding energy regarding the electronic states.

The high accuracy is also given by the measured area, which is strictly dependent on the diameter of the X-ray beam. Considering a single frequency beam of X-ray, the largest size is from 1 to 5 millimetres. The minimum analysis area ranges from 10 to 200 micrometres[289].

Last improvements in the XPS analysis gives spectroscopic resolution levels below 200 nanometers. This kind of measurements requires the use of synchrotron radiation as an X-ray source[293].

5.3 Ellipsometry

Ellipsometry is an optical technique used to analyse roughness, composition and thickness of thin films on the surface. It is an optical technique that measures the polarization change of a light beam on a surface[294]. As the polarisation change depends strongly on the thickness of the surface and on the relatively refractive index, the ellipsometry represents a universal tool for the measurement of the film thickness of any chemical composition[295]. Ellipsometry measures the thickness by the meaning of change in phase and amplitude of the electromagnetic wave before and after hitting the surface.

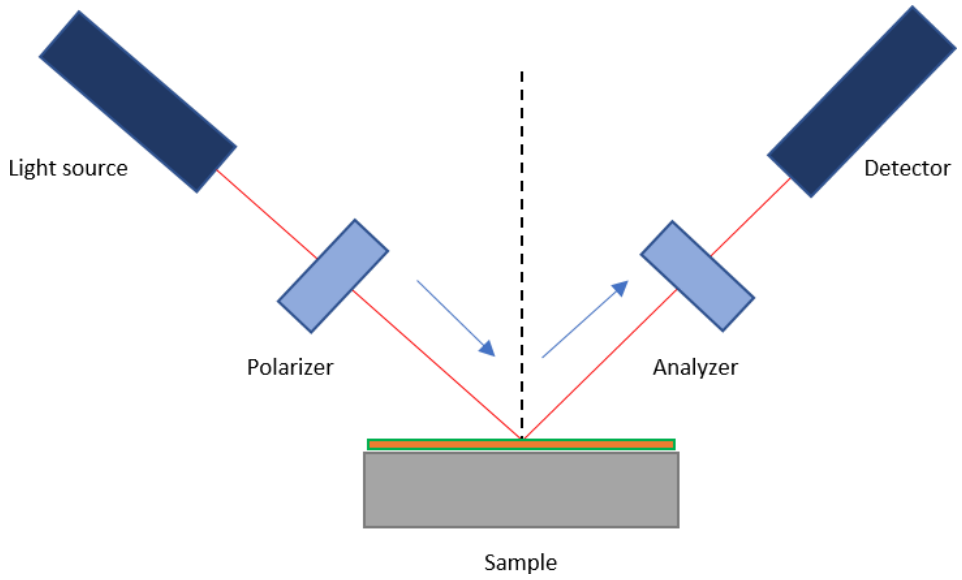

Figure 6.3 Diagram of ellipsometry. The beam is generated in the light source and is then polarised. Once it touches the sample, the beam is reflected, and an analyser is rotated until the beam is not capable of passing through and hit the detector.

As in figure 6.3, the majority of the commercial ellipsometry equipment use a rotating polarizer (analyser) method. The light, once generated by the source, it is linearly polarised changing from a multi-frequency wave to a mono-frequency wave[296]. The beam hits the surface, determining a change in phase and amplitude. This change is strictly depended on the chemical and physical composition of the surface. The reflected beam goes into the analyser. The analyser is then rotated, and the amplitude of the filter changes until the beam is capable of passing through it. The beam then hits the detector, and the difference in orientation and amplitude between the polariser and the analyser gives the change in phase and amplitude of the light, respectively. From these two components is possible to calculate the polarisation change of the light, which is strictly related to the refractive index and the thickness of the surface.

5.4 Surface plasmon resonance

SPR spectroscopy has been applied in a wide range of settings, even mimicking biological environments like membranes and surfaces with multiple binding partners[297]. It can be presented as the basis of many tools to measure the adsorption of a compound on a thin metal film.

When a single-frequency laser light beam hits a glass surface coated with a noble metal, it is possible to observe a reflected and a refracted ray. At a critical angle, it can be noted a total reflexion, and no light is refracted across the interface. Basically, at the quantum level, the laser photons are transferring energy to the electrons of the noble metal on the surface, determining a formation of an evanescent wave[298]. This establishes a difference between the incident photons and the refracted ones. This difference will be analysed and quantified by the sensor. The evanescent wave will be eventually dissipated by heat, and the quantity of energy transferred will always be depending on the amount of matter presents at the surface[297].

Depending on the intensity of the vibration and having a measure in real-time, it is possible to understand the kind of interaction that is occurring on the surface and, including if a protein is binding to the surface[299]. Thanks to the SPR signal the analyte-host molecule association and dissociation can be observed and ultimately derived from providing rate constants, as well as equilibrium constants.[300]

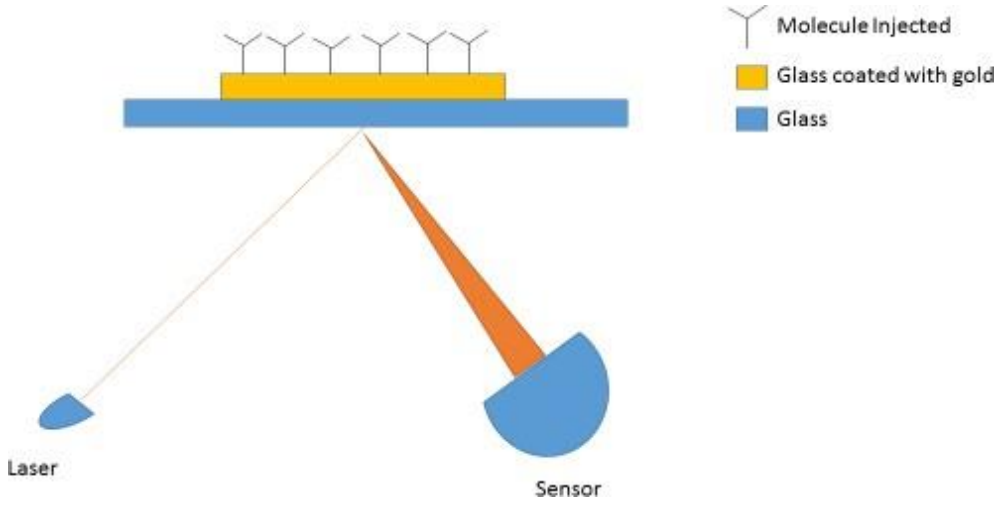

Figure 6.4 A general illustration of an SPR experiment. A laser emits a beam which is then totally refracted at a critical angle and then hitting a sensor. Depending on the matters present on the surface, the photons of the original beam and the reflected one will present different energy.

During an SPR experiment, three kinetic models can be taken into consideration:

- One-to-One kinetics $L + A \underset{k_d}{\overset{k_a}{\rightleftarrows}} LA$
- Mass-transfer kinetics $A_{bulk} \underset{k_t}{\overset{k_t}{\rightleftarrows}} A_{surface} + L \underset{k_d}{\overset{k_a}{\rightleftarrows}} LA$
- Divalent analyte $2L + A \underset{k_{d1}}{\overset{k_{a1}}{\rightleftarrows}} LA \quad + L \underset{k_{d2}}{\overset{k_{a2}}{\rightleftarrows}} LLA$

The One-to-One kinetics (fig. 6.4.1) is the simplest model, in which there is a one to one interaction between the analyte and the ligand. Binding occurs when the analyte collides with the ligand[301]. The collision occurs with a higher probability when analyte has the correct kinetic energy and orientation. Kinetic energy and orientation can be

adjusted, changing the concentration of the analyte or the flow rate. This model is applied when the molecular weight of the analyte can not be taken in consideration[301].

The mass-transfer kinetics (fig. 6.4.2) instead is a two-step event. First, the analyte is transferred out of the bulk solution towards the sensor chip surface. Second, the binding of the analyte to the ligand takes place[301]. Both events have their rate constants. The coefficient for mass transfer kt is the same in both directions. This model is applied when the analyte has a significant molecular weight (such a protein)[302].

The third model (fig 6.4.3) is the one that considers the analyte capable of bonding two substrates. These can be interpreted as one-to-two interaction in which an analyte can have two binding sites[301,302]: one site first binds and then it is closer to another ligand, the second site binds. The formation of the second binding is strictly related to the first one, and as bivalent analyte has two different equilibrium constants (Ka_1 and Ka_2). In this case, the divalent binding takes more importance than diffusion and molecular weight[303].

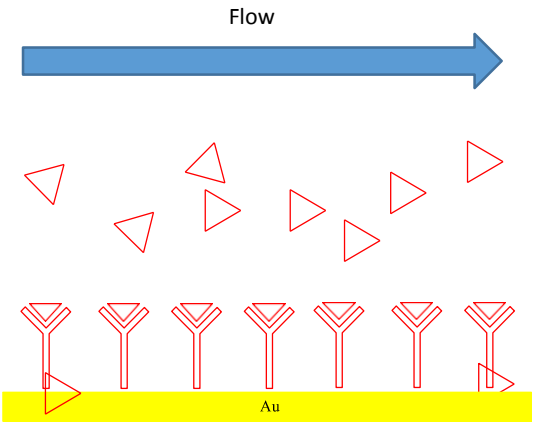

Figure 6.4.1 One-to-one representation of an SPR interaction. The analyte represented by the red triangle interact with the SAM at the surface of the gold chip.

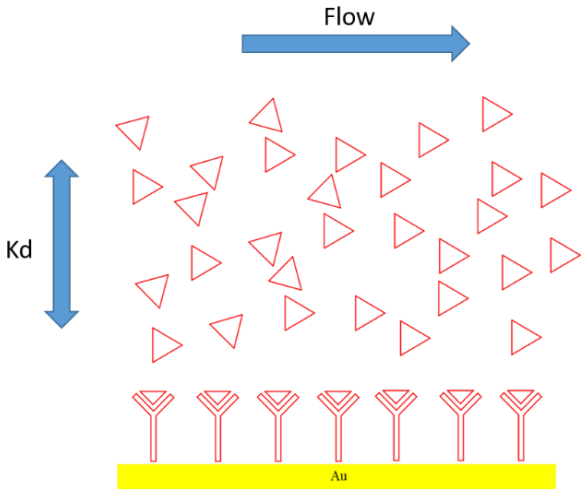

Figure 6.4.2 Mass transfer effect (K_d) is an essential factor that can influence the results for those experiments with a high flow rate involving analytes with significant molecular weight.

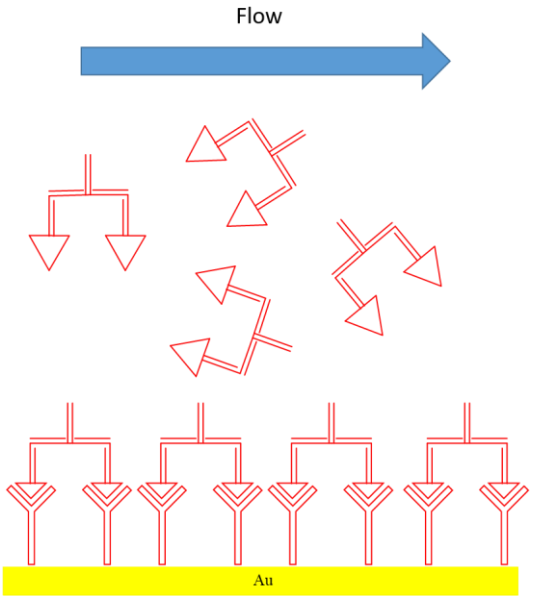

Figure 6.4.3 SPR experiment involving a divalent analyte which presents a double interaction with the SAM.

Since its introduction in biochemistry, the SPR has been a highly valuable approach for affinity measurements of biomolecules towards a functionalized surface. The concept

and the idea behind it are to detect biological entities such as carbohydrates, lipids, proteins, DNAs, RNAs, and even entire cells. In particular, SPR has been used for the kinetics measurements of interactions occurring in nature such as enzyme-substrate kinetics[304,305] ligand-receptor interactions[306,307], and more in particular antibody-antigen[308].

The SPR use is a new field raising and evolving rapidly as the identification of proteomics biomarkers could lead to the detection of specific disease at low cost, avoiding other invasive and time-consuming methods[298]. Thus, further investigations are needed to bring to the scientific community new biomarkers for even more accurate results and diagnosis.

5.5 Cyclic voltammetry

The Cyclic Voltammetry is a type of electrochemical measurement that measures the current developed in an electrochemical cell[309]. By performing different cycles of increased-decreased potential, the experiment performs reactions of oxidation and reduction cyclically. It provides qualitative information based on the peak position in the graph on the x-axis for the potential, and quantitative data based on the intensity of the peaks measured on the y axis[310].

Generally, the redox analyte used for this experiment showed a reversible plot where all the chemical species that have undergone an oxidation reaction also undergo subsequentially a reduction reaction (or vice-versa). This characterisation method is generally used to describe the electrochemical behaviour of an analyte in solution[311] or, in the case of this work, adsorbed on a surface. The Cyclic Voltammetry experiment generally implies an electrochemical cell with the three-electrode setup: the working

electrode, the reference electrode and the counter electrode. The working electrode is where the redox reaction takes place; the reference electrode is an electrode with a stable, well-known redox potential used to indicate the zero-potential in the reaction and the counter electrode used to allow the current to flow[310].

The solvents used in this kind of experiment can be different, for the test in aqueous solution an electrolytic salt will be needed to perform an improved electron transport. The analysis of cyclic voltammetry is used to investigate the stability of reaction products, electron transfer kinetics, the stoichiometry of a system and the redox potential of the analyte[312]. Furthermore, by plotting the intensity vs concentration, it is also possible to deduct the concentration of an analyte in solution. The Nernst equation determines the cell potential under non-standard conditions:

$$E = E^o - \frac{RT}{nF}\ln Q$$

The Nernst equation can be obtained from the equation of Gibbs free energy under the non-standard condition:

$$\Delta G = -nFE$$

Which under standard condition become:

$$\Delta G^o = -nFE^o$$

Where *n* is the number of electrons exchanged in a reaction (in an ideal state this number is equal to 1), *F* is the Faraday constant (equivalent to 96,500 C/mol), *E* is the cell potential, and E^o is the cell potential at standard conditions (1 atm, 298 K).

The free energy of Gibbs is also equal to :

$$\Delta G = \Delta G^{o} + RT \ln Q$$

Where *R* is the gas constant, *T* the temperature and *Q* is the quotient of reaction.

By substituting the free energy for *nFE* we obtain:

$$-nFE = -nFE^{o} + RT \ln Q$$

By dividing both sides by-*nF*, we obtain the Nernst Equation:

$$E = E^{o} - \frac{RT}{nF} \ln Q$$

In the case-specific of a characterisation of a surface, the CV has been widely used to investigate the surface coverage of a thin film[313]. By having the gold chip as a working electrode in the three-electrode setup, it is possible to obtain information regarding the correct self-assembly of a molecule on the surface[312]. The surface coverage of the analyte can be related to the peak intensity by the equation:

$$Ip = \frac{n^2F^2\,\tau A\vartheta}{4RT}$$

Where:

- F is the Faradayconstant,
- τ the surface coverage,
- A the surface area of the working electrode,
- ϑ the scan rate of the electrochemical reaction, an indication of how fast the potential has to change during the experiment.

Taking into account that

$= 1,\ A = 1\ cm^2\ ,\ F\ =\ 96\ 485.3329\ \frac{sec\ A}{mol}\ ,\ \ = 0.3\ \ \frac{}{sec}, R = 8.314\ \frac{J}{mol\ K}, T =$

$298\ K$

So considering that

$$1\ Joule = 1\ Ampere * 1\ Volt * 1\ second$$

The equation is resolved to:

$Ip = 221326\ \frac{A\ cm^2}{mol}\tau$

5.6 Time of flight – secondary ion mass spectrometry

Time of Flight-Secondary ion mass spectrometry (TOF-SIMS) is a technique useful to investigate the chemical components of films and surfaces[314]. The analysis occurs in the first place by sputtering a focused beam on the sample surface. This sputtering will cause the ejection of a secondary ion from the surface[315]. By interpreting data in a mass/charge ions ratio, it is thanks to a mass spectrometer that is possible to characterise the molecular, elemental and isotopic surface composition with an accuracy of 1 to 2 nm in depth. The analysis is qualitative due to the wide variety of ionisation possibilities. Thanks to a limit detection range from parts per million to parts per billion, TOF-SIMS represents one of the most sensitive techniques for surface qualitative analysis. A secondary mass spectrometer is constituted by:

1. A primary ion beam, generated by a primary ion gun (Caesium or Gallium),
2. A primary ion lens that focuses the beam into the sample.
3. A sample holder and a secondary ions lens which refocuses the beam
4. A mirror for the separation of the ions which separates the ions by mass-to-charge ratio

5. A detector: a Faraday cup which converts the charged particles in the electric signal
6. An electron gun which provides electrons to the sample surface. This is to keep the surface always with a net charge as a positive charge could be accumulated on the sample.

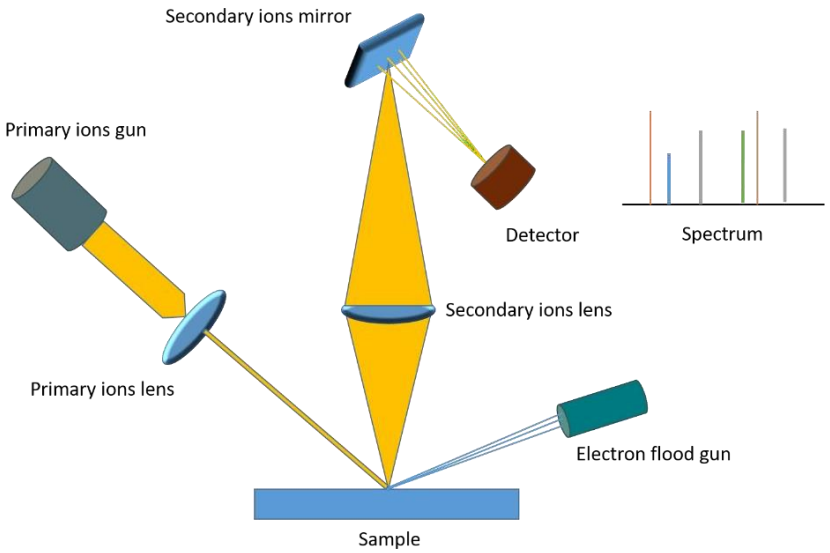

Figure 6.6 Schematic illustration of a TOF-SIMS instrument. The ions beam is generated into the primary ions gun and then focused onto a specific point on the sample by the primary ions lens. The beam charges the molecules present at the surface sample and the sample molecule, once ionised, are collected and sent to the detectors through a system of ions lenses and mirrors that separates them in terms of mass and charge.

A TOF-SIMS experiment requires pressure below 0.1 milli Pascal, to ensure the correct vaporisation of the molecules laying on the surface and to avoid the collision of the secondary ions with environmental gases on their way to the detector[314]. The high vacuum is also vital to avoid any surface contamination during the experiments. Once the sample is placed on the holder, and the vacuum is established, the ion beam is focused on

the samples and the molecules ionised. There are three ways to generate a source of ions for a SIMS experiment[316]. The first method uses Cesium (Cs) atoms that are vaporised and then ionised through a porous tungsten filament. The Cs ions are then used for the vaporisation of the sample. Another ion method uses the electrons released from a cathode to ionise nobles gas (such as Argon or Xenon which are ionised to Ar^+ and Xe^+), halogenated molecule (SF_6 to SF_5^+) and oxygen molecules (O_2 to O^-, O^+, O_2^+, O_2^-). Another ion source is the liquid metal ion gun (LMIG) that operates with metallic alloys or pure metals, liquid at room temperature (Caesium, Rubidium, Francium and Gallium and Gallium alloys). A tungsten tip is immersed in the liquid and emits ions under the influence of an intense electric field. The LMIG provide a well-focused short pulsed ions beam (<50 nm) with moderate intensity.

The choice of the ion beam is generally related to the kind of analysis desired. Caesium primary beam is often preferred to investigate electronegative elements due to the increased possibility of negative ions generation[317].

Regarding the mass analyser in the TOF method, the ions are separated in a field-free path according to their velocity. Giving the fact that all the ions will have the same kinetic energy provided by the primary ions, the time of flights changes according to the mass. The detector is a Faraday cup with an electron amplification. When the ion impacts a metal cup contained into the sensor, it starts an electron cascade, generating a signal of 10^8 electrons recorded straightway. The SIMS represents a characterisation technique with a relatively low detection limit for the most trace elements[318] in between 10^{12} and 10^{16} per cm^3. The limit value changes depending on the primary ion beam, the area analysed, and the type of instrumentation used. The amount of surface removed from the

beam depends on the dimensions of the primary beam itself and the current (either continuous or pulsed)[316].

5.7 Diamond anvil cell

The diamond anvil cell (DAC) is a device used to study the physical and chemical reactions at high pressures. Any cell can determine the compression of a sample from 3-4 GPa to typically up to 100-200 GPa. However, recent applications showed that with a DAC, it is possible to reach 750 GPa[319]. The tools have been mostly used to simulate the pressure inside stars and planets and to observe physical and chemical behaviour of atoms, molecules and cells at extreme pressures such as the observation of metallic phases of Xenon[320] and hydrogen[321] and the formation of polymeric nitrogen[322]. One of most notable example is the discovery of a new phase of water in the solid-state, so-called ICE X, portrayed by Mao and coworkers[323]. By compressing the ice and its deuterated form at a maximum pressure of 210 GPa, it was observed a phase transition at 60 GPa. This step marks a new insight into the world of physical chemistry as a new water phase was obtained. The DAC potential can also be appreciated in the formation of metallic phases of hydrogen claimed by Eremets and Troyan[324]. The hydrogen once reached a pressure of 220 GPa, and it transformed into metal as became opaque and capable of conducting electricity. At 300 GPa, the hydrogen particles showed to reflect the light. Eremets and Troyan also claim the discovery of a polymer form of a nitrogen[322], with a non-molecular phase capable of working as a semiconductor at pressures up to 240 GPa. Moreover, they also succeed to recover the pure nitrogen polymer at a temperature below 100 K but ambient pressure.

The DAC field keeps improving, constantly setting new frontiers in the field of organic chemistry and physical chemistry, including pressures in the range of TeraPascal (TPa)[325]. Innovative use of the DAC also occurs on the analysis of the durability and sustainability of life under high pressures. Cells are investigated for their possible sustainability and survival on exoplanets. In 2002, Jennifer Couzin tested strains of *Escherichia coli* at the pressure of 1.6 GPa and analysed their survival after 30 hours[326]. Even if only 1% of the bacteria survived, these bacteria were capable of adapting to extreme conditions for a long time.

Two diamonds form a DAC with the sample chamber in between the two tips of the diamonds. The pressure is measured by the method of ruby fluorescence, where ruby is inserted into the sample chamber, and its changing in refractive index corresponds to a specific pressure value. The pressure applied into the DAC can be transformed into hydrostatic pressure using a transmitting medium such as hydrogen, xenon, argon and helium[327].

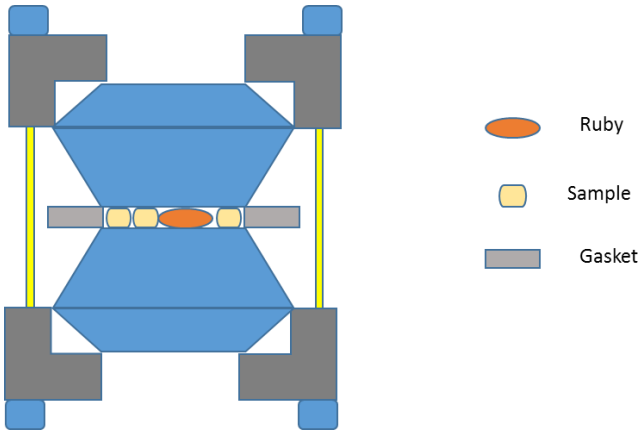

Figure 6.7 Set up of a diamond anvil cell. The two diamond (blue) are close together within between the sample mixture, the ruby and the gasket. The pressure is applied with screws (yellow).

One of the most significant advances that the diamond offer is the possibility to observe the sample directly and to perform any characterisation during the experiment: from photoluminescence to optical absorption, X-ray diffraction to fluorescence and Raman scattering. It is possible to attach electrodes to the cell or applying an external microwave field allowing magnetical and electrical measurements and heating the sample to 7000K with the laser-induced heating or cooling down to millikelvins[328]. The DAC is a tool which relies on the principle:

$$p = \frac{F}{A}$$

Where p is the pressure, F the applied force and A the area where the force is applied, in the system of the DAC, A is represented by the two diamond tips of the cell which range typically from 100 to 250 micron in diameter. In this way, even moderate forces can induce relatively high pressure on the sample. The use of the diamond is necessary to avoid deformations or disruptures of the compressing material. A diamond is one of the hardest material ever known.

The main components of the DAC are a device for the force generation, two diamonds in opposed position among each other, the gasket and a medium for the pressure in the case of a DAC designed for hydrostatic pressure. Screws or lever arm mainly constitute the tool for force generation. For much higher forces, hydraulic pressure to a membrane can be used. The two opposing diamonds generally weigh from 25 to 70 mg with the tips (culets) facing parallel one to another to avoid non-uniform pressure or deformations. A thin metal foil of generally 0.3 mm in thickness, in between the two culets serves as the gasket for the experiment. The material used for the gasket typically is rhenium steel or tungsten. These material are cheaper, but they do not allow the X-ray

to pass through it. If an X-ray analysis is required will be then necessary use gasket of a much-appropriated material for this kind of analysis such as boron[329] boron nitride[330]or even diamond[331]. The primary function of the gasket is to serve as a sample chamber and to trap the molecules in between the two diamond culets. Regarding the medium inside the sample chamber, it is meant to be a fluid to provide to the sample a homogeneous hydrostatic pressure. Hydrostatic pressure is always favoured for high-pressure experiments as, at that extreme conditions, even a smaller pressure variation can cause different molecular behaviour. A suitable DAC medium will be an inert fluid compressible to high pressures such as silicone oil, helium, argon, neon and nitrogen.

The pressure is calculated by measuring the fluorescence lines shift of a ruby inserted in the chamber[332]. In the case of higher temperature experiment, the X-ray diffraction is preferred where the equation of state of a compound is known in function of both pressure and experiment[333]. This technique can be used at high and low pressure and temperatures. However, the disadvantage is represented by the fact that it needs an X-ray source, and it required longer times for the calculation.Before the invention of the DAC, static high-pressures devices needed relatively large hydraulic pressures. It needed specialised laboratories and with a weight in the order of several tons. The DAC introduced a completely new and different approach transforming the high-pressure chemistry in a more viable science field. Thanks to its design, the DAC found a wide variety of applications: from the cryostat applications for the study of superconducting materials[334] to a huge range of spectroscopic experiment (X-ray[333], Infrared[335], Raman[336], UV-Visible[337]) due to the diamond transparency.

6. Methods

Chemicals and Materials. Commercially available chemicals and solvents were purchased from Aldrich Chemicals, Sigma Aldrich, Fisher Chemicals and used as received. The heptakis-(6-deoxy-6-thio)-β-cyclodextrin was acquired from Cyclodextrin-Shop (Tilburg, Netherlands) to > 97% purity. The 6-thio-D-glucopyranose was acquired from CarbonSynth, USA (Illinois, USA) to 95% purity. Phosphate buffered saline (PBS) solution was prepared from a 10× concentrated PBS solution (1.37 M sodium chloride, 0.027 M potassium chloride, and 0.119 M phosphate buffer) from Fisher Bio-Reagents. Polycrystalline gold substrates were purchased from George Albert PVD, Germany and consisted either of a 30 nm gold layer deposited onto glass covered with a thin layer (5 nm) of titanium as the adhesion layer (for contact angle and cyclic voltammetry analysis) or 100 nm gold layer on 100-4inch-silicon wafer, precoated with titanium as the adhesion layer (for ellipsometry and XPS analysis). Polycrystalline gold substrates employed in SPR were purchased from Reichert Technologies, USA, consisted of 49 nm gold with 1 nm chromium.

SAM Preparation of the Aminoundecanethiol cyclodextrin. The gold substrates were cleaned by immersion in piranha solution (70% H_2SO_4, 30% H_2O_2) at room temperature for 8 minutes, rinsed with ultra-high quality (UHQ) water and dried with argon flow. For the preparation of the AUT SAM, the clean gold substrates were immersed first in a solution of 1 mM of aminoundecanethiol (AUT) overnight. After that, the gold substrates were rinsed with Ethanol and UHQ water and subsequently immersed in a DMF solution of DHS 50 mM. Next, the gold substrates were not rinsed to avoid further degradation and immediately immersed in a solution of 1mM of β-cyclodextrin. The SAM preparation was performed by the author of this thesis.

SAM Preparation of the β-CD–(SH)7 SAM. The gold substrates were cleaned by immersion in piranha solution (70% H_2SO_4, 30% H_2O_2) at room temperature for 8 minutes, rinsed with ultra-high quality (UHQ) water and dried with argon flow. For the preparation of the heptakis-(6-deoxy-6-thio)-β-cyclodextrin SAMs, the clean gold substrates were immersed for 12, 24 and 48 h in 0.1 mM or 1 mM DMF solutions of heptakis-(6-deoxy-6-thio)-β-cyclodextrin. Subsequently, the gold substrates were rinsed with DMF and ultra-high quality (UHQ) water and dried under an argon flow. For the preparation of the glucose-terminated SAMs, the clean gold substrates were immersed for 24 h in 1 mM DMF solutions of 6-thio-D-glucopyranose. Subsequently, the gold substrates were rinsed with DMF and UHQ water and dried under an argon flow. The SAM preparation was performed by the author of this thesis.

Contact Angle. Contact angles were determined using a contact angle Attension apparatus, equipped with a Navitar camera that was attached to a personal computer for video capture. The dynamic contact angles were recorded as a micro-syringe was used to quasi-statistically add liquid to or remove liquid from the drop. The drop was shown as a live video image on the PC screen. Oneattension software was used for the analysis of the contact angle of a droplet of UHQ water at the three-phase intersection. The contact angle averages and standard errors were determined from three different surfaces of each type of SAM (in triplicate). The CA was performed by the author of this thesis.

Ellipsometry. The thickness of the deposited monolayers was determined by spectroscopic ellipsometry. A Jobin-Yvon UVISEL ellipsometer with a xenon light source was used for the measurements. The angle of incidence was fixed at 70°. A wavelength range of 280–820 nm was used. The Delta-Psi software was employed to determine the thickness values, and the calculations were based on a three-phase ambient/SAM/Au model, in which the SAM was assumed to be isotropic and assigned a refractive index of 1.50. The thickness reported is the average of three different surfaces of each type of SAM (in triplicate), with the errors reported as standard deviation. The ellipsometry experiment was performed by the author of this thesis.

X-ray Photoelectron Spectroscopy (XPS). XPS spectra were obtained on the K-Alpha (Thermo Scientific, East Grinstead, UK) instrument based at the University of Newcastle (NEXUS), UK. XPS experiments were carried out using a microfocused monochromatic AlKα source (Energy/Voltage/Current/Power: 1486.6 eV/12 kV/3 mA/36 W) at an emission angle of zero degrees and a spot size of 0.32 mm^2. Samples were analysed with charge neutralisation. The survey spectra were recorded with a pass energy of 150 eV, step size of 0.4 eV and dwell time of 10 ms. The high-resolution spectra were collected with a pass energy of 40 eV, the step size of 0.1 eV and a dwell time of 100 ms. For each surface type (β-CD–(SH)7 SAMs formed using different concentrations (0.1 mM and 1 mM) and times (12 h, 24 h and 48 h)), 3 measurements each from 2 individual chips were taken. XPS fitting was performed using the CASA XPS processing software. Sensitivity factors used in this study were: Au 4f 17.12; S 2p, 1.68. The XPS experiment was performed by the staff of HarwellXPS at the Research Complex at Harwell Rutherford Appleton Laboratory.

Electrochemistry. The cyclic voltammetry (CV) experiments were performed with a Gamry Instrument Reference 600 potentiostat. The reference electrode (Silver/Silver

Chloride Reference Electrode) and the cable (Reference 3000 Main Cell Cable Kit 60 cm) were both purchased from Gamry Instruments. The CV data were acquired using the Gamry Instruments Framework software and analysed with Gamry Echem Analyst software. After SAM formation, the modified gold surfaces were immersed in a 0.1 M DMF solution of ferrocene carboxylic acid((FCA) (purity 97%) for 4 hours. Subsequently, the immersed samples were rinsed in UHQ water. Cyclic voltammetry was performed on the gold modified surfaces using 0.2 M sodium sulfate as supporting electrolyte. The potential was scanned between 0 V and −0.8 V at a scan rate of 0.3 V/s. The CVs were performed in triplicate, with each replicate being a new gold modified surface as a working electrode. The geometric area was controlled by the use of a 1 cm diameter O-ring. In order to demonstrate that the reaction was only occurring at the surface and not in the electrolyte solution, the CV experiments were performed at different scan rates on the 1 mM β-CD–(SH)7 SAMs, showing linearity in the progression between scan rate and anodic peak current (for ferrocene oxidation). The linearity observed indicates that the ferrocene associated with the obtained faradaic response is confined to the β-CD–(SH)7 SAM gold surface. The electrochemistry experiment was performed by the author of this thesis.

Surface Plasmon Resonance. SPR experiments were performed with a Reichert SR7000DC Dual Channel Spectrometer (Buffalo, NY, USA) at 25˚C. For the insulin experiments, PBS was used as a buffer, while 2-ethane sulfonic acid (MES) buffer was employed for the α-chymotrypsin, RNase A and cytochrome C studies. The MES buffer was prepared by dissolving 1 g of MES in 250 ml UHQ water and adjusting the pH to 6 with 10 M sodium hydroxide solution. An aqueous 10 mM sodium dodecyl sulfonate (SDS) solution was employed as the regeneration solution. Before the binding studies between the gold-modified surfaces and the different proteins, the sensor chips were

washed by exposure to three SDS injections for 30 seconds. The proteins were then injected at various concentrations over the sensor chip for 8 min, followed by injection of buffer for 8 min to allow any dissociation of the protein from the surface. The surfaces were re-used multiple times by conducting a regeneration step involving three SDS injections for 30 seconds. The flow rate was kept constant at 15 µl/min throughout all the SPR experiments. The SPR experiment was performed by the author of this thesis.

Time of Flight Secondary-Ion Mass Spectrometry (TOF-SIMS). The 1 mM 24 h β-CD–(SH)7 SAMs and 1 mM 24 h glucose-terminated SAMs were immersed in a 1 mM Cytochrome C in PBS solution for 2 h. Following protein immobilisation, the samples were washed with PBS buffer followed by submersion in UHQ water for 1 min. The samples were then dried under argon. ToF-SIMS spectra were acquired using ToF-SIMS IV (ION-TOF GmbH, Munster, Germany). 25 keV Bi_3^+ primary ions were used for analysis. Static conditions were maintained to analyse only outermost 2 nm of the surface. Three samples of each type were analysed with 4 areas of 250x250 µm measured per sample. Three control samples, glucose-terminated SAMs and β-CD–(SH)7 SAMs without protein and bare gold were analysed to exclude the possibility of advantageous contaminants. The TOF-SIMS experiment was performed by Dr. David Scurr at the University of Nottingham.

Statistical Analysis of TOF-SIMS Results. The mass scales of the positive ion ToF-SIMS spectra were calibrated to the CH_3^+, $C_2H_3^+$, $C_3H_5^+$, and $C_7H_7^+$ peaks. Principal component analysis (PCA) was performed to compare peak intensity patterns in the cytochrome C glucose-terminated SAMs and cytochrome C β-CD–(SH)7 SAMs. For statistical analysis, a peak search was done in SurfaceLab and peaks of intensity above 100 ion counts and signal to noise ratio (S/N)>3 were added to peak list. Ion peaks are

known to be unrelated to protein, such as 23 m/z (sodium), and 39 m/z (potassium) were removed from the list. Peak areas normalised to total ion count were extracted and loaded into Matlab R2017b. PCA was run using a Matlab GUI, simsMVA. Results of the principal component analysis are shown in. First principal component (PC1) explains 86.56% of the variance in the whole dataset. Loadings and scores are co-localized. Therefore peaks on the positive side of loadings correspond to glucose-terminated SAM and peaks on the negative side of loadings correspond to β-CD–(SH)7 SAMs. Spectral intensity patterns of two types of samples are significantly different from each other, with positive loadings representing peaks more prevalent in protein on glucose-terminated SAMs and negative loadings representing peaks more prevalent in protein on β-CD–(SH)7 SAMs. Statistical Analysis was performed by Anna Kotowska at the University of Nottingham.

Synthesis of thiocucurbituril. All the reagents and solvents were purchased from Sigma-Aldrich. Glyoxal solution (20 ml, 0.13 mol), and thiourea (16 g, 0.26 mol) were added to tetrahydrofuran (20 ml) and left overnight at 60 degrees. The mixture then was cooled down and filtered to obtain a yellow compound which revealed to be the 4,5-dihydroxy-2-thioketoimidazoline (17.74 g, 0.11 mol). The second attempt was focused on making the imidazoline cycle more reactive with chlorinating agents. 4,5-dihydroxy-2-thioketoimidazoline (2.68 mg, 20 mmol) and thionyl chloride (1.460 ml, 20 mmol) were mixed to a solution of tetrahydrofuran (10 ml). In another reaction, the solution was left for 4 hours, forming a brown-black precipitate making difficult any kind of separation. For the other chlorinating reaction, p-Toluenesulfonyl chloride (3.8 g, 40 mmol) and 4,5-dihydroxy-2-thioketoimidazoline (2.68 mg, 20 mmol) were mixed to a solution of tetrahydrofuran (10 ml). After 4 hours, the reaction showed a brown precipitate (3.1 g), which was filtered and washed with ethanol first and the water. The synthesis was

performed by the author of this thesis.

Diamond Anvil Cell experiment. The cell used for this experiment is known as a LeToullec style membrane diamond anvil cell, made by BETSA company. Specifically, we used such a diamond anvil cell with 700 or 900 micron diameter culets (culet is the name of the anvil face pressing the sample), steel gaskets pre-indented to about 100 micron thickness, with a 500 micron hole drilled into it with a spark drill (EDM – electric discharge machine), ruby fluorescence to measure the pressure and no pressure medium. The diamond anvil cell experiment was performed by Dr. Dominik Daisenberg at the Diamond Light Source, Didcot, Oxfordshire.

7. Design and characterisation of the SAMs

The data reported in chapter 7 and 8 were published in the manuscript "Reversible, High-Affinity Surface Capturing of Proteins Directed by Supramolecular Assembly" Giuseppe Di Palma, Anna M. Kotowska, Lewis R. Hart, David J. Scurr, Frankie J. Rawson, Stefano Tommasone, and Paula M. Mendes. ACS Appl. Mater. Interfaces 2019, 11, 8937−8944.

7.1 The theoretical study of the complex Protein-Cyclodextrin

Before proceeding to have a thorough understanding of the supramolecular interactions occurring between our protein and the surface, a theoretical study on the possible protein-cyclodextrin interactions was first conducted. As the proteins are constituted by amino acid entities and the scaffold molecules will complex through the inclusion of the amino acid side chains, we wanted to understand how these interactions occur and eventually take advantage of such interactions. Kahle et al. carried out the first studies analysing these complexes by potentiometric titration[338].

CDs are macrocyclic host molecules that, due to their apolar cavity,[339] showed a remarkable selectivity with other hydrophobic chemical species. It is well investigated that β-CDs form complexes at the protein surface, through host-guest chemistry, with hydrophobic amino acids, namely leucine (Leu), tyrosine (Tyr), tryptophan (Trp) and phenylalanine (Phe)[339–343]. These amino acids form complexes with mM binding affinity[344] meaning that the association constant (Ka) is 1000 times higher than dissociation constant Kd, and can be included with high specificity into the β-CD cavity. Indeed, it has been demonstrated that the protein interaction with β-CD

represents a valuable way to prevent protein denaturation, restore initial protein structure and increase protein stability[344–347]. These advantages have been widely used in drug delivery[348] and pharmaceutical proteins formulations[349].

However, there are many ways in which these non-covalent interactions between β-CD and proteins can be utilised to the assembly and modulation of proteins. Under these expectations, we explored a field that demonstrates previously unmatched versatility, capability and simplicity to create stable and reversible protein surface structures. Taking in account that proteins present multiple hydrophobic amino acids at their surfaces, we have adopted and made use of the concept of multivalency[350] to modulate the binding of numerous well-oriented β-CD moieties tethered onto a gold surface to several amino acids on the protein.

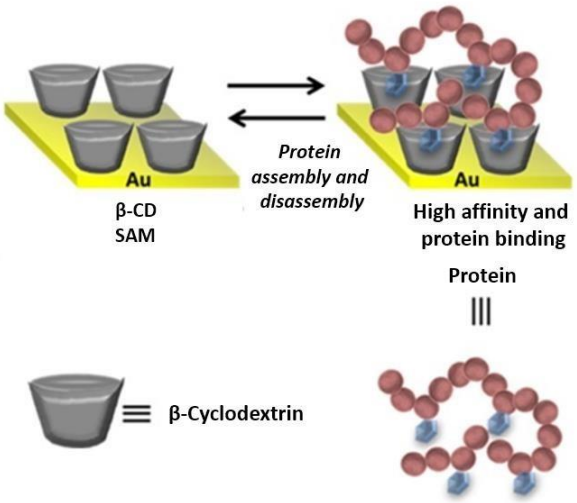

Figure 7.1.1 The concept of multivalency used in this thesis, where the β-CD SAM can have multivalent interactions with the hydrophobic moieties (shown as blue hexagons) of the protein.

The surface was functionalised with a β-CD derivative, in order to increase the affinity of the surface towards the proteins, without compromising the physiological structure of the latter. This scenario, in order to occur, needs to have the β-CD cavity exposed at the interface, facilitating the binding of the amino acid residues from the

protein surface inside the cavity. Four model proteins, namely cytochrome C, insulin, chymotrypsin and RNase A, which are distinct in structure and property and display randomly distributed hydrophobic amino acids throughout their surfaces for β-CD binding, were investigated to assess the generality of our observations. Only the amino acids at the protein surface were considered, being the only ones that can have an interaction with the environment. The amino acids selected as attaching point for the CD molecule were: Tyrosine, Phenylalanine, Leucine and Tryptophan as their side chains presents a particular affinity for the cyclodextrin[338]. The different hydrophobic amino acids on the surfaces of the proteins are also present at a different percentage (Table 1). Thus, it further highlights that the chosen four proteins can serve as general models for understanding protein - β-CD-SAM interactions.

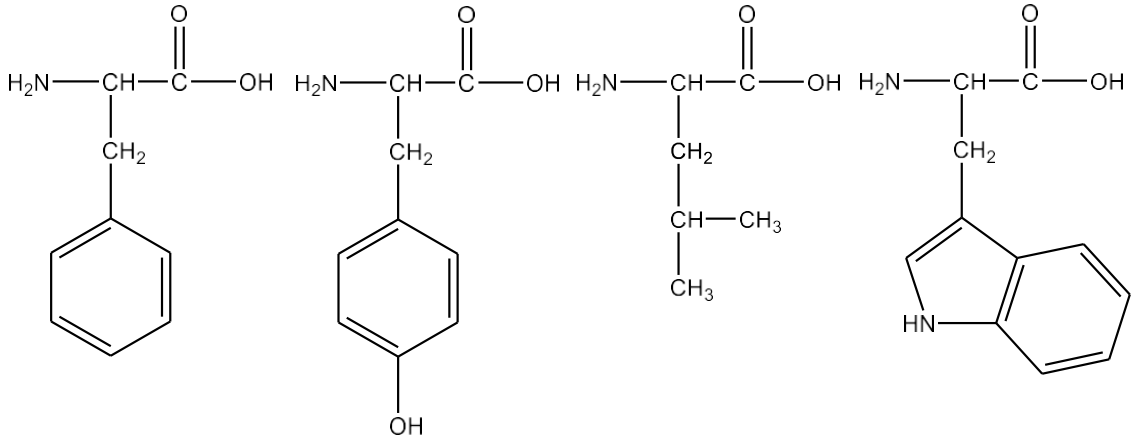

Figure 7.1.2 The amino acids were chosen as a possible attaching point due to their high hydrophobicity of the side chain. From left to right: Phenylalanine, Tyrosine, Leucine and Tryptophan.

Table 1 – Percentage of the different hydrophobic amino acids on the surfaces of proteins (i.e. Phe, Tyr, Leu and Trp) for α-chymotrypsin, insulin, RNase A and cytochrome C. The percentages were generated using PyMol.Above a list of the Molecular Weight (MW) and Isoelectric point(Ip) of each protein.

Protein	MW (KDa)	Ip
α-Chymotrypsin	25	8.8
Insulin	5.7	5.3
RNAse A	13.7	8.6
Cytochrome C	11.7	9.6

Protein	% Phe	%Tyr	%Leu	%Trp
α-Chymotrypsin	26.1	20.2	35.0	18.7
Insulin	32.8	47.4	19.8	0
RNAse A	12.2	54.6	30.0	3.2
Cytochrome C	28.7	44.6	21.0	5.7

As a result of this theoretical study, we were able to investigate further the CD in the 3D structure of the protein. In figure 7.1.3, 7.1.4, 7.1.5 and 7.1.6 the hydrophobic-side chain amino acids have been marked with blue coverage in order to highlight them from the rest of the biomolecule. The blue coverage represents the attaching points of the CD cavity with the protein. The Cyt C (Fig. 7.1.3) presents a relatively high number of attaching points. The Leucine is the most present hydrophobic-side chain amino acid at the surface, followed by Phenylalanine, Tyrosine and Tryptophan.

The Insulin (Fig. 7.1.4) shows several attaching points for the CD with a major presence in the order Tyr > Phe > Leu, as shown in Table 1. As the amino acids are quite

external to the protein, this might indicate that likely no histeric issues will occur during the complexation.

In the case of the RNAse A (Fig. 7.1.5), the protein shows several attaching points with no sterical impedance with a major presence of Tyr > Leu > Phe > Trp. It was also assumed that due to the high number of attaching point, this protein would have a strong interaction with our surface.

The Chymotrypsin (Fig. 7.1.6) also showed an elevated presence of attaching point, giving us the same conclusion as in the case of the RNAse A . All the attaching points seems to have no hysterical impedance with a major presence of Leu > Phe > Tyr > Trp. Backed up by these initial theoretical studies, we started the nanofabrication of our first cyclodextrin SAM.

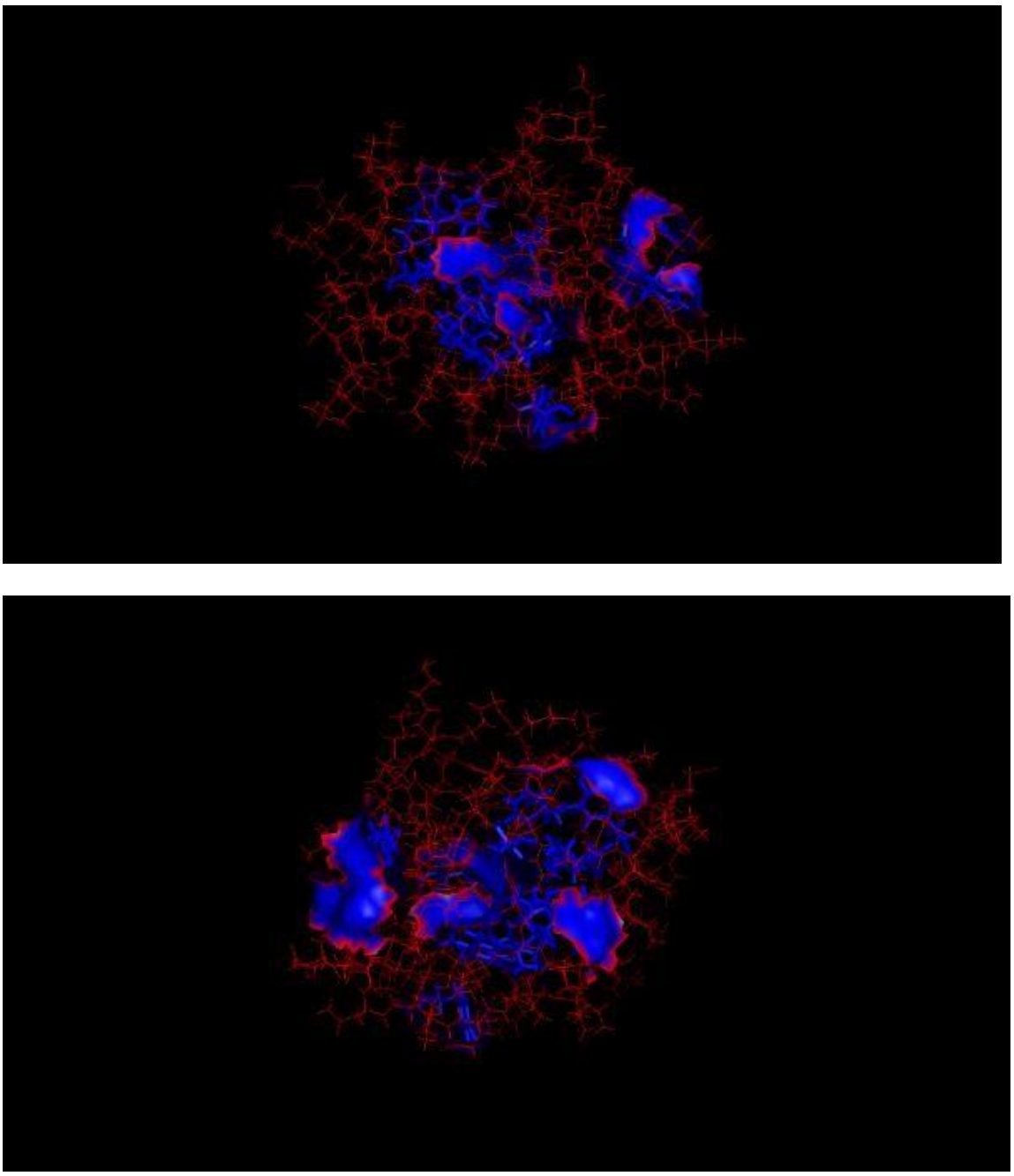

Figure 7.1.3 Cytochrome C and its possible attaching points with CD (blue) 0°-180° (up) 180°-360° (bottom).

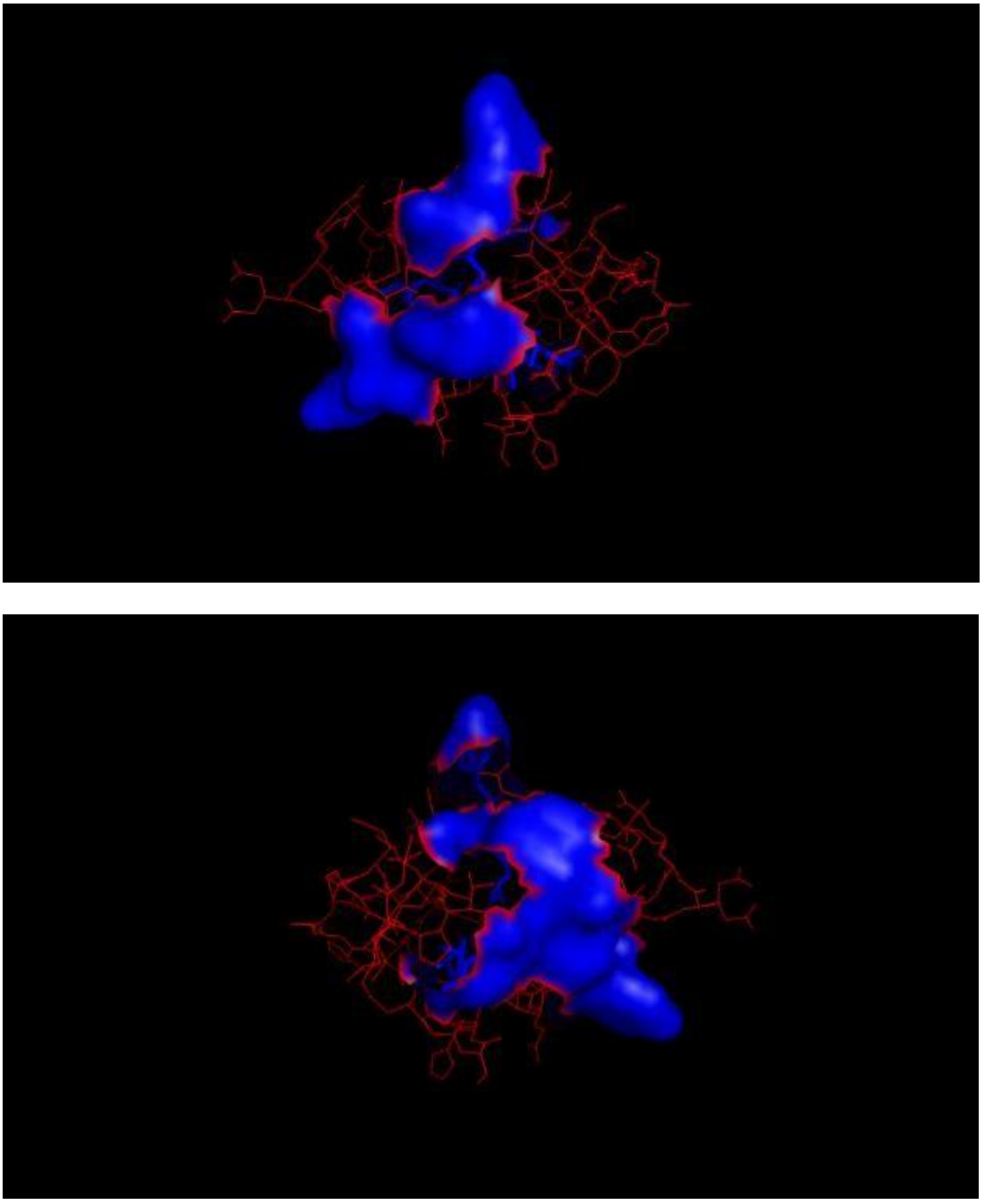

Figure 7.1.4 Insulin and its possible attaching point with CD (blue) 0°-180° (up) 180°-360° (bottom).

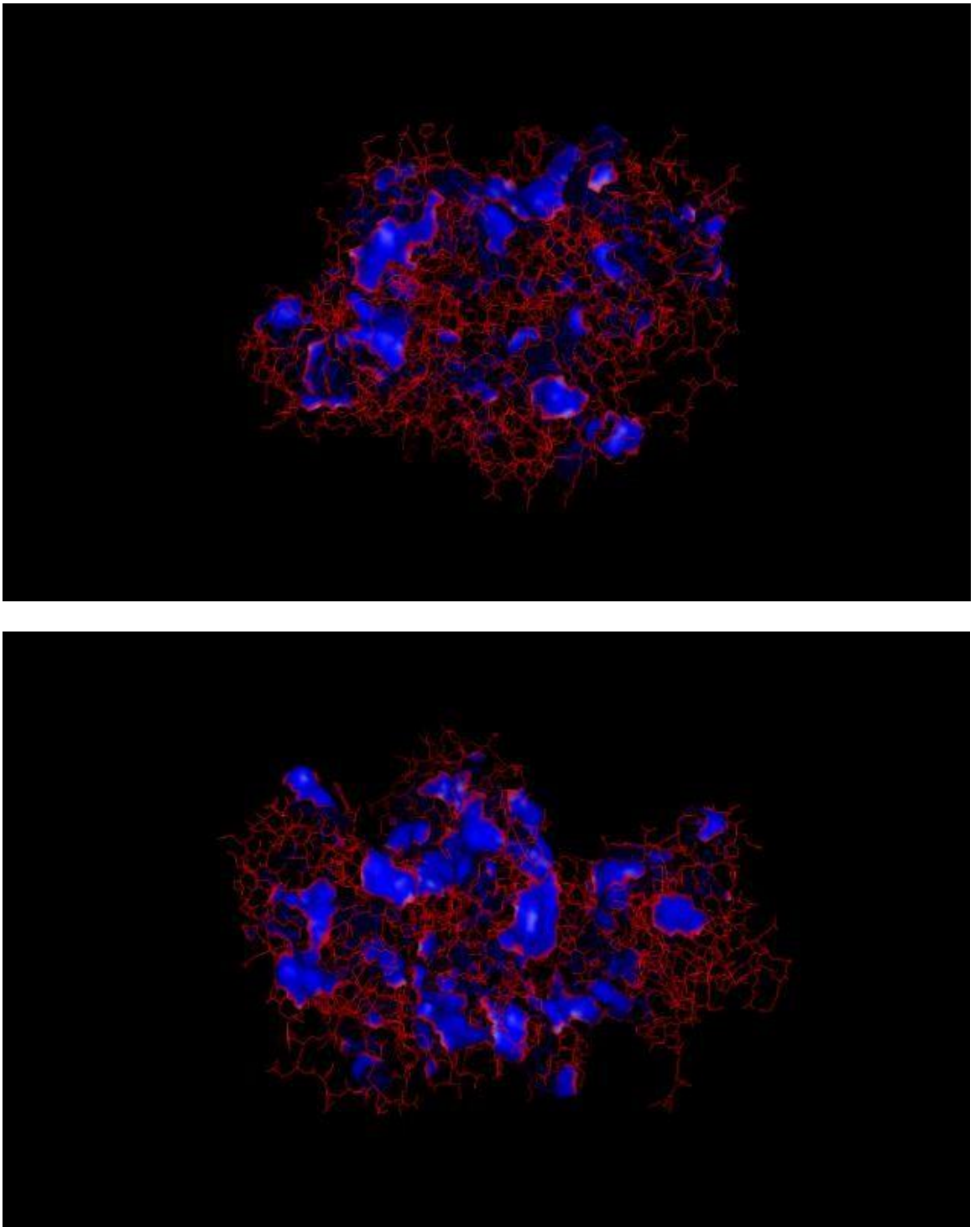

Figure 7.1.5 RNAase and its possible attaching point CD (blue) 0°-180° (up) 180°-360° (bottom).

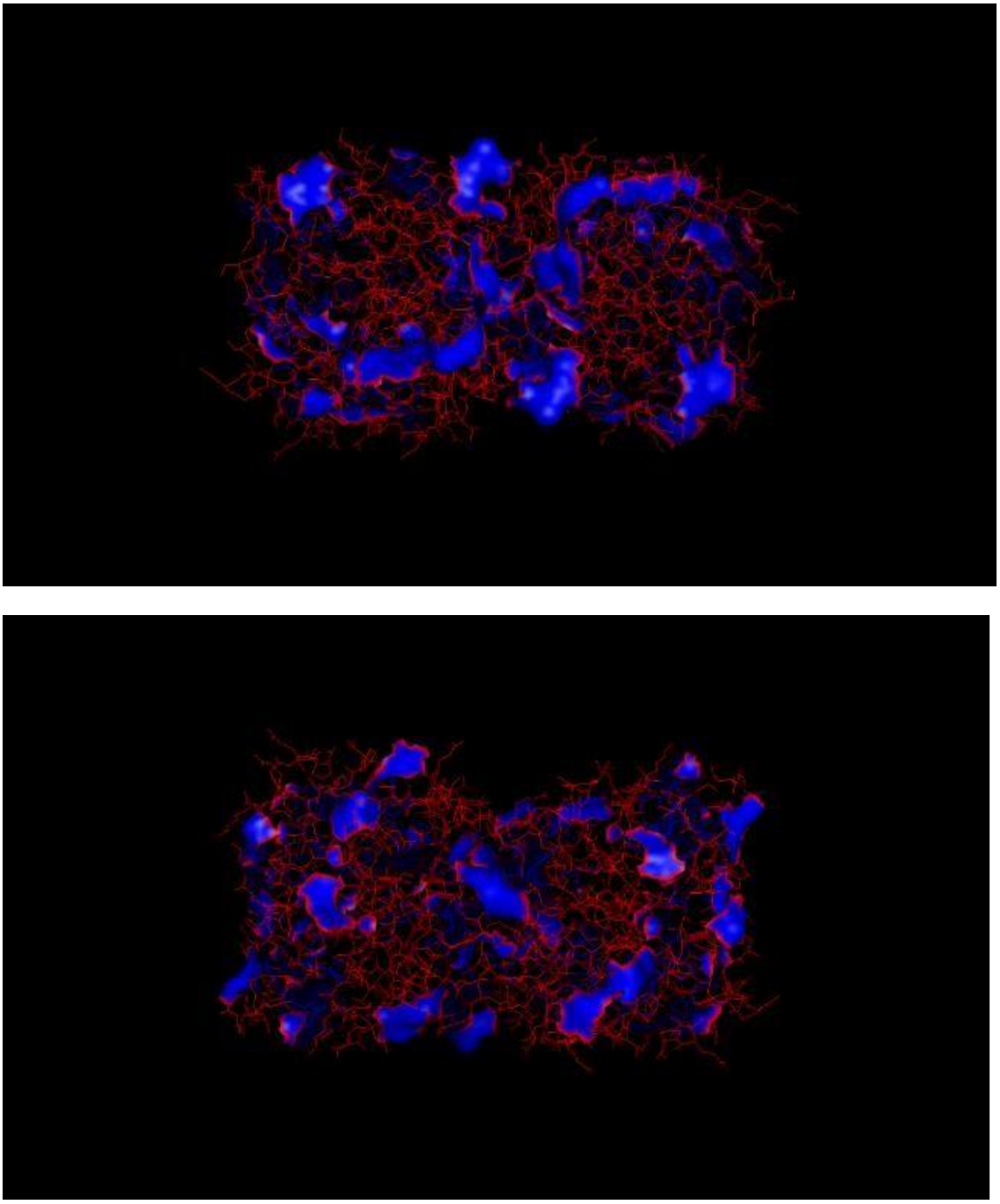

Figure 7.1.6 Chymotrypsin and its possible attaching point with CD (blue) 0°-180° (up) 180°-360° (bottom).

7.2 Nanofabrication of the cyclodextrin SAMs

Once the proteins were investigated through computational studies, the next step was the nanofabrication of the surface responsible for the protein immobilisation. The nanofabrication of the SAM used in this thesis was previously reported by Campiña et al. [351] (fig.7.2) It was a bottom-up fabrication in which a monolayer of aminoundecanethiol (AUT) is self-assembled on the gold surface and rinsed with ethanol. Then the surface is immersed in a solution of dihydroxy succinimide (DSC) which render it active for the next and final addition of cyclodextrin.

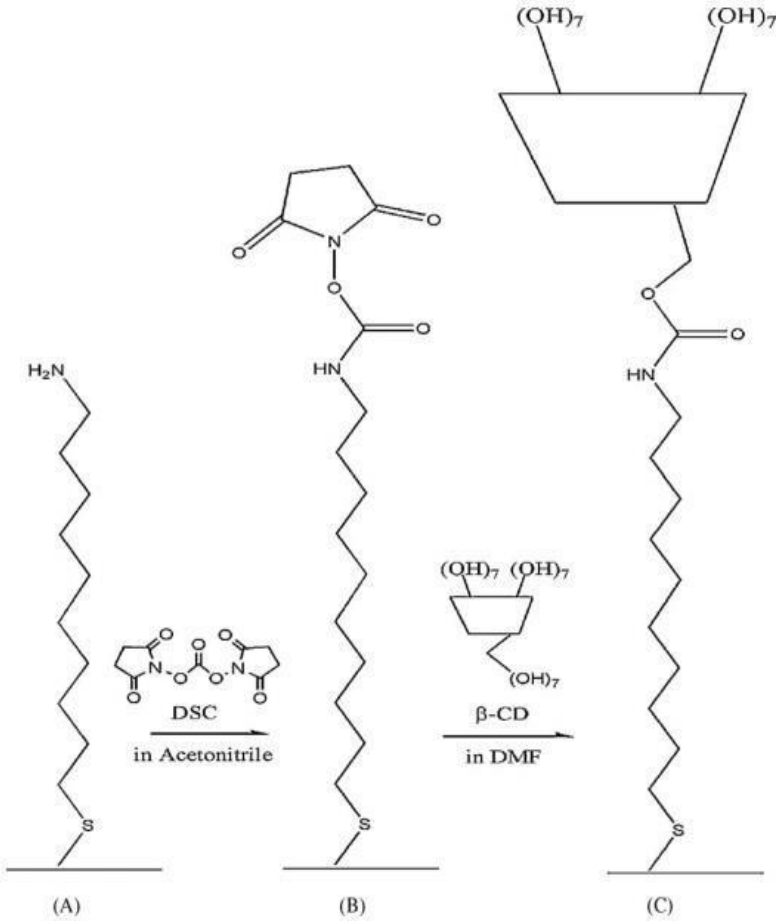

Figure 7.2 First attempting of bottom-up fabrication of the supramolecular surface. In the first step, the aminothiol is assembled on the surface, forming the SAM. The next step

represents the activation of the surface with DSC, followed by the covalent immobilisation of the cyclodextrin on the surface. A) Surface functionalized with Aminoundecanethiol (AUT). B) AUT+Activator (DSC). C) AUT+Cyclodextrin. The picture was taken from reference[351]

7.3 Characterisation of the Cyclodextrin SAM

The results showed a monolayer thicker than the length of the theoretical one. The theoretical value of the AUT molecule is 1.75 nm, the one measured by ellipsometry was 3.5 nm. It was assumed that the monolayer obtained was effectively assembling as a dimer on the surface. It was later understood that it might due to the amino group of one molecule interacting with the amino group of the next one as shown in Figure 7.3.1.[352].

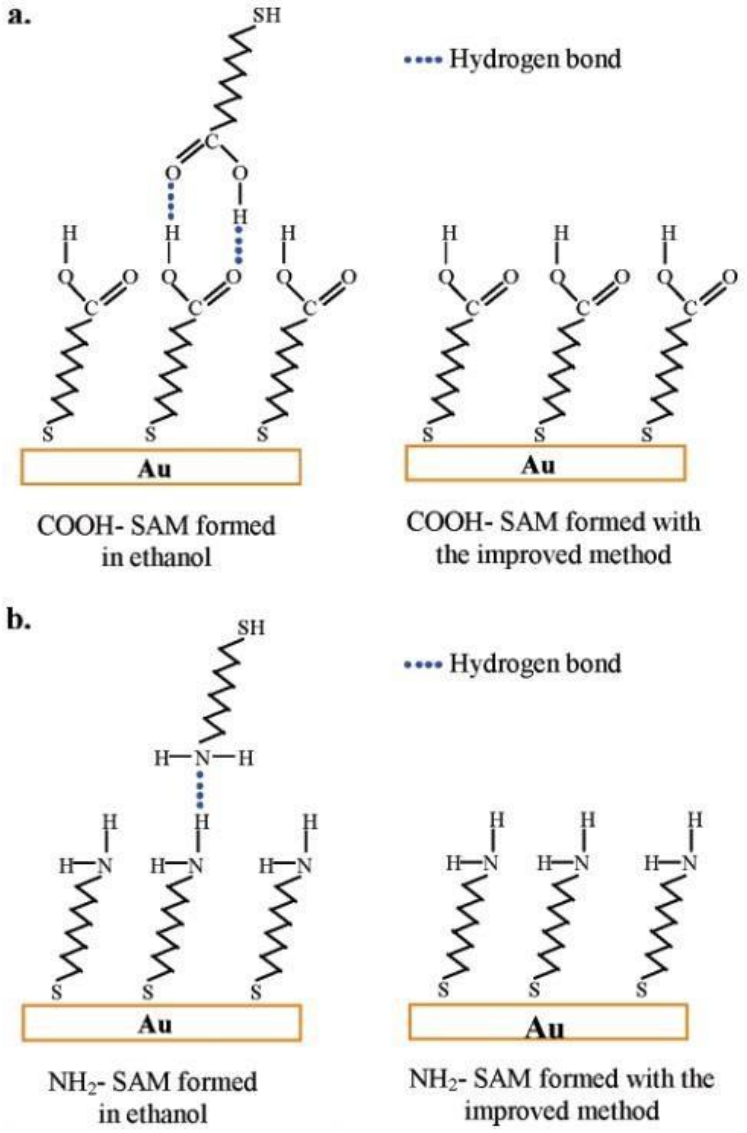

Figure 7.3.1 Dimerisation of the thiol molecules comprising either carboxyl terminated moieties (A) or amino terminated moieties(B). The picture was taken from reference[352].

A 10% of trimethylamine (TEA) was added to this step. As indicated by literature TEA reacts with the amino terminated molecule[352] and thus prevents other thiols from interacting with the amino group. Then the chips were rinsed with ethanol and 10% acetic acid, to clean off the surface from the triethylamine. The ellipsometry, in this case, showed much better results: with a thickness of around 1.5 nm, which correspond to our aminoundecanethiol oriented at a certain angle on the surface as indicated by literature[40].

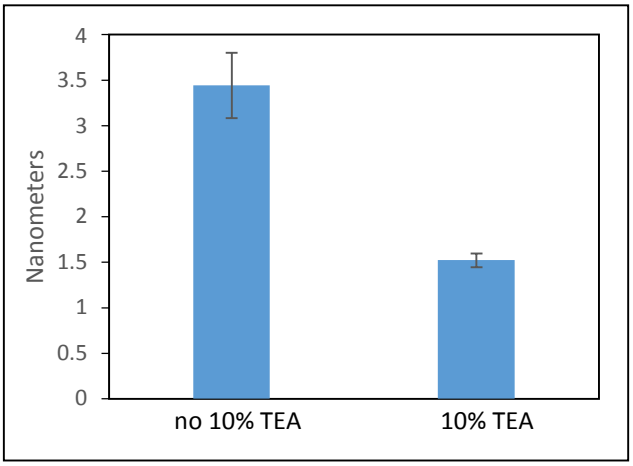

Figure 7.3.2 Comparison of the ellipsometry results between the two methods with and without the use of TEA. The method not using TEA presents a thickness of 3.5 nm and the 10% TEA method a thickness of 1.5 nm.

Also, the contact angle showed much better results in comparison with the lack of TEA during preparation due to a decreased in hysteresis in the case of the 10% TEA nanofabrication method. The smaller hysteresis (the difference between advancing and receding angle) provides evidence of a better surface packing[286].

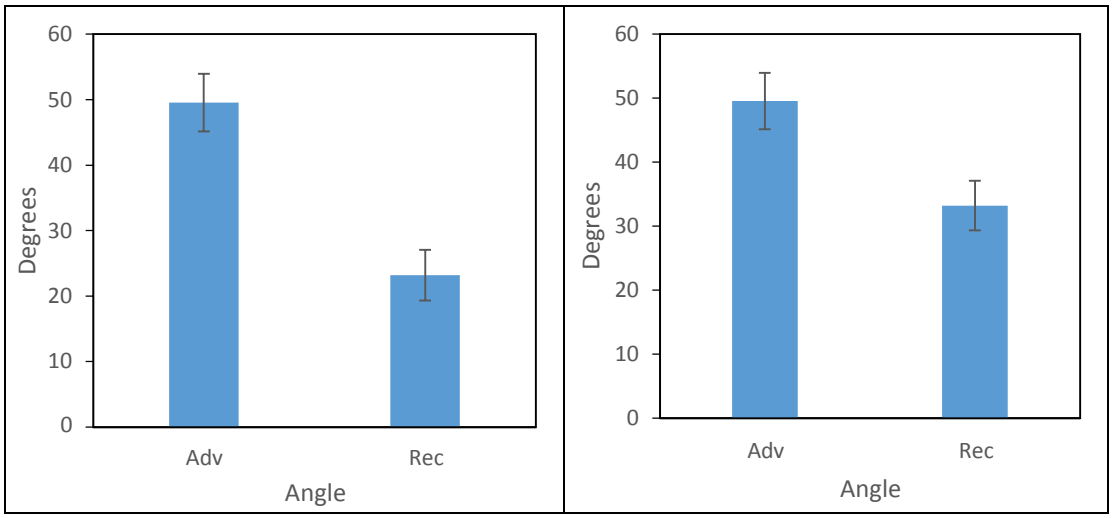

Figure 7.3.3 Contact angle of AUT surface comparing the two methods without TEA (left) and with TEA (right).

As the results showed a high-quality AUT monolayer, the second step was performed. No characterisation was made on this new surface (AUT+Activator) due to the high reactivity of the activator dihydroxysuccinimide (DHS) with water and oxygen, bringing to an unsuitable monolayer for the next step. Once leaving the AUT chip into the activation solution overnight, the chip was straightway put in the new solution of CD, for the last step, as indicated in Campina et al[351] (Fig 7.2).

Following functionalization, the characterisation of the AUT+CD monolayer was performed. The analysis was conducted on three chips with six measurements for each chip. We were considering an expected length of 2.1 nm for the molecule AUT+CD[351]. The average of all the measurement gives us a thickness of 2.9 nm with a standard deviation of 2.2 nm. The results were very different from the desired value. The high standard deviation at 2.2 nm indicates a heterogeneous film on the surface. The advancing angle contact angle was 57^{o} and under 20 degrees for the receiving angle:

Ellipsometry	Contact Angle
Thickness = 2.9 nm	Adv = 57° Rec < 20°
St Dev = 2.2 nm	St Dev Adv = 10° St Dev Rec = 5°

Figure 7.3.4 Ellipsometry and contact angle data of the AUT+CD surface.

No significant changes were observed in the contact angle data comparing with the AUT surface. This provides the first indication that the cyclodextrin functionalisation may have failed, with the water from the analysis washing off the cyclodextrin from the surface. Substantial changes in the ellipsometry data confirm instead the presence of the

cyclodextrin on the surface but with a standard deviation too high (2.2 nm) to prove the correct chemical adsorption of the cyclodextrin on the AUT surface.

An innovative and different approach was needed, as it was assumed that the problems might be related during the activation step due to faster degradation of the DHS[351], determining the CD unable to attach the surface. To prove that, a parallel synthesis was performed in solution at a higher concentration trying to understand if the activator was not degrading too fast and the CD was capable of bonding to our surface covalently. Cysteamine (2-carbon chain) (1) instead of AUT (12-carbon chain) was used as it presents a higher solubility at higher concentrations and the amino and thiol groups exhibit the same reactivity in both molecules. The Cysteamine 0.5 M and the DHS 0.5 M (Fig 7.3.5 compounds 1 and 2) were mixed in 5 ml DMF, after two hours CD 0.5 M was added to the solution.

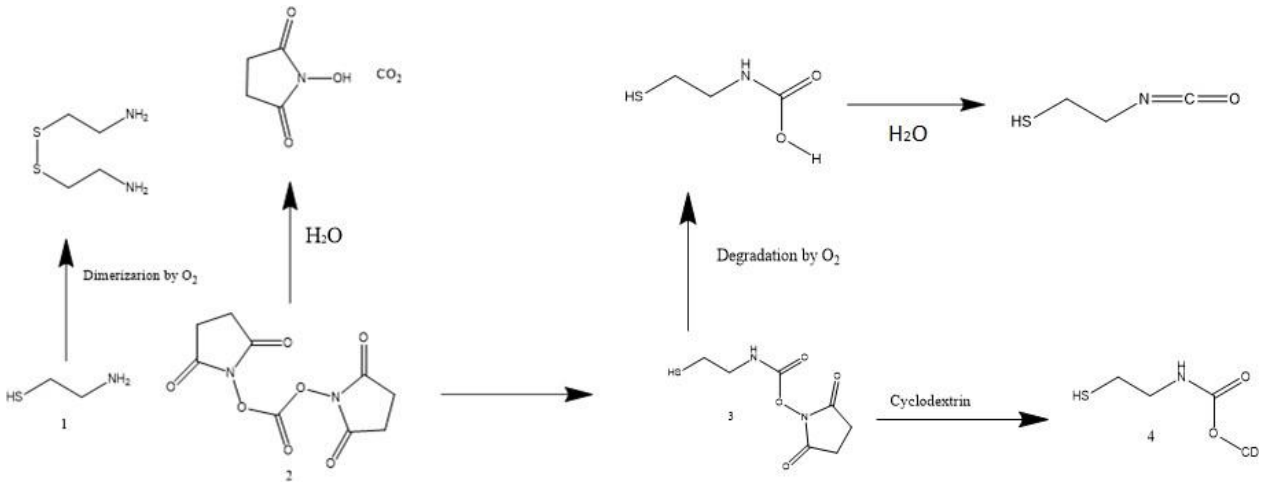

Figure 7.3.5 Scheme of degradation steps of the synthesis of Thiol-CD. Both reagents reaction, Cysteamine (1) and DHS(2), and intermediary compound (3) may be degraded by exposition to the air or water, leading to a low yield product (4).

A mass spectra showed only the cyclodextrin non-functionalized. From the mass spectra, it was expected a signal at 1237 m/z related to compound 4 in figure 7.3.5.It was evident that the cyclodextrin has not been reacting with the succinimidyl Cysteamine (compound 3 fig 7.3.5) as it presents two signal belonging to the original molecular weight 1135 m/z and 1152 m/z (fig 7.3.6). This proves that the DHS degrades too fast to provide an efficient synthesis, as also theorised by this study[351].

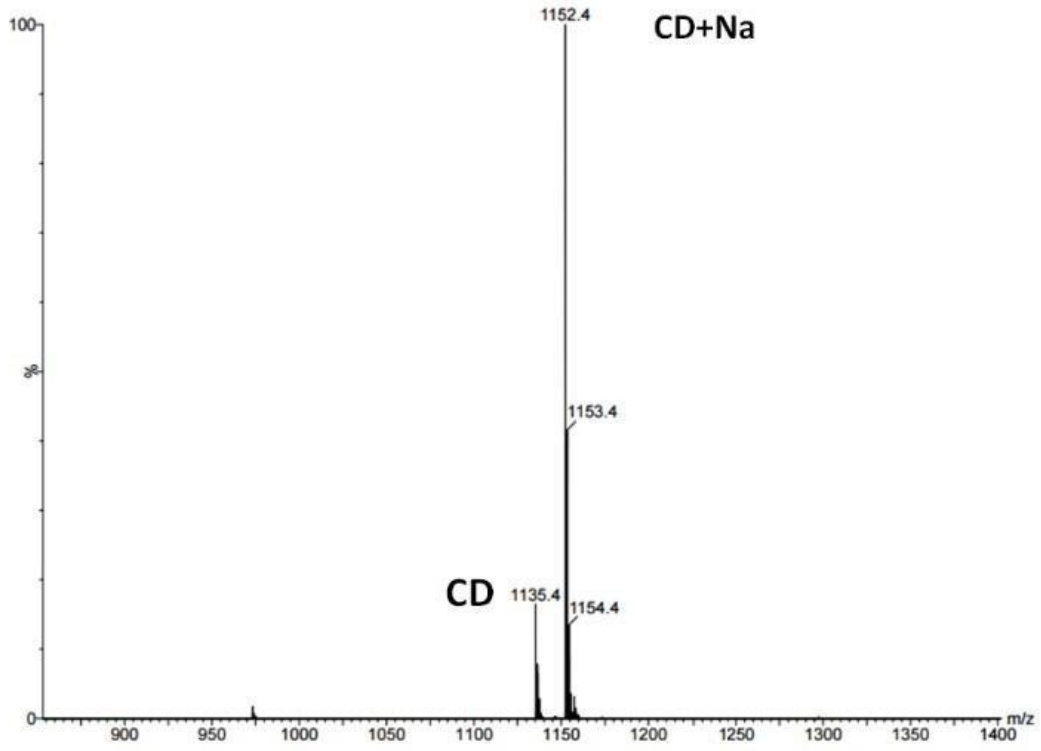

Figure 7.3.6. Mass spectra of unreacted CD. Two signals can be noticed of the unreacted CD: 1135 m/z which is the signal for the pure CD, and 1152 m/z the signal of the cyclodextrin carries a sodium atom in its cavity.

Although this represented a novel fabrication technique, there are inherent issues with the system as shown previously. The activator used in the second step goes fast under

degradation, inducing many imperfections in the system after the nanofabrication, as was also confirmed by literature[351]. Another problematic aspect is represented by the self-assembly of thiolated amines, due to their tendency to dimerise as commented by Riet et al[36]. They proposed that the strong hydrogen bonding between two amino groups or two acid groups, resulting in dimers, is the cause of the formation of a bilayer during the self-assembly on the surface (fig 7.3.1).

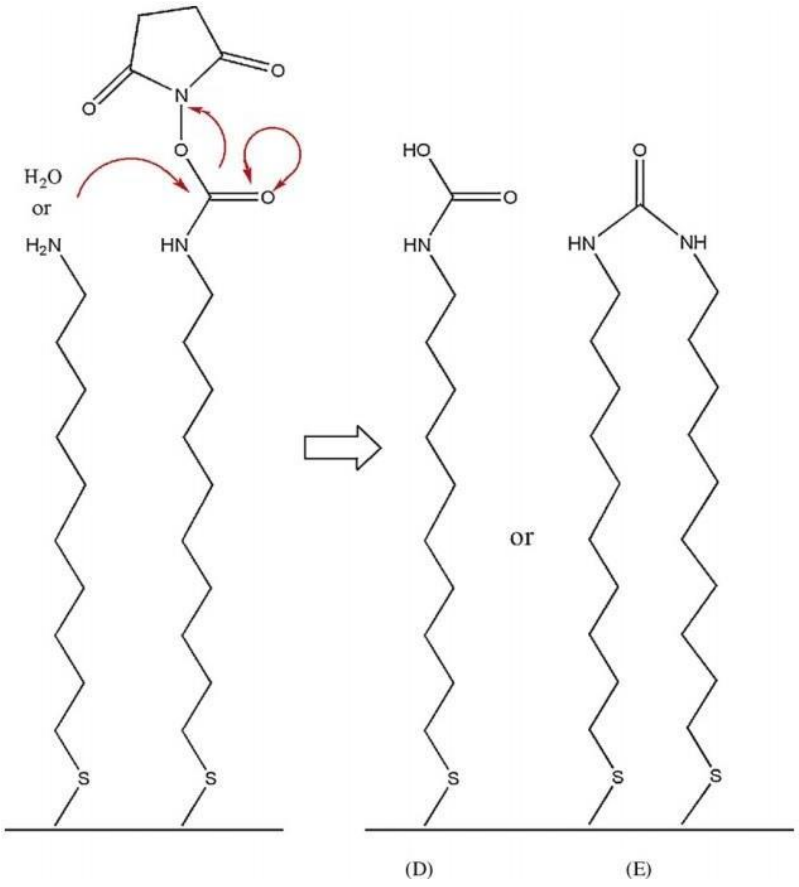

Figure 7.3.7 The secondary reaction is affecting the SAM nanofabrication. Once the SAM is activated with DSC (Fig 7.2-B), it may react with the water of the environment determining two scenarios unable to bind the Cyclodextrin (D and E).

As the monolayer presents many difficulties in fabrication, it was decided to simplify the nanofabrication method by functionalizing the cyclodextrin directly with the

thiol due to their high affinity to gold[353].With this new approach the entire carbon chain of the aminoundecanethiol is completely removed (molecule C fig 7.2) and now the thiol group is part of the glucose monomer (fig 7.3.8). From Stoddart's work [354], the chemical absorption of the Heptakis-(6-deoxy-6-mercapto)-beta- Cyclodextrin (β-CD–(SH)7) on the surface was analyzed, even if some imperfections onto the layer were observed by Cyclic Voltammetry.

Based on these results, new surface design and concept were created. New molecules were designed to provide a facile bottom-up fabrication, avoiding the use of any highly reactive molecule. In this way, no degradation can interfere with the correct packing of the SAM. In this new strategy, the CD is functionalized directly with the thiol group forming the β-CD–(SH)7 (fig. 7.3.8).

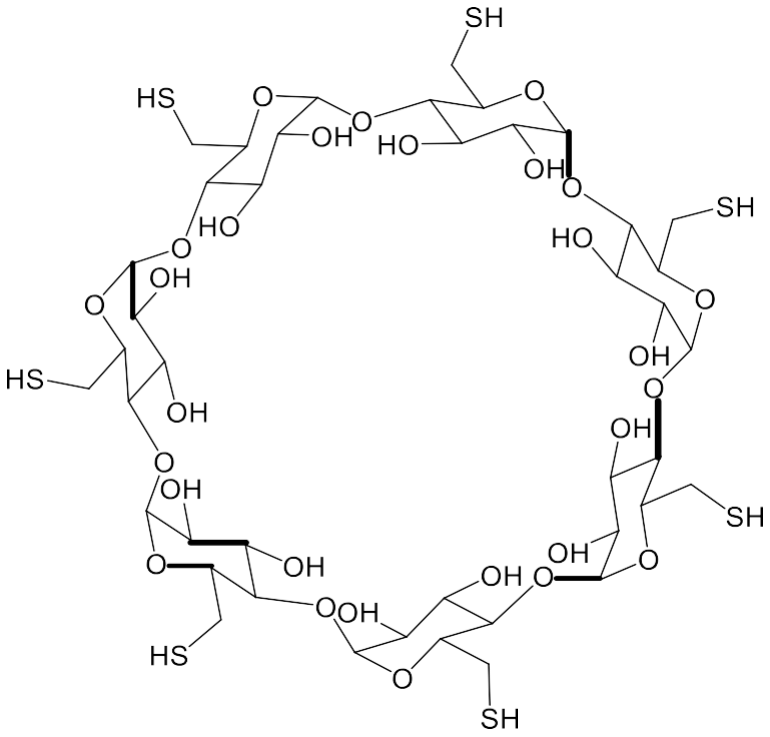

Figure 7.3.8 The β-CD–(SH)7 used in the following series of experiments. It can be noticed that the thiol group (SH) is now substituting the previous hydroxyl group. This is in order to allow the self-assembly of the cyclodextrin to the gold surface.

7.4 Nanofabrication and characterisation of the β-CD–(SH)7 SAM

7.4.1 Contact angle, ellipsometry and XPS characterisation

The molecule used for the new functionalization method was the β-CD–(SH)7. First studies were performed for obtaining the best conditions for SAM formation. Several chips were used for these experiments at different concentrations and incubation times:

- 0.1 mM in Dimethylformamide (DMF) for 12h
- 0.1 mM in DMF for 24h
- 0.1 mM in DMF for 48h
- 1 mM in DMF for 12h
- 1 mM in DMF for 24h
- 1 mM in DMF for 48h

DMF was selected to have the maximum solubility power. For the contact angle data, the β-CD–(SH)7 SAM shows a hydrophilic property (Figure 7.4.1), due to their value lower than 90°, as hydrophobic surfaces are the one exposing a contact angle above 90°[355]. These hydrophilic surface characteristics are due to the hydroxyl groups on the external wall of the CD molecules. It is possible to observe a decreasing in their hydrophilicity and in other words an increasing in hydrophobicity, with an advancing contact angle varying from 25^0 degrees for the 0.1 mM 12 h, to 55^0 degrees for the 1 mM 48 h sample.

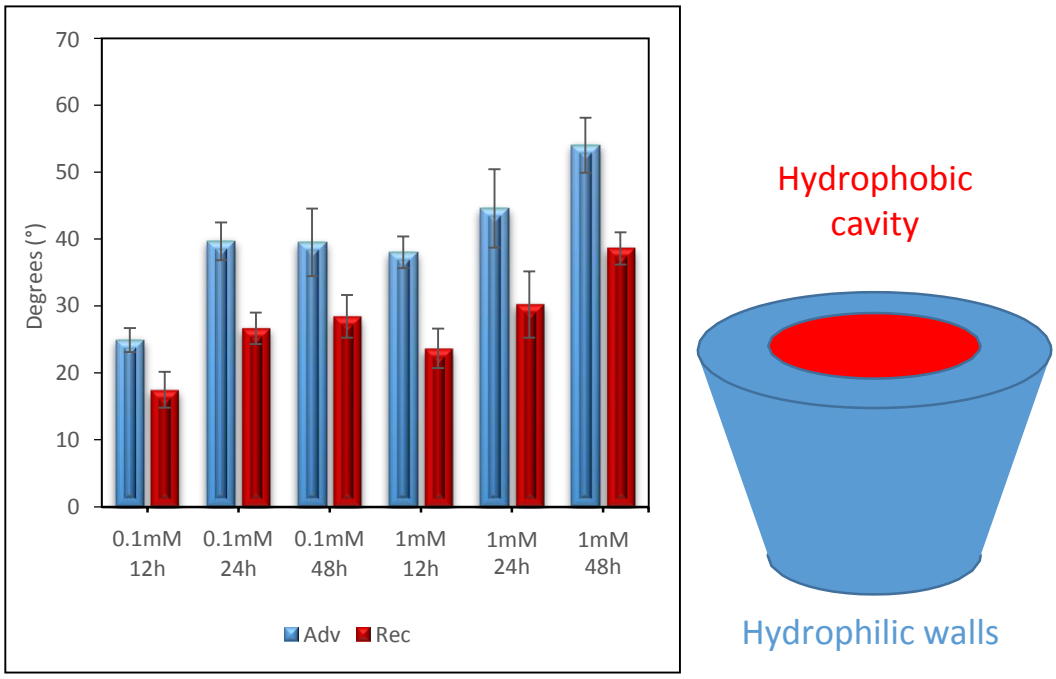

Figure 7.4.1 Contact angle data of β-CD–(SH)7. The hydrophobicity increases by increasing concentration and incubation time, probably meaning that the β-CD–(SH)7 is assembly with the cavity (the main contributor to the hydrophobic character) facing up.

The sample incubated at 0.1 mM for 12 h, showed the highest hydrophilicity among all the other samples with an advancing angle of 25.6 degrees with a standard deviation (SD) of ±2.5, and a receding angle of ≅18 degrees and a SD of ±2.1. This is likely since the cyclodextrin is laying on the surface but with the side walls facing the surface. The samples 0.1 mM for 24 and 48 h and the sample 1mM for 12 hours showed a pretty similar polarity, showing an advancing contact angle respectively of 40.1, 39.7 and 38.9 degrees with a SD of ±1.5, 1.8 and 1.3 respectively, and a receding angle of 26.7, 27.9 and 23.4 degrees with a SD respectively of ±1.6, 1.9 and 2.0. With the samples of 1 mM for 24 h, the hydrophilicity decreased even further with an advancing angle of 45.1 degrees and a SD of 4.5 and a receding angle of 29.3 degrees and a SD of ±3.6. The last sample measured was the 1 mM for 48 h that showed the lowest hydrophilicity with an

advancing angle of 53.2 degrees and a SD of 3.6, and a receding angle of 39.3 degrees and a SD of ±2.7. These increased trending in hydrophilicity can provide some indication of the orientation of the CD macrocycle on the surface with a more exposed hydrophobic cavity at the interface. Remarkable differences were observed between 0.1 mM for 24h and 1 mM for 48h; the other conditions show comparable (intermediate) advancing and receding contact angles.

The hysteresis, which means the difference between the advancing and the receding angle (θ_{Adv} -θ_{Rec}), for all the β-CD–(SH)7 SAMs range between 8^0 to 15^o (fig 7.4.1). This relatively small hysteresis indicates the possibility of a SAM with an ordered self-assembly and low amount of imperfections.

From the contact angle data, it is possible to see an increase in the hydrophobic property by increasing the concentration and the incubation time. Based on the fact that the cyclodextrin has a hydrophobic cavity with a hydrophilic external part, it is possible that not only the cyclodextrin is retained on the surface, but it is also facing up the cavity. These data suggest that the cyclodextrin is also acquiring the ideal orientation to make the surface interact expectedly with our proteins.

The β-CD–(SH)7 results were compared with the 6-thiol glucopyranoside (TGP) which represents the monomer of the β-CD–(SH)7. This approach was chosen to verify if the cavity or the rigidness of the molecule provides certain specific characteristics to the SAM (fig.7.4.2).

The same conditions and concentration solutions were kept with the only difference that instead of β-CD–(SH)7, TGP was used for SAM formation. Again, the solutions used were:

- 0.1 mM in (Dimethylformamide) DMF for 12h
- 0.1 mM in DMF for 24h
- 0.1 mM in DMF for 48h
- 1 mM in DMF for 12h
- 1 mM in DMF for 24h
- 1 mM in DMF for 48h

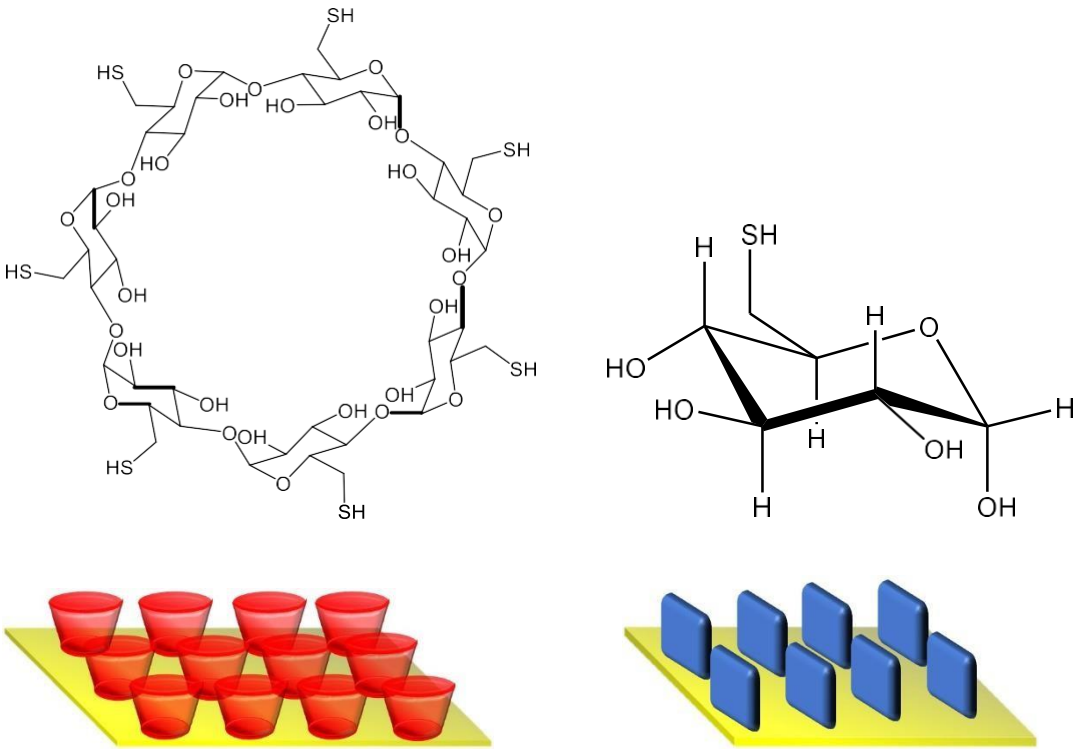

Figure 7.4.2 The eptamer β-CD–(SH)7 and the monomer TGP and their related 3D projection.

Different behaviour was observed in the case of TGP contact angle measurements (fig. 7.4.3). For the 0.1 mM for 12h, it was possible to observe an advancing angle of 25.2±2.3 degree and a receding angle of 20.5±3.7 degree. Slightly increased hydrophobicity was observed in 1mM 24 h sample with an advancing angle of 33.2±1.8

degrees and a receding angle of 27.3±2.6. Similar polarity was observed in the other samples 0.1 mM 48 h and 1 mM 12, 1 mM 24, and 1mM 48 h, which showed respectively an advancing angle of 29.1±1.7, 28.5±1.6, 32.1±1.8, 33.3±1.6 degrees and a receding angle of 28.9±1.8, 25.1±1.6, 30.5±1.9, 24.9±1.3. In the case of the β-CD–(SH)7, it was noticed a crescent hydrophobicity by increasing the concentration and incubation time (fig 7.4.1). Instead for the contact angle of the TGP (fig 7.4.3), relatively high hydrophilicity was observed, and no trends were possible to be suggested as the results are similar among them despite different concentrations and incubation times. However, the hysteresis seems to be relatively small also in this case (fig 7.4.3), suggesting that also TGP surface possesses a relatively high grade of the order.

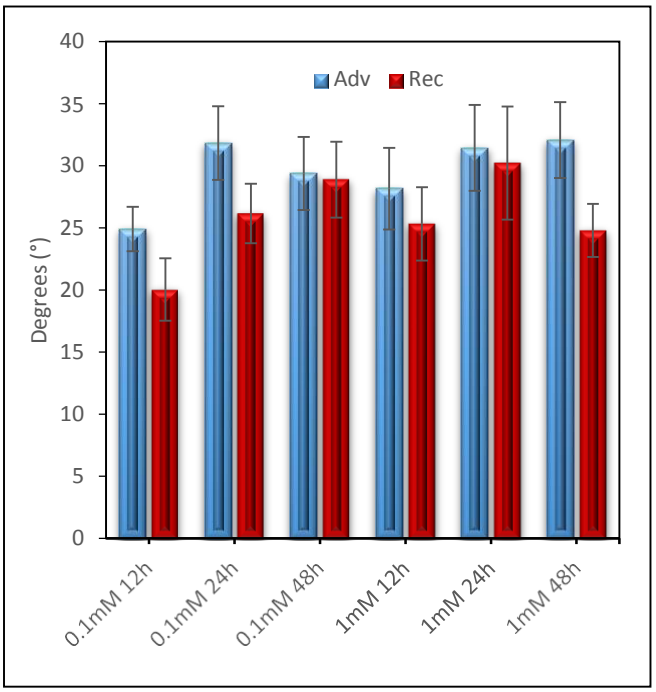

Figure 7.4.3 Contact angle data of the TGP at a concentration of 0.1 and 1 mM with an incubation time of 12, 24 and 48 hours.

Following contact angle analysis, the studies progressed to understand how the thickness changes for all different SAM preparation conditions. The ellipsometry data

show thickness values close to the theoretical dimensions of the CD molecules, i.e. 0.78 nm[356], except for the 0.1 mM 12h sample. These findings are in agreement with these SAMs being packed with the CD orientated with the macrocycle parallel to the plane of the gold surface. The theoretical outer diameter of the CD is approximately 1.54 nm[356], suggesting that for the 0.1 mM 12h β-CD–(SH)7 SAM the macrocycle might be orientated perpendicular to the gold surface. The experiment were conducted with 3 sample surface for each condition change, with the thickness measured in three different spot for every surface. The surfaces were cleaned with piranha solution and then immersed into different β-CD–(SH)7 solutions. The sample of the β-CD–(SH)7 (Fig 7.4.4 left) of 0.1 mM for 12 h showed a thickness of 1.61±0.19 nm. Samples of 0.1 mM 24 h with a thickness of 0.79±0.21 nm. The 0.1 mM 48h condition shows a thickness of 0.78±0.16 nm. 1 mM 12 h : 1.05±0.10 nm. 1 mM 24 h: 0.99±0.11 nm. 1mM 48 h: 0.92±0.07 nm. The ellipsometry data of TGP (Fig.7.4.4 right) showed a thickness of : 1.00±0.09, 0.78±0.11, 0.79±0.07, 0.58±0.08, 0.78±0.07, 0.93±0.03 nm respectively for 0.1 mM 12, 24, 48 h and 1 mM 12, 24 and 48 h. Differences, especially for the 0.1 mM 12h, were noticed between the ellipsometry data of TGP (Fig.7.4.4 right) and β-CD–(SH)7 (Fig 7.4.4 left), but all of them relatively close to the theoretical value of β-CD–(SH)7 and TGP of 0.78 nm. So far, with the ellipsometry data and the contact angle data, we were capable to assume respectively that the SAM formation is taking place on the surface and that the β-CD–(SH)7 is orienting with the cavity facing up for higher concentration and time incubation.

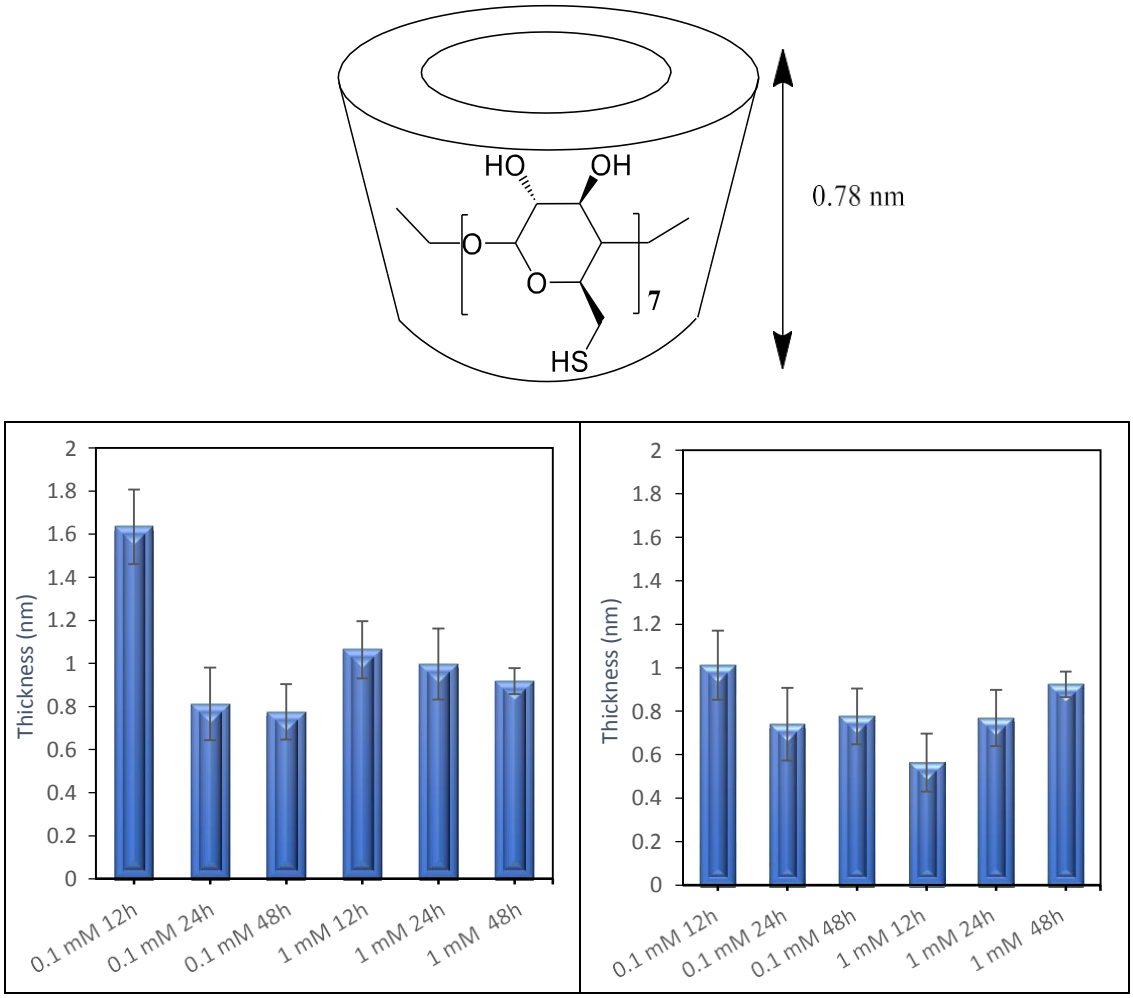

Figure 7.4.4 Ellipsometry data of the β-CD–(SH)7 (left) and TGP (right) at a concentration of 0.1 and 1 mM, with an incubation time of 12, 24 and 48 hours. The 1 mM concentration for 48h incubation is the results similar to the expected measurement (0.78 nm) with the smallest standard deviation either for the β-CD–(SH)7(left) and TGP (right).

The XPS experiments provided a further understanding of the SAMs packing. XPS data confirms the formation of the β-CD–(SH)7, showing on all surfaces signals from binding energies of the S (2p), (Fig 7.4.6, 7.4.7, 7.4.8). In all the pictures it was

evident a peak in the area of 162 eV and another at 164 eV, which indicated the presence respectively of sulphur bonded to gold and sulphur unbounded in the form of the thiol group (SH)[66]. It was possible to notice that in the case of the samples with higher incubation concentration (1 mM 12h, 24h and 48h) if compared with those at lower concentration 0.1 mM 12 h, 24h and 48h), the peak at 164 eV increased in area, proving that more unbounded sulphur was observable by increasing the concentration incubation. Interestingly, also the ratios of S/Au (Fig 7.4.5 left) and bound (S-Au) to unbound (SH) sulfur (Fig 7.4.5 right) vary, depending mainly on the concentration used. Taking into account the ratio S/Au for the samples 0.1 mM 12 h and 0.1 mM 24h we observed a similar value: 0.059±0.005 and 0.058±0.002 respectively. For the 0.1 mM 48h, we observed an increased ratio of S/Au of 0.071±0.009. These initial numbers determine that more β-CD–(SH)7 and thus more thiol groups, are laying on the surface but not all the thiol groups are bounding to it. This increase in S/Au ratio was even more remarkable for the 1 mM concentration samples. For 1 mM 12 h we had a ratio S/Au of 0.099±0.009. 1 mM 24 h with a ratio of 0.110±0.004 and for 1 mM 48h a ratio of 0.139 ±0.019). More evidence of β-CD–(SH)7 laying down on the surface without bonding to it completely was pointed out by calculating the percentage coverage of sulfur bounded and unbounded. For the 0.1 mM 12h, we calculated a 72/28 % bounded/ unbounded sulfur. For the 0.1 mM 24h: 75/25% , 0.1 mM 48h: 63/27%, 1mM 12h: 51/49%, 1mM 24h: 52/48%, and 1 mM 48h: 41/59%.

The SAMs created by incubation of a 0.1 mM β-CD–(SH)7 solution exhibited the highest ratio of bound sulfur, even after only 12 h of incubation. Taking into account that β-CD–(SH)7 has a total of 7 thiol group (SH), and counting that the 0.1 mM has a percentage 72, 75 and 63 % of bounded sulfur (respectively for 12, 24 and 48 h). We

assumed that the β-CD–(SH)7 is bounding the surface via an average of five or four sulfur group. The same observation, in the case of the 1 mM we calculate 51, 52 and 41 % of bounded sulfur. Leading us to think that β-CD–(SH)7 is bounding the surface via an average of 3-4 sulfur group.

As previously reported[357], this difference in the number of covalent bonds formed can affect lateral diffusion during SAM formation and consequently surface molecular coverage. Indeed, the increased mobility restrictions imposed by the multiple thiol anchors associated with SAMs fabricated from 0.1 mM solutions could explain the lower sulfur content at these surfaces as established by calculating the XPS S/Au ratios. On the other hand, the higher sulfur content in SAMs formulated in a 1 mM solution indicates a more tightly packed monolayer when compared with the SAMs formed from the 0.1 mM concentration. This characteristic is essential for protein surface immobilisation since sparsely packed CDs on the surface could lead to non-specific binding.

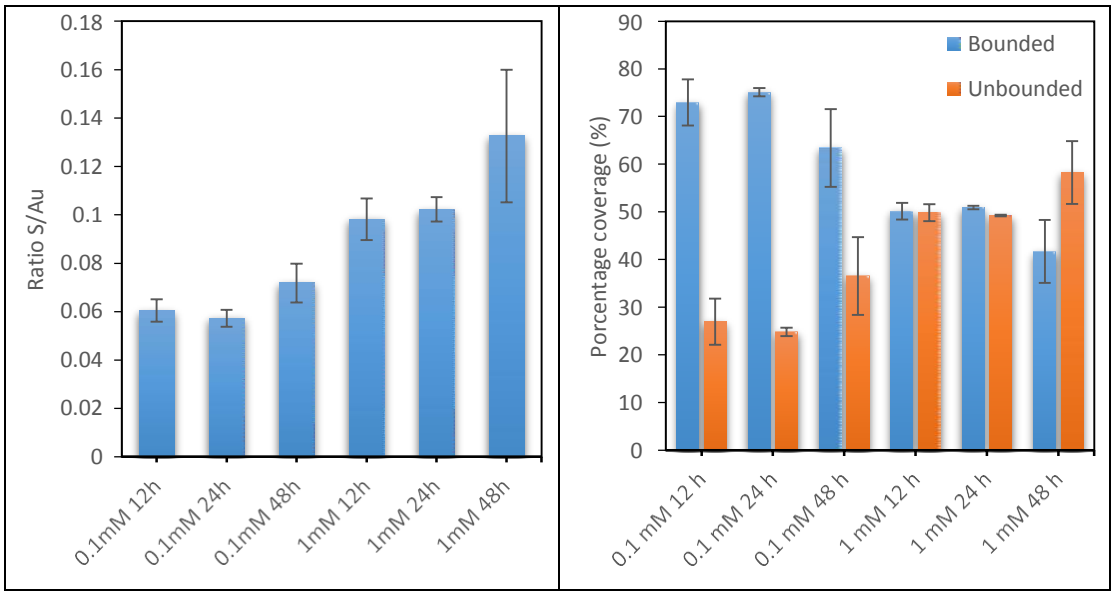

Figure 7.4.5 The amount of sulphur/gold ratio (left) and the percentage coverage of sulphur for each SAM preparation condition as analysed on the surface during XPS experiments.

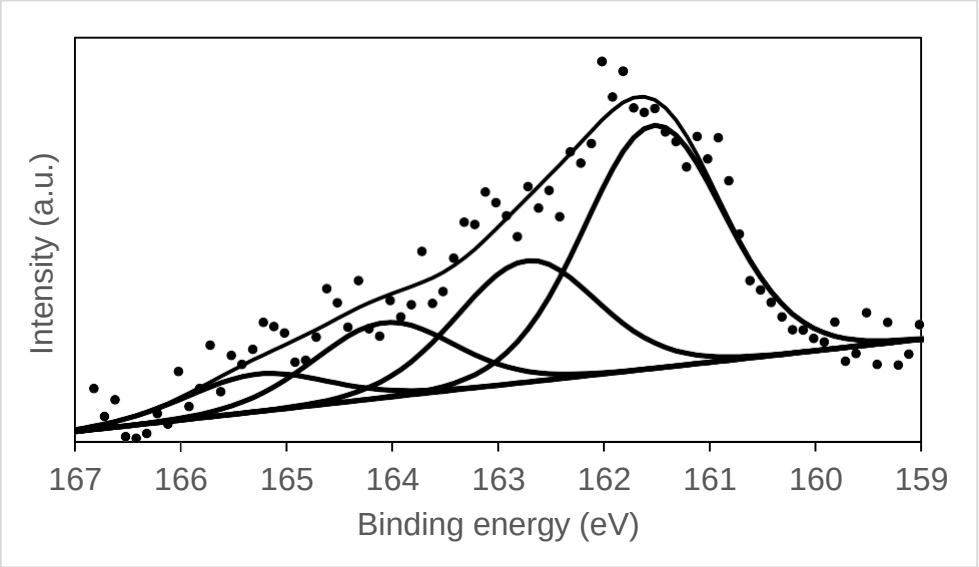

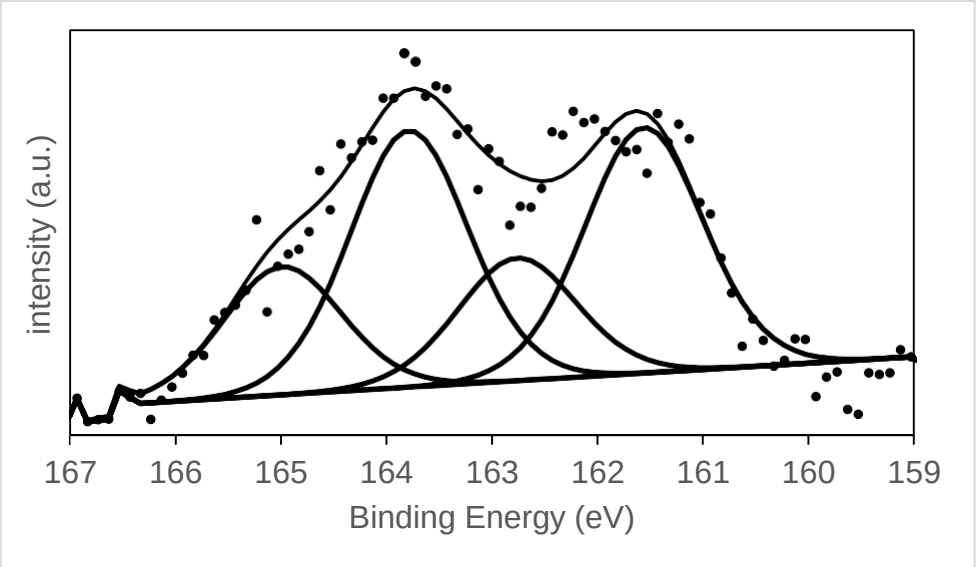

Figure 7.4.6 XPS sulphur signal β-CD–(SH)7 at incubation concentration of 0.1 mM (up) and 1 mM (down) and an incubation time of 12 hours. The peak of the unbounded sulphur (SH) has increased with the increasing of the concentration.

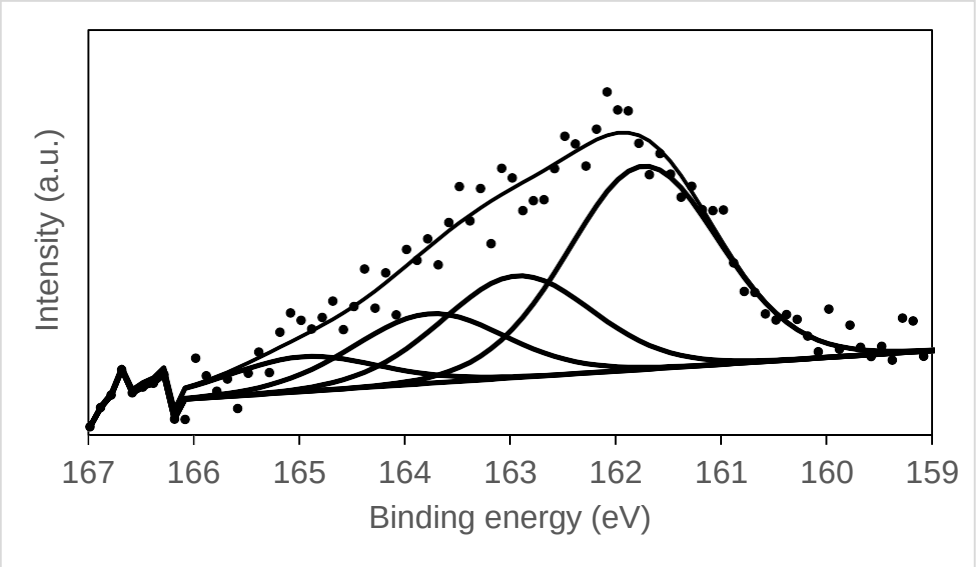

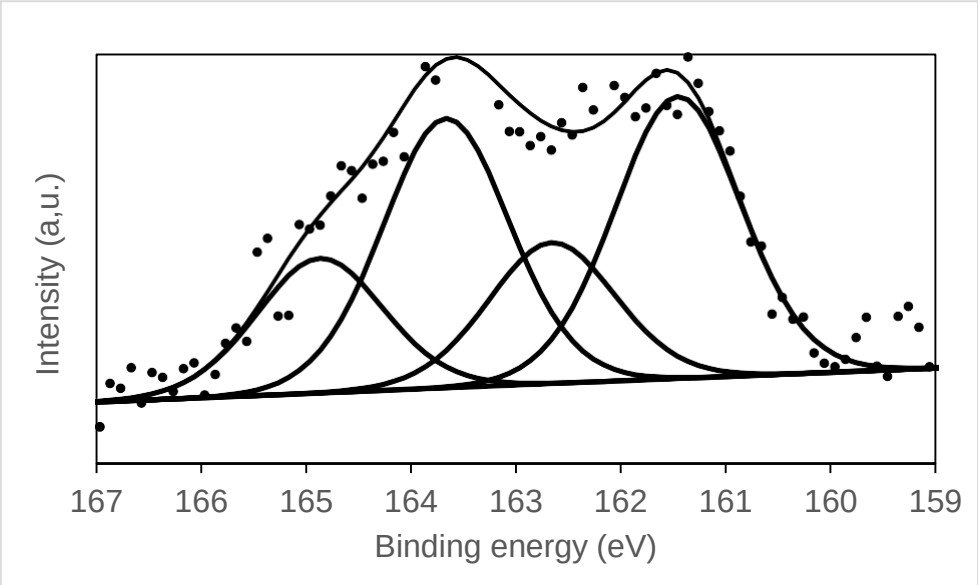

Figure 7.4.7 XPS Sulphur signal β-CD–(SH)7 at incubation concentration of 0.1 mM (up) and 1 mM (down) and an incubation time of 24 hours. Again as in figure 7.4.6, the peak of the unbounded sulphur (SH, 164 eV) has increased with the increasing of the concentration.

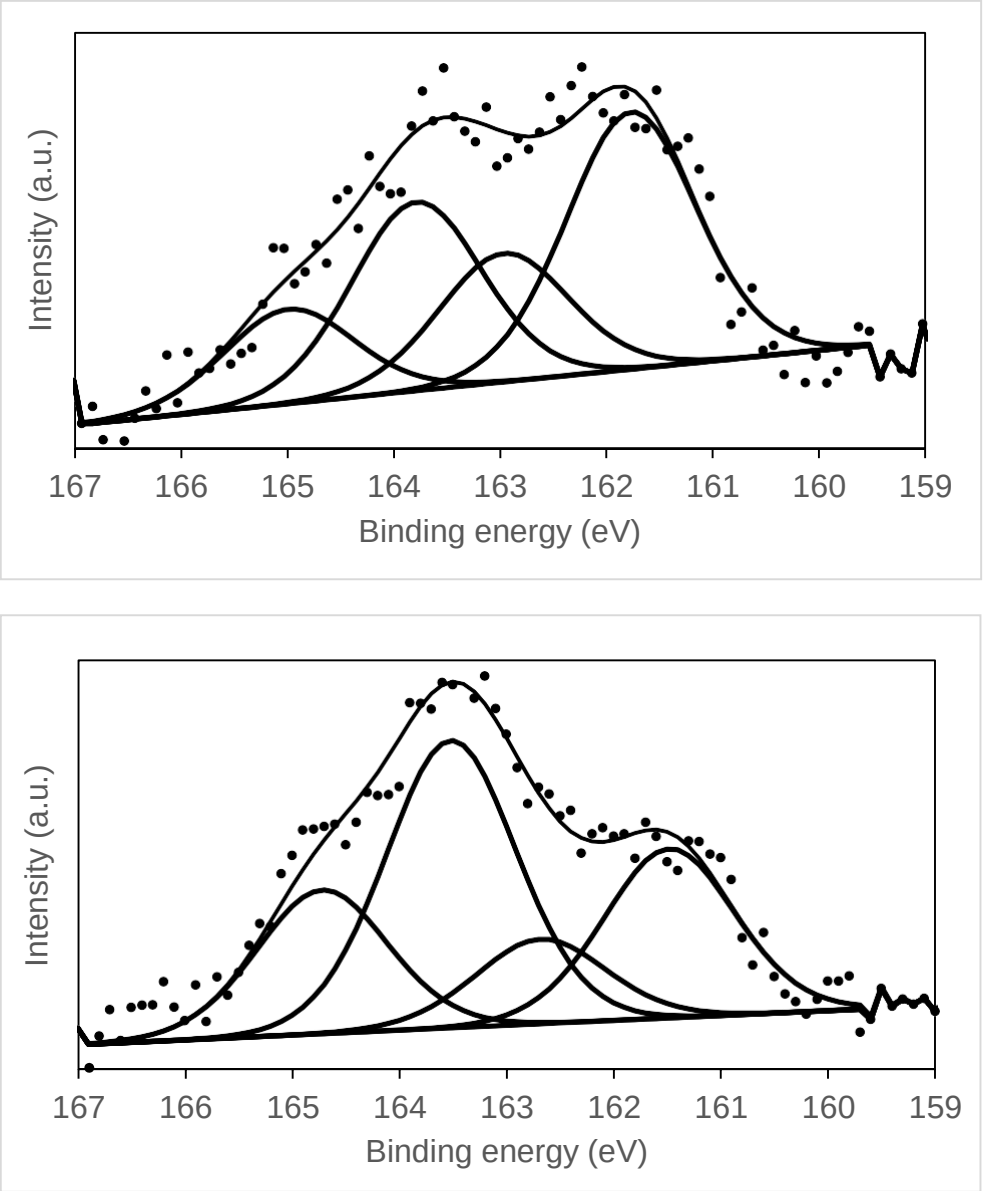

Figure 7.4.8 XPS Sulphur signal β-CD–(SH)7 at incubation concentration of 0.1 mM and 1 mM and an incubation time of 48 hours.

The XPS of the TGP was taken at 0.1 mM and 1 mM for 24 hours. The analysis was done to prove the self-assembly of the sulfur-based molecules was effectively occurring on the surface. The same behaviour was observed for both example concentration 0.1 mM and 1 mM TGP where the surface coverage of bounded sulphur was higher of the unbounded sulfur.

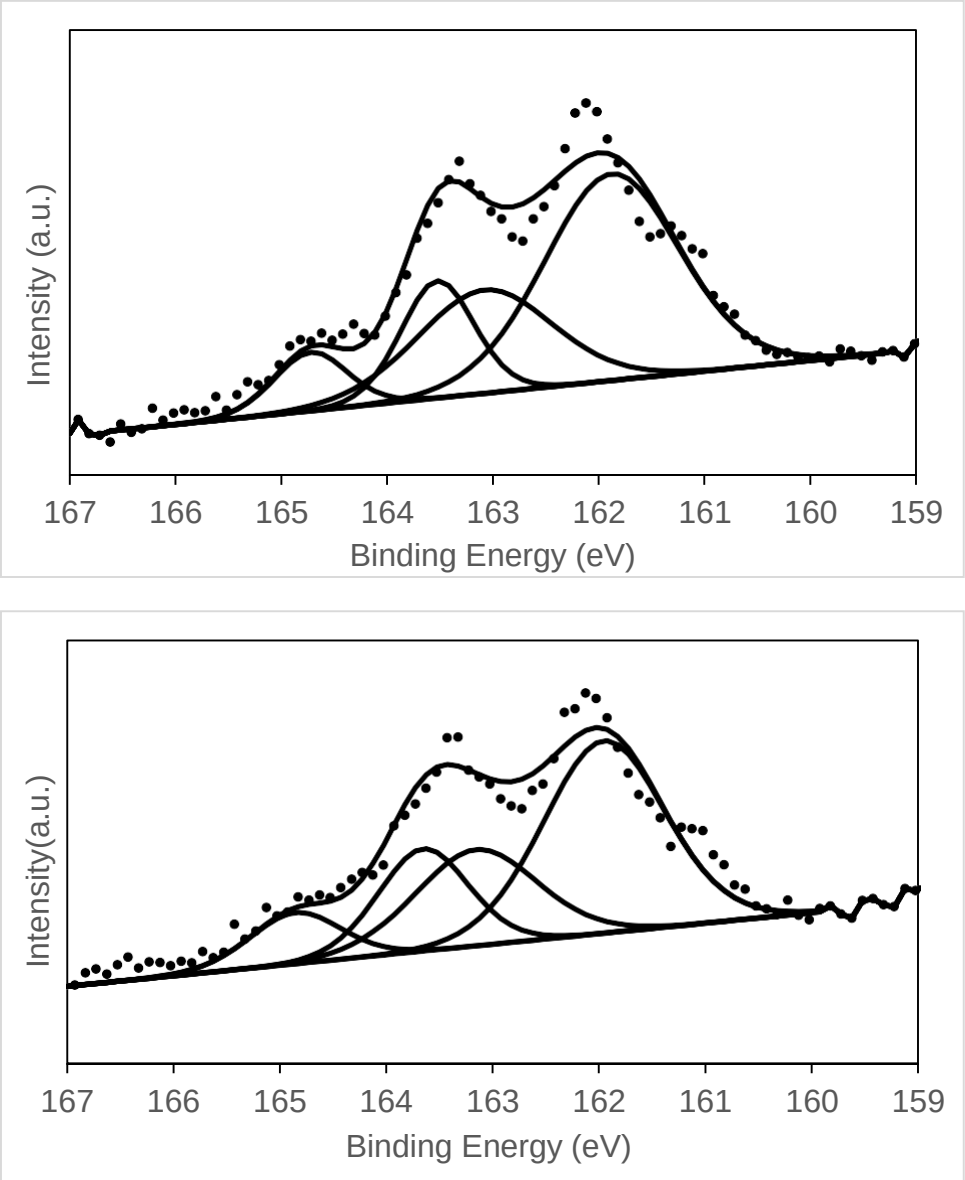

Figure 7.4.9 XPS spectra of TGP at 0.1 mM (above) and 1 mM (down) for 24 hours. The peak at 162 is the sulfur bonded to gold, at 164 the sulfur unbonded (SH).

7.4.2 Cyclic Voltammetry

Cyclic Voltammetry (CV) studies were carried out to further ascertain the density or permeability of the β-CD–$(SH)_7$ SAMs. Since β-CD moieties are known to form stable complexes with ferrocene and its derivatives[354], ferrocene carboxylic acid (FCA), which

is water-soluble, was used as a redox-active molecule to quantify the β-CD surface coverage or potential space between β-CDs. The chips were incubated as usual in the β-CD–$(SH)_7$ solutions following the first step procedure of cleaning the gold in a piranha solution for 8 minutes, then washed with Milli-Q water and dried under an argon flow. The chips were also incubated in solutions of 0.1 & 1 mM of β-CD–$(SH)_7$ for 12, 24 and 48h and then directly incubated for 4 hours in a solution of 0.1 M of FCA in DMF.

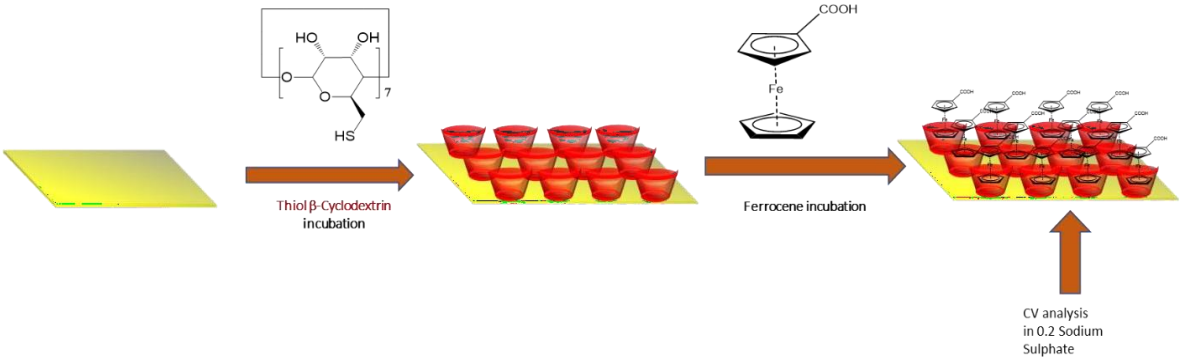

Figure 7.5.1 Scheme of the cyclic voltammetry experiment. In the first step, the surface is functionalized with CD, following by chip incubation into a solution of ferrocene to measure the electrical conductivity of the SAM.

After the incubation, the chip was washed gently again with Milli-Q water to eliminate the excess of FCA accumulated on the surface. During the FCA incubation, the electrochemical chamber for the CV experiment was prepared. The electrolytic solution used during the CV experiment was a solution of 0.2 M of sodium sulphate previously degassed with continuous argon flow. The analysis was conducted in a range of 0.1 V and 0.8 V at different scan rates going from 300 mV/sec to 3 mV/sec. Subsequently, the

oxidation and the reduction processes of FCA at the modified gold surfaces were investigated by cyclic voltammetry (Figure 7.5.2).

The cyclic voltammograms associated with surfaces modified with 1 mM SAM displayed the lowest anodic and cathodic current peak intensities. Interestingly, the peak separation observed at CVs obtained with the bare gold and at the 0.1 mM and 1 mM SAM-modified surfaces yielded peak separations of 49 mV, 41 mV and 32 mV respectively. When peak separations fall below 59 mV, this is indicative of an electrochemical surface-bound process[358]. This is also supported by the data in Figure 7.5.2, which represents the average of anodic peak currents obtained at varying scan rates of the different concentration at different incubation time (i.e. 0.1 mM for 12h, 24h, 48h and 1 mM for 12h, 24h, 48h).

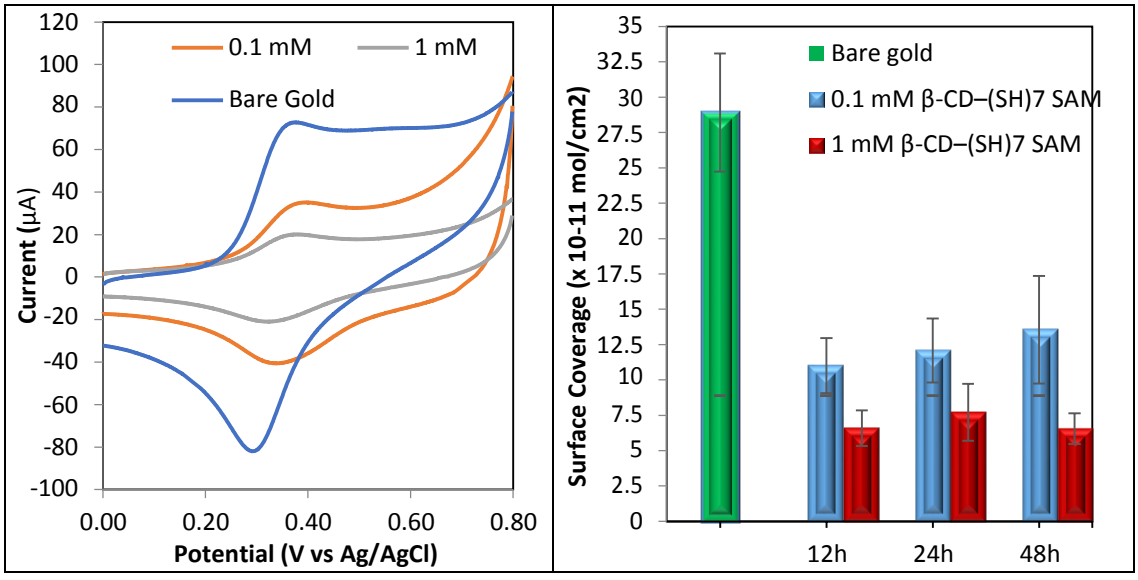

Figure 7.5.2 Cyclic voltagramm of SAMs fabricated with DMF solution of β-CD–(SH)$_7$ at the concentration of 0.1 mM, 1 mM, and bare gold (left). Coverage of the ferrocene (right) over the surface at bare gold, 0.1 mM and 1 mM.

Linearity in the growing of peak current with scan rate indicates that the ferrocene is bound to the surface[354] (Figure 7.5.3). If it were under diffusion control, the peak current would be predicted to grow in an exponential rate. Interestingly, the higher concentration of CD results in a lower peak separation, which is indicative of a faster electron transfer kinetics vs the modified surface with the lower concentration.

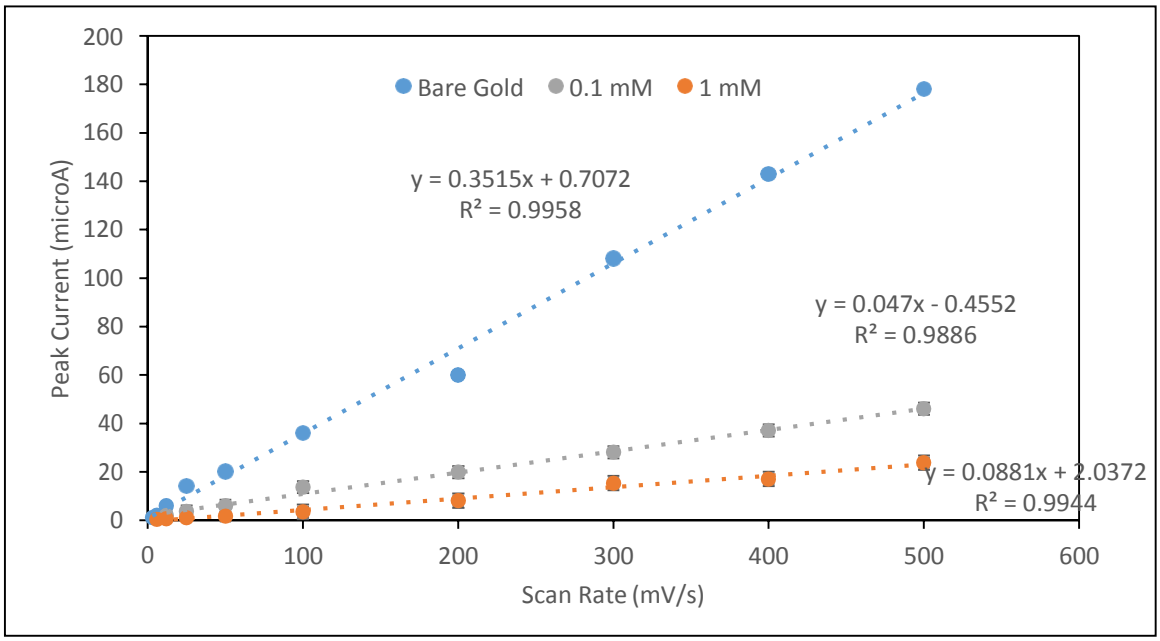

Figure 7.5.3 Plot of the peak current vs the scan rate at different CD SAMs concentration. The linear trend of all the measurements indicates that the redox reactions are occurring only at the surface of the gold chips (electrode).

Based on the CV data collected for all different SAM conditions (i.e. 0.1 mM, 12h, 24h and 48h and 1 mM, 12h, 24h and 48h) significant peak intensity signal could be observed only in the cases of different SAM concentrations (0.1 mM and 1 mM) but not for different incubation times (12h, 24h, 48h). The surface coverages (Γ) were determined according to the Laviron-derived equation for surface-confined electroactive species[359]:

$$\Gamma = \frac{I_p 4RT}{n^2 F^2 A \nu} \quad (1)$$

Where I_p represents the peak current, R the gas constant, T the temperature, n the number of electrons involved in the Fe redox reaction (n=1), F the Faraday Constant, A the electroactive area (A= 0.785 cm^2) and ν the scan rate (ν = 0.3 V/s).

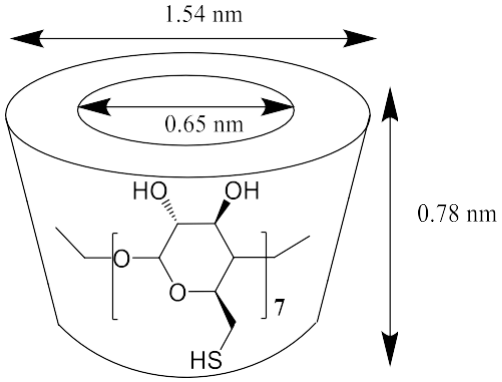

Figure 7.5.4 The β-CD–(SH)7 dimensions. It is a basket-shape molecule with an external diameter of 1.54 nm, an internal diameter of 0.65 nm, and a length of 0.78 nm.

For reference purposes, we calculated the maximum theoretical ferrocene coverage (MTFC) on a β-CD–$(SH)_7$ SAM. It was determined by considering the 1:1 complexation between the CD and ferrocene and a theoretical outer diameter of the β-CD of 1.54 nm [356] (Figure 7.5.4). The MTFC found to be 8.9 x 10^{-11} moles/cm^2 as demonstrated by the following: we take into consideration the outer diameter of the cyclodextrin to assume that the area occupied by a single cyclodextrin molecule (A_{CD}) standing up is equal to the area of the circle.

$$A_{CD} = \pi r^2 \qquad (1)$$

where r = 0.77 nm, considering a diameter of 1.54 nm

$$A_{CD} = 1.86\ nm^2 \qquad (2)$$

All converted in cm^2

$$A_{CD} = 1.86\,e10^{-14}\,cm^2 \qquad (3)$$

We multiply the A_{CD} for the Avogadro constant (N_A) to know the area occupied by one mole of β-CD–(SH)7 (A_{mol})

$$A_{mol} = N_A * A_{CD}$$

$$A_{mol} = 6.022\ e10^{23} * 1.86\ e10^{-14}$$

$$Amo = 11.21\,e10^{9}\ \frac{cm^2}{mol}$$

And then inverted as we want to express the surface coverage of a determined amount of moles over 1 cm^2

$$\Gamma = 8.9\ e10^{-11}\ \frac{mol}{cm^2} \qquad (4)$$

When comparing this value with the higher values obtained for the 0.1 mM SAMs, it becomes evident that on the 0.1 mM SAMs the ferrocene is also interacting directly with the gold surface, thus increasing the overall current associated with the ferrocene electrochemistry. This behaviour is likely to be due to entrapment of ferrocene between the CD moieties indicated by the relatively larger peak separation.

In cyclic voltammetry, the resultant current has two contributions. One is faradaic, and another is capacitance (charging currents). The charging current is higher (~16.2 μA) at the surface modified with the lower concentration of CD versus higher concentration (~8.0 μA). This behaviour occurs due to the lower packing density of the SAM, meaning that ions can migrate to and from the electrode surface more readily in a given time, giving rise to the observed increase in charging current.[360–362] Thus, the results suggest that the 0.1 mM SAMs form loosely-packed structures, wherein the spaces between β-CD–(SH)7

molecules are large enough for the ferrocene molecules to partake in the electrochemical reaction at the bare gold surface. This brings to an electrochemically active area greater, which results in the larger currents. In contrast, the 1 mM SAMs display ferrocene surface coverages below but closer to the MTFC on a CD SAM, thus suggesting that ferrocene mainly complexes with CDs on the surface due to the presence of a close-packed monolayer. The results comparison indicates that the optimal condition was reached when a CD concentration of 1 mM. Among all the samples in 1 mM concentration the 24h was the one closer to the MTFC and thus the sample that was chosen for our SPR analysis.

7.5 Conclusions

In this chapter, a protein structure survey was performed in order to determine possible attaching points on the protein, capable of fitting into the cavity of the β-CD–(SH)7. In all of the proteins analysed, there were several attaching points that render the protein suitable for our cyclodextrin surface. Once this was established, the analytical techniques on the surface provided information regarding the packing and orientation of the CDs on the different β-CD–(SH)7 SAMs (i.e. 0.1 mM, 12h, 24h and 48h and 1 mM, 12h, 24h and 48h). The ellipsometry provided information regarding the SAM thickness, and it was close to the one expected for almost all the samples except for 0.1 mM concentration for 12 hours. The contact angle indicates that the cyclodextrin is exposing the cavity during the self-assembly at high concentrations and for longer periods (1 mM for 24 and 48 hours). The cyclic voltammetry provided information regarding the surface coverage. Different peak signals could be observed only in the cases of different SAM concentrations (0.1 mM and 1 mM) but not for different incubation times (12h, 24h, 48h), and providing an optimal behaviour for the samples incubated at 1 mM. The XPS, as the

cyclic voltammetry, also indicate as optimal surface those samples incubated at 1 mM, since they exhibit more surface diffusion, which leads to a better surface packing. Each of the analytical techniques provided information regarding the packing and orientation of the CDs on the different β-CD-(SH)7 SAMs. Based on hydrophilicity, the thickness of the monolayers, and the number of bound thiols, the CDs in both 0.1 and 1 mM SAMs are predominantly oriented with the macrocycle cavity exposed at the interface. This orientation allows for maximum contact between the hydrophobic amino acid in the protein and the apolar CD cavity. However, the concentration used for SAM formation affects the packing of the CDs on the gold surface. As highlighted by the reduced amount of S/Au ratio and increased permeability as demonstrated by CV, SAMs fabricated with 0.1 mM solutions exhibited a less well-packed structure of CDs. Among all the 1 mM series analysis performed with the cyclic voltammetry (fig 7.5.2 right) the 24 hours incubation was the one that showed a surface coverage closest to the theoretical one (page 115 equation 4).Thus, based on these findings, 1 mM SAMs incubated for 24 h was chosen as the optimum surface to promote high protein binding while simultaneously limiting the nonspecific binding through the presence of a packed CD surface.

8. Affinity characterisation of the protein-surface system

Now that the optimised conditions of SAM formation have been defined, the second phase of the research work was to demonstrate that protein immobilisation on the surface could occur. In this chapter, the attention will be focused on the interaction of the surfaces with the proteins. Two kinds of analysis were conducted to demonstrate the protein interaction with cyclodextrin-functionalised surfaces:

i) surface plasmon resonance (SPR) for the plasmonic detection of the protein-surface interaction,

ii) Time of flight secondary mass spectrometry (TOF-SIMS) to give data on the chemical composition of the surface after the interaction with the protein.

For any analysis, we will briefly introduce the recent advances of these tools to demonstrate the effectiveness and the importance of the related data to our research. Thanks to the TOF-SIMS and by analysing the data, we will also suggest an indirect observation of the possible protein orientation (Cyt C) on our supramolecular surface. The experiments were carried out by Dr David J. Scurr and Anna M. Kotowska at School of Pharmacy, University of Nottingham.

8.1 Surface plasmon resonance (SPR)

The β-CD–(SH)7 surface was investigated by SPR to identify the binding affinity of this functionalised surface with different proteins. The experiments were performed on 1 mM for 24h. The cleaned surface was immersed into a solution of 1 mM of β-CD–(SH)7 in DMF. The surface was rinsed with MilliQ water and inserted into the sample chamber of SPR. The experiment was performed at 15 µl/min flow rate.

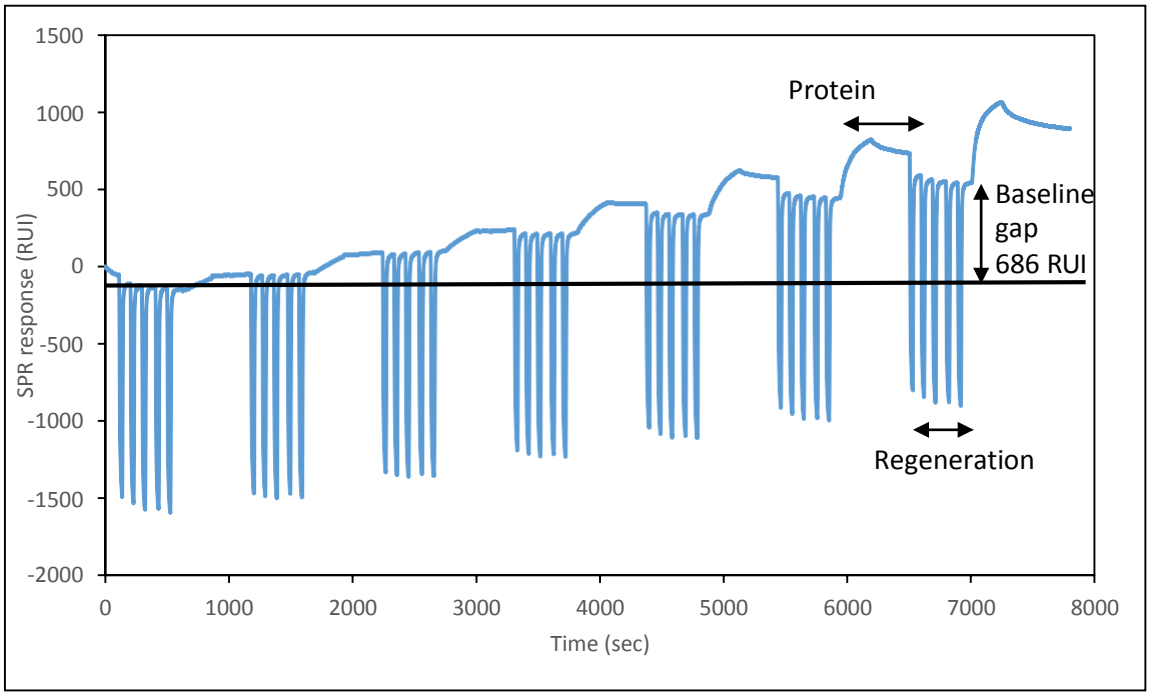

Figure 8.1.1 SPR sensorgram illustrating several cycles of Cyt C injection (0.07, 0.15, 0.3, 0.6, 1.2, 2.5, 5 mM) and regeneration (NaOH 10 mM) and their relatively SPR response.

Figure 8.1.1 shows an increased baseline on the last injection of 686 RUI. The protein was injected several times, each time with a double-increased concentration (0.07, 0.15, 0.3, 0.6, 1.2, 2.5, 5 mM). Between any protein injection, a regeneration step was needed to restore the surface from any possible protein traces. The regeneration step was

a five-time injection of sodium hydroxide 10 mM. The surface was not completely restored due to two possible factors: the first is represented by a regeneration solution that is not capable of breaking the interaction between the protein-surface.

The second problem to consider is that the non-well packed surface exposes the bare gold to the protein interaction (physical adsorption) (fig 8.1.2). This could represent a problem giving the fact that metal square surfaces can denaturate proteins[113] compromising the SPR analysis. To discard both problem possibilities, it was used sodium dodecyl sulphate (SDS) 10 mM solution for three injections, as indicated in the literature for protein desorption on surface[363].

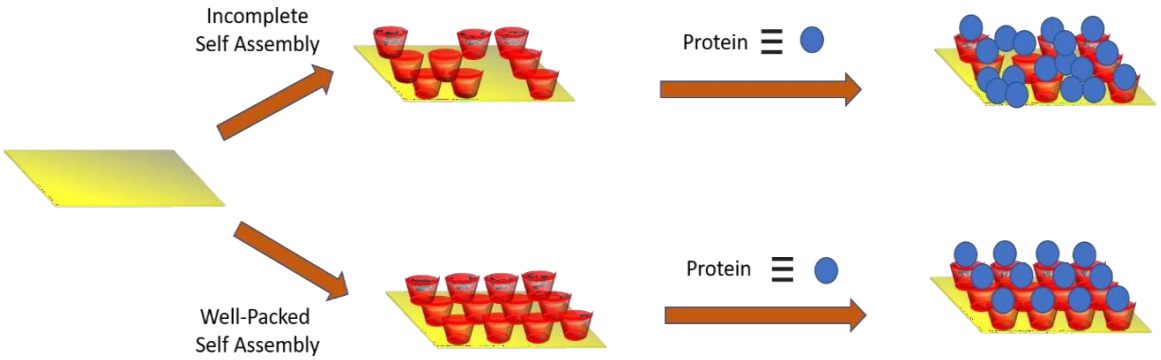

Figure 8.1.2 The two possible outcomes of the SPR analysis involving either a well-packed assembly or incomplete self-assembly.

Fig 8.1.3 showed improved experimental conditions. The baseline gap has decreased compared to the previous experiment, and the regeneration cycles from 5 times were dropped to 3. This effect represents an improvement as it proves that the SDS is regenerating the surface in a better way than NaOH.

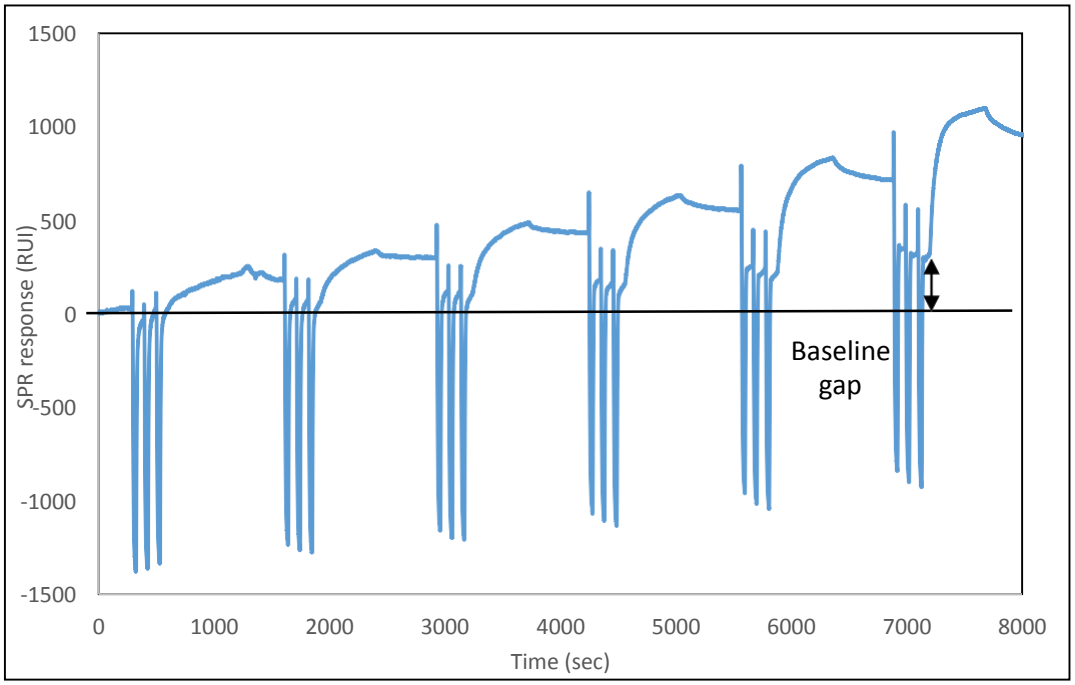

Figure 8.1.3 SPR sensorgram illustrating several cycles of Cyt C injection (0.15, 0.3, 0.6, 1.2, 2.5, 5 μM) and using SDS as regeneration molecule. The baseline gap has now decreased from 686 RUI (figure 8.1.1) to 314 RUI.

After the first series of experiments, it was believed that the imperfections in the SAM were still too crucial in the interactions between the surface and the protein. To minimise this problem, an additional step was introduced before using the chips on the SPR. The chips were incubated in a solution of 2-mercaptoethanol 1 mM for 2 hours to fill up the bare gold spaces (fig 8.1.4).

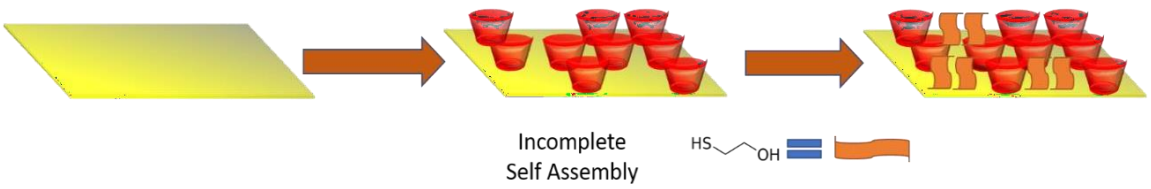

Figure 8.1.4 Diagram of the self-assembly of the spacer for the minimisation of layer imperfection. In the second step, the 2-mercaptoethanol is used in order to cover possible imperfections given by the first self-assembly of the cyclodextrin on the surface.

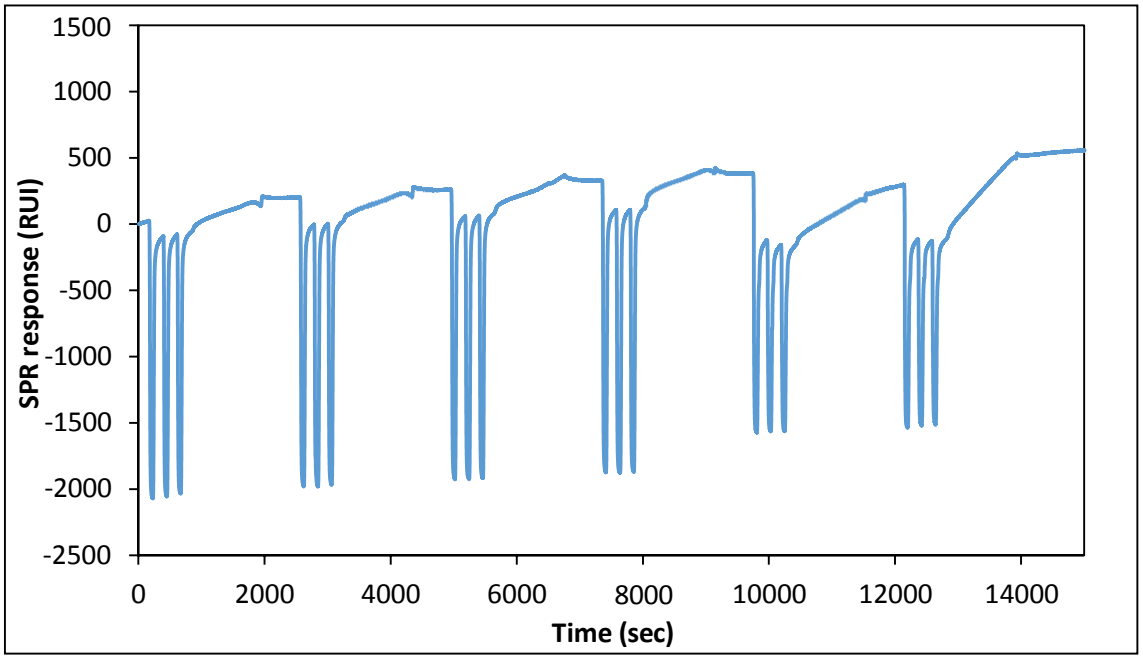

Figure 8.1.5 SPR sensorgram illustrating several cycles of Cyt C injection (0.15, 0.3, 0.6, 1.2, 2.5, 5 μM) and regeneration after the addition of the spacer.

In case of only cyclodextrin contribution in the interaction, we should observe an initial exponential growth of the signal followed by a plateau. The plateau indicates that the surface is saturated and no more signal growth can be observed by increasing the concentration. However, the protein signals in the figure 8.1.5 present a linear growth in compared to the protein curves in fig 8.1.3, and major concentration of protein is needed to reach a saturation point. This was due as the spacer is not inert and now plays an essential role during the SPR experiment. By not letting the protein anymore to be retained on the surface with a specific bond, now the saturation point and the plateau are much more difficult to reach as the spacer play an even more prominent role than the cyclodextrin cavity. The sensorgram, in this case, showed a decrease in affinity for the surface-protein system. By considering this scenario, the spacer was not further explored as a viable way to fill up the potential imperfections on the surface.

Another possibility to improve the general surface performance was to explore other buffers. The phosphate buffer was changed to the 2-(N-morpholino)ethanesulfonic acid (MES) buffer as proved to be suitable for SPR experiments[364].

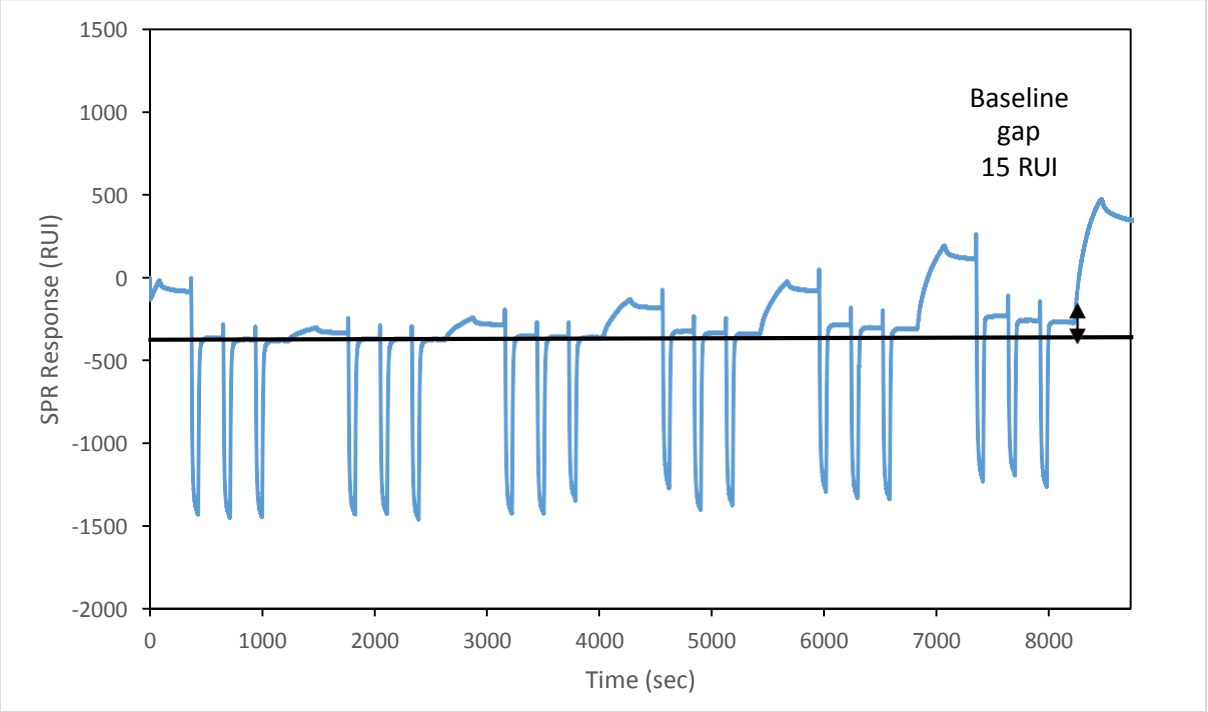

Figure 8.1.6 SPR sensorgram illustrating several cycles of Cyt C injection (0.15, 0.3, 0.6, 1.2, 2.5, 5 μM) under the MES buffer with an improved baseline gap of 15 RUI.

The baseline gap dropped to 15 RUI after six injections, indicating that the MES buffer was performing better than PBS for the overall outcome of the experiments. This condition was applied to the other proteins investigated in this study.

Once we adjusted the best conditions for our proteins, we were capable of extrapolating the SPR curves. Again as for XPS, contact angle and ellipsometry, the β-CD–(SH)7 surfaces were compared with the TGP. For the preparation of the glucose-terminated SAMs, the clean gold substrates were immersed for 24h in 1 mM DMF solutions of 6-thio-D-glucopyranose. Subsequently, the gold substrates were rinsed with

DMF and UHQ water and dried under an argon flow. The formation of the CD inclusion complexes with hydrophobic amino acids on the protein's surface has a significant contribution to the SPR response, and other non-covalent interactions, such as hydrogen bonding, between the protein and the CD glucose units, also play a role. This effect has been demonstrated by creating a gold-tethered SAM of glucose moieties and conducting SPR analysis upon exposure to the different proteins. CDs are comprised of glucose monomers, and thus the glucose-terminated SAM embodies similar functionalities at the interface but where the apolar cavity is not present. All the proteins bind to the glucose-terminated SAMs even if the SPR response is significantly lower than that seen for the β-CD–(SH)7 SAMs.

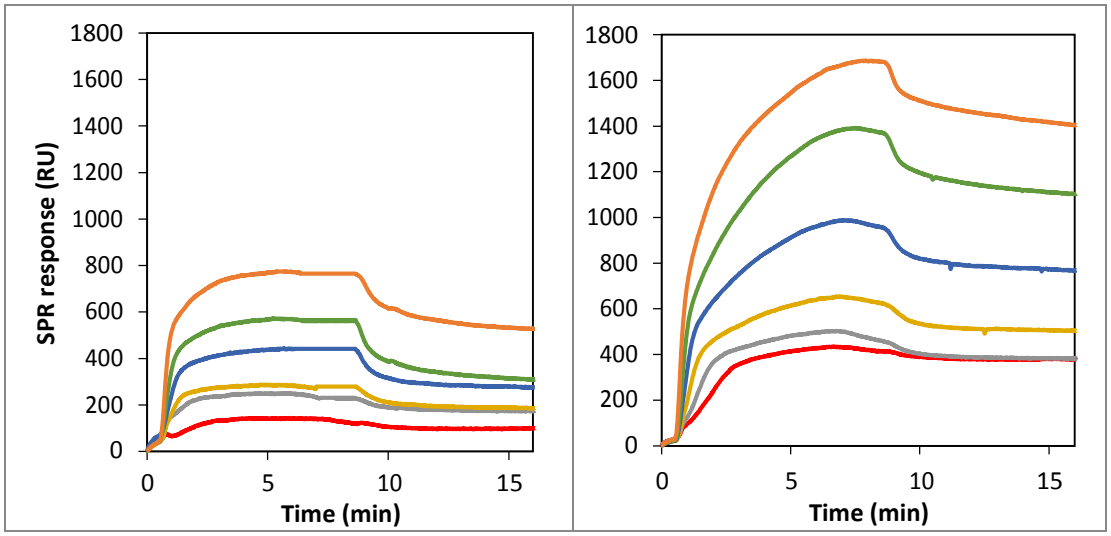

Figure 8.1.7 Cytochrome C comparation response with TGP SAM(left) and with β-CD–(SH)7 SAM (right). Experiment concentrations 20 μM (orange), 10 μM (green), 5 μM (blue), 2.5 μM (yellow), 1.25 μM (grey), 0.6 μM (red).

From the experiment with cytochrome C, it is visible a remarkable improvement on the protein-surface affinity, due to increased response for the curves with the same concentration. The increased response was observed in both association and dissociation phase.

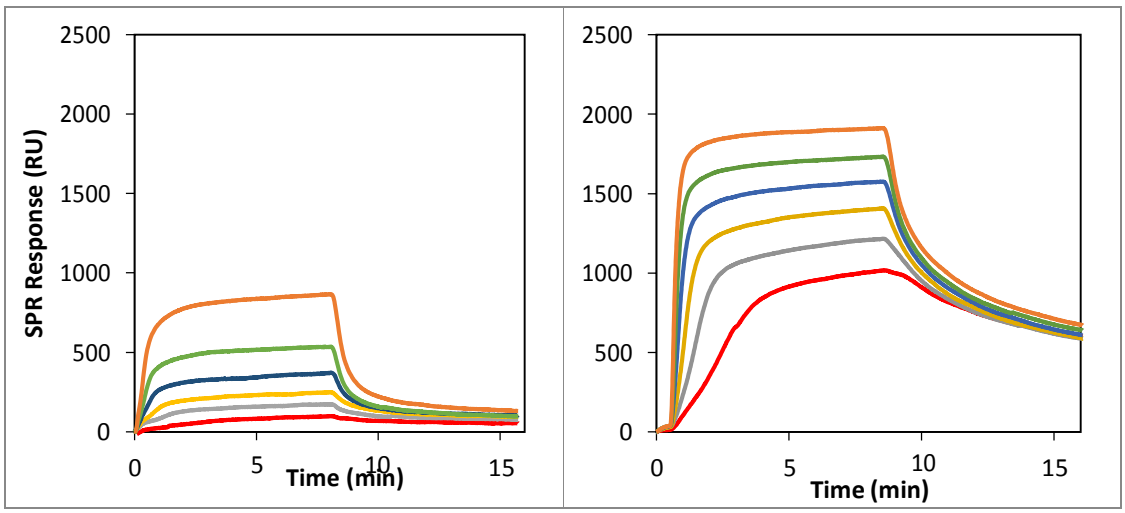

Figure 8.1.8 Chymotrypsin comparison response between TGP SAM(left) and with β-CD–(SH)7 SAM (right). Experiment concentrations 20 μM (orange), 10 μM (green), 5 μM (blue), 2.5 μM (yellow), 1.25 μM (grey), 0.6 μM (red).

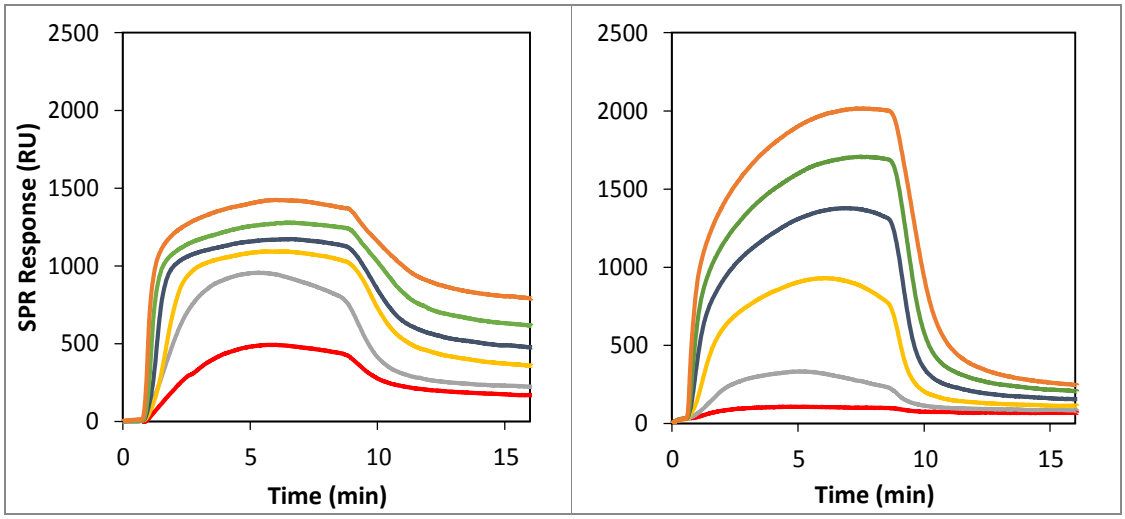

Figure 8.1.9 RNase A comparation response between TGP SAM (left) and with β-CD–(SH)7 SAM (right). Experiment concentrations 20 μM (orange), 10 μM (green), 5 μM (blue), 2.5 μM (yellow), 1.25 μM (grey), 0.6 μM (red).

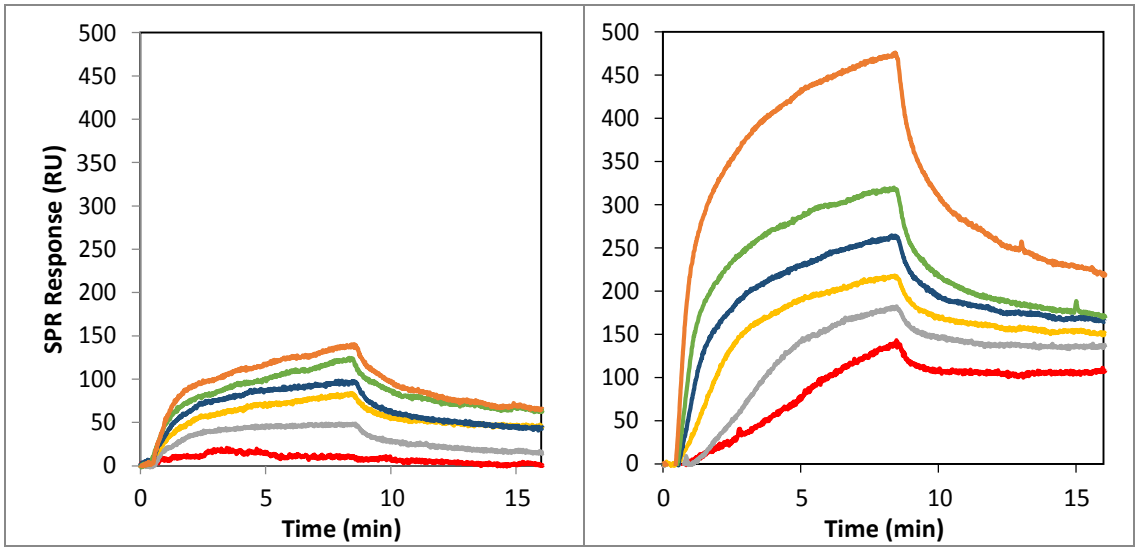

Figure 8.1.10 Insulin comparation response between TGP SAM(left) and with β-CD–(SH)7 SAM (right). Experiment concentrations 5 μM (orange), 2.5 μM (green), 1.25 μM (blue), 0.6 μM (yellow), 0.3 μM (grey), 0.15 μM (red).

Protein immobilisation studies using SPR demonstrate the assembly of the chymotrypsin, insulin, RNase A and cytochrome C proteins on the β-CD–$(SH)_7$ SAMs. The binding properties are dependent on the protein characteristics, but all proteins bound to the functionalized surfaces with high nanomolar/low micromolar dissociation constants (K_{Ds}) as shown in Table 2.

The K_{Ds} were calculated based on the SPR responses at equilibrium (R_{eq}), which were plotted against the concentration of injected protein (C_p) and fitted to a 1:1 steady-state affinity model. The model utilises a nonlinear least-squares regression method to fit data to the Langmuir adsorption isotherm (Equation 2). The equation not only allows calculating K_D but also the surface saturation response, R_{max}.

Table 2. SPR-derived K_D values for the interaction between the 1 mM β-CD–$(SH)_7$ SAM and the different proteins and protein binding capacity of the surface.

Protein	K_D (μM)	Protein binding capacity (ng/nm^2)
Chymotrypsin	0.63 ± 0.20	1.93
Insulin	0.82 ± 0.35	0.55
RNase A	1.12 ± 1.04	1.48
Cytochrome C	3.21 ± 0.90	1.78

$$R_{eq} = \left(\frac{C_p}{C_p + K_D}\right) R_{max} \qquad (2)$$

The interaction between a single CD and a hydrophobic ligand on the surface of a protein is weak, with K_{Ds} lying in the mM range.[23] Thus, the recognition events occurring between the studied proteins and the CD–$(SH)_7$ SAMs are characterised by multiple interactions acting simultaneously, affording more than 1000-fold increase in affinity. Chymotrypsin, insulin and RNase A display, within the error, comparable binding affinities, while cytochrome C binds to the surface with the lowest affinity (K_D=3.21 μM). The lowest affinity obtained for cytochrome C might be associated with the lowest surface percentage

of hydrophobic amino acids in this protein (insulin 25.5%; RNase A 19.9%; chymotrypsin 19.0%; cytochrome C 15.6%). However, other parameters, which can include type, orientation and accessibility of hydrophobic amino acids at the protein surface, might play a role in the overall affinity obtained.

As anticipated, the SPR response for the β-CD–(SH)7 SAMs and the different proteins is dependent on the molecular protein weight (Mw), with the lower Mw insulin displaying the lowest response. By considering R_{max} and that 100 response units (RUs) are equivalent to 0.1 ng/mm^2 [38-39], the maximum protein binding capacity of the β-CD–(SH)7 SAM can be determined. As illustrated in Table 2, the β-CD–(SH)7 SAM possess a high capacity for protein binding with protein densities ranging from ~0.5 ng/mm^2 to ~2 ng/nm^2, which are mainly dependent on the protein Mw.

Moreover, due to the noncovalent nature of the CD–amino acid interactions, the captured proteins could be quickly released from the surface by exposure to sodium dodecyl sulfate (SDS). The sodium dodecyl sulphate is a surfactant capable of interacting with the cavity of the cyclodextrin weakly, but strong enough to remove any other hydrophobic moieties inside the cavity[365]. This makes the sodium dodecyl sulphate perfect for regenerating cyclodextrin cavities already occupied, and this "use-regenerate" cycle could be repeated multiple times with the minimal loss of binding capability. (Figure 8.1.12)

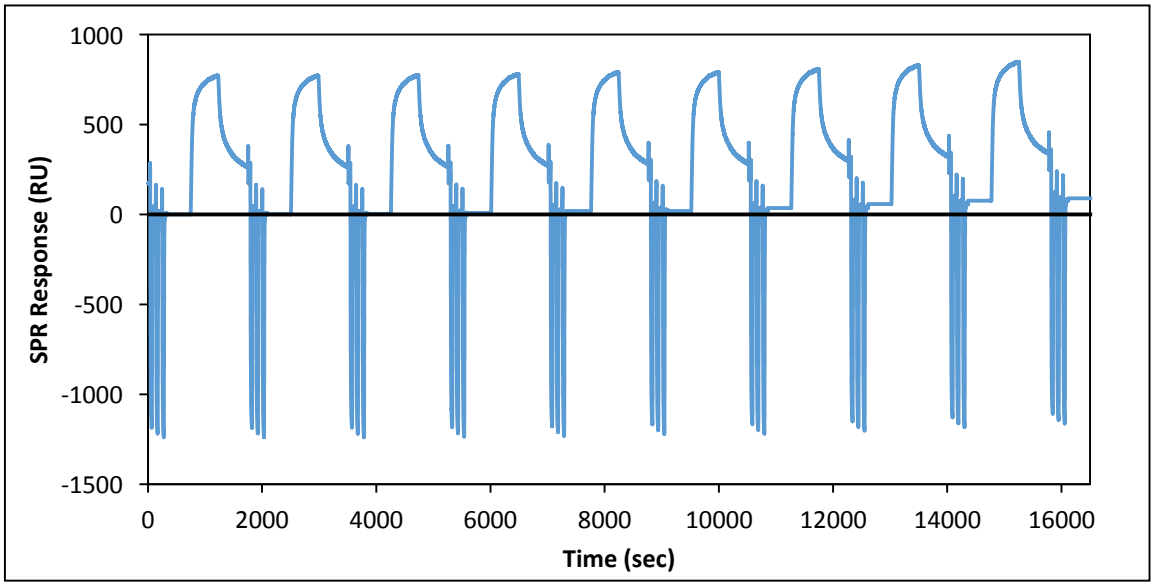

Figure 8.1.12. SPR responses from 9 SPR cycles that were performed using 2.5 μM Chymotrypsin PBS solution on 1 mM 24 h β-CD–(SH)7 SAMs, with three cycles of regeneration.

To further demonstrate the effect and the importance of the β-CD–(SH)7 SAM for protein immobilisation, similar experiments were performed on clean gold surfaces, i.e. non-functionalised surfaces. The gold substrates were immersed in a piranha solution for 8 minutes and rinsed with alcohol and straightway analysed on the SPR. For the protein injection, a concentration of 2.5 μM for each protein was chosen and compared with the ones that were carried on a β-CD–(SH)7 SAM.

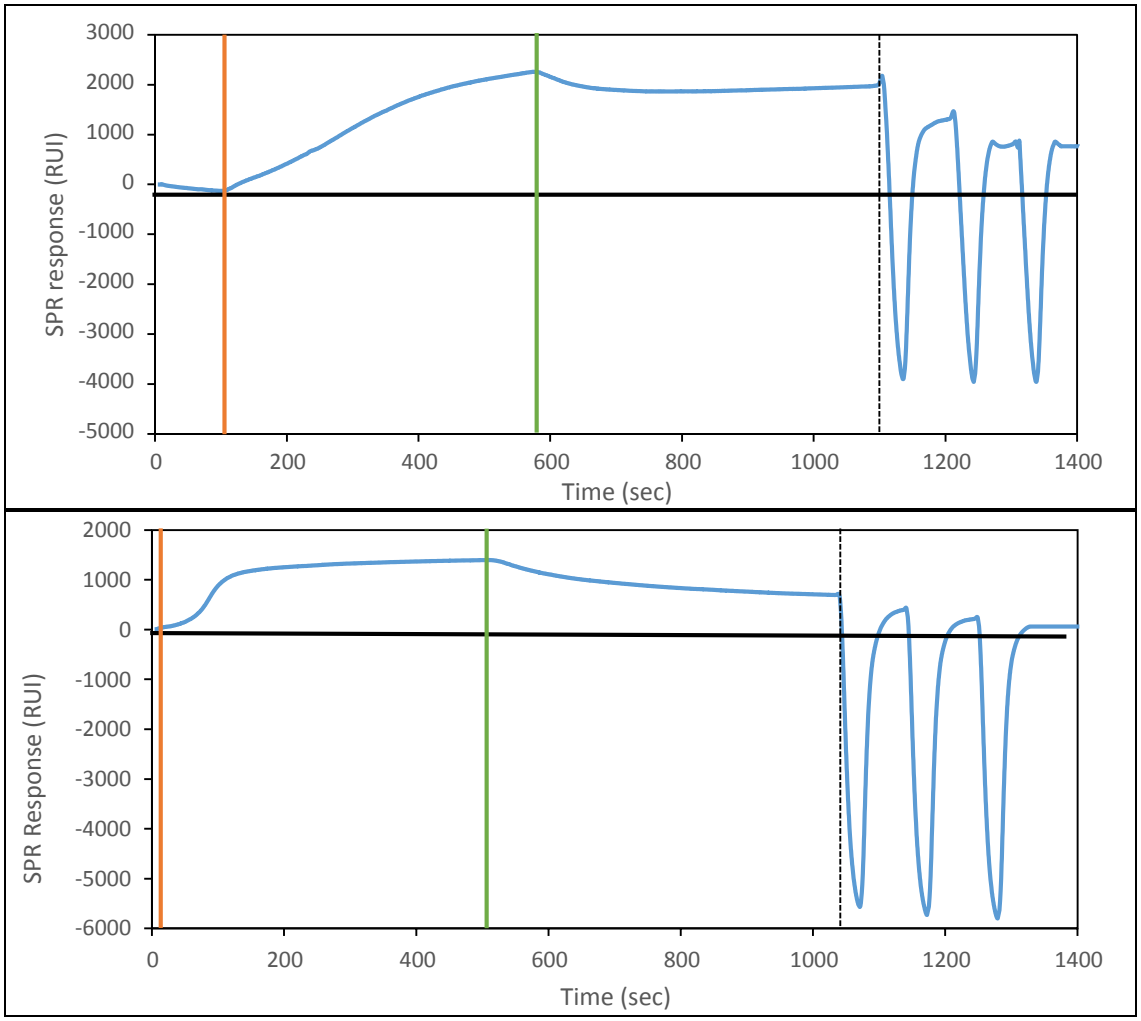

Figure 8.1.13 Injection of 2.5 μM of α-chymotrypsin on bare gold (up) and β-CD–(SH)7 SAM (bottom). Both experiments lasted 1400 seconds in which there was a single injection of α-chymotrypsin followed by three regeneration steps with SDS 10 mM. The black line indicates the baseline. The SPR experiments include three major steps: protein injection (orange line), rinsing (green line), regeneration (dotted line).

As the bare surface presents a high hydrophobicity, the protein tends to denaturate, meaning that also other protein parts start to interact with the surface[104,105,122]. It induces an increase in the SPR response when compared to the CD SAM surface. This interaction also seems more challenging to disrupt as the protein is not easily removed from the surface compared with the CD SAM surfaces (Fig. 8.1.13, 8.1.14, 8.1.15 and 8.1.16). The

injection signal on bare gold resulted in higher intensity when compared to the CD SAM. This fact, together with the impossibility to restore the surface, indicates a non-specific interaction between any protein analysed and the bare gold.

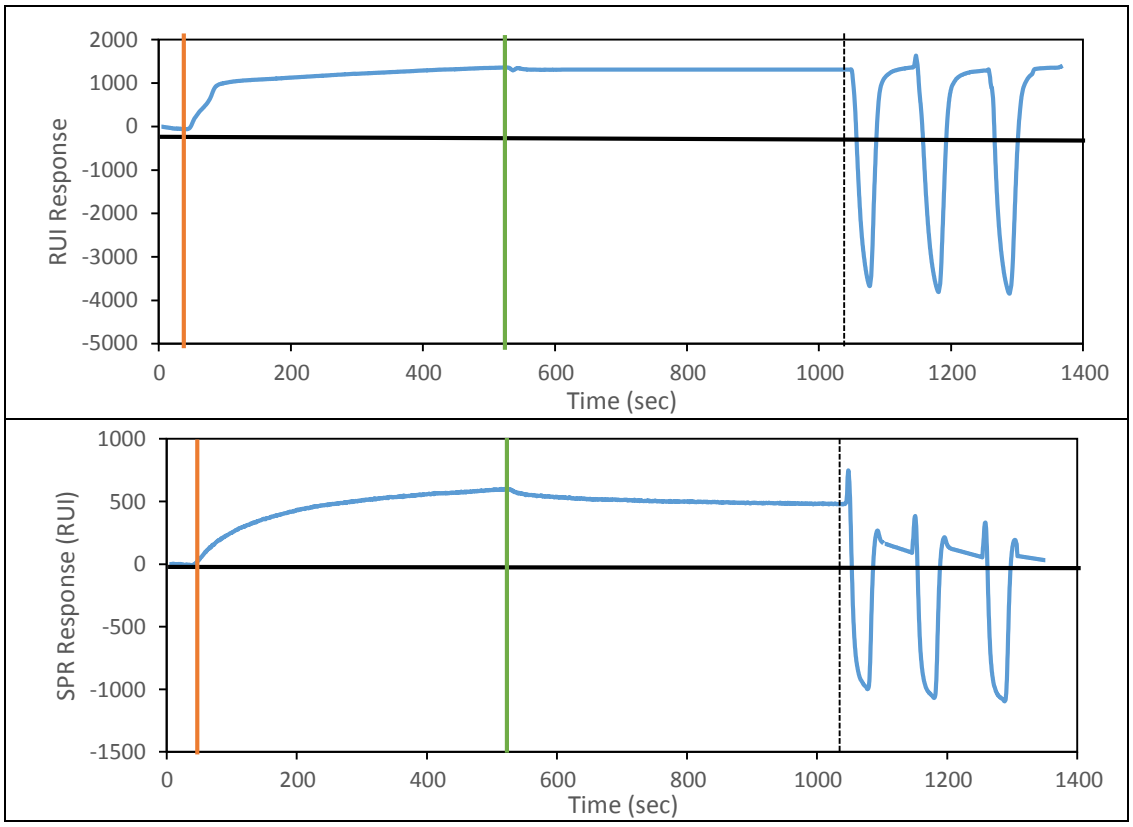

Figure 8.1.14 Injection of 2.5 μM of Cytochrome C on bare gold (up) and β-CD–(SH)7 SAM (bottom) The black line indicates the baseline. The SPR experiments include three major steps: protein injection (orange line), rinsing (green line), regeneration (dotted line).

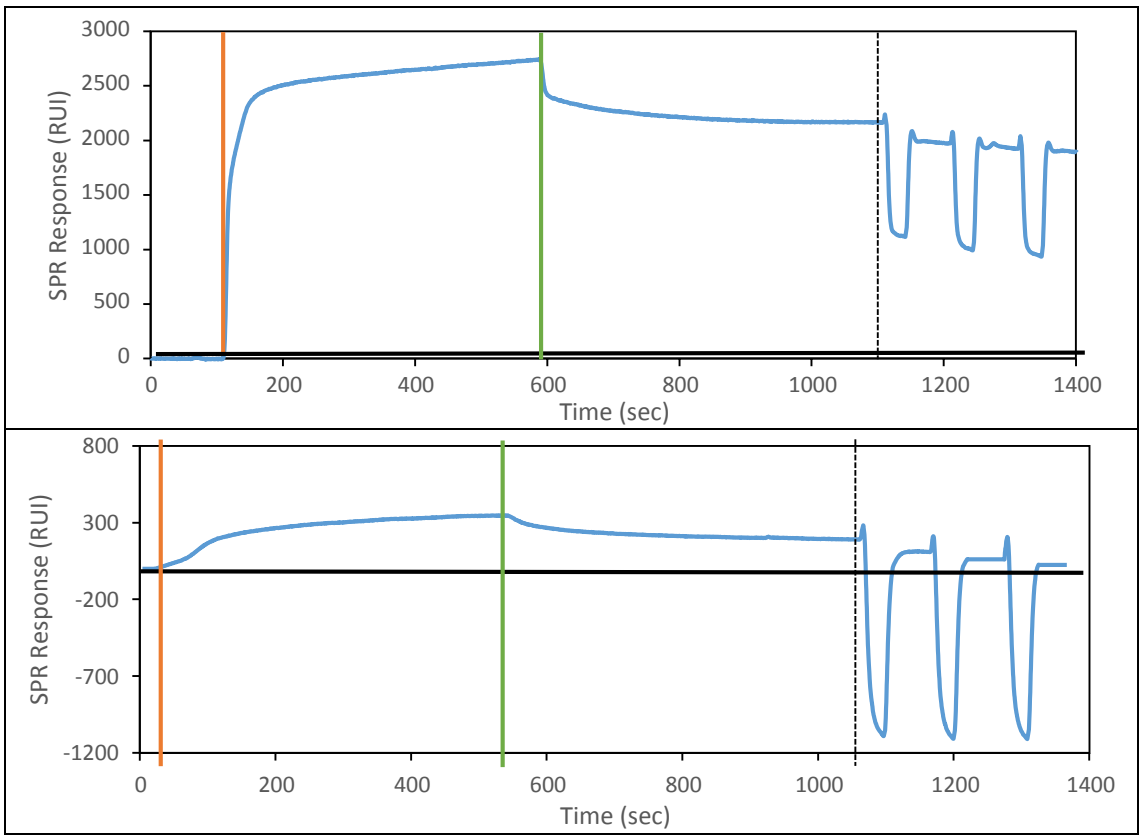

Figure 8.1.15 SPR sensorgram of 2.5 µM of Insulin on bare gold (up) and β-CD–(SH)7 SAM (bottom). For the Insulin on bare gold again, the SPR response was increased and the regeneration impossible. The black line indicates the baseline. Three steps can be noticed: protein injection (orange line), rinsing (green line), regeneration (dotted line).

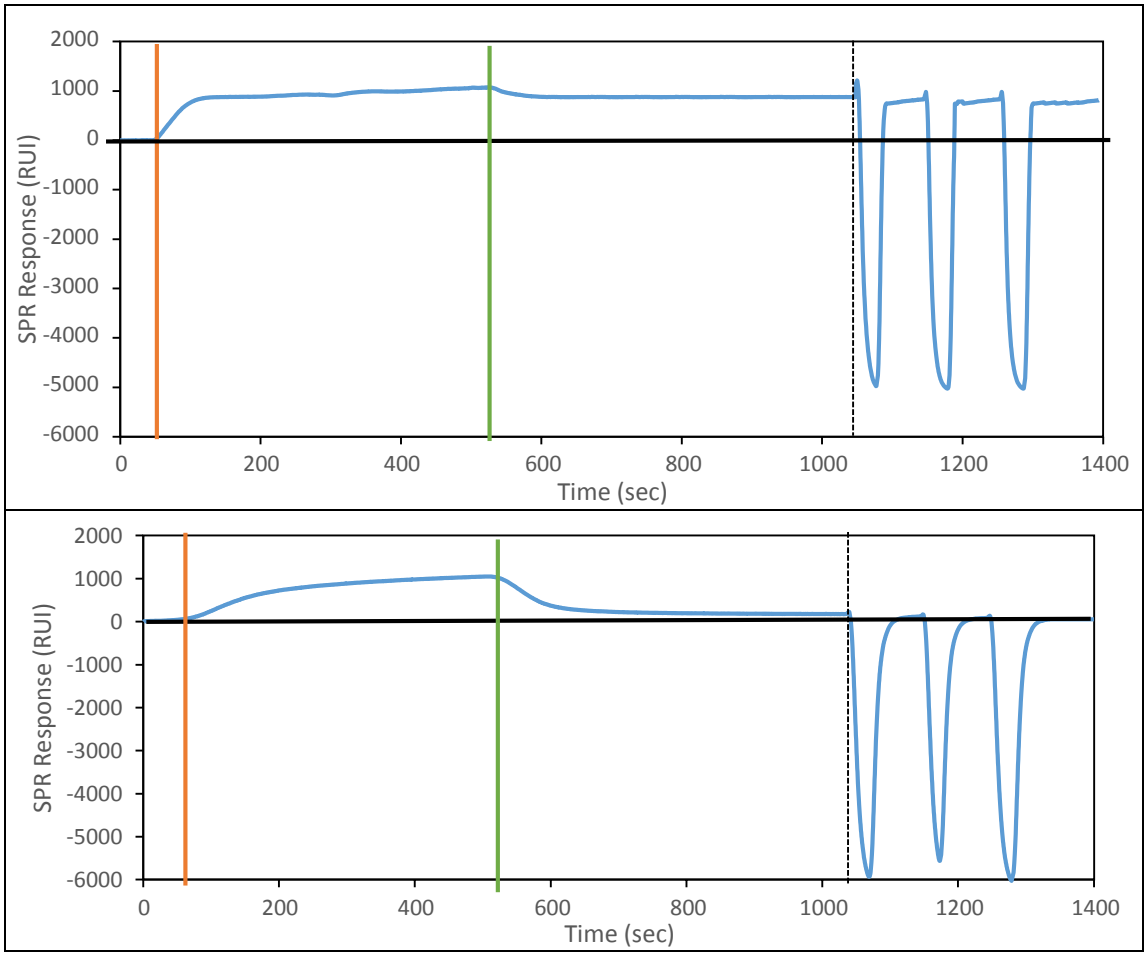

Figure 8.1.16 Injection of 2.5 μM of RNase on bare gold(up) and β-CD–(SH)7 SAM (bottom). The black line indicates the baseline. Three steps can be noticed: protein injection (orange line), rinsing (green line), regeneration (dotted line).

For these SPR experiments we were capable to finally have a better understanding between the surface and the protein. SPR experiments performed with TGP SAM and with β-CD–(SH)7 SAM highlight the fact that the cavity plays an essential role in the interaction surface-protein. In some cases the SPR signal increased twice for the experiments using the β-CD–(SH)7 SAM. Later on, another control experiment was performed using the bare gold as surface with no SAM functionalising it, To further demonstrate the effect and the importance of the β-CD–(SH)7 SAM for protein

immobilisation. The signal appears to be higher than any experiment conducted with the SPR. This is since any group of the protein is interaction with the surface (not only the hydrophobic side chains) and the unspecific bonding such as (hydrogen bonding and dipole-dipole interaction are the main interaction for this kind experiments. On the contrary the use of β-CD–(SH)7 SAM allows us to have specific bonding by aiming only to hydrophobic side chains, allowing us to have a strong interaction without any protein denaturation.

8.2 The TOF-SIMS analysis

The TOF-SIMS experiment was performed by Dr David J. Scurr and Anna M. Kotowska, School of Pharmacy, University of Nottingham.

TOF-SIMS studies were conducted to understand whether the β-CD–(SH)7 SAM can induce a particular protein orientation on the surface. Static TOF-SIMS, which allows analysing the outermost 2 nm of the surface with high chemical specificity, has been previously used[366,367] to investigate the identity and orientation of surface-tethered proteins and a similar strategy was employed herein.

Cytochrome C, which contains a rigid porphyrin ring coordinated with a single iron atom, was used as the model protein to be studied by TOF-SIMS. The SAM fabricated by incubation of a 1 mM solution of β-CD–(SH)7 for 24 hours was exposed to a 1 mM cytochrome C solution in PBS for 2 hours and subsequently rinsed in UHQ water. As a control, glucose-terminated SAMs were also exposed to identic cytochrome C incubation conditions. As further controls, TOF-SIMS analysis was also performed on bare gold and both β-CD–(SH)7 and glucose-terminated (TGP) SAMs (Figure 8.2.1).

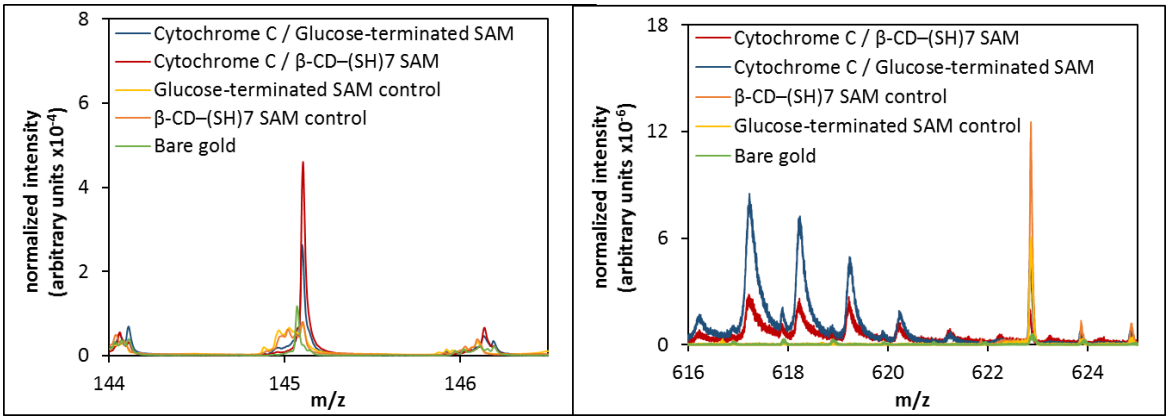

Figure 8.2.1. Overlay of spectra showing glucose-terminated SAMs and β-CD–(SH)7 SAMs with and without protein and bare gold samples. Regions of spectra focused on a) $C_5H_9N_2O_3^+$ and b)$C_{34}H_{33}N_4O_4Fe^+$ peaks and show no advantageous contaminations from SAM layer.

Since two types of chips, cytochrome C on glucose-terminated SAMs and cytochrome C on β-CD–(SH)7 SAMs, have the same overall chemical composition, statistical analysis was required to identify more subtle differences between samples. Variance patterns within the TOF-SIMS secondary ion peak intensities between cytochrome C on the β-CD–(SH)7 SAM and the glucose-terminated SAM were analysed by multivariate analysis to understand if differences in protein orientation could be inferred[368,369]. The TOF-SIMS relative ion intensities for cytochrome C on a β-CD–(SH)7 SAM and cytochrome C on a glucose-terminated SAM are significantly different from each other (Figure 8.2.2) meaning that proteins are immobilised in two different way. To obtain more detailed information about protein orientation, the distinctive iron-porphyrin fragment ($C_{34}H_{33}N_4O_4Fe^+$, 617.27 m/z) of cytochrome C was examined on both surfaces (Figure 8.2.3).

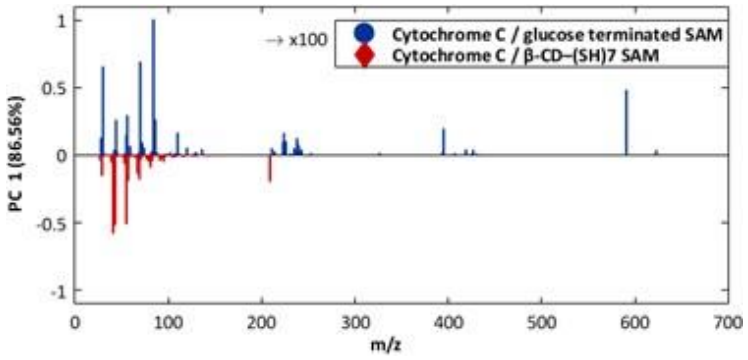

Figure 8.2.2. TOF-SIMS spectra of the Cyt C on a β-CD–(SH)7 SAM(red) and on glucose terminated SAM (blue). The different patterns between the two SAMs indicate a difference in orientation of the protein on the surface.

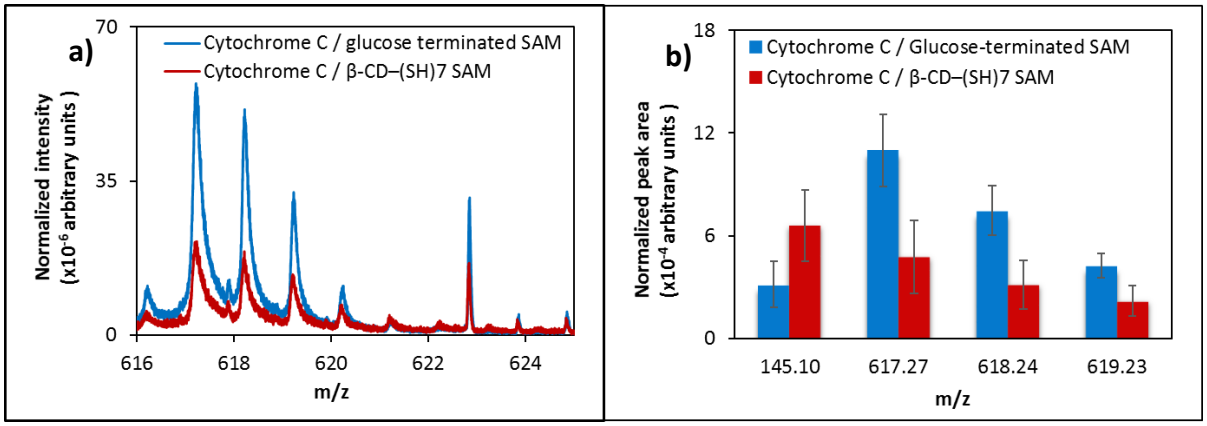

Figure 8.2.3. (a) Pattern peak intensities for cytochrome C iron-porphyrin fragment, wherein the protein has been immobilised on either a glucose-terminated SAM or a β-CD–(SH)7 SAM. (b) Peak areas are normalised to total ion count. Each bar shows the peak area average of 12 measurements and standard deviation within the sample set.

The ion intensity of the iron-porphyrin (Mw = 618 Da) in both protein surfaces are remarkably different, with a lower ion intensity for the protein immobilised on the β-CD–(SH)7 functionalized SAM (Figure 8.2.3 a). As static TOF-SIMS collects chemical information from outermost 2 nm of the surface, these results indicate that on the β-CD–

(SH)7 functionalized SAM, the cytochrome C prevalently adopts an orientation with the porphyrin ring pointing down towards the CD molecules and less available to the primary ion beam. On the glucose-terminated SAMs, the cytochrome C porphyrin ring is more exposed to the analytical probe, resulting in higher peak intensity. To support this hypothesis, other distinct fragments of cytochrome C were calculated using the following table from a previous study[366].

Table 3 The fragments signal list used to interpret the TOF-SIMS data. The table was taken from reference[366].

number	m/z	Possible fragment	Possible fragment origin
1	30.035045	CH_4N+	G
2	44.011967	CH_2NO+	N
3	44.05002	C_2H_6N+	A
4	44.977484	CHS+	C
5	56.052034	C_3H_6N+	K
6	59.048265	CH_5N_3+	R
8	61.00994	C_2H_5S+	M
9	68.050638	C_4H_6N+	P
11	70.026859	C_3H_4NO+	N
12	70.067311	C_4H_8N+	R
13	71.008958	C_3H_3O_2+	S
14	72.043131	C_3H_6NO+	A
15	72.080382	C_4H_10N+	V
16	74.058291	C_3H_8NO+	T
17	76.01996	C_2H_6SN+	C
18	81.034538	C_4H_5N_2+	H
19	83.047355	C_5H_7O+	V
20	84.039661	C_4H_6NO+	E/Q
21	84.084236	C_5H_10N+	I, L, K
22	86.098747	C_5H_12N+	I, L
23	87.050386	C_3H_7N_2O+	N
24	88.037913	C_3H_6NO_2+	D
25	98.019202	C_4H_4NO_2+	N
26	100.081987	C_4H_10N_3+	R
27	102.053314	C_4H_8NO_2+	E
28	107.044322	C_7H_7O+	T
29	110.074632	C_5H_8N_3+	H
30	120.07827	C_8H_10N+	F
31	130.05619	C_9H_8N+	W
32	136.074878	C_8H_10NO+	T
33	145.093772	C_10H_11N+	W
34	159.080828	C_10H_11N_2+	W
35	170.061642	C_11H_8NO+	W

We focused on the signal at 145.10 m/z ($C_5H_9N_2O_3^+$), as a different behaviour was observed during the analysis on both glucose-terminated and β-CD–(SH)7 SAMs as the

peak is in this case is higher in the β-CD–(SH)7 SAMs (Figure 8.2.3 b). Following the table 3, the signal could correspond to tryptophan (W). However, it did not correspond to what we found (Figure 8.2.4) as if the signal at 145 is the tryptophan, also the signals at 159 and 170 should have the same behaviour as they are fragments coming from the same molecule.

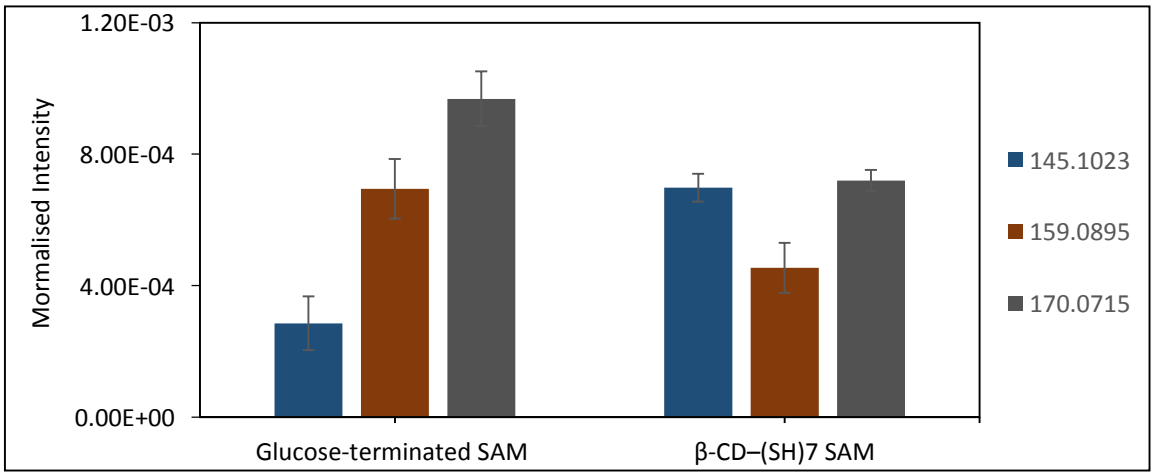

Figure 8.2.4 signals from Glucose-terminated SAM and β-CD–(SH)7 SAM.

It was clear from the beginning that something else was influencing the signal at 145.10, as 145.10 should have the same trends as 159.08 and 170.07 m/z in both SAM samples. It was supposed that a dimer or even a trimer of amino acids should influence the analysis. Through combinatorial calculus of all the amino-acids with the peptide fragmentation calculator, it was discovered that the signal at 145.10 can also indicate the Gly1-Asp2 residue at the beginning of the amino-acid chain of the cytochrome C (Figure 8.2.5), which is located at the opposite side of the cytochrome C compared to the porphyrin ring (Figure 8.2.6). In this case, the trend in both protein surfaces is inverted, with a higher ion intensity for the protein immobilised on the β-CD–(SH)7 SAM (Figure 8.2.3b). This suggests that the CD cavities in the β-CD–(SH)7 functionalized SAM are capable of inducing a defined protein orientation, which is different from that caused by other non-covalent interactions as in the case of the glucose-terminated SAM. There is the

likelihood that, this orientation is dictated by the position of the hydrophobic amino acids on the protein surface that can form stronger interactions with the surface-tethered CDs.

10 20 30

GDVEKGKKIF VQKCAQCHTV EKGGKHKTGP

40 50 60

NLHGLFGRKT GQAPGFTYTD ANKNKGITWK

70 80 90

EETLMEYLEN PKKYIPGTKM IFAGIKKKTE

100 104

REDLIAYLKK ATNE

Figure 8.2.5 The amino acid sequence of Horse heart Cytochrome C. The dimer analysed (145.10 m/z) is underlined (orange).

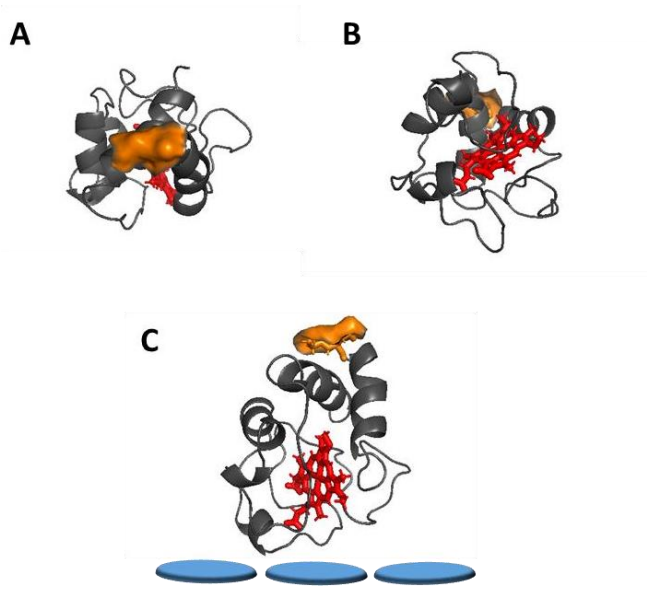

Figure 8.2.6 The possible orientation of the Cytochrome C. The section of the protein facing up (A), facing down (B) and a lateral section (C). The dimer Gly1-Asp2 is represented in orange. The porphyrin is represented in red. The blue circles indicate the β-CD–(SH)7 cavities.

8.3 Conclusions

Herein, a surface molecular design was devised and developed that harnessed supramolecular chemistry to enable, for the first time, the construction of reversible, high-affinity protein assemblies on material surfaces solely through tailor-designed non-covalent interfaces. The simple approach does not require any protein modification process. While this study used gold-thiol SAMs, the methodology is sufficiently flexible to be applied to other substrate geometries (e.g. nanoparticles) and chemistries. Even though the exact binding properties and orientation of the protein on the CD-modified surface will always be dictated by the protein structure (i.e. unique distribution of hydrophobic groups on the surface of proteins), the strategy can be applied to a wide range of proteins, immobilize single or multiple proteins and provide high nanomolar to low micromolar dissociation constants.

Additionally, while the proteins are tightly bound to the surface due to the specific formation of inclusion complexes and multivalency, the CD-terminated surfaces can be readily addressed to regenerate the free CDs. Moreover, the surface can be reused for protein immobilisation post-regeneration. Considering all these attributes of broad applicability and versatility of CD-terminated surfaces to immobilise proteins, this work opens up unprecedented routes to develop advanced bioanalytic platforms, in which the stable, reversible protein layer can act to efficiently promote the catch and release of target cells or other biological entities for downstream analysis[370]. Furthermore, the stability and recyclability associated with the new protein immobilisation process provide a basis for meeting the demand for building re-usable biosensors and diagnostic devices[371].

9. The Synthesis of thioCucurbituril

9.1 The theoretical study of the complex Protein-Cucurbituril

After having functionalized the gold surface with cyclodextrin derivatives, we start exploring the idea to modulate the affinity of our surface towards the proteins, by changing the functional molecule during the self-assembly of our SAM. In another study[372], a supramolecular interaction of the cucurbituril (CB) with the amino acid in vapour phases, showed that the CB might complex with any amino acid but with high specificity for those amino acids having a positive side chain, due to an Ion-Dipole interaction. This effect is given by the high density of electron at the two scaffold entrances of the CB[373], giving to the molecule a high affinity for those molecule lacking in electrons such as a positive ion. The amino acids selected as attaching point for the CB molecule were Arginine and Lysine as they present a high affinity for cucurbiturils[372].

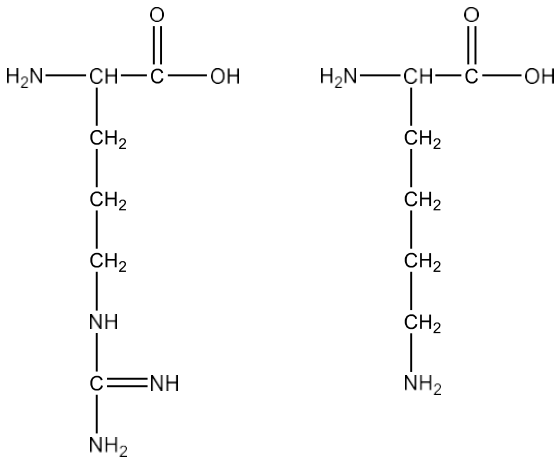

Figure 9.1 The Arginine (left) and Lysine (right) amino acids that interact strongly with the Cucurbituril. The bond is mostly given by the polarity of the amino group at the end of the side chain.

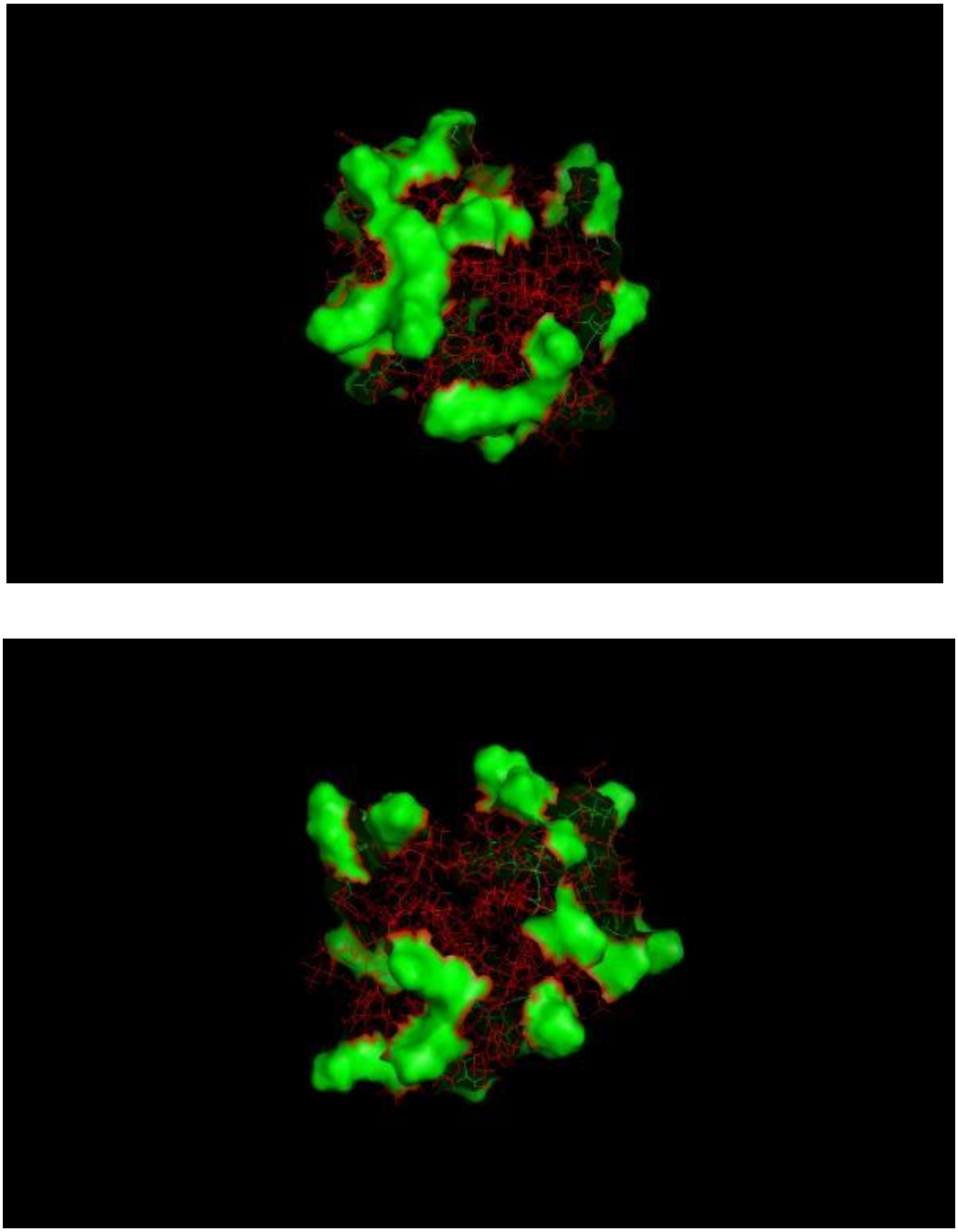

Figure 9.1.1 Cytochrome C and its possible attaching point with CB (green) 0°-180° (left) 180°-360° (right).

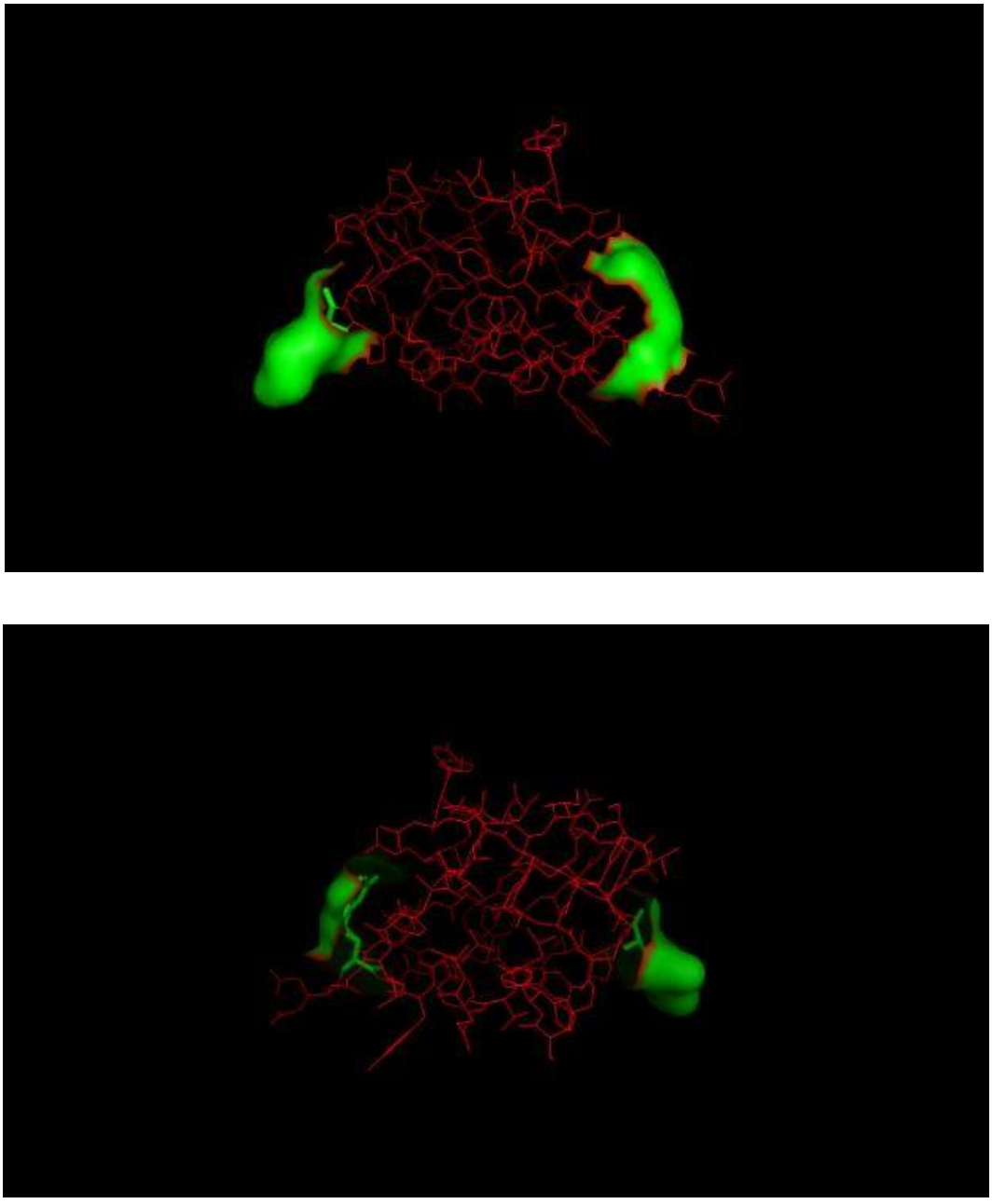

Figure 9.1.2 Insulin and its possible attaching point with CB (green) 0°-180° (left) 180°-360° (right).

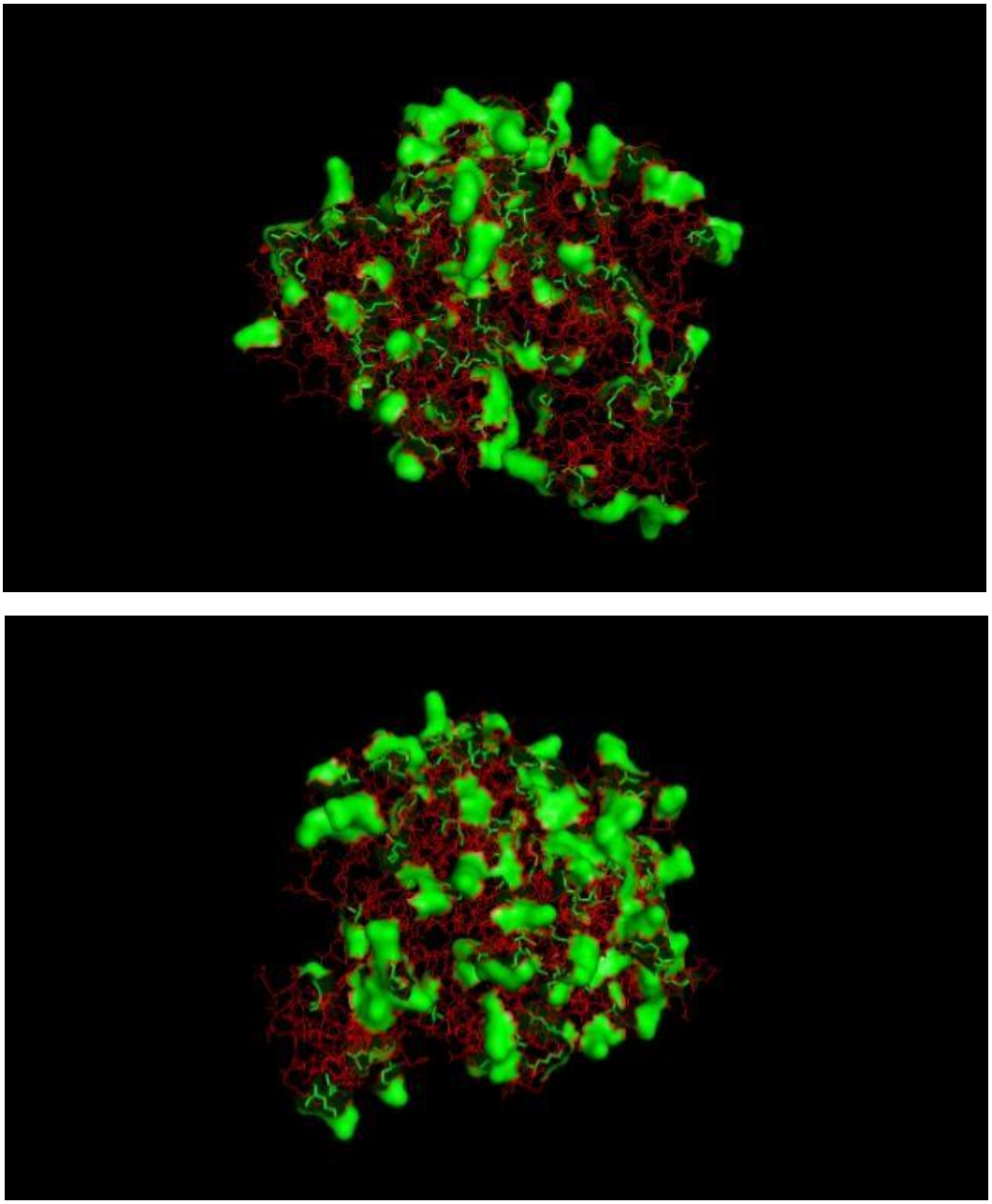

Figure 9.1.3 RNAase and its possible attaching point with CB (green) 0°-180° (left) 180°-360° (right).

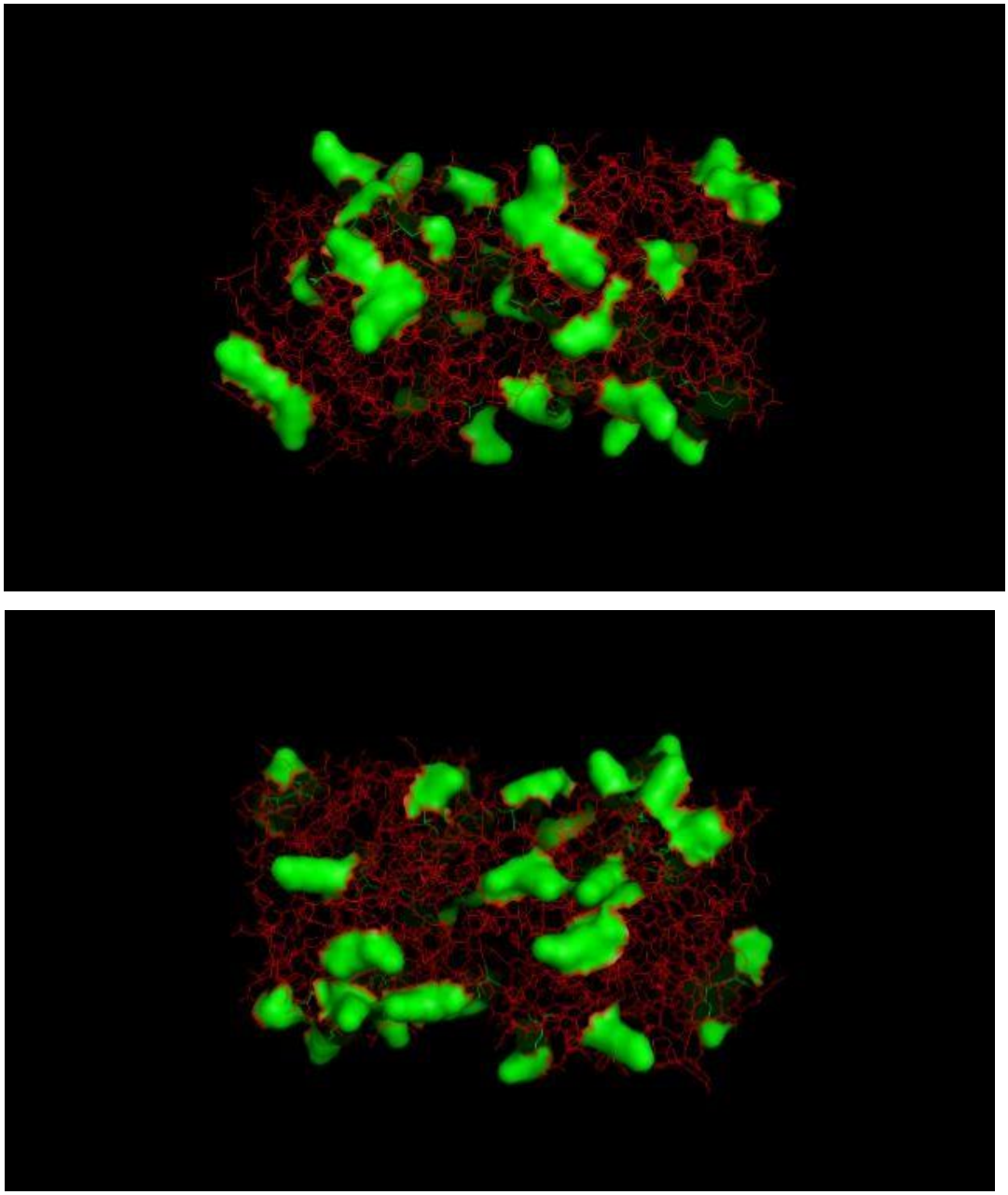

Figure 9.1.4 Chymotrypsin and its possible attaching point with CB (green) 0°-180° (left) 180°-360° (right).

9.2 *The traditional synthetic approach*

Since the cucurbituril structure was clarified in 1981, several approaches have been proposed for the synthesis of new cucurbiturils derivatives. Kim et al[374] expanded the field by synthesising and isolating cycles of 5,7 and 8 glycourils monomers. Other studies explored the idea of functionalizing the cycle in a different way, among them: cucurbiturils substituted on methylene bridge[375], hydroxyl addition[376], amino and phenyl functionalisation[377]. In our case, none of the functionalisation already proposed could be adapted to our purpose. They all propose a type of functionalisation that would not ensure our cucurbituril to assemble in the correct way on the surface, with the cavity facing up the surface (fig 9.2).

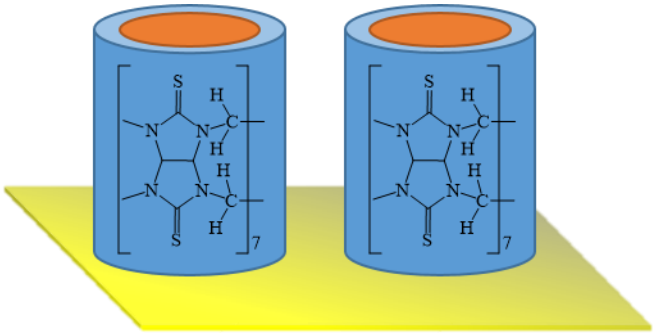

Figure 9.2 Ideal orientation of cucurbituril for this study. The cavity facing up will allow the protein to interact with it.

We designed a new type of cucurbituril, so-called thiocucurbituril, with a sulphur atom on the ring substituting the oxygen atom. To achieve this, we investigated the use of the universal cucurbituril synthesis[50] and replaced the urea (fig 9.2.1 compound 1) for the thiourea (fig. 9.2.2 compound 1). An equivalent of glyoxal was mixed with two equivalents of thiourea (fig 9.2.2 step 1) in tetrahydrofuran (THF) solution.

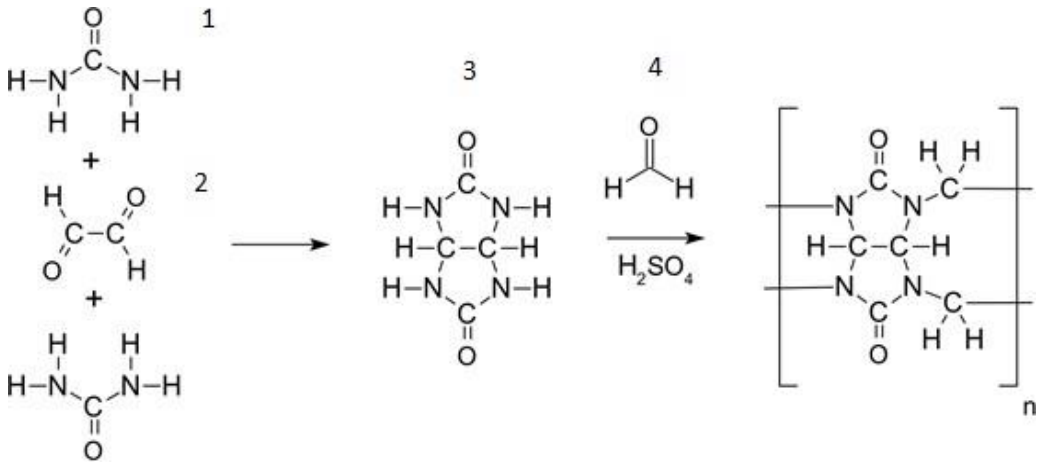

Figure 9.2.1 Common synthesis of cucurbiturils. Two ureas(1) are added to the Glyoxal (2) to form the glycouril (3). With a condensation reaction with formaldehyde (4) in the acidic condition, the ring is formed.

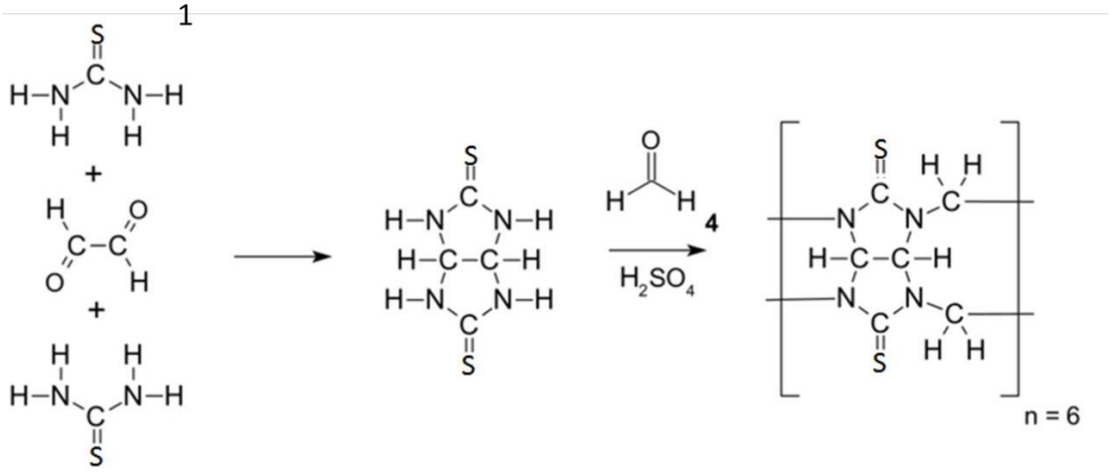

Figure 9.2.2 Proposed synthesis of thiocucurbiturils. Only the thiourea (1) has changed from the original synthesis of cucurbiturils.

The first thiourea addition determines the formation of a racemic solution (Fig 9.2.3 product 1) followed by a second thiourea addition forming, the monomer of the cucurbituril: the thiolglycouril (fig 9.2.3 product 2)

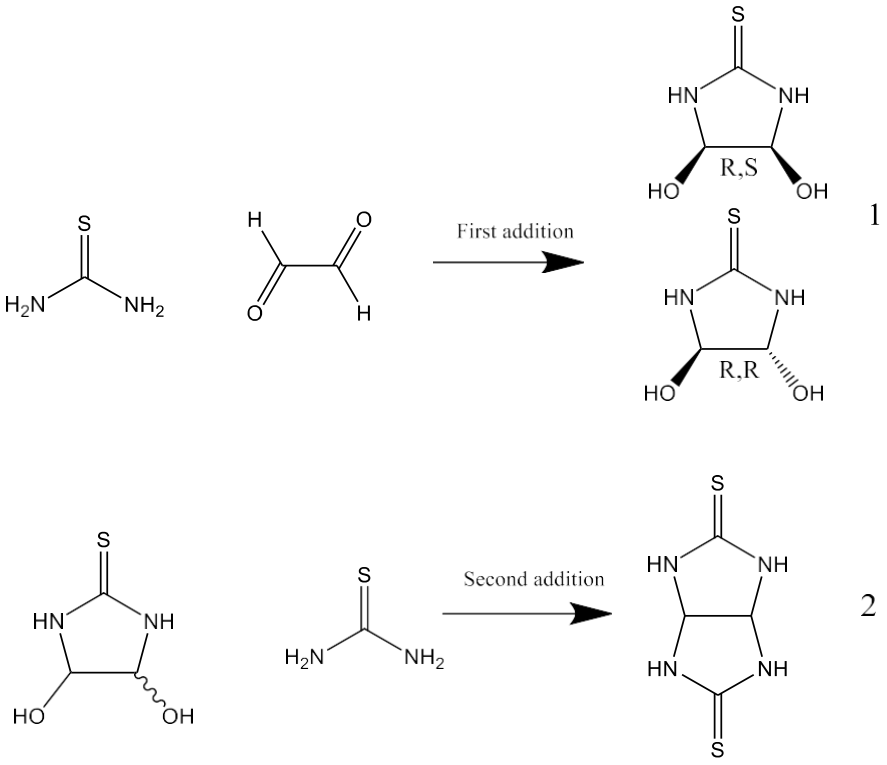

Figure 9.2.3 The first (1) and the second (2) addition in the first step of the synthesis of the thiocucurbituril. The first addition brings to the formation of a racemic solution (R, S) and (R, R). The second addition brings to the thioglycouril (2).

From the NMR spectra (fig 9.2.4) it is clear that only the first thiourea addition has occurred. A broad peak at 7.0 ppm indicates that there is still some thiourea non-reacting with the product. All the peaks indicated a high concentration of the 4,5-dihydroxy-2-thioketo-imidazole (DTI) in racemic solution (fig 9.2.3, first step). The reaction was left overnight to let the second thiourea addition to occurr and then precipitated with pure water. The mixture was then filtered, dried and then dissolved in deuterated chloroform for the NMR analysis. From the NMR spectra (fig 9.2.5) it was

clear that only the intermediary product was formed and that the subsequent addition of thiourea did not occur. The two spectra (fig 9.2.4 and 9.2.5) are similar and only the thiourea peak at 7.0 ppm has disappeared as results of the previous purification and precipitation.

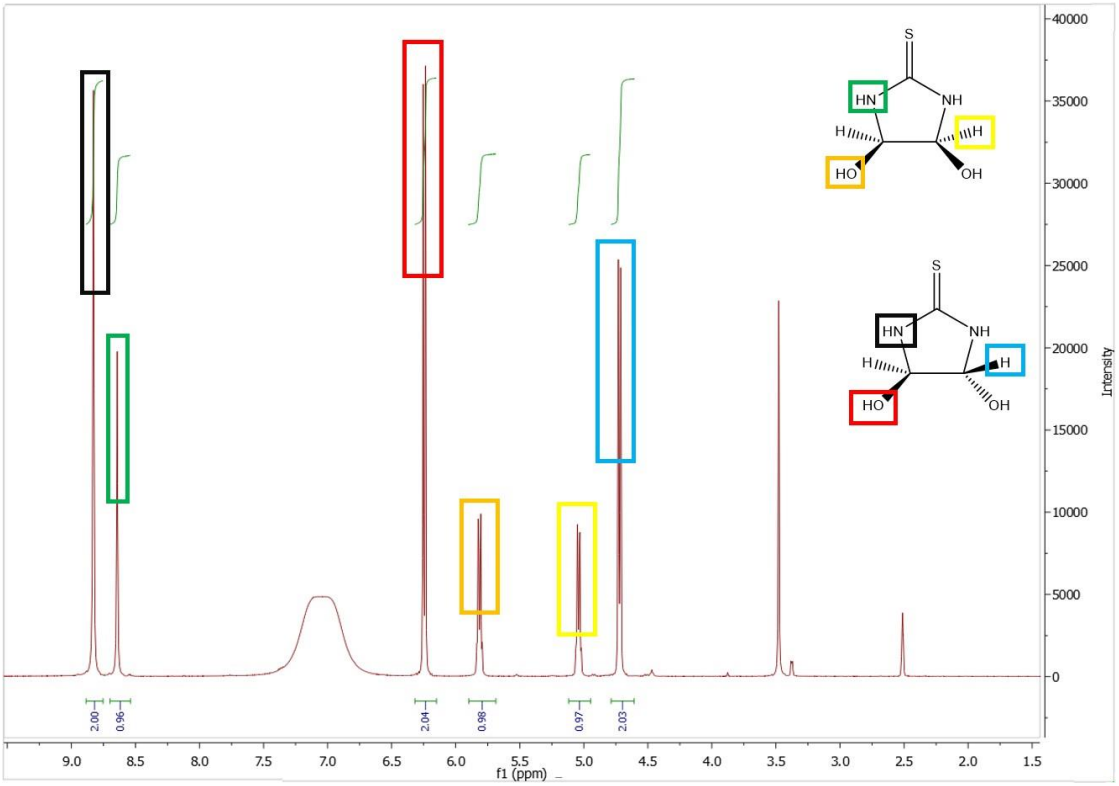

Figure 9.2.4 The NMR of the first step. Each peak is marketed with a coloured mark related to the hydrogen of the functional group.

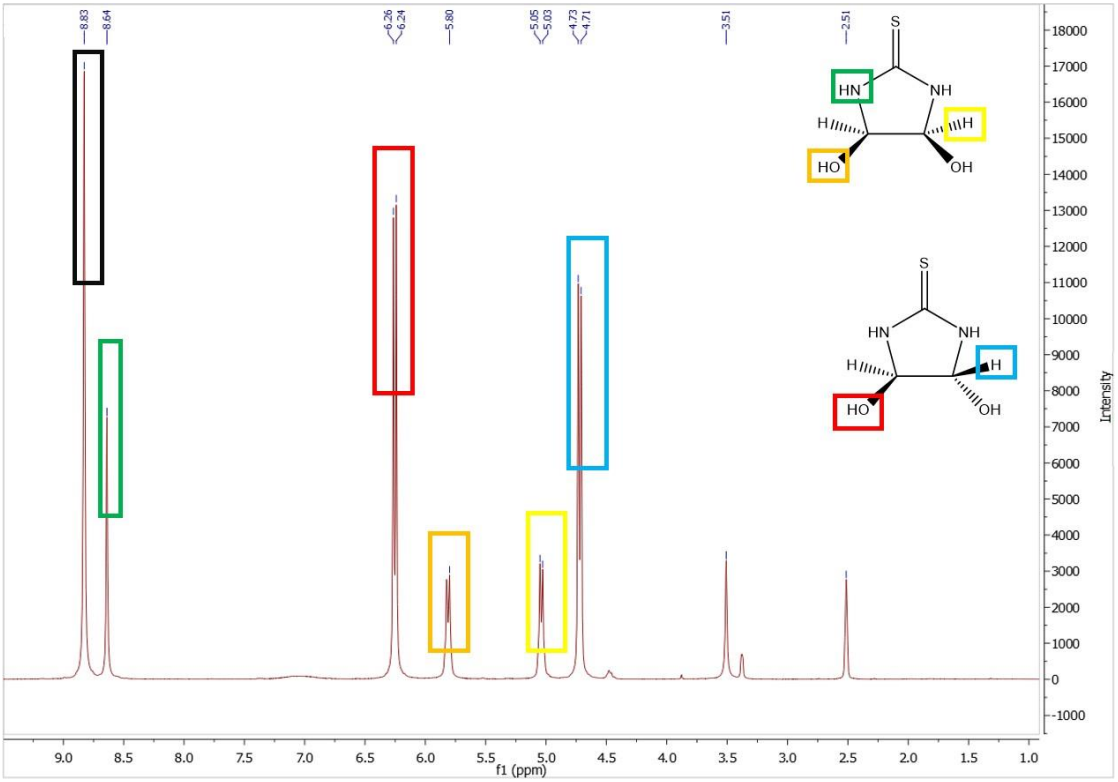

Figure 9.2.5 NMR spectra after the purification and precipitation. All the peaks describing our molecule have essentially not changed from the previous NMR analysis (fig. 9.2.4).

After these results, it is likely that the reaction is not occurring due to the low reactivity of the DTI to reach the second thiourea. To resolve this issue, the synthesis strategy was focused on making the imidazole derivate more reactive. The idea to substitute the two hydroxyl groups with two halogens using the sulphonyl chloride was investigated (Figure 9.2.6)

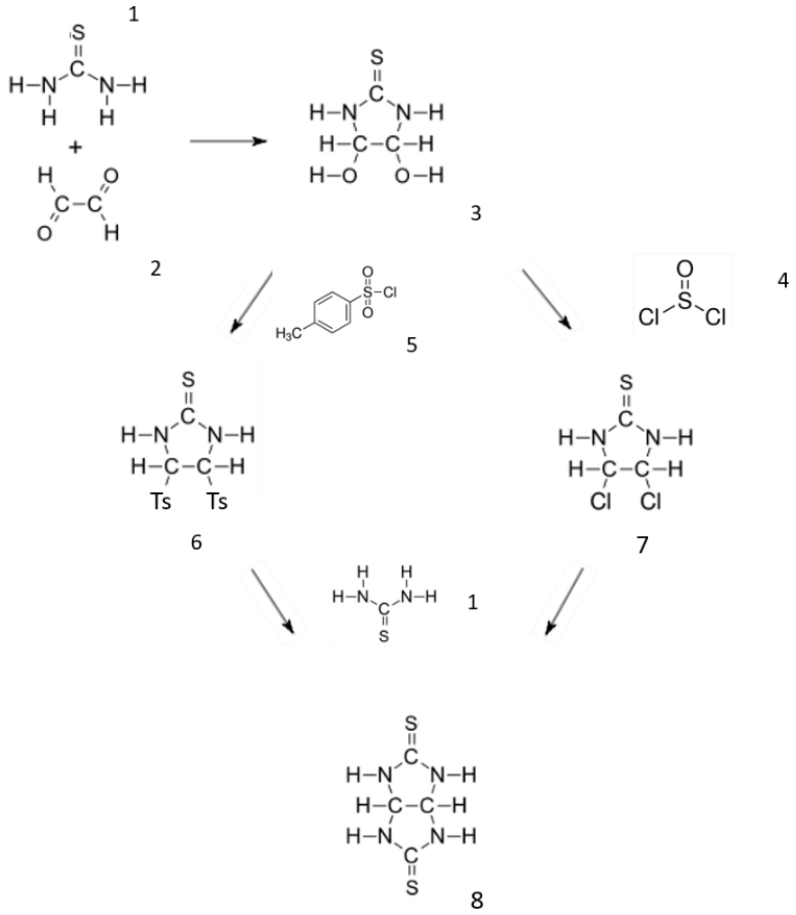

Figure 9.2.6 Alternative synthesis for the thioglycouril. The thiourea (1) and the glyoxal (2) form the DTI (3) and the hydroxyl groups. After that, before the second addition of the thiourea, the DTI is mixed with the thionyl chloride(4) or the tosyl chloride (5). Both reagents are used to improve the reactivity of the imidazole ring for the addition of the second thiourea.

In both cases, the most challenging step was the purification of the compound after the reactions addressed in figure 9.2.6. Specifically on those steps that require the purification of the tosylate derivative (compound 6) from the tosyl chloride (compound 5) and the chloride derivative (compound 7) from the thionyl chloride (compound 4)

Both NMR spectra (fig. 9.2.7) presented several peaks making it difficult to carry out any kind of detailed analysis.

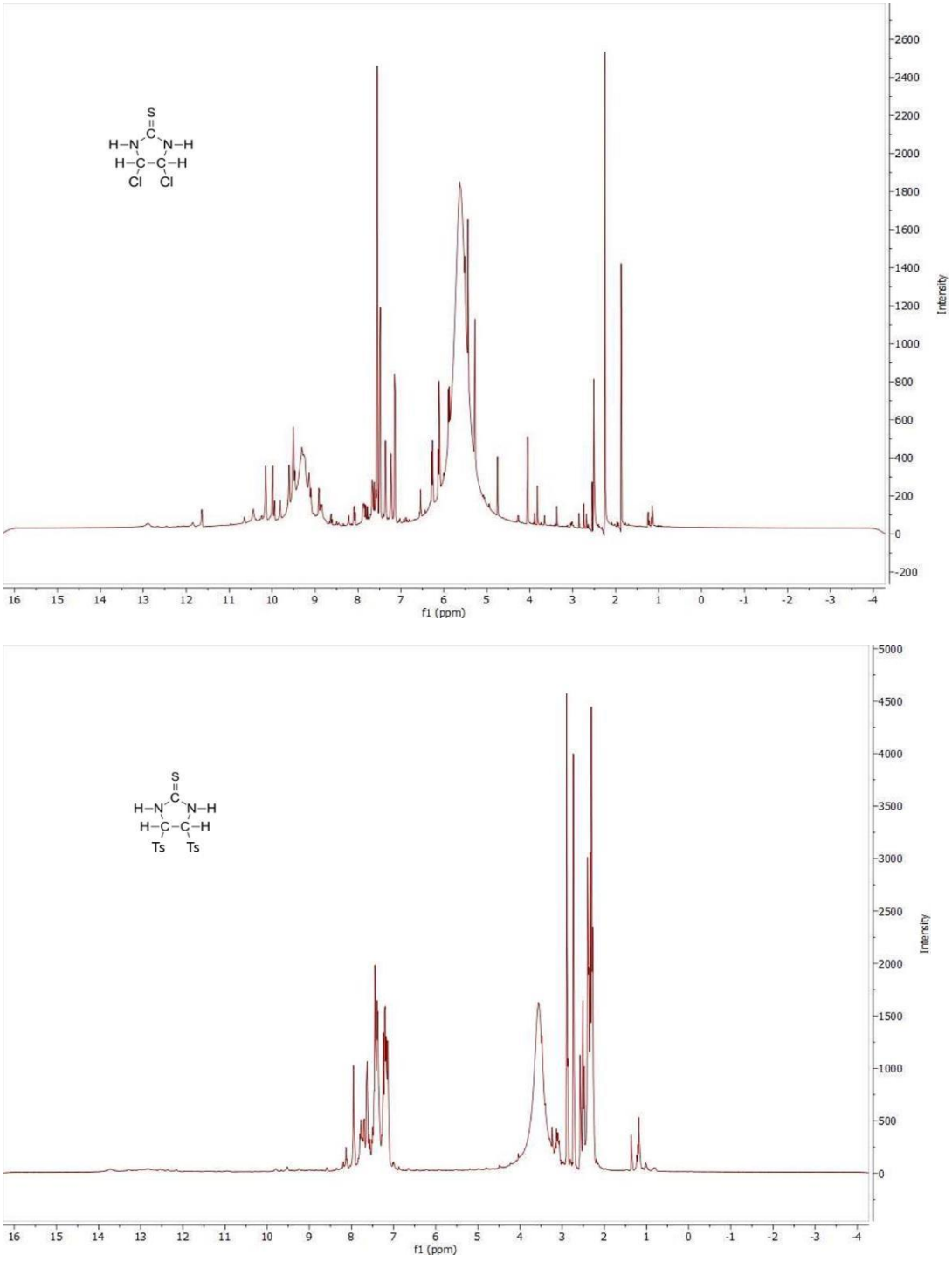

Figure 9.2.7 NMR spectra of the reaction with thionyl chloride (up) and tosyl chloride (down).

As the traditional synthetic pathway was demonstrated not to be viable, an entire different synthetic strategy was investigated. The cucurbiturils possess unique host-guest features that can cover a vast range of applications such as catalysis, chemical sensing, and metal complexation. Based on these characteristics, it is quite surprising that few attempts have been proposing for the synthesis of the thiocucurbituril. It highlights the difficulties of synthesising the sulphur derivatives of the cucurbituril[378]. The inclusion of a sulphur atom into the structure of macrocycles seems to be a successful strategy capable of leading to several molecules with unique and very peculiar features. As proposed in this thesis and also by Stoddart et al.,[354] the inclusion of the thiol group into the carbon-6 of the glucose unit of the β-CD–(SH) offers unique characteristics and specific binding to surfaces. Calixarene molecules having a thiophenol as monomer instead of the common phenol seems to provide new insights into the field of host-guest chemistry[379].

9.3 The diamond anvil cell synthesis approach

Although the cucurbituril is a stable compound, the synthesis of the sulphur derivative has proven to be significantly challenging. To face this challenge, the functionalisation step was performed in a Diamon Anvil Cell (DAC) at a reaction pressure of 9 GigaPascal (GPa). This approach was considered for its extreme pressure, which could represent the driving force of the reaction to occur. Since its design, the diamond anvil cell has served an advancing tool for chemical and physical discoveries[327].

In our work, the aim of using the DAC was coming from the fact that attempts to synthesise the cucurbituril, following the traditional organic synthesis methods, has failed. For the DAC synthesis, we started directly from the cucurbit[6]uril already synthesised and tried to change the ketone group for a thioketone group (fig 9.3.1).

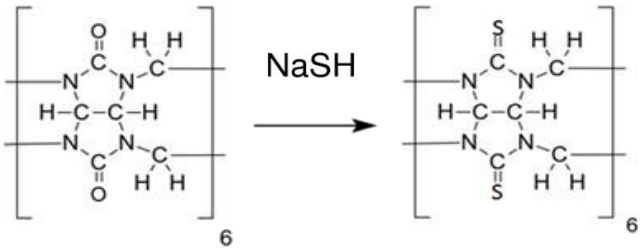

Figure 9.3.1 Proposed mechanism synthesis of the thiocucurbituril. Over the entire molecular structure, it was theorised only to exchange the carbonyl group (C=O) for a thiocarbonyl (C=S).

This strategy was taken to reduce the synthetic steps into the DAC to one reaction only. The reactive for the sulphonation process was sodium sulphide. The 10 milligrams (10.1 μmol) of cucurbit[6]uril and 6.7 milligrams (120 μmol) of Sodium Hydrogen Sulphide (NaSH) were mixed and grinded in an argon atmosphere as the sodium sulphide seems to be particularly hygroscope if exposed to air. For the two compounds, a ratio of 1:12 in moles was chosen as the carbonyl group is repeated 12 times in a single molecule of cucurbit[6]uril. Then the mixture was inserted into the DAC together with the ruby for the pressure detection. The mixture was measured at different pressures and analysed through Raman Spectroscopy. We took first a Raman Spectra of the initial compounds before the mixing inside the diamond anvil cell in order to have our peak assignment compared with the literature.

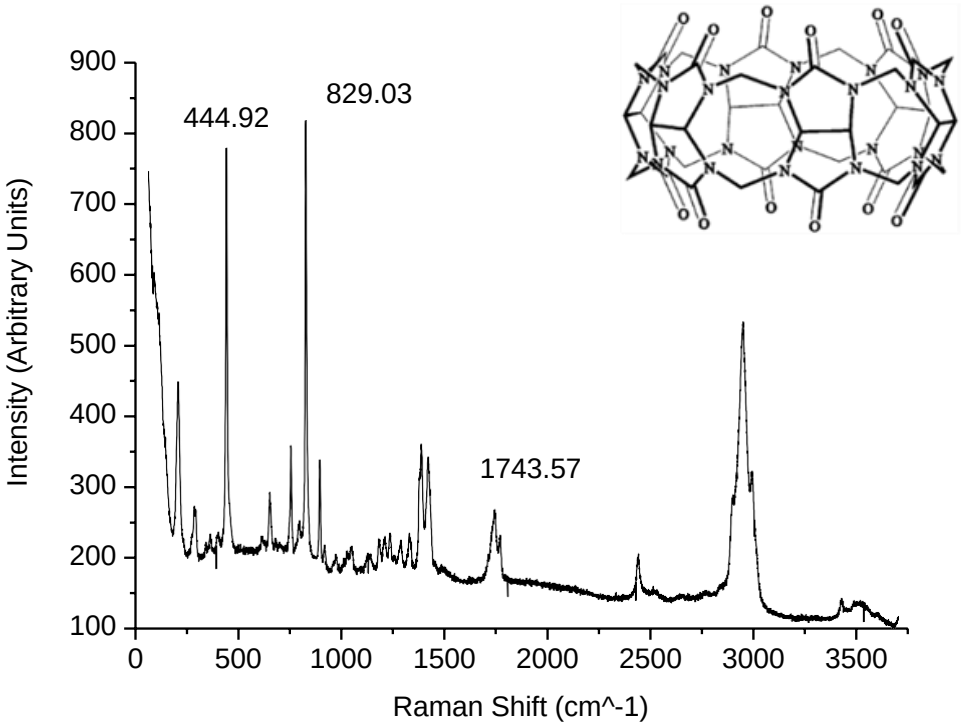

Figure 9.3.2 Raman Spectra of the cucurbitu[6]uril. The peaks at 444.92 cm^{-1} indicate the N-C-N vibration, at 829.03 cm^{-1} indicates the C-N-C vibration and at 1743.57 indicates the C=O vibration[380].

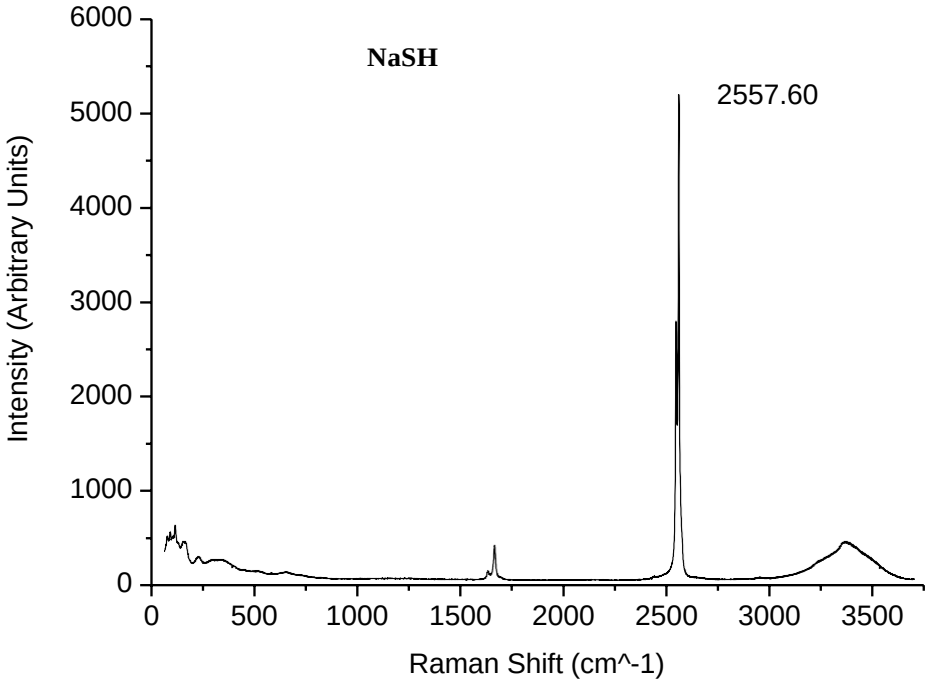

Figure 9.3.3 Raman Spectra of Sodium Hydrogen Sulfide (NaSH). The peak at 2557.60 represents the thiol group[381].

These two preliminary measurements were taken at ambient pressure in order to be capable of visualising and assigning the peaks of our interest. As the analysis inside the cell chamber cannot be performed with NMR, we used instead Raman spectroscopy and the peaks were assigned based on previous literature studies[382,383], and our desired thioketone peak[384] should be found at 500-710 cm^{-1} . Following analysis of the individual components, Raman analysis was performed on a mixed compound. The first spectrum was taken at the 0.6 Gigapascal(GPa), showing the expected[385] diamond peak at 1332 cm^{-1} , the peak of the S-H bond at 2557.60 cm^{-1} (both at figure 9.3.4 left) and the peak of the Na-S stretch in between 400 and 500 cm^{-1} (indicated with a circle in figure 9.3.4 right).[381]

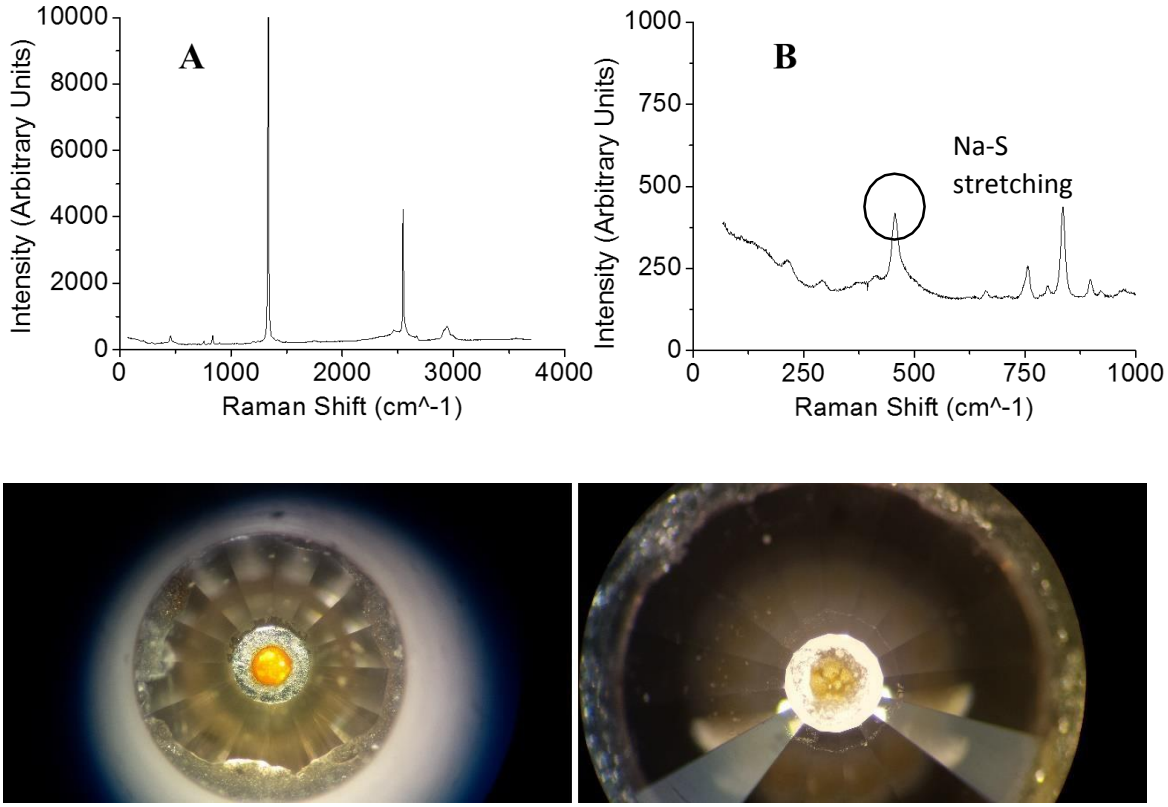

Figure 9.3.4 Raman Spectra (up) of the mixture into the DAC right after the mixing at 0.6 GPa: the entire spectra (A) and the magnification of the area (B) where the vibration carbon-sulphur should be visible (500-710 cm^{-1})[384]*. Actual photos (down) taken at the microscope of the DAC chamber with the compound mixture.*

As the peak of the interaction carbon-sulfur was not observed, it was decided to increase the pressure and perform further analysis. Finally, after one hour at the pressure of 5.0 GPa, the thiocarbonyl group peak was observed. The interaction between the carbon and the sulphur was observed at 575.09 cm^{-1} (Fig. 9.3.5). To explore in more detail this reaction, the pressure inside the system was further increased. The DAC was raised to 9.3 GPa and left overnight. Following 24 hours under reaction, another Raman Spectra was taken showing moderately higher peak (figure 9.3.6).

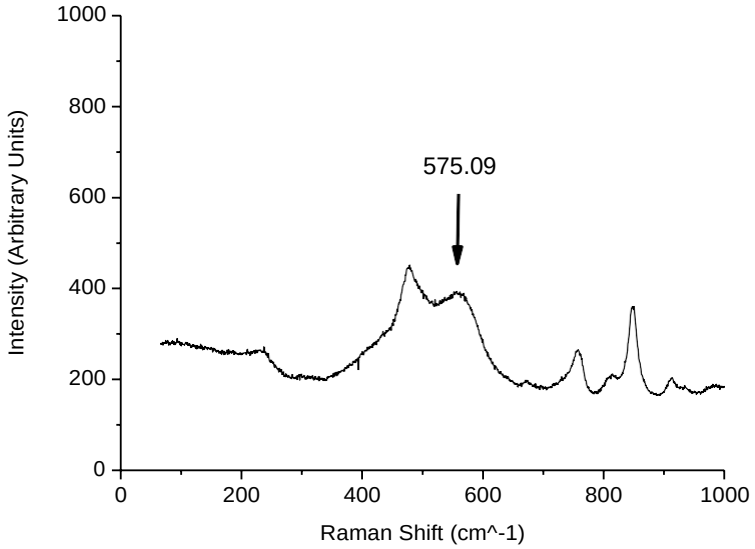

Figure 9.3.5 Raman Spectra at 5.0 GPa after one hour from the mixture.

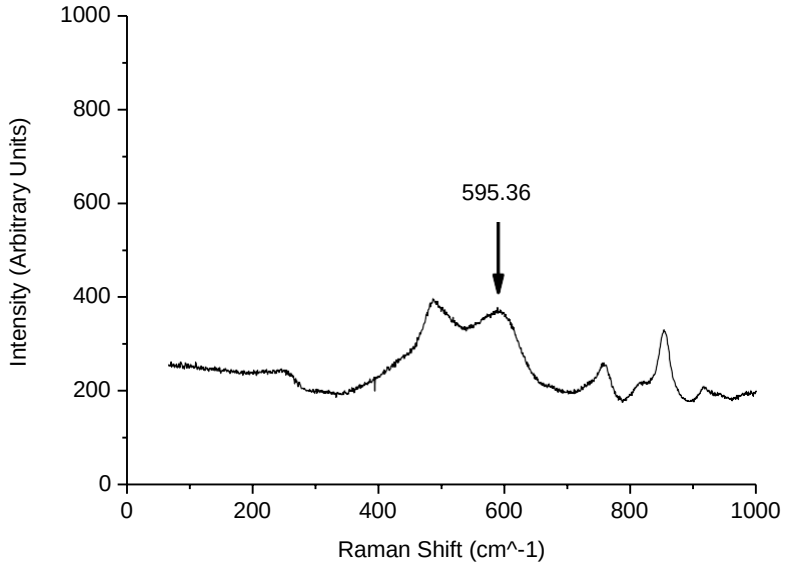

Figure 9.3.6 Raman Spectra at 9.3 GPa for 24 hours. The peak carbon-sulphur[384] *is evident at 595.36 cm*$^{-1}$.

All the peaks seem to have a shift of 30-20 cm^{-1}. This is the expected behaviour of any DAC experiments as the interaction between atoms tend to increase with the

increase of the pressure[386]. As the pressure increase and the distance between atoms decrease, the sulfur forms a bond with the carbon, generating a peak found to be at 710-580 cm^{-1} after literature investigation[387]. After this, the pressure inside the DAC was decreased at 7.7 GPa and then 5.0 GPa, 1.8 GPa and 0.7 GPa to observe if the molecule may exist at ambient pressure.

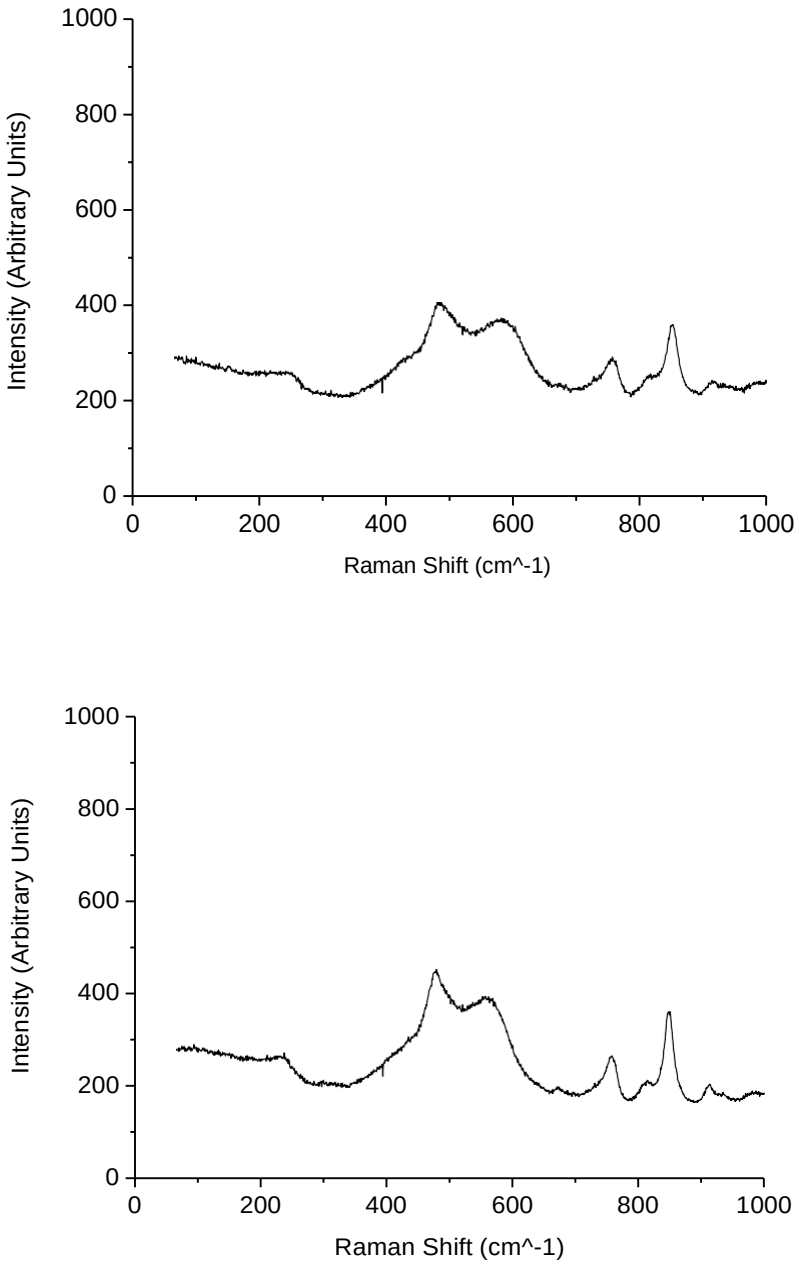

Figure 9.3.7 Raman Spectra 7.7 GPa for 26 hours (above) and 5.0 GPa for 30 hours(below). The carbon sulphur peak area is decreasing, showing that the two atoms are again splitting apart.

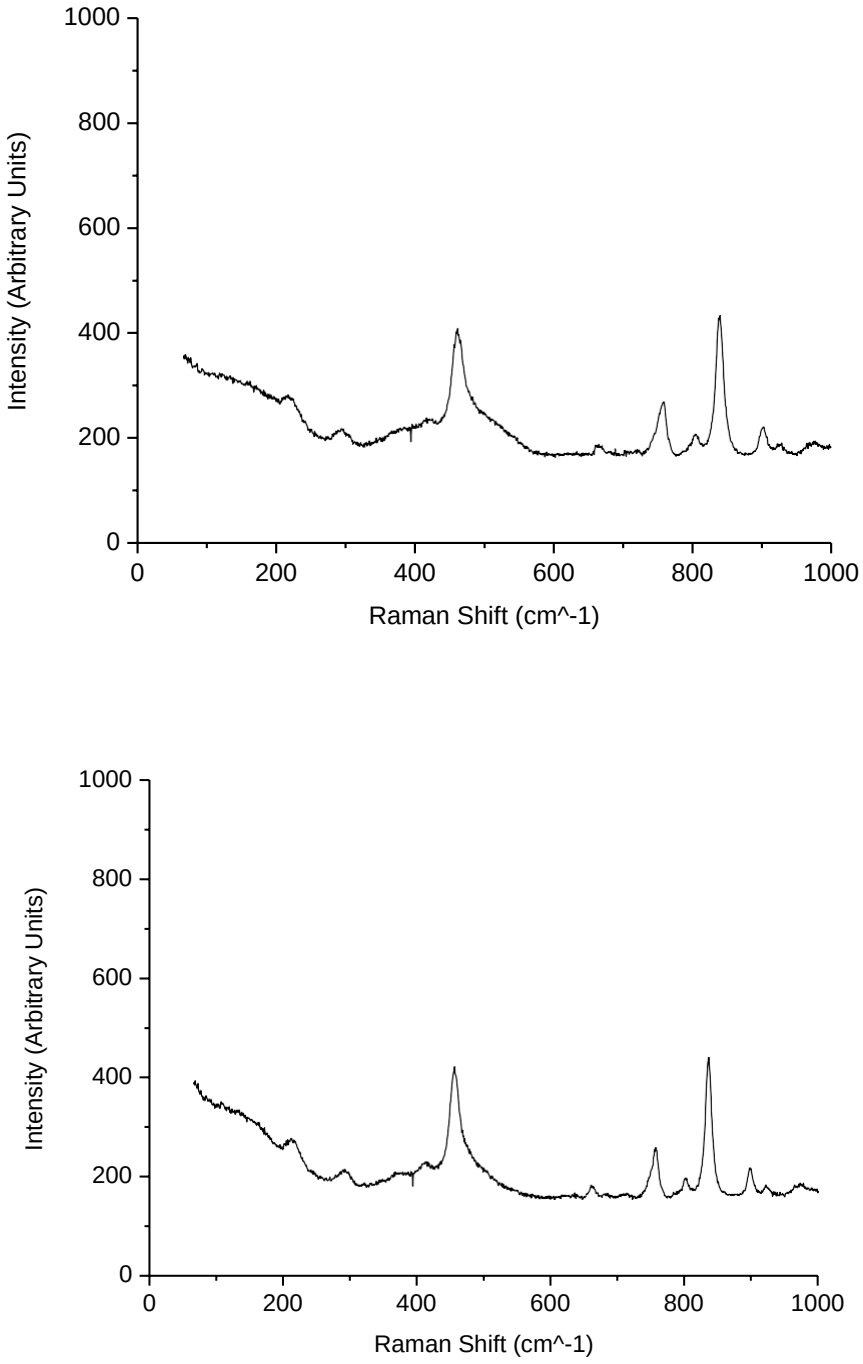

Figure 9.3.8 Raman Spectra at 1.8 GPa (above) and 0.7 GPa (below). The peak now has completely disappeared, proving that there is no more interaction among the carbon and the sulphur atom.

By decreasing the pressure, it was observed a decrease in the peak intensity until it disappeared at the pressure of 0.7 GPa. These analyses suggest that, at a pressure similar to the ambient pressure, the molecules reverse back to their initial state with the carbon binding the oxygen, giving again the cucurbituril in its original chemical composition and with no new functionalised group.

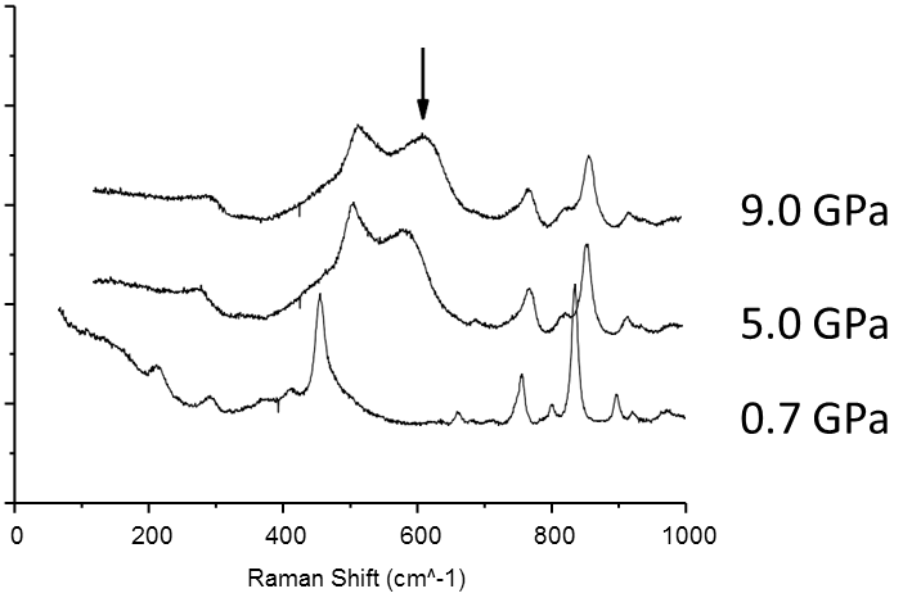

Figure 9.3.9 Raman Spectra at 0.7 GPa, 5.0 GPa and 9.0 GPa. The black arrow indicates the new peak formed. The small shift of the entire spectra between 0.7 GPa and 5.0 GPa indicates an increased interaction between atoms.

9.4 The blank experiments of the NaSH salt

In order to prove the validity of the high-pressure functionalisation, even if only at high pressure, we ran two different experiments where the chemicals were inserted inside the anvil cell as a single component. The Raman spectra were observed at different pressures in order to prove that the peak at 595.36 cm^{-1} in the figure 9.3.6 was a peak obtained by mixing the two reagents and not from an intermolecular reaction of one of them. The first reagent analysed was the NaSH salt. The compound was ground into an argon inert environment. Once the powder was fine enough, it was introduced into the anvil cell chamber together with the ruby. The Raman spectra were performed at different pressure conditions focusing again on the area of our interest where the peak C-S was spotted (400-600 cm^{-1}). The first Raman spectra were taken at ambient pressure (fig. 9.4.1), then the pressure was initially increased at 0.6 GPa (fig. 9.4.2) and then at 1.96 GPa (fig. 9.4.3). From these three analyses, only the peak of the Na-S stretching was spotted at around 400-450 cm^{-1}. By applying pressure, it was initially noticed a change in peak intensity and shifted due to the interactions of the atoms being changed. The pressure then was further increased to 2.94 GPa (figure 9.4.4), 4.42 GPa (figure 9.4.5), 7.78 GPa (figure 9.4.6) and 9.44 GPa (figure 9.4.7). The changing in shape of the peak was easily noticed proving again that the pressure was high enough to create different vibration among atoms. At the pressure 9.44 GPa was noticed a small peak at 590.36 cm^{-1} similar to the one of our interest. This peak was believed coming from the interaction of the sulphur probably start to interact with the carbon at the surface of the diamond. However this interaction was excluded from being the same interaction observed in figure 9.3.5 and 9.3.6 for a simple reason: the peak coming from the mixture (fig 9.3.5 & 9.3.6) started to be observed at the anvil pressure of 5.0 GPa, in opposition with the NaSH analysed as single component which starts to be observed only at the pressure 9.44 GPa (figure 9.4.7).

After this analysis the pressure was brought back at near-ambient pressure observing the peak at 590.36 cm^{-1} disappearing entirely and the spectra assuming its overall original shape at the pressure of 7.78 (fig. 9.4.8), 5.59 (fig. 9.4.9), 3.53 (fig. 9.4.10), 2.78 (fig. 9.4.11), 1.37 (fig. 9.4.12) and 0.78 GPa (fig. 9.4.13).

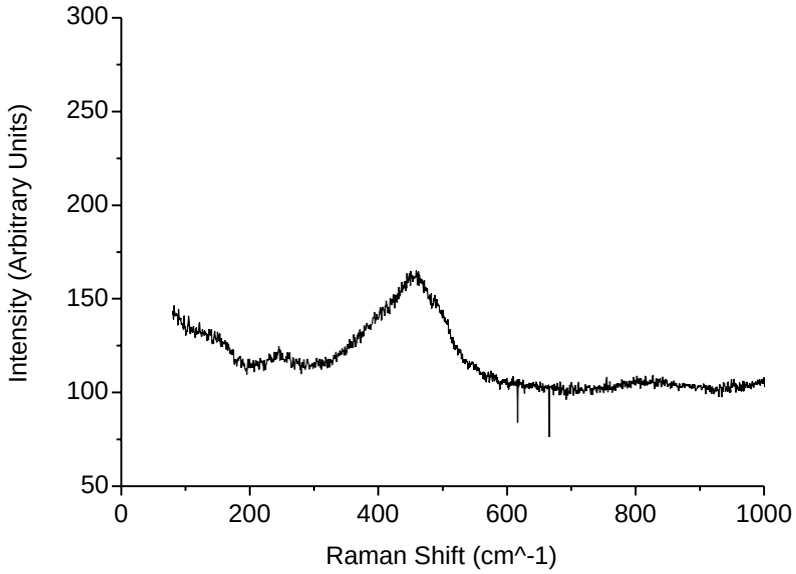

Figure 9.4.1 Raman spectra 0-1000 cm^{-1} area of the NaSH salt in a diamond anvil cell at the ambient pressure. The characteristic peak in this area is the peak of the stretch of the Na-S bond.

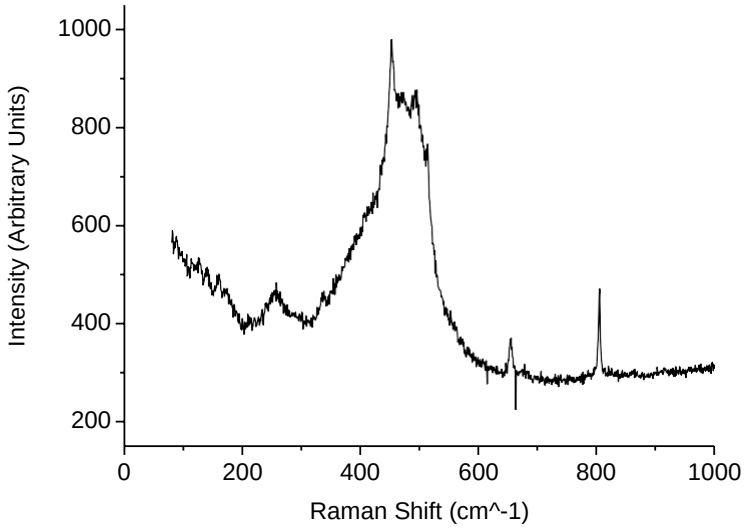

Figure 9.4.2 Raman spectra 0-1000 cm^{-1} area of the NaSH salt in a diamond anvil cell at the pressure of 0.6 GPa.

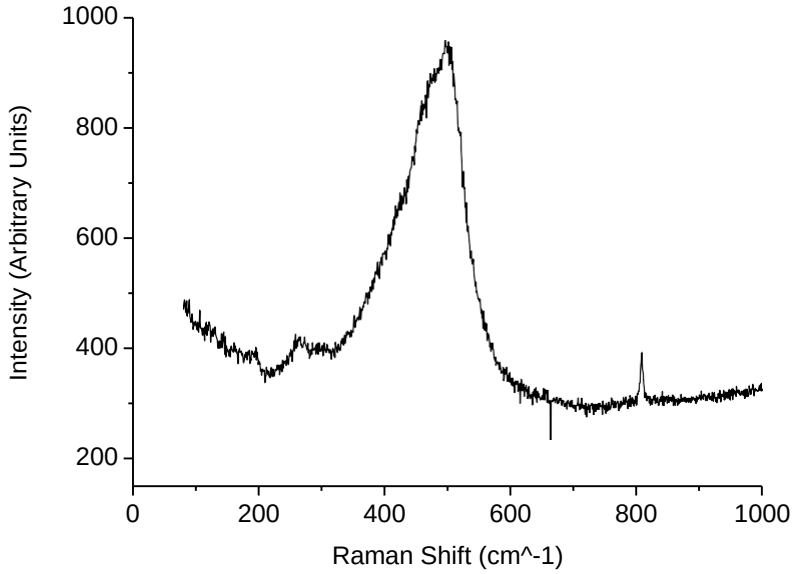

Figure 9.4.3 Raman spectra 0-1000 cm^{-1} area of the NaSH salt in a diamond anvil cell at the pressure of 1.92 GPa.

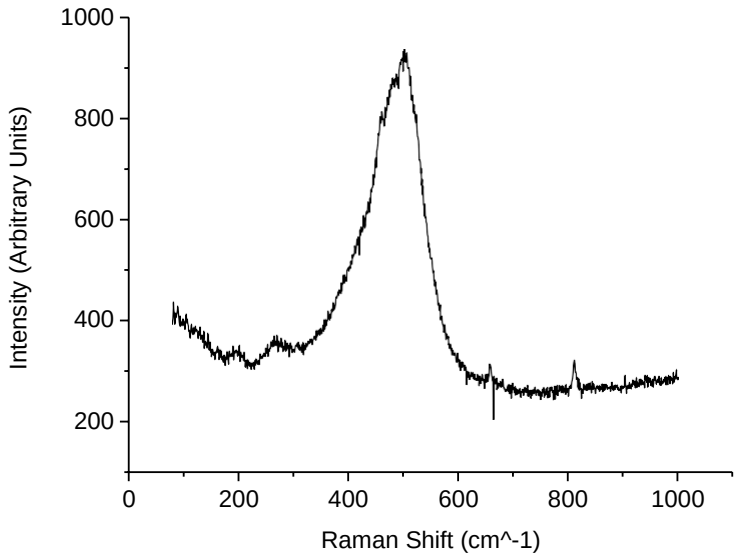

Figure 9.4.4 Raman spectra 0-1000 cm^{-1} area of the NaSH salt in a diamond anvil cell at the pressure of 2.94 GPa.

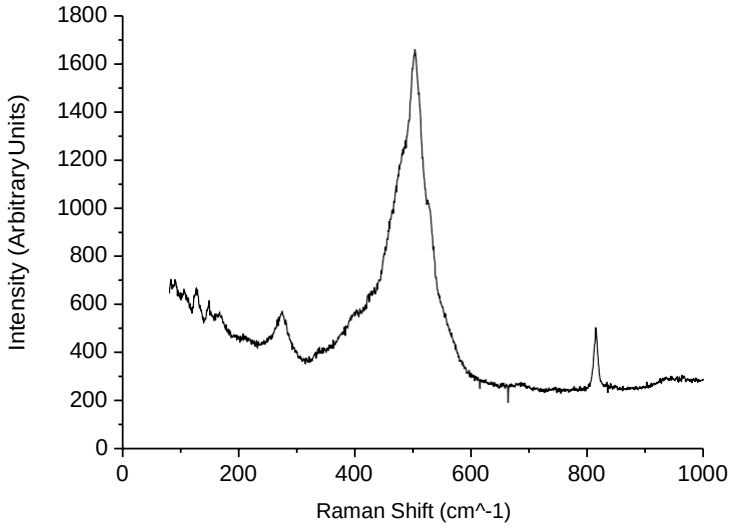

Figure 9.4.5 Raman spectra 0-1000 cm^{-1} area of the NaSH salt in a diamond anvil cell at the pressure of 4.42 GPa.

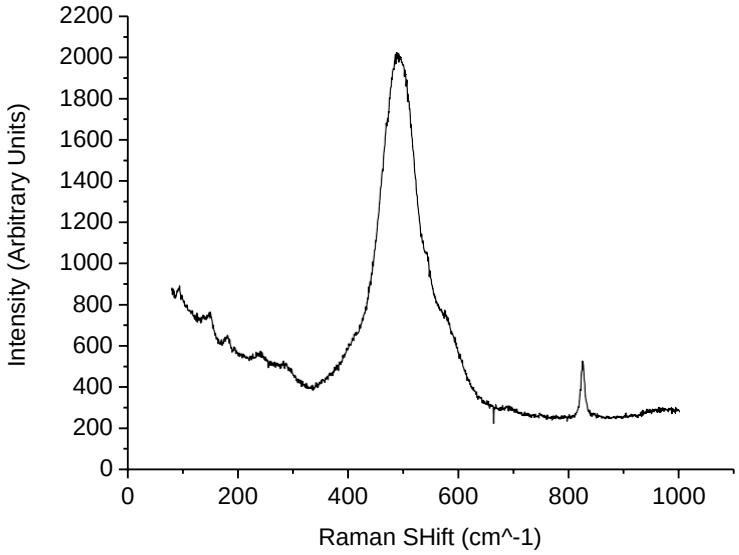

Figure 9.4.6 Raman spectra 0-1000 cm^{-1} area of the NaSH salt in a diamond anvil cell at the pressure of 7.78 GPa.

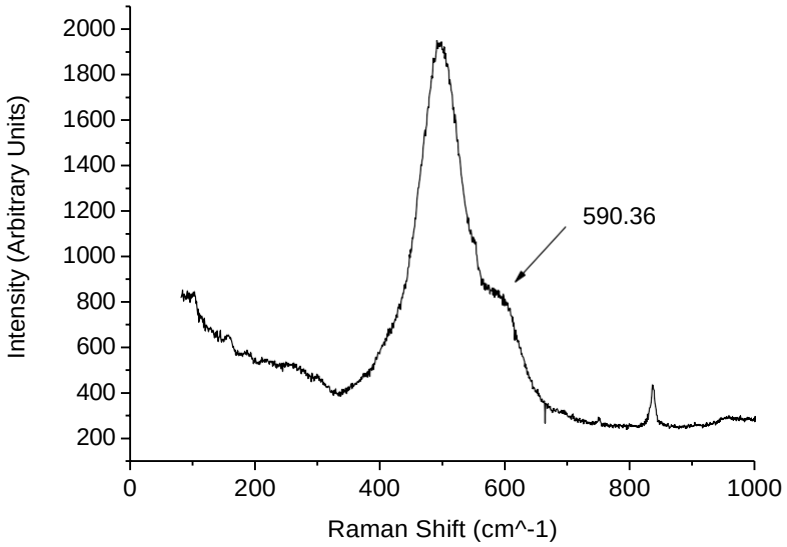

Figure 9.4.7 Raman spectra 0-1000 cm^{-1} area of the NaSH salt in a diamond anvil cell at the pressure of 9.44 GPa.

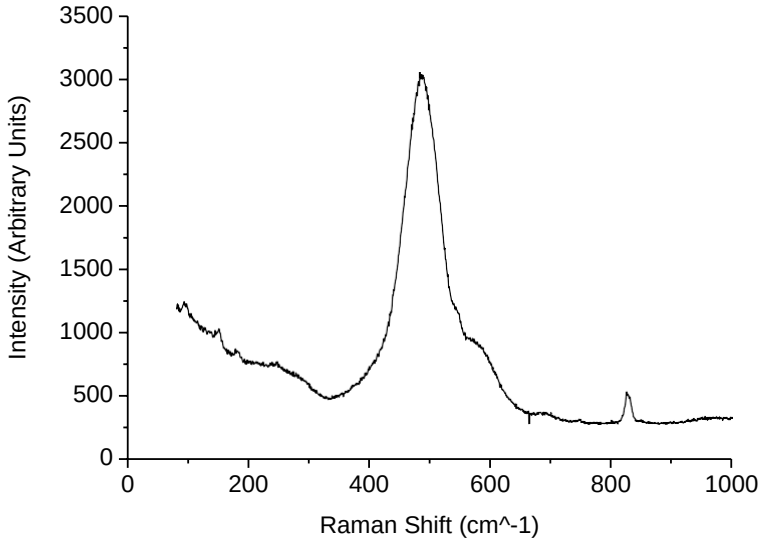

Figure 9.4.8 Raman spectra 0-1000 cm^{-1} area of the NaSH salt in a diamond anvil cell at the pressure of 7.78 GPa.

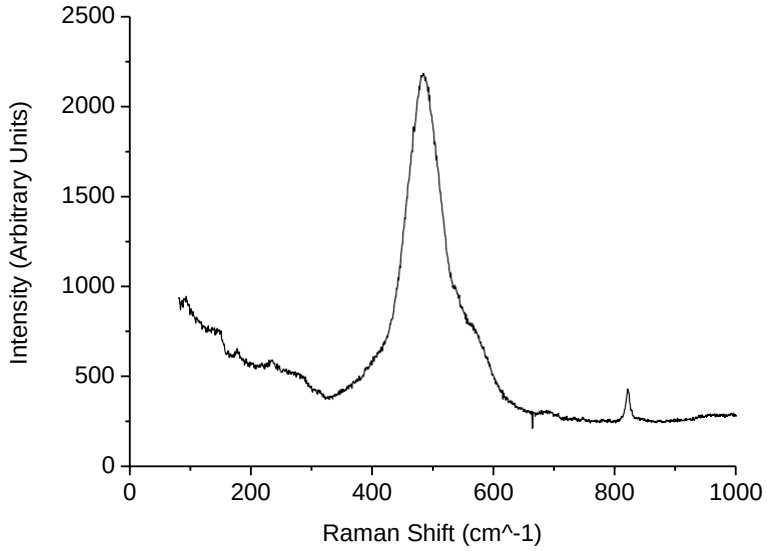

Figure 9.4.9 Raman spectra 0-1000 cm^{-1} area of the NaSH salt in a diamond anvil cell at the pressure of 5.59 GPa.

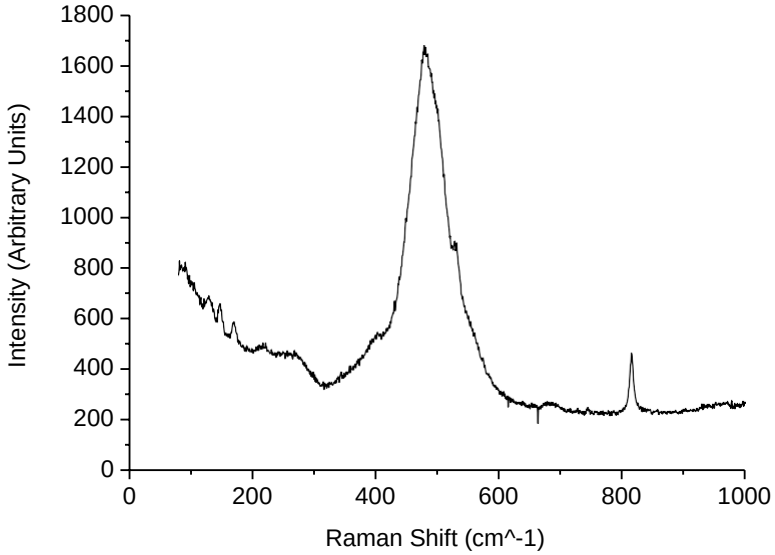

Figure 9.4.10 Raman spectra 0-1000 cm^{-1} area of the NaSH salt in a diamond anvil cell at the pressure of 3.53 GPa.

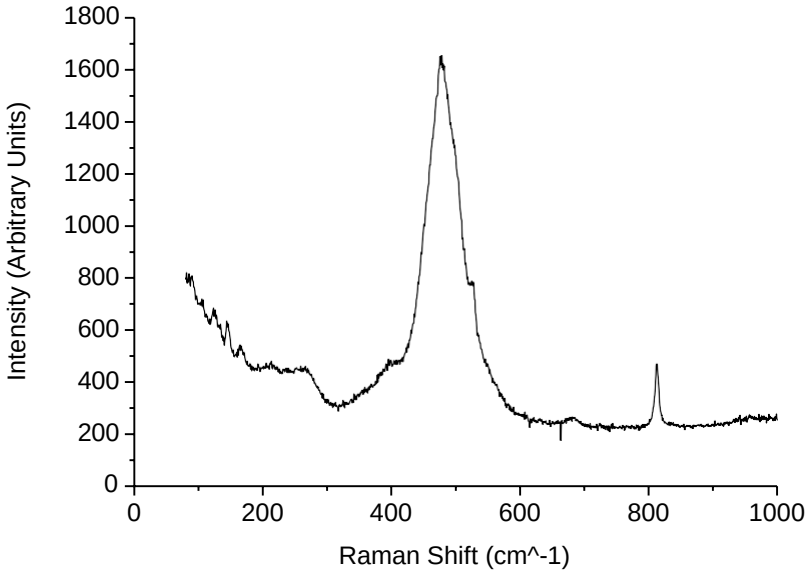

Figure 9.4.11 Raman spectra 0-1000 cm^{-1} area of the NaSH salt in a diamond anvil cell at the pressure of 2.78 GPa.

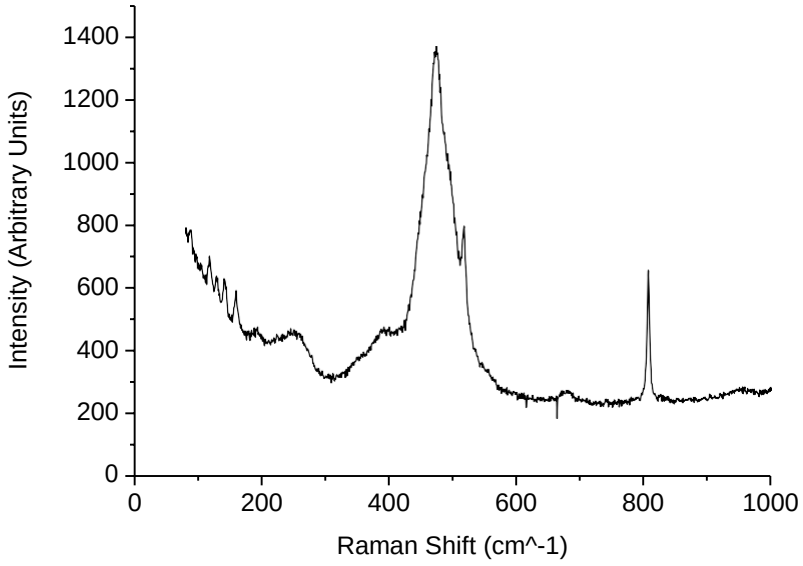

Figure 9.4.12 Raman spectra 0-1000 cm^{-1} area of the NaSH salt in a diamond anvil cell at the pressure of 1.37 GPa.

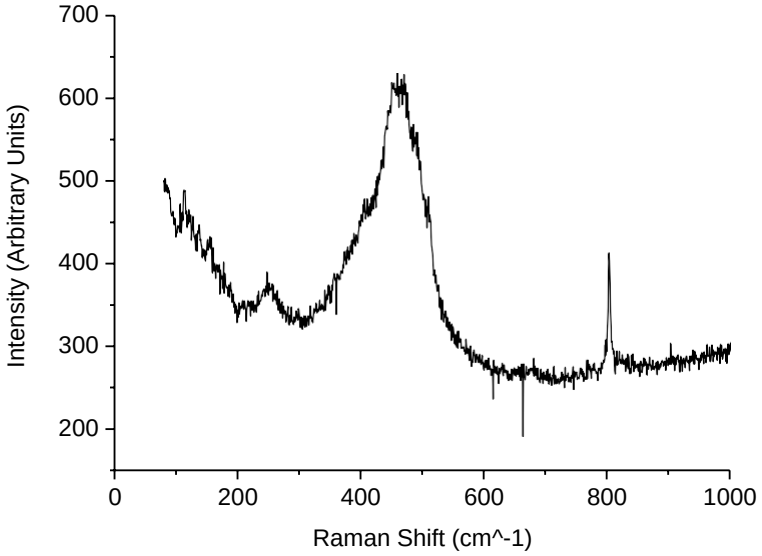

Figure 9.4.13 Raman spectra 0-1000 cm^{-1} area of the NaSH salt in a diamond anvil cell at the pressure of 0.78 GPa.

9.5 The blank experiment of the Cucurbituril

After the analysis of the NASH salt, we performed the analysis of the cucurbituril molecule as a single compound into the DAC. For the preparation, it was followed by the same procedure as the NaSH in the previous section. The cucurbituril powder was finely grinded in an argon atmosphere in order to avoid any possible hygroscopicity that the compound could present, interfering with our analysis. Once inserted into the DAC the molecule was initially observed at the pressure of 0.85 GPa. The first Raman spectra present similarity with the one observed into the figure 9.3.2. The pressure was then increased in order to possibly encounter in any trace of the peak at 595.36 cm^{-1}. Again it was observed a change in peak shape and Raman shift, proving that the pressure was high enough to create a sort of disturbance into the ground state of the molecule. The pressure

was slowly increased at 2.02 (fig. 9.5.2), 4.97 (fig. 9.5.3), 6.62 (fig. 9.5.4), 8.31 (fig. 9.5.5), and 9.53 GPa (fig. 9.5.6). However, no peak at 595.36 cm^{-1} was observed proving further that the peak coming from the mixture in the figure 9.3.6, was effectively the one indicating the C-S stretching. The pressure inside the DAC was subsequently decreased in the order of 7.07 (fig. 9.5.7), 4.72 (fig. 9.5.8), 2.72 (fig. 9.5.9), 1.51 (fig 9.5.10), and 0.46 GPa (fig. 9.5.11). The molecular behaviour observed was in accordance with the one observed in the previous DAC experiments, where at the decreasing of the pressure, the Raman analysis reacquires their initial spectra.

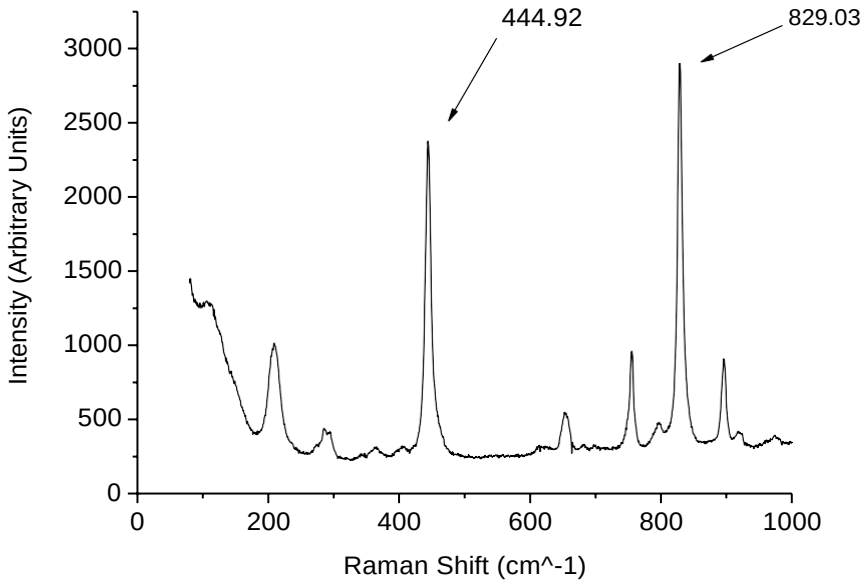

Figure 9.5.1 Raman spectra 0-1000 cm^{-1} area of the cucurbituril in a diamond anvil cell at the pressure of 0.85 GPa. The peaks at 444.92 cm^{-1} indicate the N-C-N vibration, at 829.03 cm^{-1} indicates the C-N-C vibration[380].

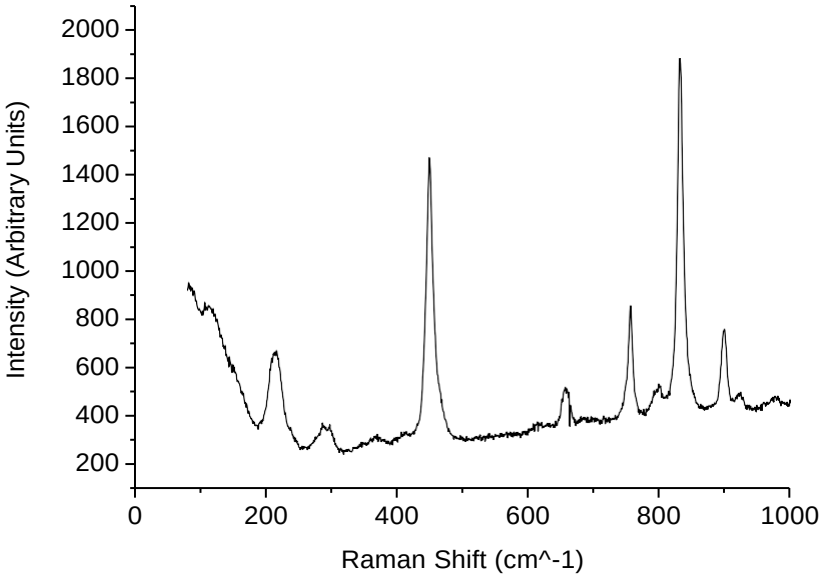

Figure 9.5.2 Raman spectra 0-1000 cm^{-1} area of the cucurbituril in a diamond anvil cell at the pressure of 2.02 GPa.

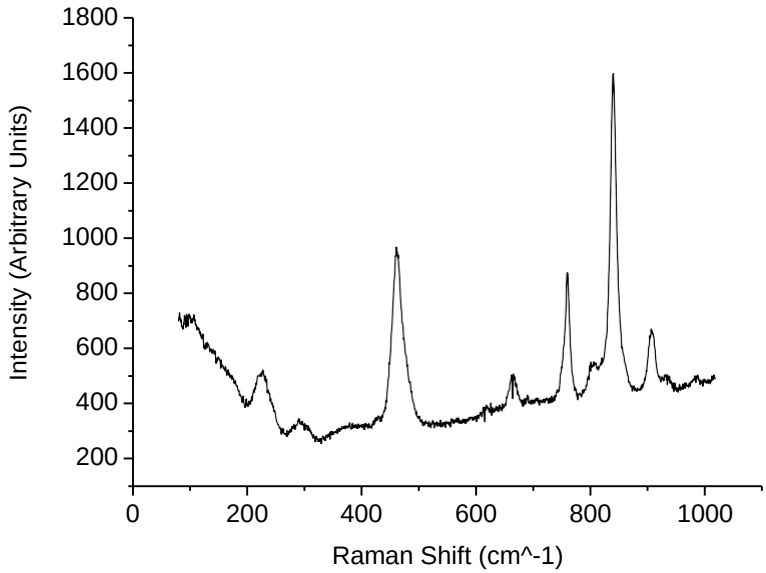

Figure 9.5.3 Raman spectra 0-1000 cm^{-1} area of the cucurbituril in a diamond anvil cell at the pressure of 4.97 GPa.

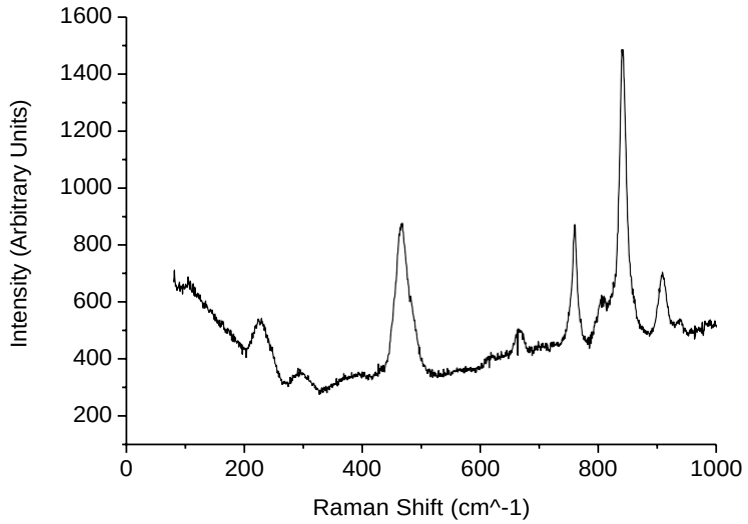

Figure 9.5.4 Raman spectra 0-1000 cm^{-1} area of the cucurbituril in a diamond anvil cell at the pressure of 6.62 GPa.

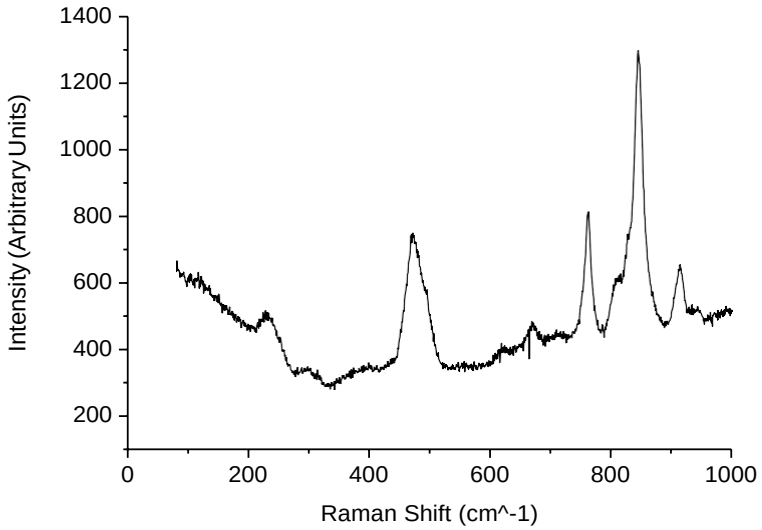

Figure 9.5.5 Raman spectra 0-1000 cm^{-1} area of the cucurbituril in a diamond anvil cell at the pressure of 8.31 GPa.

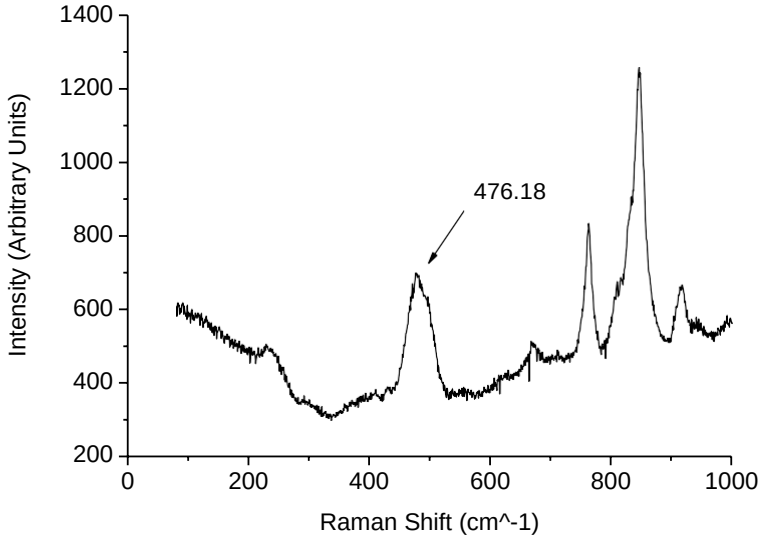

Figure 9.5.6 Raman spectra 0-1000 cm^{-1} area of the cucurbituril in a diamond anvil cell at the pressure of 9.53 GPa.

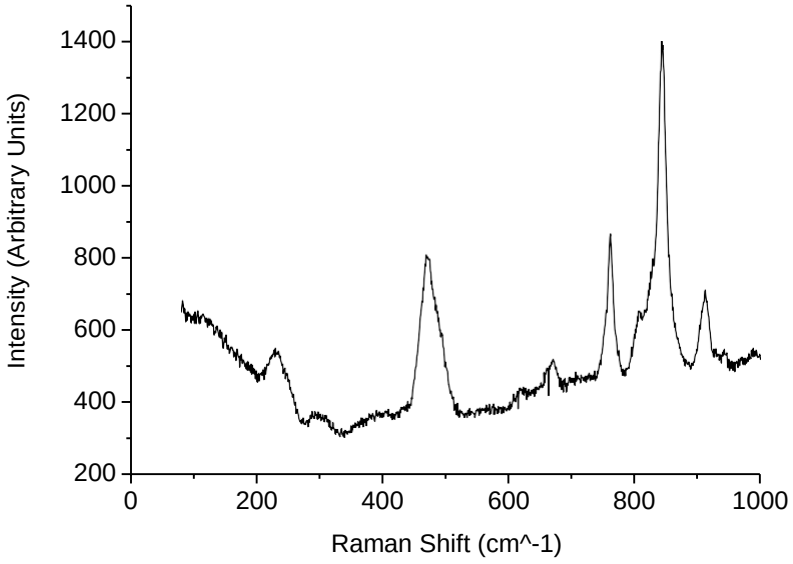

Figure 9.5.7 Raman spectra 0-1000 cm^{-1} area of the cucurbituril in a diamond anvil cell at the pressure of 7.07 GPa.

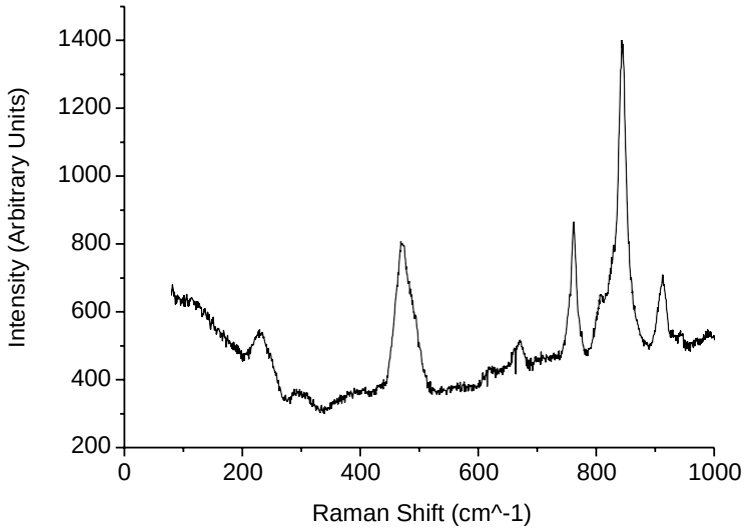

Figure 9.5.8 Raman spectra 0-1000 cm^{-1} area of the cucurbituril in a diamond anvil cell at the pressure of 4.72 GPa.

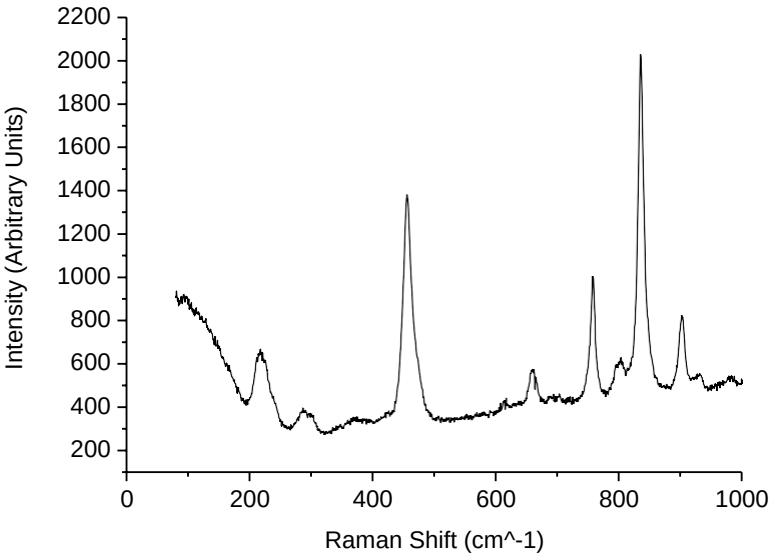

Figure 9.5.9 Raman spectra 0-1000 cm^{-1} area of the cucurbituril in a diamond anvil cell at the pressure of 2.72 GPa.

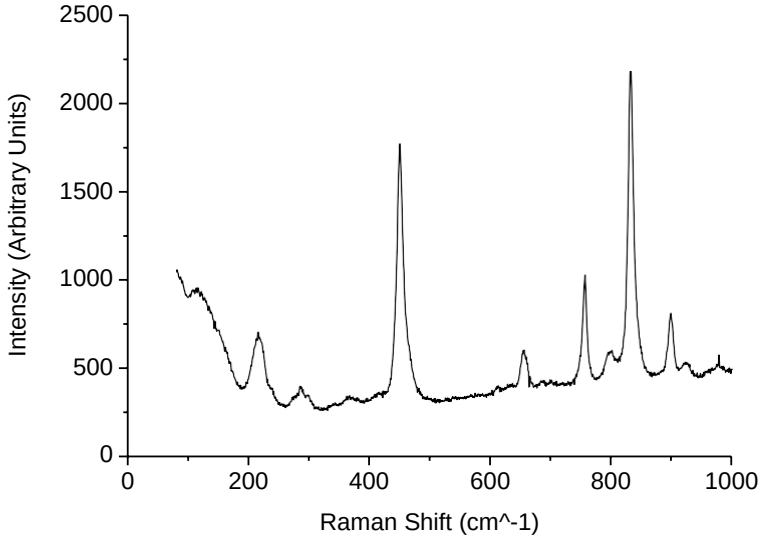

Figure 9.5.10 Raman spectra 0-1000 cm^{-1} area of the cucurbituril in a diamond anvil cell at the pressure of 1.51 GPa.

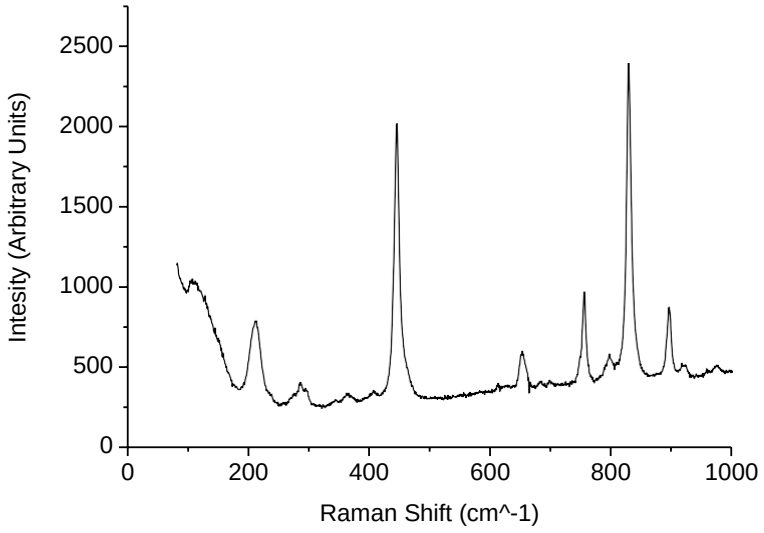

Figure 9.5.11 Raman spectra 0-1000 cm^{-1} area of the cucurbituril in a diamond anvil cell at the pressure of 0.46 GPa.

9.6 Conclusions

In this chapter, the synthesis of thiocucurbituril was attempted in order to obtain a new molecule for capturing proteins. The previous methods of thiocucurbituril common synthesis have failed despite the numerous trials. It is believed that the failure is given by the fact that the new reagent introduced (thiourea) presents a much lower reactivity and much higher temperature instability compared to the oxygen derivate molecule (urea). A different and new synthetic approach was explored by DAC. The DAC can offer elevated pressure levels that can be used as a driving force for the reaction to occur. This method provided us with new inputs and encouraging data to keep exploring further this new approach. The DAC provides that pressure capable of approaching atoms among each other, even in the case of the condensed matter, determining the formation of new interactions and bonds. However, even if the experiment was successful at the beginning, it was impossible to observe at ambient pressure the peak we were looking for. The data collected until now suggested that the functionalisation might occur if the reaction can be brought at elevated pressure and the blank experiment further demonstrate that the peak at 595.36 cm^{-1} was effectively the one indicating an interaction among the carbon of the cucurbituril and the sulfur of the NaSH salt. The pressure inside the DAC chamber may be not the only variable needed to have this compound also at ambient pressure. In order to challenge this problem, a new sulphur donor may be chosen instead of the sodium hydrosulfide, capable of pushing the equilibrium towards the formation of the bond carbon sulphur.

10. Overall conclusions and future works

In this thesis, a new way of immobilising proteins on surfaces was investigated. The approach involved a supramolecular method different from the previous methodologies (i.e. physical adsorption, chemical adsorption). The supramolecular approach is needed in order to ensure the preserving of the physiological protein structure during immobilisation. The molecule chosen for our supramolecular surface was the cyclodextrin: a ring-shaped molecule capable of capturing the amino acids present in the outer part of the protein. The first attempt to fabricate the supramolecular surface involved a synthesis of the layer directly on the surface. The fabrication method was constituted by 4 steps. A long carbon chain was firstly assembled on the surface (AUT). It was then activated (DHS) to allow the cyclodextrin to react with it. Every single step presents a certain amount of error that at the end of the fabrication, brought us a non-well designed surface. The first surface underwent characterisation, showing a heterogeneous surface in terms of thickness, polarity and chemical composition.

In order to overcome the problems encountered with a multi-step nanofabrication procedure, we adopted a different approach that simplifies all the procedure by reducing the fabrication steps from 4 to one. The β-CD–(SH)7 was then chosen as a viable route, having the two key features needed to succeed in this project: the cavity to trap proteins and the thiol group to increase the affinity of the cyclodextrin towards the gold surface. The characterisation methods, for higher concentration and incubation time, showed a homogeneous thickness and decreased polarity of the surface. The thickness is important to prove a well-packed SAM, the decreasing of the polarity to prove that the single component of the SAM is assembling with the orientation desired, in other words with

the cavity facing up. SPR studies were performed to prove the affinity of the surface towards proteins. As the thiol glucose is the monomer of the β-CD–(SH)7 the only difference among these two surfaces was the cavity-shaped surface typically of the cyclodextrin. The results showed an increased affinity for the β-CD–(SH)7 in compared with the surface functionalised with the thiol glucose. These results highlight the importance of having a cavity-shaped molecule on surface for the supramolecular complex and thus the immobilisation desired in this thesis. Without the cavity-shaped molecule the surface will only be capable of forming hydrogen bonds with the protein, leading to unspecific binding and a weak interaction that can be easily broken with any procedure.

After this encouraging results, we investigated if the affinity of the surface towards different proteins could be modified by changing the cyclodextrin for the cucurbituril. Again in order to have the cucurbituril assembling on a gold surface, a sulphur group on the molecules was needed. To meet this requirement, the thiocucurbituril was designed and the synthesis attempted. After several failed attempts, the synthetic concept was completely changed, and the DAC used to obtain the cucurbituril derivative by increasing the pressures. The Raman data of the mixture cucurbituril-NaSH salt showed that the interaction carbon sulphur has occurred, but it was not possible to bring this compound to ambient pressure. The Raman data of the single component analysed inside the DAC further prove that the functionalisation of the sulfur on the cucurbituril might have occurred. In the future, new sulphur compounds which react irreversibly should be investigated to prevent the reversibility of the reaction and obtain a product stable at ambient pressure. Another potential approach will also be to push the reaction by decreasing the diameter of the particles reagents involved in the reaction, in this way the

surface area of any single particle will be increasingly favouring the number of hits necessary for the advancing of any reaction. Advanced grinder methods could be studied and performed to achieve this objective.

Once this molecule is synthesised, SPR studies could be performed to fully understand how protein immobilisation can be controlled with cucurbituril-functionalised surfaces. Finally, more SPR experiments could be carried out also using different types of disease biomarkers to further demonstrate the diagnostic applicability of our supramolecular surfaces.

11. References

1 G. V. Oshovsky, D. N. Reinhoudt and W. Verboom, *Angew. Chemie - Int. Ed.*, 2007, **46**, 2366–2393.

2 E. V. Anslyn and D. A. Dougherty, *Modern Physical Organic Chemistry*, University Science Books, 2005.

3 H. Lodish, A. Berk, S. L. Zipursky, P. Matsudaira, D. Baltimore and J. Darnell, *Noncovalent Bonds*, W. H. Freeman, 2000.

4 S. L. Cockroft and C. A. Hunter, *Chem. Soc. Rev.*, 2007, **36**, 172–188.

5 T. L. Brown, P. Woodward, C. J. Murphy, B. E. Bursten and J. H. E. LeMay, *Chemistry : the central science*, Pearson Prentice Hall, 2009.

6 M. N. Eisler, in *Encyclopedia of Nanoscience and Society*, SAGE Publications, Inc., 2010.

7 J. H. Williams, in *Crystal Engineering How molecules build solids*, IOP Publishing, 2017.

8 A. M. Sapse, M. T. Rayez-Meaume, J. C. Rayez and L. J. Massa, *Nature*, 2005, **278**, 332–333.

9 E. Matijević, *J. Colloid Interface Sci.*, 1979, **70**, 399–405.

10 E. A. Meyer, R. K. Castellano and F. Diederich, *Angew. Chemie - Int. Ed.*, 2003, 42, 1210–1250.

11 D. A. Anslyn,E.V. & Dougherty, *Modern Physical Organic Chemistry*, 2006.

12 B. Breiten, M. R. Lockett, W. Sherman, S. Fujita, M. Al-Sayah, H. Lange, C. M. Bowers, A. Heroux, G. Krilov and G. M. Whitesides, *J. Am. Chem. Soc.*, 2013, **135**, 15579–15584.

13 D. Chandler, *Nature*, 2005, 437, 640–647.

14 B. Breiten, M. R. Lockett, W. Sherman, S. Fujita, M. Al-Sayah, H. Lange, C. M. Bowers, A. Heroux, G. Krilov and G. M. Whitesides, *J. Am. Chem. Soc.*, 2013, **135**, 15579–15584.

15 K. Ariga, J. P. Hill, M. V Lee, A. Vinu, R. Charvet and S. Acharya, *Sci. Technol. Adv. Mater*, 2008, **9**, 14109–96.

16 S. Bureekaew, S. Shimomura and S. Kitagawa, *Sci. Technol. Adv. Mater.*, 2008, **9**, 1–12.

17 K. D. Daze, T. Pinter, C. S. Beshara, A. Ibraheem, S. A. Minaker, M. C. F. Ma, R. J. M. Courtemanche, R. E. Campbell, F. Hof, M. Vedadi, A. Tripathy, P. J. Brown, C. H. Arrowsmith, J. Jin, W. P. Janzen and S. V. Frye, *Chem. Sci.*, 2012, **3**, 2695–2699.

18 Z. N. Vermeulen, K., Van Bockstaele, D.R., Berneman, K. Vermeulen, D. R. Van Bockstaele and Z. N. Berneman, *Cell Prolif.*, 2003, **36**, 131–149.

19 M. B. Kastan and J. Bartek, *Nature*, 2004, **432**, 316–323.

20 G. D. Simonson, A. C. Vincent, K. J. Roberg, Y. Huang and V. Iwanij, *J. Cell Sci.*, 1994, **107**, 1065–1072.

21 M. C. Good, J. G. Zalatan and W. A. Lim, *Science (80-.).*, 2011, **332**, 680–686.

22 S. Zhao, W. Xu, W. Jiang, W. Yu, Y. Lin, T. Zhang, J. Yao, L. Zhou, Y. Zeng, H. Li, Y. Li, J. Shi, W. An, S. M. Hancock, F. He, L. Qin, J. Chin, P. Yang, X. Chen, Q. Lei, Y. Xiong and K.-L. Guan, *Science*, 2010, **327**, 1000–1004.

23 J. E. Dueber, G. C. Wu, G. R. Malmirchegini, T. S. Moon, C. J. Petzold, A. V Ullal, K. L. J. Prather and J. D. Keasling, *Nat. Biotechnol.*, 2009, **27**, 5–8.

24 P. M. Ridker, R. J. Glynn and C. H. Hennekens, *Circulation*, 1998, **97**, 973–979.

25 P. M. Ridker, J. E. Buring, J. Shih, M. Matias and C. H. Hennekens, *Circulation*, 1998, **98**, 731–733.

26 J. B. Delehanty and F. S. Ligler, *Anal. Chem.*, 2002, **74**, 5681–5687.

27 G. Zheng, F. Patolsky, Y. Cui, W. U. Wang and C. M. Lieber, *Nat. Biotechnol.*, 2005, **23**, 1294–1301.

28 J. LaBaer and N. Ramachandran, *Curr. Opin. Chem. Biol.*, 2005, **9**, 14–19.

29 G. Siegal and J. G. Hollander, *Curr. Top. Med. Chem.*, 2009, **9**, 1736–1745.

30 A. Lueking, D. J. Cahill and S. Müllner, *Drug Discov. Today*, 2005, **10**, 789–794.

31 H. J. Lee, A. W. Wark and R. M. Corn, *Analyst*, 2008, **133**, 975–983.

32 P. Jonkheijm, D. Weinrich, H. Schröder, C. M. Niemeyer and H. Waldmann, *Angew. Chemie Int. Ed.*, 2008, **47**, 9618–9647.

33 F. Rusmini, Z. Zhong and J. Feijen, *Biomacromolecules*, 2007, **8**, 1775–1789.

34 L. S. Wong, F. Khan and J. Micklefield, *Chem. Rev.*, 2009, **109**, 4025–4053.

35 P. Jonkheijm, D. Weinrich, H. Schröder, C. M. Niemeyer and H. Waldmann, *Angew. Chemie - Int. Ed.*, 2008, **47**, 9618–9647.

36 J. L. Stair, M. Watkinson and S. Krause, *Biosens. Bioelectron.*, 2009, **24**, 2113–2118.

37 G. L. Gaines, *J. Colloid Interface Sci.*, 1991, **147**, 289–293.

38 H. Haick and D. Cahen, *Prog. Surf. Sci.*, 2008, **83**, 217–261.

39 S. Flink, F. C. J. M. Van Veggel and D. N. Reinhoudt, *Adv. Mater.*, 2000, **12**, 1315–1328.

40 A. Ulman, *Chem. Rev.*, 1996, **96**, 1533–1554.

41 J. C. Love, L. a. Estroff, J. K. Kriebel, R. G. Nuzzo and G. M. Whitesides, *Chem. Rev.*, 2005, **105**, 1103–1170.

42 T. Wimmer, *Ullmann's Encycl. Ind. Chem.*, 2012, **11**, 23–31.

43 C. Bouchiat, *Appl. Microbiol. Biotechnol.*, 2005, **59**, 609–617.

44 V. A. Marcolino, G. M. Zanin, L. R. Durrant, M. D. T. Benassi and G. Matioli, *J. Agric. Food Chem.*, 2011, **59**, 3348–3357.

45 V. N. P. Le, P. Leterme, A. Gayot and M. P. Flament, *PDA J. Pharm. Sci. Technol.*, 2006, **60**, 314–322.

46 J. Li, S. Geng, B. Liu, H. Wang and G. Liang, *Food Res. Int.*, 2018, **112**, 136–142.

47 G. Crini, *Chem. Rev.*, 2014, **114**, 10940–10975.

48 S. J. Barrow, S. Kasera, M. J. Rowland, J. Del Barrio and O. A. Scherman, *Chem. Rev.*, 2015, **115**, 12320–12406.

49 Z. Huang, K. Qin, G. Deng, G. Wu, Y. Bai, J. F. Xu, Z. Wang, Z. Yu, O. A.

Scherman and X. Zhang, *Langmuir*, 2016, **32**, 12352–12360.

50 J. W. Lee, S. Samal, N. Selvapalam, H. J. Kim and K. Kim, *Acc. Chem. Res.*, 2003, **36**, 621–630.

51 N. J. Wheate and C. Limantoro, *Supramol. Chem.*, 2016, **28**, 849–856.

52 E. V. de Carvalho, C. H. A. C. de Sá, J. da Luz da Costa, F. S. Afférri and S. C. Siebeneichler, *Rev. Cienc. Agron.*, 2010, **41**, 387–392.

53 N. Barooah, J. Mohanty, H. Pal and A. C. Bhasikuttan, *J. Phys. Chem. B*, 2012, **116**, 3683–3689.

54 R. Khurana, N. Barooah, A. C. Bhasikuttan and J. Mohanty, *Org. Biomol. Chem.*, 2017, **15**, 8448–8457.

55 P. Montes-Navajas, A. Corma and H. Garcia, *ChemPhysChem*, 2008, **9**, 713–720.

56 A. Ulman, *An Introduction to Ultrathin Organic Films: From Langmuir-Blodgett to Self-Assembly*, Elsevier Inc., 2013.

57 C. Vericat, M. E. Vela, G. Benitez, P. Carro and R. C. Salvarezza, *Chem. Soc. Rev.*, 2010, **39**, 1805–1834.

58 C. Vericat, M. E. Vela and R. C. Salvarezza, *Phys. Chem. Chem. Phys.*, 2005, **7**, 3258–3268.

59 S. Nakatsu, Y. Takama, T. Ueno, C. Inuinaka, S. Takeishi, A. Kondo, T. Okitsu, H. Nagashima, M. Fukuzawa and S. Miyagawa, *Transplant. Proc.*, 2012, **44**, 1134–1135.

60 T. Bertok, A. Sediva, J. Katrlik, P. Gemeiner, M. Mikula, M. Nosko and J. Tkac,

Talanta, 2013, **108**, 11–18.

61 B. R. A. Neves, M. E. Salmon, E. B. Troughton and P. E. Russell, *Nanotechnology*, 2001, **12**, 285–289.

62 D. K. Schwartz, *Annu. Rev. Phys. Chem.*, 2001, **52**, 107–137.

63 L. L. Rouhana, M. D. Moussallem and J. B. Schlenoff, *J. Am. Chem. Soc.*, 2011, **133**, 16080–16091.

64 N. T. K. Thanh and L. A. W. Green, *Nano Today*, 2010, **5**, 213–230.

65 H. Schönherr and G. J. Vancso, *Langmuir*, 1997, **13**, 3769–3774.

66 D. G. Castner, K. Hinds and D. W. Grainger, *Langmuir*, 1996, **12**, 5083–5086.

67 M. S. Thompson, T. P. Vadala, M. L. Vadala, Y. Lin and J. S. Riffle, *Polymer (Guildf).*, 2008, **49**, 345–373.

68 R. R. Kolega and J. B. Schlenoff, *Langmuir*, 1998, **14**, 5469–5478.

69 Q. M. Xu, L. J. Wan, C. Wang, C. L. Bai, Z. Y. Wang and T. Nozawa, *Langmuir*, 2001, **17**, 6203–6206.

70 A. D. Filimon, P. Jacob, R. Hergenröder and A. Jürgensen, *Langmuir*, 2012, **28**, 8692–8699.

71 M. Dijksma, B. Kamp, J. C. Hoogvliet and W. P. Van Bennekom, *Langmuir*, 2000, **16**, 3852–3857.

72 J. Zhang, Q. Chi, J. U. Nielsen, E. P. Friis, J. E. T. Andersen and J. Ulstrup, *Langmuir*, 2000, **16**, 7229–7237.

73 P. A. Lewis, R. K. Smith, K. F. Kelly, L. A. Bumm, S. M. Reed, R. S. Clegg, J.

D. Gunderson, J. E. Hutchison and P. S. Weiss, *J. Phys. Chem. B*, 2001, **105**, 10630–10636.

74 S. Y. Oh, Y. J. Yun, D. Y. Kim and S. H. Han, *Langmuir*, 1999, **15**, 4690–4692.

75 E. Cooper and G. J. Leggett, *Langmuir*, 1998, **14**, 4795–4801.

76 E. Delamarche and B. Michel, *Thin Solid Films*, 1996, **273**, 54–60.

77 J. Zhang, Q. Chi, R. R. Nazmutdinov, T. T. Zinkicheva and M. D. Bronshtein, *Langmuir*, 2009, **25**, 2232–2240.

78 J. C. Love, L. A. Estroff, J. K. Kriebel, R. G. Nuzzo and G. M. Whitesides, *Chem. Rev.*, 2005, **105**, 1103–1169.

79 G. L. Liang, D. W. Noid, B. G. Sumpter and B. Wunderlich, *J. Phys. Chem.*, 1994, **98**, 11739–11744.

80 F. Frederix, K. Bonroy, W. Laureyn, G. Reekmans, A. Campitelli, W. Dehaen and G. Maes, *Langmuir*, 2003, **19**, 4351–4357.

81 C. L. Yeunz, P. Iqbal, M. Allan, M. Lashkor, J. A. Preece and P. M. Mendes, *Adv. Funct. Mater.*, 2010, **20**, 2657–2663.

82 D. T. Valley, M. Onstott, S. Malyk and A. V Benderskii, *Langmuir*, 2013, **29**, 11623–11631.

83 A. Pranzetti, S. Mieszkin, P. Iqbal, F. J. Rawson, M. E. Callow, J. A. Callow, P. Koelsch, J. A. Preece and P. M. Mendes, *Adv. Mater.*, 2013, **25**, 2181–2185.

84 J. P. Collman, N. K. Devaraj and C. E. D. Chidsey, *Langmuir*, 2004, **20**, 1051–1053.

85 J. H. Kang, H. J. Choi, S. Y. Hwang, S. H. Han, J. Y. Jeon and E. K. Lee, *J. Chromatogr. A*, 2007, **1161**, 9–14.

86 Y. Jung, M. L. Jeong, H. Jung and H. C. Bong, *Anal. Chem.*, 2007, **79**, 6534–6541.

87 T. L. Ogorzalek, S. Wei, Y. Liu, Q. Wang, C. L. Brooks, Z. Chen and E. N. G. Marsh, *Langmuir*, 2015, **31**, 6145–6153.

88 S. Chen, L. Liu, J. Zhou and S. Jiang, *Langmuir*, 2003, **19**, 2859–2864.

89 C. D. Walkey, J. B. Olsen, H. Guo, A. Emili and W. C. W. Chan, *J. Am. Chem. Soc.*, 2012, **134**, 2139–2147.

90 D. Li, Q. Zheng, Y. Wang and H. Chen, *Polym. Chem.*, 2014, **5**, 14–24.

91 K. Oura, M. Katayama, A. V. Zotov, V. G. Lifshits and A. A. Saranin, 2003, pp. 1–2.

92 L. Vinet and A. Zhedanov, *Biomater. Sci. An Introd. to Mater. Third Ed.*, 2010, 1–1555.

93 J. Meissner, A. Prause, B. Bharti and G. H. Findenegg, *Colloid Polym. Sci.*, 2015, **293**, 3381–3391.

94 A. M. Moulin, S. J. O'Shea, R. A. Badley, P. Doyle and M. E. Welland, *Langmuir*, 1999, **15**, 8776–8779.

95 M. S. Wagner, S. L. McArthur, M. Shen, T. A. Horbett and D. G. Castner, *J. Biomater. Sci. Polym. Ed.*, 2002, **13**, 407–428.

96 F. Hook, P. Brzezinski, M. Rodahl and B. Kasemo, *Proc. Natl. Acad. Sci.*, 1997,

95, 12271–12276.

97 L. Silva, *Curr. Protein Pept. Sci.*, 2005, **6**, 387–395.

98 Q. Wei, T. Becherer, S. Angioletti-Uberti, J. Dzubiella, C. Wischke, A. T. Neffe, A. Lendlein, M. Ballauff and R. Haag, *Angew. Chemie - Int. Ed.*, 2014, **53**, 8004–8031.

99 N. Kumar, O. Parajuli, A. Gupta and J. I. Hahm, *Langmuir*, 2008, **24**, 2688–2694.

100 S. Song, K. Ravensbergen, A. Alabanza, D. Soldin and J. I. Hahm, *ACS Nano*, 2014, **8**, 5257–5269.

101 D. R. Absolom, W. Zingg and A. W. Neumann, *J. Biomed. Mater. Res.*, 1987, **21**, 161–171.

102 N. Dragneva, O. Rubel and W. B. Floriano, *J. Chem. Inf. Model.*, 2016, **56**, 706–720.

103 L. Tang, T. P. Ugarova, E. F. Plow and J. W. Eaton, *J. Clin. Invest.*, 1996, **97**, 1329–1334.

104 X. Zhang, C. Helbing, M. M. L. Arras, K. D. Jandt and I. Firkowska-Boden, *Langmuir*, 2017, **33**, 6563–6571.

105 P. Roach, D. Farrar and C. C. Perry, *J. Am. Chem. Soc.*, 2006, **128**, 3939–3945.

106 D. Fine, A. Grattoni, R. Goodall, S. S. Bansal, C. Chiappini, S. Hosali, A. L. van de Ven, S. Srinivasan, X. Liu, B. Godin, L. Brousseau, I. K. Yazdi, J. Fernandez-Moure, E. Tasciotti, H. J. Wu, Y. Hu, S. Klemm and M. Ferrari, *Adv. Healthc.*

Mater., 2013, **2**, 632–666.

107 Y. Zhukova and E. V. Skorb, *Adv. Healthc. Mater.*, 2017, **6**, 1–18.

108 M. Kurylowicz, H. Paulin, J. Mogyoros, M. Giuliani and J. R. Dutcher, *J. R. Soc. Interface*, 2014, **11**, 1–9.

109 C. P. Shaw, D. A. Middleton, M. Volk and R. Lévy, *ACS Nano*, 2012, **6**, 1416–1426.

110 M. Hulander, A. Lundgren, M. Berglin, M. Ohrlander, J. Lausmaa and H. Elwing, *Int. J. Nanomedicine*, 2011, **6**, 2653–2666.

111 G. Raffaini and F. Ganazzoli, *Langmuir*, 2013, **29**, 4883–4893.

112 Z. Gu, Z. Yang, Y. Chong, C. Ge, J. K. Weber, D. R. Bell and R. Zhou, *Sci. Rep.*, 2015, **5**, 10886.

113 A. A. Vertegel, R. W. Siegel and J. S. Dordick, *Langmuir*, 2004, **20**, 6800–6807.

114 N. Giamblanco, E. Martines and G. Marletta, *Langmuir*, 2013, **29**, 8335–8342.

115 S. Höhn, S. Virtanen and A. R. Boccaccini, *Appl. Surf. Sci.*, 2019, **464**, 212–219.

116 S. E. Harandi, P. C. Banerjee, C. D. Easton and R. K. Singh Raman, *Mater. Sci. Eng. C*, 2017, **80**, 335–345.

117 A. Yamamoto and S. Hiromoto, *Mater. Sci. Eng. C*, 2009, **29**, 1559–1568.

118 J. McColl, G. E. Yakubov and J. J. Ramsden, *Langmuir*, 2007, **23**, 7096–7100.

119 L. Y. Cui, X. T. Li, R. C. Zeng, S. Q. Li, E. H. Han and L. Song, *Front. Mater. Sci.*, 2017, **11**, 284–295.

120 R. C. Zeng, X. T. Li, S. Q. Li, F. Zhang and E. H. Han, *Sci. Rep.*, 2015, **5**, 13026.

121 C. Liu, Y. Xin, X. Tian and P. K. Chu, *J. Mater. Res.*, 2007, **22**, 1806–1814.

122 P. Roach, D. Farrar and C. C. Perry, *J. Am. Chem. Soc.*, 2005, **127**, 8168–8173.

123 V. Tangpasuthadol, N. Pongchaisirikul and V. P. Hoven, *Carbohydr. Res.*, 2003, **338**, 937–942.

124 M. M. Ouberai, K. Xu and M. E. Welland, *Biomaterials*, 2014, **35**, 6157–6163.

125 K. Rechendorff, M. B. Hovgaard, M. Foss, V. P. Zhdanov and F. Besenbacher, *Langmuir*, 2006, **22**, 10885–10888.

126 I. Kiesel, M. Paulus, J. Nase, S. Tiemeyer, C. Sternemann, K. Rüster, F. J. Wirkert, K. Mende, T. Büning and M. Tolan, *Langmuir*, 2014, **30**, 2077–2083.

127 D. Sarkar and D. K. Chattoraj, *J. Colloid Interface Sci.*, 1996, **178**, 606–613.

128 K. Kolman, M. M. Makowski, A. A. Golriz, M. Kappl, J. Pigłowski, H. J. Butt and A. Kiersnowski, *Langmuir*, 2014, **30**, 11650–11659.

129 M. Paga´n, D. Suazo, N. del Toro and K. Griebenow, *Biosens. Bioelectron.*, 2014, **64**, 138–146.

130 T. Heck, G. Faccio, M. Richter and L. Thöny-Meyer, *Appl. Microbiol. Biotechnol.*, 2013, 97, 461–475.

131 T. Ito, R. Sadamoto, K. Naruchi, H. Togame, H. Takemoto, H. Kondo and S. I. Nishimura, *Biochemistry*, 2010, **49**, 2604–2614.

132 M. P. Madej, G. Coia, C. C. Williams, J. M. Caine, L. A. Pearce, R. Attwood, N. A. Bartone, O. Dolezal, R. M. Nisbet, S. D. Nuttall and T. E. Adams, *Biotechnol.*

Bioeng., 2012, **109**, 1461–1470.

133 S. R. Ahmed, A. T. Lutes and T. A. Barbari, *J. Memb. Sci.*, 2006, **282**, 311–321.

134 G. Faccio, S. Senkalla, L. Thöny-Meyer and M. Richter, 2015, **5**, 22319–22325.

135 G. Faccio, M. M. Kämpf, C. Piatti, L. Thöny-Meyer and M. Richter, *Sci. Rep.*, 2014, **4**, 5370.

136 J. Tominaga, N. Kamiya, S. Doi, H. Ichinose, T. Maruyama and M. Goto, *Biomacromolecules*, 2005, **6**, 2299–2304.

137 M. Campàs, B. Prieto-Simón and J. L. Marty, *Semin. Cell Dev. Biol.*, 2009, 20, 3–9.

138 C. Gauchet, G. R. Labadie and C. D. Poulter, *J. Am. Chem. Soc.*, 2006, **128**, 9274–9275.

139 T. Liu, Y. Wang, X. Luo, J. Li, S. A. Reed, H. Xiao, T. S. Young and P. G. Schultz, *Proc. Natl. Acad. Sci.*, 2016, **113**, 5910–5915.

140 Y. Ge, X. Fan and P. R. Chen, *Chem. Sci.*, 2016, **7**, 7055–7060.

141 S. Ye, C. Köhrer, T. Huber, M. Kazmi, P. Sachdev, E. C. Yan, A. Bhagat, U. L. RajBhandary and T. P. Sakmar, *J. Biol. Chem.*, 2008, **283**, 1525–1533.

142 B. K. Raliski, C. A. Howard and D. D. Young, *Bioconjug. Chem.*, 2014, **25**, 1916–1920.

143 N. G. Welch, J. A. Scoble, B. W. Muir and P. J. Pigram, *Biointerphases*, 2017, **12**, 02D301.

144 J. W. W. Studd, J. S. Crawford, N. M. Duignan, C. J. F. Rowbotham and A. O.

Hughes, *BJOG An Int. J. Obstet. Gynaecol.*, 1980, **87**, 1015–1021.

145 V. Crivianu-Gaita, A. Romaschin and M. Thompson, *Biochem. Biophys. Reports*, 2015, **2**, 23–28.

146 B. Lim, J. I. Park, K. J. Lee, J. W. Lee, T. W. Kim and Y. P. Kim, *Sensors*, 2015, **15**, 17977–17989.

147 T. W. Cha, A. Quo and X. Y. Zhu, *Proteomics*, 2005, **5**, 416–419.

148 S. M. Tomásio and T. R. Walsh, *J. Phys. Chem. C*, 2009, **113**, 8778–8785.

149 S. Wang, E. S. Humphreys, S. Y. Chung, D. F. Delduco, S. R. Lustig, H. Wang, K. N. Parker, N. W. Rizzo, S. Subramoney, Y. M. Chiang and A. Jagota, *Nat. Mater.*, 2003, **2**, 196–200.

150 T. Serizawa, K. Iida, H. Matsuno and K. Kurita, *Chem. Lett.*, 2007, **36**, 988–989.

151 Y. Kumada, Y. Tokunaga, H. Imanaka, K. Imamura, T. Sakiyama, S. Katoh and K. Nakanishi, *Biotechnol. Prog.*, 2006, **22**, 401–405.

152 E. M. Krauland, B. R. Peelle, K. D. Wittrup and A. M. Belcher, *Biotechnol. Bioeng.*, 2007, **97**, 1009–1020.

153 T. J. Park, S. Y. Lee, S. J. Lee, J. P. Park, K. S. Yang, K. B. Lee, S. Ko, J. B. Park, T. Kim, S. K. Kim, Y. B. Shin, B. H. Chung, S. J. Ku, D. H. Kim and I. S. Choi, *Anal. Chem.*, 2006, **78**, 7197–7205.

154 M. Ganesana, G. Istarnboulie, J. L. Marty, T. Noguer and S. Andreescu, *Biosens. Bioelectron.*, 2011, **30**, 43–48.

155 K. Zhang, M. R. Diehl and D. A. Tirrell, *J. Am. Chem. Soc.*, 2005, **127**, 10136–

10137.

156 Z. Naal, J. H. Park, S. Bernhard, J. P. Shapleigh, C. A. Batt and H. D. Abruña, *Anal. Chem.*, 2002, **74**, 140–148.

157 B. W. Berger and N. D. Sallada, *J. Biol. Eng.*, 2019, **13**, 10–15.

158 M. Soikkeli, K. Kurppa, M. Kainlauri, S. Arpiainen, A. Paananen, D. Gunnarsson, J. J. Joensuu, P. Laaksonen, M. Prunnila, M. B. Linder and J. Ahopelto, *ACS Appl. Mater. Interfaces*, 2016, **8**, 8257–8264.

159 M. Qin, L. K. Wang, X. Z. Feng, Y. L. Yang, R. Wang, C. Wang, L. Yu, B. Shao and M. Q. Qiao, *Langmuir*, 2007, **23**, 4465–4471.

160 M. S. Grunér, G. R. Szilvay, M. Berglin, M. Lienemann, P. Laaksonen and M. B. Linder, *Langmuir*, 2012, **28**, 4293–4300.

161 M. Graille, E. A. Stura, A. L. Corper, B. J. Sutton, M. J. Taussig, J.-B. Charbonnier and G. J. Silverman, *Proc. Natl. Acad. Sci.*, 2000, **97**, 5399–5404.

162 J. Sjöhol, *Eur. J. Biochem.*, 1975, **51**, 55–61.

163 M. C. Coen, R. Lehmann, P. Gröning, M. Bielmann, C. Galli and L. Schlapbach, *J. Colloid Interface Sci.*, 2001, **233**, 180–189.

164 A. Karimzadeh, M. Hasanzadeh, N. Shadjou and M. de la Guardia, *TrAC Trends Anal. Chem.*, 2018, **107**, 1–20.

165 H. R. Culver, J. R. Clegg and N. A. Peppas, *Acc. Chem. Res.*, 2017, **50**, 170–178.

166 W. Lu, X. Le, J. Zhang, Y. Huang and T. Chen, *Chem. Soc. Rev.*, 2017, **46**, 1284–1294.

167 Y. C. Qian, P. C. Chen, G. J. He, X. J. Huang and Z. K. Xu, *Molecules*, 2014, **19**, 9850–9863.

168 X. Tong, S. Lee, L. Bararpour and F. Yang, *Macromol. Biosci.*, 2015, **15**, 1679–1686.

169 C. Fan, Q. Gao, D. Zhu, G. Wagner and G. Li, *Analyst*, 2001, **126**, 1086–1089.

170 S. Tan, X. Tan, J. Xu, D. Zhao, J. Zhang and L. Liu, *Anal. Methods*, 2011, **3**, 110–115.

171 J. C. Chen, J. C. Chou, T. P. Sun and S. K. Hsiung, *Sensors Actuators, B Chem.*, 2003, **91**, 180–186.

172 H. chung Tsai and R. an Doong, *Biosens. Bioelectron.*, 2007, **23**, 66–73.

173 K. Omidfar, A. Dehdast, H. Zarei, B. K. Sourkohi and B. Larijani, *Biosens. Bioelectron.*, 2011, **26**, 4177–4183.

174 S. K. Jha, A. Topkar and S. F. D'Souza, *J. Biochem. Biophys. Methods*, 2008, **70**, 1145–1150.

175 T. Bertok, P. Gemeiner, M. Mikula, P. Gemeiner and J. Tkac, *Microchim. Acta*, 2013, **180**, 151–159.

176 C. S. Pundir, B. Sandeep Singh and J. Narang, *Clin. Biochem.*, 2010, **43**, 467–472.

177 Y. C. Tsai, J. D. Huang and C. C. Chiu, *Biosens. Bioelectron.*, 2007, **22**, 3051–3056.

178 J. Pang, C. Fan, X. Liu, T. Chen and G. Li, *Biosens. Bioelectron.*, 2003, **19**, 441–

445.

179 S. Lowe, N. M. O'Brien-Simpson and L. A. Connal, *Polym. Chem.*, 2015, **6**, 198–212.

180 T. Riedel, Z. Riedelová-Reicheltová, P. Májek, C. Rodriguez-Emmenegger, M. Houska, J. E. Dyr and E. Brynda, *Langmuir*, 2013, **29**, 3388–3397.

181 E. M. Muñoz, H. Yu, J. Hallock, R. E. Edens and R. J. Linhardt, *Anal. Biochem.*, 2005, **343**, 176–178.

182 H. R. Kermis, Y. Kostov, P. Harms and G. Rao, *Biotechnol. Prog.*, 2002, **18**, 1047–1053.

183 H. Vaisocherová, E. Brynda and J. Homola, *Anal. Bioanal. Chem.*, 2015, **407**, 3927–3953.

184 S. Elhag, K. Khun, V. Khranovskyy, X. Liu, M. Willander and O. Nur, *Sensors*, 2016, **16**, 222–225.

185 A. Jain, A. Homayoun, C. W. Bannister and K. Yum, *Biotechnol. J.*, 2015, **10**, 447–459.

186 V. K. Yadavalli, W. G. Koh, G. J. Lazur and M. V. Pishko, *Sensors Actuators, B Chem.*, 2004, **97**, 290–297.

187 A. Al-Halhouli, S. Demming, L. Alahmad, A. Liobera and S. Büttgenbach, *Sensors (Switzerland)*, 2014, **14**, 15749–15759.

188 F. Wang, M. Anderson, M. T. Bernards and H. K. Hunt, *Sensors (Switzerland)*, 2015, **15**, 18040–18060.

189 E. Gibon, D. F. Amanatullah, F. Loi, J. Pajarinen, A. Nabeshima, Z. Yao, M. Hamadouche and S. B. Goodman, *J. Biomed. Mater. Res. Part B Appl. Biomater.*, 2017, **105**, 2162–2173.

190 A. J. Zaitouna, J. Joyce, R. L. Cerny, P. H. Dussault and R. Y. Lai, *Anal. Chem.*, 2015, **87**, 6966–6973.

191 M. Veerapandian, Y. T. Seo, K. Yun and M. H. Lee, *Biosens. Bioelectron.*, 2014, **58**, 200–204.

192 H. Akbulut, G. Bozokalfa, D. N. Asker, B. Demir, E. Guler, D. Odaci Demirkol, S. Timur and Y. Yagci, *ACS Appl. Mater. Interfaces*, 2015, **7**, 20612–20622.

193 M. Cui, Z. Song, Y. Wu, B. Guo, X. Fan and X. Luo, *Biosens. Bioelectron.*, 2016, **79**, 736–741.

194 D. P. O'Neal, M. A. Meledeo, J. R. Davis, B. L. Ibey, V. A. Gant, M. V. Pishko and G. L. Coté, *IEEE Sens. J.*, 2004, **4**, 728–734.

195 N. Ahmad, J. Abdullah, N. Yusof, A. Ab Rashid, S. Abd Rahman and M. Hasan, *Biosensors*, 2016, **6**, 31–35.

196 J. Enomoto, Z. Matharu and A. Revzin, *Methods Enzymol.*, 2013, **526**, 107–121.

197 C. Sun, J. Miao, J. Yan, K. Yang, C. Mao, J. Ju and J. Shen, *Electrochim. Acta*, 2013, **89**, 549–554.

198 L.-C. Su, Y.-C. Tian, Y.-F. Chang, C. Chou and C.-S. Lai, *J. Biomed. Opt.*, 2013, **19**, 011013.

199 S. Li, D. Zhang, Q. Zhang, Y. Lu, N. Li, Q. Chen and Q. Liu, *Sensors Actuators*,

B Chem., 2016, **232**, 219–225.

200 N. Li, L. Qi, Y. Shen, J. Qiao and Y. Chen, *ACS Appl. Mater. Interfaces*, 2014, **6**, 17289–17295.

201 S. Lee, B. L. Ibey, G. L. Coté and M. V. Pishko, *Sensors Actuators, B Chem.*, 2008, **128**, 388–398.

202 M. J. Yin, M. Yao, S. Gao, A. P. Zhang, H. Y. Tam and P. K. A. Wai, *Adv. Mater.*, 2016, **28**, 1394–1399.

203 P. Kasák, J. Mosnáček, M. Danko, I. Krupa, G. Hloušková, D. Chorvát, M. Koukaki, S. Karamanou, A. Economou and I. Lacík, *RSC Adv.*, 2016, **6**, 83890–83900.

204 F. Audouin, R. Larragy, M. Fox, B. O'Connor and A. Heise, *Biomacromolecules*, 2012, **13**, 3787–3794.

205 J. T. Suri, D. B. Cordes, F. E. Cappuccio, R. A. Wessling and B. Singaram, *Angew. Chemie - Int. Ed.*, 2003, **42**, 5857–5859.

206 X. Yang, X. Pan, J. Blyth and C. R. Lowe, *Biosens. Bioelectron.*, 2008, **23**, 899–905.

207 B. Vilozny, A. Schiller, R. A. Wessling and B. Singaram, *J. Mater. Chem.*, 2011, **21**, 7589–7595.

208 A. M. L. Nickel, F. Seker, B. P. Ziemer and A. B. Ellis, *Chem. Mater.*, 2001, **13**, 1391–1397.

209 Bin Ding, M. Kikuchi, M. Yamazaki and S. Shiratori, in *Proceedings of IEEE*

Sensors, 2004., IEEE, 2004, pp. 685–688.

210 S. Singh and B. D. Gupta, *Sensors Actuators B*, 2012, **173**, 268–273.

211 S. Herber, J. Bomer, W. Olthuis, P. Bergveld and A. van den Berg, *Biomed. Microdevices*, 2005, **7**, 197–204.

212 J. Z. Hilt, A. K. Gupta, R. Bashir and N. A. Peppas, *Biomed. Microdevices*, 2003, **5**, 177–184.

213 J. Sorber, G. Steiner, V. Schulz, M. Guenther, G. Gerlach, R. Salzer and K. F. Arndt, *Anal. Chem.*, 2008, **80**, 2957–2962.

214 E. M. Ahmed, *J. Adv. Res.*, 2015, **6**, 105–21.

215 L. Ionov, *Mater. Today*, 2014, **17**, 494–503.

216 M. R. Romero, D. Peralta, C. I. Alvarez Igarzabal, A. M. Baruzzi, M. C. Strumia and F. Garay, *Sensors Actuators, B Chem.*, 2017, **244**, 577–584.

217 T. Yang, M. Chen, Q. Kong, X. Luo and K. Jiao, *Biosens. Bioelectron.*, 2017, **89**, 538–544.

218 M. Choudhary, R. Brink, D. Nandi, S. Siwal and K. Mallick, *J. Mater. Sci.*, 2017, **52**, 770–781.

219 H. Wang, H. Han and Z. Ma, *Bioelectrochemistry*, 2017, **114**, 48–53.

220 D. I. Torres, M. V. Miranda and V. Campo Dall' Orto, *Sensors Actuators, B Chem.*, 2017, **239**, 1016–1025.

221 K. Van Nguyen, Y. Holade and S. D. Minteer, *ACS Catal.*, 2016, **6**, 2603–2607.

222 Z. Wang, Z. Wang, H. Zhang, X. Duan, J. Xu and Y. Wen, *RSC Adv.*, 2015, **5**,

12237–12247.

223 K. S. Masters, *Macromol. Biosci.*, 2011, **11**, 1149–1163.

224 L. L. Y. Chiu and M. Radisic, *Biomaterials*, 2010, **31**, 226–241.

225 Y. J. Park, K. H. Kim, J. Y. Lee, Y. Ku, S. J. Lee, B. M. Min and C. P. Chung, *Biotechnol. Appl. Biochem.*, 2006, **43**, 17.

226 H. E. Davis, E. M. Case, S. L. Miller, D. C. Genetos and J. K. Leach, *Biotechnol. Bioeng.*, 2011, **108**, 2727–2735.

227 D. Odedra, L. L. Y. Chiu, M. Shoichet and M. Radisic, *Acta Biomater.*, 2011, **7**, 3027–35.

228 K. Moore, M. Macsween and M. Shoichet, *Tissue Eng.*, 2006, **12**, 267–278.

229 Y. Miyagi, L. L. Y. Chiu, M. Cimini, R. D. Weisel, M. Radisic and R. K. Li, *Biomaterials*, 2011, **32**, 1280–1290.

230 J. S. Choi, K. W. Leong and H. S. Yoo, *Biomaterials*, 2008, **29**, 587–596.

231 K. Alberti, R. E. Davey, K. Onishi, S. George, K. Salchert, F. P. Seib, M. Bornhäuser, T. Pompe, A. Nagy, C. Werner and P. W. Zandstra, *Nat. Methods*, 2008, **5**, 645–650.

232 L. Almany and D. Seliktar, *Biomaterials*, 2005, **26**, 2467–2477.

233 M. Gonen-Wadmany, L. Oss-Ronen and D. Seliktar, *Biomaterials*, 2007, **28**, 3876–3886.

234 Y. Z. Zhang, J. Venugopal, Z. M. Huang, C. T. Lim and S. Ramakrishna, *Biomacromolecules*, 2005, **6**, 2583–2589.

235 M. Ngiam, S. Liao, A. J. Patil, Z. Cheng, F. Yang, M. J. Gubler, S. Ramakrishna and C. K. Chan, *Tissue Eng Part A*, 2009, **15**, 535–546.

236 W. Yu, W. Zhao, C. Zhu, X. Zhang, D. Ye, W. Zhang, Y. Zhou, X. Jiang and Z. Zhang, *BMC Neurosci.*, 2011, **12**, 68–72.

237 S. S. Liao and F. Z. Cui, *Tissue Eng.*, 2004, **10**, 73–80.

238 S. S. Liao, F. Z. Cui, W. Zhang and Q. L. Feng, *J. Biomed. Mater. Res. - Part B Appl. Biomater.*, 2004, **69**, 158–165.

239 J.-P. Chen, S.-F. Li and Y.-P. Chiang, *J. Nanosci. Nanotechnol.*, 2010, **10**, 5393–5398.

240 S. S. Silva, J. F. Mano and R. L. Reis, *Crit. Rev. Biotechnol.*, 2010, **30**, 200–221.

241 T. Jiao, B. D. Leca-Bouvier, P. Boullanger, L. J. Blum and A. P. Girard-Egrot, *Colloids Surfaces A Physicochem. Eng. Asp.*, 2010, **354**, 284–290.

242 H. Guan, F. Zhang, J. Yu and D. Chi, *Food Res. Int.*, 2012, **49**, 15–21.

243 S. Bratakou, G. P. Nikoleli, D. P. Nikolelis and N. Psaroudakis, *Electroanalysis*, 2015, **27**, 2608–2613.

244 D. P. Nikolelis and M. Mitrokotsa, *Biosens. Bioelectron.*, 2002, **17**, 565–572.

245 Y. Murakami, Z. Zhang, T. Taniguchi, M. Sohgawa, K. Yamashita and M. Noda, *Procedia Eng.*, 2016, **168**, 565–568.

246 C. G. Siontorou and K. N. Georgopoulos, *J. Clean. Prod.*, 2016, **111**, 133–142.

247 L. Zheng, L. Xiong, D. Zheng, Y. Li, Q. Liu, K. Han, W. Liu, K. Tao, S. Yang and J. Xia, *Talanta*, 2011, **85**, 43–48.

248 J. S. Graça, R. F. de Oliveira, M. L. de Moraes and M. Ferreira, *Bioelectrochemistry*, 2014, **96**, 37–42.

249 M. B. Fritzen-Garcia, V. C. Zoldan, I. R. W. Z. Oliveira, V. Soldi, A. A. Pasa and T. B. Creczynski-Pasa, *Biotechnol. Bioeng.*, 2013, **110**, 374–382.

250 G. P. Nikoleli, D. P. Nikolelis, N. Tzamtzis and N. Psaroudakis, *Electroanalysis*, 2014, **26**, 1522–1527.

251 D. P. Nikolelis, M. G. Simantiraki, C. G. Siontorou and K. Toth, *Anal. Chim. Acta*, 2005, **537**, 169–177.

252 G. Gopalakrishnan, I. Rouiller, D. R. Colman and R. B. Lennox, *Langmuir*, 2009, **25**, 5455–5458.

253 C. G. Siontorou, in *Advanced Bioelectronic Materials*, John Wiley & Sons, Inc., Hoboken, NJ, USA, 2015, pp. 309–353.

254 D. P. Nikolelis, G. Raftopoulou, M. Simantiraki, N. Psaroudakis, G. P. Nikoleli and T. Hianik, *Anal. Chim. Acta*, 2008, **620**, 134–141.

255 O. G. Weingart and M. J. Loessner, *Toxicol. Appl. Pharmacol.*, 2016, **313**, 16–23.

256 H. Suzuki, K. V. Tabata, H. Noji and S. Takeuchi, *Biosens. Bioelectron.*, 2007, **22**, 1111–1115.

257 A. Hirano-Iwata, M. Niwano and M. Sugawara, *TrAC Trends Anal. Chem.*, 2008, **27**, 512–520.

258 C. G. Siontorou and F. A. Batzias, *Crit. Rev. Biotechnol.*, 2010, **30**, 79–98.

259 C. G. Siontorou, D. P. Nikolelis, U. J. Krull and K. L. Chiang, *Anal. Chem.*, 1997, **69**, 3109–3114.

260 Z. Zhang, M. Sohgawa, K. Yamashita and M. Noda, *Sensors Actuators, B Chem.*, 2016, **236**, 893–899.

261 D. P. Nikolelis and G. Theoharis, *Electroanalysis*, 2002, **14**, 1661–1667.

262 S. Majd, E. C. Yusko, Y. N. Billeh, M. X. Macrae, J. Yang and M. Mayer, *Curr. Opin. Biotechnol.*, 2010, **21**, 439–476.

263 D. P. Nikolelis, C. G. Siontorou, U. J. Krull and P. L. Katrivanos, *Anal. Chem.*, 1996, **68**, 1735–1741.

264 P. Gurnev and E. Nestorovich, *Toxins (Basel).*, 2014, **6**, 2483–2540.

265 L. C. Kam, *J. Struct. Biol.*, 2009, **168**, 3–10.

266 D. Wasserberg, J. Cabanas-Danés, J. Prangsma, S. O'Mahony, P.-A. Cazade, E. Tromp, C. Blum, D. Thompson, J. Huskens, V. Subramaniam and P. Jonkheijm, *ACS Nano*, 2017, **11**, 9068–9083.

267 N. L. Weineisen, C. A. Hommersom, J. Voskuhl, S. Sankaran, A. M. A. Depauw, N. Katsonis, P. Jonkheijm and J. J. L. M. Cornelissen, *Chem. Commun.*, 2017, **53**, 1896–1899.

268 D. Wasserberg, J. Cabanas-Danés, V. Subramaniam, J. Huskens and P. Jonkheijm, *Chem. Commun.*, 2018, **54**, 1615–1618.

269 J. F. Young, H. D. Nguyen, L. Yang, J. Huskens, P. Jonkheijm and L. Brunsveld, *ChemBioChem*, 2010, **11**, 180–183.

270 W. Zhan, T. Wei, Q. Yu and H. Chen, *ACS Appl. Mater. Interfaces*, 2018, **10**, 36585–36601.

271 Y. Zhang, Q. Tu, D.-E. Wang, Y. Chen, B. Lu, M.-S. Yuan and J. Wang, *New J. Chem.*, 2013, **37**, 2358–2364.

272 D. O. Demirkol, H. B. Yildiz, S. Sayın and M. Yilmaz, *RSC Adv.*, 2014, **4**, 19900–19907.

273 A. González-Campo, M. Brasch, D. A. Uhlenheuer, A. Gómez-Casado, L. Yang, L. Brunsveld, J. Huskens and P. Jonkheijm, *Langmuir*, 2012, **28**, 16364–16371.

274 Y. Lee, E. K. Lee, Y. W. Cho, T. Matsui, I.-C. Kang, T.-S. Kim and M. H. Han, *Proteomics*, 2003, **3**, 2289–2304.

275 Y. Qu, T. Wei, W. Zhan, C. Hu, L. Cao, Q. Yu and H. Chen, *J. Mater. Chem. B*, 2017, **5**, 444–453.

276 S. Van Dun, C. Ottmann, L. G. Milroy and L. Brunsveld, *J. Am. Chem. Soc.*, 2017, **139**, 13960–13968.

277 M. P. Conte, K. H. A. Lau and R. V. Ulijn, *ACS Appl. Mater. Interfaces*, 2017, **9**, 3266–3271.

278 E. Krieg, S. Albeck, H. Weissman, E. Shimoni and B. Rybtchinski, *PLoS One*, 2013, **8**, 63188–63195.

279 T. D. Martins, A. C. C. Ribeiro, F. Colmati, G. A. de Souza, H. S. de Camargo, D. L. Dias, P. A. da C. Filho and D. de S. Cordeiro, *Supramolecular Materials for Optical and Electrochemical Biosensors*, InTech, 2015.

280 V. Martos, P. Castreño, J. Valero and J. de Mendoza, *Curr. Opin. Chem. Biol.*, 2008, **12**, 698–706.

281 W. Zhan, T. Wei, L. Cao, C. Hu, Y. Qu, Q. Yu and H. Chen, *ACS Appl. Mater. Interfaces*, 2017, **9**, 3505–3513.

282 M. L. Rennie, G. C. Fox, J. Pérez and P. B. Crowley, *Angew. Chemie Int. Ed.*, 2018, **57**, 13764–13769.

283 W. Li, A. T. Bockus, B. Vinciguerra, L. Isaacs and A. R. Urbach, *Chem. Commun.*, 2016, **52**, 8537–8540.

284 K. L. Mittal, *Advances in Contact Angle, Wettability and Adhesion*, Scrivener/Wiley, 2015.

285 J. Kasanen, J. Salstela, M. Suvanto and T. T. Pakkanen, *Applied Surface Science*, Taylor & Francis, 2011, vol. 258.

286 Z. Shi, Y. Zhang, M. Liu, D. A. H. Hanaor and Y. Gan, *Colloids Surfaces A Physicochem. Eng. Asp.*, 2018, **555**, 365–371.

287 C. J. van Oss and I. H. J. Busscher, *Colloids Surfaces B Biointerfaces*, 2002, **9**, 121–125.

288 P. M. A. Sherwood, *Anal. Bioanal. Chem.*, 2013, **405**, 2415–2416.

289 P. van der Heide, *X-Ray Photoelectron Spectroscopy: An Introduction to Principles and Practices*, John Wiley & Sons, Inc., Hoboken, NJ, USA, 2011.

290 S. Oswald, in *Encyclopedia of Analytical Chemistry*, John Wiley & Sons, Ltd, Chichester, UK, 2013.

291 D. D. Sarma, P. K. Santra, S. Mukherjee and A. Nag, *Chem. Mater.*, 2013, **25**, 1222–1232.

292 N. H. Turner, *Appl. Spectrosc. Rev.*, 2000, **35**, 203–254.

293 J. Q. Zhong, M. Wang, W. H. Hoffmann, M. A. Van Spronsen, D. Lu and J. A. Boscoboinik, *Appl. Phys. Lett.*, 2018, **112**, 091602.

294 H. Fujiwara, *Spectroscopic Ellipsometry*, John Wiley & Sons, Ltd, Chichester, UK, 2007.

295 H. Tompkins, E.A. Irene *Handbook of Ellipsometry*, 2005.

296 R. Pascu and M. Dinescu, *Spectroscopic ellipsometry*, 2012.

297 K. S. Phillips and Q. J. Cheng, in *Molecular Biomethods Handbook*, Humana Press, Totowa, NJ, 2008, pp. 809–820.

298 J. Homola, S. S. Yee and G. Gauglitz, *Sensors Actuators B Chem.*, 1999, **54**, 3–15.

299 J. Zhao, X. Zhang, C. R. Yonzon, A. J. Haes and R. P. Van Duyne, *Nanomedicine*, 2006, **1**, 219–228.

300 P. Pattnaik, *Appl. Biochem. Biotechnol.*, 2005, **126**, 79–92.

301 J. Homola and M. Piliarik, in *Surface Plasmon Resonance (SPR) Sensors*, 2006, pp. 45–67.

302 J. Homola, *Chem. Rev.*, 2008, **108**, 462–493.

303 E. Petryayeva and U. J. Krull, *Anal. Chim. Acta*, 2011, **706**, 8–24.

304 C. C. Fong, W. P. Lai, Y. C. Leung, S. C. L. Lo, M. S. Wong and M. Yang, *Biochim. Biophys. Acta - Protein Struct. Mol. Enzymol.*, 2002, **1596**, 95–107.

305 G. J. Wegner, A. W. Wark, H. J. Lee, E. Codner, T. Saeki, S. Fang and R. M. Corn, *Anal. Chem.*, 2004, **76**, 5677–5684.

306 C. J. Day, L. E. Hartley-Tassell and V. Korolik, in *Methods in Molecular Biology*, Humana Press, New York, NY, 2017, vol. 1512, pp. 51–63.

307 C. J. Day and V. Korolik, in *Methods in Molecular Biology*, Humana Press, New York, NY, 2018, vol. 1729, pp. 303–317.

308 S. Hearty, P. Leonard, H. Ma and R. O'Kennedy, in *Methods in Molecular Biology*, Humana Press, Totowa, NJ, 2018, vol. 1827, pp. 421–455.

309 F. Marken, A. Neudeck and A. M. Bond, in *Electroanalytical Methods*, Springer Berlin Heidelberg, Berlin, Heidelberg, 2010, pp. 57–106.

310 N. Elgrishi, K. J. Rountree, B. D. McCarthy, E. S. Rountree, T. T. Eisenhart and J. L. Dempsey, *J. Chem. Educ.*, 2018, **95**, 197–206.

311 L. Leonat, G. Sbârcea and I. V. Branzoi, *UPB Sci. Bull. Ser. B Chem. Mater. Sci.*

312 J. F. Rusling and S. L. Suib, *Adv. Mater.*, 1994, **6**, 922–930.

313 C. Costentin and J.-M. Saveant, *J. Phys. Chem. C*, 2015, **119**, 12174–12182.

314 A. Ishitani, *Kobunshi*, 1994, **43**, 90–97.

315 D. Pleul and F. Simon, in *Polymer Surfaces and Interfaces*, Springer Berlin Heidelberg, Berlin, Heidelberg, 2008, pp. 91–102.

316 T. Henkel and J. Gilmour, in *Treatise on Geochemistry*, Elsevier, 2014, pp. 411–424.

317 A. M. Belu, D. J. Graham and D. G. Castner, *Biomaterials*, 2003, **24**, 3635–3653.

318 A. V. Walker, in *Encyclopedia of Spectroscopy and Spectrometry*, Elsevier, 2017, pp. 44–49.

319 L. Dubrovinsky, N. Dubrovinskaia, E. Bykova, M. Bykov, V. Prakapenka, C. Prescher, K. Glazyrin, H. P. Liermann, M. Hanfland, M. Ekholm, Q. Feng, L. V. Pourovskii, M. I. Katsnelson, J. M. Wills and I. A. Abrikosov, *Nature*, 2015, **525**, 226–229.

320 C. L. Harper, S. B. Jacobsen, B. G. Pfrommer, F. Mauri, S. G. Louie and R. Jeanloz, *Science (80-.).*, 1996, **273**, 1814–1818.

321 R. P. Dias and I. F. Silvera, *Science (80-.).*, 2017, **355**, 715–718.

322 M. I. Eremets, R. J. Hemley, H. K. Mao and E. Gregoryanz, *Nature*, 2001, **411**, 170–174.

323 V. V. Struzhkin, M. S. Somayazulu, R. J. Hemley, A. F. Goncharov and H. K. Mao, *Science (80-.).*, 2006, **273**, 218–220.

324 M. I. Eremets and I. A. Troyan, *Nat. Mater.*, 2011, **10**, 927–931.

325 A. Dewaele, P. Loubeyre, F. Occelli, O. Marie and M. Mezouar, *Nat. Commun.*, 2018, **9**, 2913–2916.

326 J. Couzin, *Science (80-.).*, 2002, **295**, 1444b – 1445.

327 D. R. Lide, in *A Century of Excellence in MEASUREMENTS, STANDARDS, and*

TECHNOLOGY, ed. D. R. Lide, CRC Press, 2018, pp. 100–103.

328 A. Jayaraman, *Rev. Sci. Instrum.*, 1986, **57**, 1013–1031.

329 J. F. Lin, J. Shu, H. K. Mao, R. J. Hemley and G. Shen, *Rev. Sci. Instrum.*, 2003, **74**, 4732–4736.

330 N. Funamori and T. Sato, *Rev. Sci. Instrum.*, 2008, **79**, 053903.

331 G. Zou, Y. Ma, H. K. Mao, R. J. Hemley and S. A. Gramsch, *Rev. Sci. Instrum.*, 2001, **72**, 1298–1301.

332 K. Syassen, *High Press. Res.*, 2008, **28**, 75–126.

333 R. Boehler, *Rev. Sci. Instrum.*, 2006, **77**, 115–118.

334 J. Y. Zhao, W. Bi, S. Sinogeikin, M. Y. Hu, E. E. Alp, X. C. Wang, C. Q. Jin and J. F. Lin, *Rev. Sci. Instrum.*, 2017, **88**, 1–9.

335 J. C. Chervin, B. Canny, J. M. Besson and P. Pruzan, *Rev. Sci. Instrum.*, 1995, **66**, 2595–2598.

336 J. E. Proctor, E. Gregoryanz, K. S. Novoselov, M. Lotya, J. N. Coleman and M. P. Halsall, *Phys. Rev. B*, 2009, **80**, 1–7.

337 T. Kume, Y. Fukaya, S. Sasaki and H. Shimizu, *Rev. Sci. Instrum.*, 2002, **73**, 2355–2359.

338 C. Kahle and U. Holzgrabe, *Chirality*, 2004, **16**, 509–515.

339 F. L. Aachmann, D. E. Otzen, K. L. Larsen and R. Wimmer, *Protein Eng. Des. Sel.*, 2004, **16**, 905–912.

340 F. Aachmann, K. L. Larsen, B. R. Knudsen, D. E. Otzen and R. Wimmer, *Protein*

Sci., 2002, **11**, 1779–1787.

341 Y. Dotsikas and Y. L. Loukas, *J. Pharm. Biomed. Anal.*, 2002, **29**, 487–494.

342 J. Horsk and J. Pitha, *J. Incl. Phenom. Mol. Recognit. Chem.*, 1994, **18**, 291–300.

343 M. Khajehpour, T. Troxler, V. Nanda and J. M. Vanderkooi, *Proteins Struct. Funct. Bioinforma.*, 2004, **55**, 275–287.

344 T. Serno, R. Geidobler and G. Winter, *Adv. Drug Deliv. Rev.*, 2011, **63**, 1086–1106.

345 S. Ghosh, C. Ghosh, S. Nandi and K. Bhattacharyya, *Phys. Chem. Chem. Phys.*, 2015, **17**, 8017–8027.

346 M. Vandevenne, G. Gaspard, E. M. Belgsir, M. Ramnath, Y. Cenatiempo, D. Marechal, M. Dumoulin, J. M. Frere, A. Matagne, M. Galleni and P. Filee, *Biochim. Biophys. Acta - Proteins Proteomics*, 2011, **1814**, 1146–1153.

347 H. S. Samra, F. He, A. Bhambhani, J. D. Pipkin, R. Zimmerer, S. B. Joshi and C. R. Middaugh, *J. Pharm. Sci.*, 2010, **99**, 2800–2818.

348 R. Challa, A. Ahuja, J. Ali and R. K. Khar, *AAPS PharmSciTech*, 2006, **6**, E329–E357.

349 G. H. C. Varca, N. Andreo-Filho, P. S. Lopes and H. G. Ferraz, *Curr. Protein Pept. Sci.*, 2010, **11**, 255–263.

350 J. D. Badjić, A. Nelson, S. J. Cantrill, W. B. Turnbull and J. F. Stoddart, *Acc. Chem. Res.*, 2005, **38**, 723–732.

351 J. M. Campiña, A. Martins and F. Silva, *Electrochim. Acta*, 2009, **55**, 90–103.

352 H. Wang, S. Chen, L. Li and S. Jiang, *Langmuir*, 2005, **21**, 2633–2636.

353 E. Pensa, E. Cortés, G. Corthey, P. Carro, C. Vericat, M. H. Fonticelli, G. Benítez, A. A. Rubert and R. C. Salvarezza, *Acc. Chem. Res.*, 2012, **45**, 1183–1192.

354 M. T. Rojas, R. Koniger, J. F. Stoddart and a E. Kaifer, *J. Am. Chem. Soc.*, 1995, **117**, 336–343.

355 In *Membrane Science and Technology*, Elsevier, 2005, vol. 11, pp. 40–104.

356 N. Sharma and A. Baldi, *Drug Deliv.*, 2016, 23, 739–757.

357 G. Nelles, M. Weisser, R. Back and P. Wohlfart, *J. …*, 1996, **23**, 125–128.

358 J. A. Rogers, A. A. Maznev, M. J. Banet and K. A. Nelson, in *Annual Review of Materials Science*, Wiley, 2000, vol. 30, pp. 117–157.

359 E. Laviron, *J. Electroanal. Chem.*, 1979, **101**, 19–28.

360 T. Laredo, J. Leitch, M. Chen, I. J. Burgess, J. R. Dutcher and J. Lipkowski, *Langmuir*, 2007, **23**, 6205–6211.

361 A. Świetlow, M. Skoog and G. Johansson, *Electroanalysis*, 1992, **4**, 921–928.

362 M. Luo and J. Frechette, *J. Phys. Chem. C*, 2010, **114**, 20167–20172.

363 S. H. Khan, K. Farkas, R. Kumar and J. Ling, *Anal. Biochem.*, 2012, **421**, 385–390.

364 S. Perspicace, D. Banner, J. Benz, F. Müller, D. Schlatter and W. Huber, *J. Biomol. Screen.*, 2009, **14**, 337–349.

365 Y. Liu, Y. Liu and R. Guo, *J. Colloid Interface Sci.*, 2010, **351**, 180–189.

366 H. Wang, D. G. Castner, B. D. Ratner and S. Jiang, *Langmuir*, 2004, **20**, 1877–1887.

367 M. S. Wagner and D. G. Castner, in *Applied Surface Science*, 2004, vol. 231–232, pp. 366–376.

368 J. W. Park, I. H. Cho, D. W. Moon, S. H. Paek and T. G. Lee, *Surf. Interface Anal.*, 2011, **43**, 285–289.

369 G. F. Trindade, M. L. Abel and J. F. Watts, *Chemom. Intell. Lab. Syst.*, 2018, **182**, 180–187.

370 H. Liu, X. Liu, J. Meng, P. Zhang, G. Yang, B. Su, K. Sun, L. Chen, D. Han, S. Wang and L. Jiang, *Adv. Mater.*, 2013, **25**, 922–927.

371 B. S. Gomes, B. Simões and P. M. Mendes, *Nat. Rev. Chem.*, 2018, **2**, 120–126.

372 E. Kovalenko, M. Vilaseca, M. Díaz-Lobo, A. N. Masliy, C. Vicent and V. P. Fedin, *J. Am. Soc. Mass Spectrom.*, 2016, **27**, 265–276.

373 J. Lagona, P. Mukhopadhyay, S. Chakrabarti and L. Isaacs, *Angew. Chemie Int. Ed.*, 2005, **44**, 4844–4870.

374 J. Kim, I. S. Jung, S. Y. Kim, E. Lee, J. K. Kang, S. Sakamoto, K. Yamaguchi and K. Kim, *J. Am. Chem. Soc.*, 2000, **122**, 540–541.

375 L. Gilberg, M. S. A. Khan, M. Enderesova and V. Sindelar, *Org. Lett.*, 2014, **16**, 2446–2449.

376 N. Dong, J. He, T. Li, A. Peralta, M. R. Avei, M. Ma and A. E. Kaifer, *J. Org. Chem.*, 2018, **83**, 5467–5473.

377 K. Kim, N. Selvapalam, Y. H. Ko, K. M. Park, D. Kim and J. Kim, *Chem. Soc. Rev.*, 2007, **36**, 267–279.

378 M. Singh, G. Parvari, M. Botoshansky, E. Keinan and O. Reany, *European J. Org. Chem.*, 2014, **2014**, 933–940.

379 F. Hamada, G. W. Orr, A. W. Coleman, H. Zhang, S. G. Bott and J. L. Atwood, *J. Incl. Phenom. Mol. Recognit. Chem.*, 2005, **9**, 195–206.

380 R. Keuleers, H. O. Desseyn, B. Rousseau and C. Van Alsenoy, *J. Phys. Chem. A*, 1999, **103**, 4621–4630.

381 O. El Jaroudi, E. Picquenard, N. Gobeltz, A. Demortier and J. Corset, *Inorg. Chem.*, 1999, **38**, 2917–2923.

382 S. Mahajan, T. C. Lee, F. Biedermann, J. T. Hugall, J. J. Baumberg and O. A. Scherman, *Phys. Chem. Chem. Phys.*, 2010, **12**, 10429–10433.

383 R. L. Garrell, C. Szafranski and W. Tanner, in *Raman and Luminescence Spectroscopies in Technology II*, eds. F. Adar and J. E. Griffiths, International Society for Optics and Photonics, 2005, vol. 1336, pp. 264–271.

384 G. Liu, Q. Fang, W. Xu, H. Chen and C. Wang, *Spectrochim. Acta Part A Mol. Biomol. Spectrosc.*, 2004, **60**, 541–550.

385 S. A. Solin and A. K. Ramdas, *Phys. Rev. B*, 1970, **1**, 1687–1698.

386 A. F. Goncharov, *Int. J. Spectrosc.*, 2012, **2012**, 1–16.

387 G. Socrates, in *Journal of Raman Spectroscopy*, 2001, pp. 347–352.